# Nonlinear surface waves over topography

*Niet-lineaire oppervlaktegolven over variabele diepte*

# Nonlinear surface waves over topography

Proefschrift

ter verkrijging van de graad van doctor
aan de Technische Universiteit Delft,
op gezag van de Rector Magnificus prof.dr.ir. J.T. Fokkema,
voorzitter van het College voor Promoties,
in het openbaar te verdedigen op dinsdag 23 mei 2006 om 15:00 uur

door

Tim Thijs JANSSEN
civiel ingenieur
geboren te Heumen

Dit manuscript is goedgekeurd door de promotoren:
 Prof.dr.ir. J.A. Battjes
 Prof.dr.ir. T.H.C. Herbers

Samenstelling promotiecommissie:
 Rector Magnificus                    voorzitter
 Prof.dr.ir. J.A. Battjes             Technische Universiteit Delft, promotor
 Prof.dr.ir. T.H.C. Herbers           Naval Postgraduate School, USA, promotor
 Prof.dr.ir. E.W.C. van Groesen       Technische Universiteit Twente
 Prof.dr.ir. A.W. Heemink             Technische Universiteit Delft
 Prof.dr. P.A. Madsen                 Danmarks Tekniske Universitet
 Prof. J. Monbaliu                    Katholieke Universiteit Leuven
 Dr.ir. A.J.H.M Reniers               Technische Universiteit Delft

Cover design by Anke Pierik

# Acknowledgments

# Abstract

## Nonlinear surface waves over topography

As ocean surface waves radiate into shallow coastal areas and onto beaches, their lengths shorten, wave heights increase, and the wave shape transforms from near-sinusoidal to the characteristic saw-tooth shapes at the onset of breaking; in the ensuing breaking process the wave energy is cascaded to small-scale turbulent motions in the surf zone. This nearshore transformation of ocean waves, and the modeling thereof, is the subject of this thesis. In particular, the integral objective of the present work is to develop and verify a stochastic model for directionally spread random wave fields over topography in the nearshore.

We have developed a deterministic spectral evolution model based on a multi-frequency, angular spectrum decomposition of the wave field. The model consists of a set of coupled-mode transport equations for the spectral amplitudes. Two-dimensional topography is accounted for through a scattering mechanism, which redistributes the angular component amplitudes such that the resulting ray geometry corresponds to the actual (two-dimensional) topography. The model is an extension of previous work in the sense that (i) arbitrary resonance mismatch for quadratic interactions is accounted for, thus including both the Stokes-regime and the shallow-water (Boussinesq) regime; (ii) the model accounts for cubic (quadruplet) interactions without the shallow-water break-down typically associated with Stokes-type expansions. The model is verified through comparison to well-known analytical expressions in both the deep- and shallow-water regime. Empirical verification with laboratory observations of nonlinear wave evolution confirms (i) the unified description of the quadratic and cubic nonlinear effects, and (ii) the robustness of the scattering approach to account for the interaction with the topography.

On the basis of the deterministic model a stochastic model is derived which computes the wave field statistics directly without the need for repeated simulation (as in a Monte-Carlo simulation). This gain in efficiency comes at the expense of an additional approximation: a so-called closure hypothesis. The stochastic model consists of a coupled set of transport equations for the spectrum and bi-spectrum respectively and as such accounts for quadratic interactions; cubic nonlinear effects are not accounted for in this model. The model is closed in the linear sense which implies that it accounts for the (linear) effects of refraction and diffraction with the same accuracy as the underlying deterministic model. Moreover, and in contrast to conventional stochastic wave models

based on the energy balance equation, the present model thus accounts for directional coherence in crossing waves which is important e.g. in focal regions and around thin barriers. To extend modeling capability to the surf zone, parameterizations for depth-induced wave breaking and stochastic relaxation are developed and incorporated. Verification of the resulting model with laboratory and field observations for a range of wave conditions and topographies, confirms the model's robustness and its suitability for application to wave propagation in the nearshore, including the surf zone.

In conclusion: the present study has resulted in the development and verification of both a deterministic and stochastic model for nearshore wave propagation. The deterministic model is suitable for larger propagation distances and deeper water, whereas the stochastic model is particularly aimed at the nearshore, including the surf zone. Both models are verified analytically and empirically, which demonstrates the robustness and potential of the present approaches to operational modeling of nearshore wave field evolution.

<div style="text-align: right;">

Tim Janssen
May 2006

</div>

# Samenvatting

## Niet-lineaire oppervlaktegolven over variabele diepte

Wanneer windgolven ondiepe kustgebieden binnenlopen en het strand naderen, neemt hun lengte af, hun hoogte neemt toe en hun vorm verandert van bijna sinusoïdaal tot de typische zaagtandvorm vlakbij het breekpunt; met het uiteindelijk breken van de golven wordt de energie omgezet in turbulentie. Deze transformatie van golven in het kustgebied is het onderwerp van dit proefschrift. Meer specifiek, het integrale doel van dit werk is het afleiden en verifiëren van een stochastisch model geschikt voor realistische golfvelden over twee-dimensionale bodemvormen in de kustzone.

Allereerst is een deterministisch spectraal model ontwikkeld, gebaseerd op een multi-frequentie, hoek-spectrum decompositie van het golfveld. Dit model bestaat uit een gekoppeld stelsel transportvergelijkingen voor de spectrale amplituden van het golfveld. De twee-dimensionaliteit van de bodem is verdisconteerd middels een verstrooiingsterm, zodanig dat de golfstraalgeometrie in overeenstemming is met de feitelijke (twee-dimensionale) bodemtopografie. Het model is een uitbreiding van eerder werk omdat het (i) geldig is voor arbitraire afwijking van resonantie voor de kwadratische wisselwerkingen en als zodanig ten aanzien van deze wisselwerkingen zowel het zogenaamde Stokes (diep water) als het Boussinesq (ondiep water) regime omvat; (ii) het model beschrijft de effecten van kubische niet-lineariteiten maar blijft geldig in ondiep water waar standaard Stokes-type expansies divergeren. Het model is geverifieerd middels vergelijking met beschikbare analytische uitdrukkingen voor de diep- en ondiepwaterlimieten; empirische verificatie met laboratoriummetingen bevestigt (i) de geünificeerde beschrijving van kwadratische en kubische niet-lineaire koppelingen; (ii) de robuustheid van de modellering ten aanzien van de wisselwerkingen van het golfveld met de twee-dimensionale bodem.

Op basis van het deterministische model is een stochastisch model afgeleid dat de golfveldstatistiek berekent zonder dat daarvoor herhaalde berekeningen (zoals in een Monte-Carlo simulatie) nodig zijn; deze winst in efficiëntie vereist een additionele aan-name, te weten een zogenaamde sluitingshypothese. Het stochastisch model bestaat uit een gekoppeld stelsel transportvergelijkingen voor het spectrum en het bispectrum, en als zodanig beschrijft het kwadratische niet-lineaire effecten; kubische golf-golf koppelingen zijn niet verdisconteerd in dit model. In de lineaire benadering is het stochastische model gesloten, wat impliceert dat het model de (lineaire) effecten van refractie en diffractie met dezelfde nauwkeurigheid beschrijft als het onderliggende deterministische model. Het model – en hierin verschilt het van conventionele fase-middelende modellen gebaseerd op

de energiebalansvergelijking – beschrijft dus tevens de coherentie in twee-dimensionale golfvelden en is als zodanig geschikt voor heterogene golfveldcondities, inclusief sterke diffractieëffecten, zoals bijvoorbeeld relevant is in convergentiezones en in de nabijheid van obstakels. Teneinde modellering van de brandingszone mogelijk te maken, is een dissipatieterm voor diepte-geïnduceerd breken en een stochastische relaxatieterm ontwikkeld en geïmplementeerd. Verificatie van het model met een uiteenlopende set van laboratorium- en veldmetingen bevestigt de robuustheid en het potentieel van het model voor operationele golfveldvoorspellingen in de kustzone, inclusief de brandingszone.

Concluderend: deze studie heeft geleid tot de ontwikkeling en succesvolle verificatie van zowel een deterministisch als een stochastisch golfmodel. Het deterministische model is – dankzij de toevoeging van hogere orde niet-lineariteiten – geschikt voor relatief langere ontwikkelingsafstanden en dieper water; het stochastische model is – door de geparameteriseerde beschrijving van dissipatie van golfenergie door breking en relaxatie van niet-lineaire koppelingen – bij uitstek geschikt voor ondiepe kustgebieden, inclusief de brandingszone. Zowel analytische als empirische verificatie van beide modellen is gepresenteerd en deze bevestigt de robuustheid van de modelleringsaanpak en het potentieel voor operationele voorspelling van de golfveld-evolutie in het kustgebied.

<div align="right">

Tim Janssen
mei 2006

</div>

# Contents

# Introduction 1

When visiting an exposed ocean beach on a 'big' day, the sight and roaring of powerful large, long-period ocean waves, breaking as they enter shallow water, are captivating; the rapid transition from sinusoidal wave forms to the characteristic sawtooth shapes with near-vertical faces at the onset of breaking; the turning-over of the wave, the violent (and deafening) plunging of the crest through the smooth surface just in front of it, and – finally – the transition from ordered wave motion into an increasingly chaotic and turbulent ('white') water mass, progressively dissipating the energy associated with the incident wave motion.

The esthetics are best appreciated holistically. However, the incessant and often powerful wave-induced fluid motions have important implications for e.g. the nearshore marine biology/ecology, coastal engineering and recreation, which provides the impetus behind scientific research into the dynamics of ocean waves in coastal waters, to which this study is intended to contribute.

As ocean waves advance from deep water into shallow coastal areas and onto beaches they transform owing primarily to refraction and nonlinear wave interactions, the latter dominated by near-resonant quadratic interactions involving triplets of waves. These nonlinear effects cause the transformation to the characteristic skewed, pitched-forward shapes of waves observed on beaches [e.g. Elgar & Guza, 1985], they induce the formation of multi-crest wave trains behind submerged obstacles [e.g. Johnson *et al.*, 1951; Byrne, 1969], and radiate long wave motion in the nearshore region. These effects are recognized as major factors in the study of nearshore morphological evolution [e.g. Roelvink & Stive, 1989; Hoefel & Elgar, 2003] and are of paramount importance in the design of coastal structures and harbors.

Although advances in modern water wave theory were reported as early as in the $17^{th}$ century by Newton [Craik, 2004], and a fully nonlinear description of water waves was already given by Gerstner in 1802 [Lamb, 1932, §article 251], it is probably fair to say that our present-day conceptual and theoretical understanding of nonlinear surface wave motion derives primarily from the pioneering observations and experiments by Russell [1838, 1844], and the monumental theoretical work by Stokes [1847][†]. These milestone

---

[†]Historically it is appropriate to remark that Kelland [1840], based on what Craik referred to as a 'dubious analysis' [Craik, 2004], published a dispersion relation for water waves that included what is now usually referred to as Stokes' amplitude dispersion correction, at least for deep water; in finite depth it is incorrect. Nonetheless, it preceded Stokes' deep-water result by seven years and it was not until forty years later that Stokes finally presented the (correct) finite depth expressions [Stokes, 1880].

works implied an acute paradigm shift and were certainly not without controversy initially. For instance, with respect to Stokes' weakly nonlinear theory Rayleigh remarked [Rayleigh, 1876, pp 270] '...it seems to me by no means certain that any such (Stokes, ed.) type exists, capable of propagating itself unchanged with uniform velocity...'. Likewise, Russell's observation of what he referred to as a 'solitary' wave (and descriptively designated as the 'Great Primary Wave of Translation') led to a controversy with Airy, who was unconvinced that these waves where external to the existing body of theory for nonlinear long waves [Rayleigh, 1876; Ablowitz & Segur, 1981]; the latter was not resolved until the theoretical work on shallow-water waves by Boussinesq [1872], Rayleigh [1876], and later Korteweg & De Vries [1895](KdV hereafter). These (and other) early advances in the theoretical understanding of what Whitham later referred to as 'Laplace's equation with strange boundary conditions at the free surface' [Whitham, 1974, pp. 4] formed the basis from which the more recent developments in nonlinear wave theory and modeling, starting in the 1960's with the advent of modern computers, could flourish.

In the 1960's renaissance, Boussinesq theory was made suitable for non-uniform depth [Mei & LeMéhauté, 1966; Peregrine, 1967], and subsequently used to study evolution of solitary [e.g. Madsen & Mei, 1969], and time-periodic [e.g. Madsen *et al.*, 1970] waves over variable depth. Since then a continual extension of Boussinesq theory has been ongoing [see e.g. Madsen & Sørensen, 1992; Nwogu, 1993; Chen & Liu, 1995] with major recent advances in their application to extremely nonlinear waves and deeper water [see e.g. Wei *et al.*, 1995; Madsen & Schäffer, 1998; Madsen *et al.*, 2003; Fuhrman *et al.*, 2004]. Excellent overviews on the state of development are given in e.g. Kirby [1995], Dingemans [1997] Chapter 5, and Madsen & Schäffer [1999].

Advances in nonlinear solids renewed interest in Russell's 'Primary Wave of Translation'. Triggered by the pioneering observations of recurrence in numerical simulations of a weakly nonlinear lattice [Fermi *et al.*, 1955], Zabusky & Kruskal [1965] re-derived the KdV equation and discovered particle-like behavior of the KdV solitary waves (the hyperbolic secant squared), which they subsequently labeled as 'solitons'. With the advent of the inverse scattering transform [Gardner *et al.*, 1967, 1974] these soliton-type wave forms were soon shown to exist for other equations also [Zakharov & Shabat, 1972; Ablowitz *et al.*, 1973*a,b*, 1974], which aroused great interest in many branches of physics and mathematics. This is probably one of the first accounts where the judicious use of numerical simulation [Fermi *et al.*, 1955; Zabusky & Kruskal, 1965] led to the discovery of a whole new field of science [Zabusky, 1981]; an overview is given in Ablowitz & Segur [1981]. Two-dimensional generalizations of the periodic cnoidal-wave solutions of the KdV equation were given by Segur & Finkel [1985] based on a multi-parameter family of exact solutions for the KP equation [Kadomtsev & Petviashvili, 1970], a weakly two-dimensional extension of the KdV equation. Hammack *et al.* [1989, 1995] empirically verified the existence of such two-dimensional bi-periodic wave forms (in both spatial dimensions of the fluid surface) that propagate in shallow water without change of shape.

Based on a spectral generalization of a Stokes-type expansion, Phillips [1960] demonstrated that secular terms at the third order in wave steepness allow a continuous flow of energy across spectral components, which implies leading-order dynamical consequences over asymptotic length scales. Hasselmann [1962, 1963] embedded this paradigm in a statistical description of the sea surface and derived a stochastic model for the non-linear evolution of the wave field, accounting for such quartet resonances. (See also Phillips [1981] for an historical account of these advances in a much wider context than considered here.) This unification of small-amplitude wave theory with the concepts of statistical physics stands at the heart of widely-used, present-day operational wave models [Komen *et al.*, 1994; Booij *et al.*, 1999], and gave impetus to further advances of the statistical description of nonlinear wave evolution [e.g. Benney & Saffman, 1966; Benney & Newell, 1969; Newell & Aucoin, 1971]. The work by Hasselmann and – in a deterministic context – the development of the Zakharov equation [e.g. Zakharov, 1968; Stiassnie & Shemer, 1984], and the narrow-band NLS and Dysthe equation [e.g. Zakharov, 1968; Chu & Mei, 1970; Hasimoto & Ono, 1972; Dysthe, 1979] consider cubic resonances, while treating quadratic interactions as non-secular, i.e. forced excitations of small amplitude. This premise is suitable in finite depth where the dispersion relation precludes resonance at the second-order, but is invalid in shallow water where – as already indicated by Phillips [1960] – quadratic interactions approach resonance and therefore have dynamical implications.

*Near-resonant theory: amplitude evolution equations*
Although Phillips (rightly) anticipated that second-order interactions (both sum and difference interactions) have dynamical consequences in shallow water, his expansion was incompatible with such near-resonances. This led Bretherton [1964] to devise a formalism based on multiple scales that supported modeling of near-secular contributions. Based on Bretherton's work and contemporary advances in nonlinear optics [Armstrong *et al.*, 1962], Mei & Ünlüata [1972] and Bryant [1973] were the first to apply these ideas to shallow-water wave modeling; they demonstrated that energy and phase modifications associated with these interactions allow for nonlinear wave evolution in shallow water on much shorter space and time scales than those associated with (higher-order) quartet resonances, consistent with observations [Jolas, 1960] and Phillips' remarks. Freilich & Guza [1984] successfully modeled nearshore evolution of ocean waves on natural beaches utilizing evolution equations derived from Boussinesq theory [Peregrine, 1967]. A myriad of models based on these near-resonant principles emerged since then, suitable for unidirectional wave propagation [e.g. Agnon *et al.*, 1993; Bredmose *et al.*, 2004], directional waves over laterally uniform bathymetry [e.g. Herbers & Burton, 1997; Sheremet, 1996; Eldeberky & Madsen, 1999], and small-angle wave propagation over two-dimensional topography [e.g. Kaihatu & Kirby, 1995]. The later advances include full dispersion in the linear terms and interaction coefficients, and account for arbitrary

resonance mismatch [Bredmose *et al.*, 2002; Janssen *et al.*, 2004; Bredmose *et al.*, 2005][†];
nonetheless, they do not account for tertiary interactions, which implies a restriction to
fairly moderate water depth where the near-secularity (and thus dynamical relevance)
of quadratic contributions is warranted.

To illustrate the concept of amplitude evolution equations for shallow-water wave
propagation, consider for instance the KdV equation [see e.g. Dingemans, 1997, §6.1]

$$\frac{\partial \eta}{\partial t} + \sqrt{gh}\frac{\partial \eta}{\partial x} + \frac{3}{2}\sqrt{\frac{g}{h}}\eta\frac{\partial \eta}{\partial x} + \frac{1}{6}h^2\sqrt{gh}\frac{\partial^3 \eta}{\partial x^3} = 0, \tag{1.1}$$

which describes the free surface elevation ($\eta$) associated with unidirectional wave pro-
pagation over uniform depth in fairly shallow water. In (1.1), $g$ denotes gravitational
acceleration and $h$ represents (uniform) water depth. To solve this partial differential
equation as an amplitude evolution equation we write the surface elevation $\eta$ by means
of a Fourier series as

$$\eta(x,t) = \sum_{p=-\infty}^{\infty} \zeta_p(x) \exp\left[i\omega_p\left(\frac{x}{\sqrt{gh}} - t\right)\right] \tag{1.2}$$

such that the $\zeta_p(x)$ can be interpreted as slowly varying amplitudes of a time-periodic,
wave-like signal with the associated phase function $\omega_p(x/\sqrt{gh} - t)$. Since $\eta$ is a real
function, $\zeta_p = \zeta_{-p}^*$ with $*$ denoting the complex conjugate. The slow modulation of
the $\zeta_p(x)$ in the spatial dimension (the slowness can be formalized through multiple
scales but is simply postulated here) accounts for frequency dispersion and nonlinear
corrections. Upon substituting (1.2) into (1.1), omitting contributions involving $d\zeta_p/dx$
from the nonlinear and dispersive term (which are assumed small), we find the ordinary
differential equation for the spatial evolution of the component amplitudes $\zeta_p(x)$

$$\frac{d\zeta_p}{dx} = i\frac{\omega_p^3}{6}\sqrt{\frac{h}{g^3}}\zeta_p - i\frac{3\omega_p}{4\sqrt{gh^3}}\sum_{n=-\infty}^{\infty}\zeta_{p-n}\zeta_n. \tag{1.3}$$

The first term on the *RHS* of (1.3) accounts for a dispersion correction on account of
the dispersive term in (1.1); the convolution term on the *RHS* of (1.3) accounts for the
nonlinearity through a weighted mode-coupling of the spectral components and results
from the nonlinear term in (1.1). Thus by imposing a solution in the form of a superpo-
sition of time-periodic, wave-like functions, the partial differential equation in $x$ and $t$
is transformed to an (infinite) set of ordinary differential equations in one-dimensional

---

[†]Bryant's so-called $\mu$-exact model [Bryant, 1973] also includes full frequency dispersion *and* accounts
for arbitrary resonance mismatch. His derivation assumes uniform depth and is remarkably compact as
it describes the modulation in time of spatially periodic waves; later advances that include full frequency
dispersion and arbitrary resonance mismatch of quadratic interactions [Bredmose *et al.*, 2002; Janssen
*et al.*, 2004; Bredmose *et al.*, 2005; Janssen *et al.*, 2006] evolve time-periodic wave components through
space, which is better suited for waves advancing over variable depth.

space, which involve a spectral convolution term on account of the nonlinearity present in eq. (1.1). From a heuristic viewpoint it may appear somewhat troubling that the closed-form representation of (1.1) results in an infinite set of equations, but this merely reflects that the time variable is treated as continuous. As numerical evaluation of (1.1) requires discretization, this in turn implies a truncation of the series (1.2) rendering the set finite, say consisting of $N$ equations. Thus instead of solving for the surface elevation $\eta$ at $N$ time steps, we solve $O(N)$ equations for the spectral amplitudes $\zeta_p$. Such a coupled set of ordinary differential equations can generally be solved with simple and efficient numerical techniques [Bredmose $et\ al.$, 2004, 2005; Canuto $et\ al.$, 1987] and on account of the fact that the rapid spatial phase is split off (viz. (1.2)), the spatial evolution can be computed utilizing larger step sizes.

Although the integration of such amplitude evolution equations is relatively efficient, such considerations may not always be decisive in a deterministic context. After all, with the ever-increasing capacity of modern-day computers, numerical evaluation of time-domain, higher-order Boussinesq approximations [Wei $et\ al.$, 1995; Shi $et\ al.$, 2001; Fuhrman $et\ al.$, 2004] or even more general models [Westhuis, 2001; Stelling & Zijlema, 2003] come within reach. Such time-domain models are orders of magnitude computationally more demanding but potentially include more physics and are less approximate; in particular, they are generally more accurate on steep slopes and in the presence of strong nonlinearity. Then, apart from the fact that amplitude evolution equations are readily interpretable in terms of interacting 'waves', a concept so deeply ingrained in our conceptual understanding of nonlinear waves, it is primarily on account of the intrinsic random character of ocean waves that amplitude evolution equations, which provide a suitable platform for so-called stochastic modeling (see below), are pursued; such stochastic models provide an efficient means of modeling random waves on typical coastal scales, for which the computational effort associated with time-domain models is (still) prohibitive.

*Stochastic modeling in shallow water*

Ocean waves are generally considered as realizations of a stochastic process. As a consequence, the deterministic details of a single realization are usually of little interest and, moreover, phase-resolving boundary conditions, required to compute such detail, are unavailable. Statistical properties of the wave field can – in principle – be estimated through repeated simulation with a suitable deterministic model [Freilich & Guza, 1984] but this Monte-Carlo approach is computationally intensive. Alternatively, on the basis of amplitude evolution equations, stochastic models can be derived that consist of a set of transport equations for the statistical moments [e.g. Saffman, 1967], thus describing the evolution of the statistics without the need for repeated simulation. This efficiency gain, however, comes at the expense of an additional approximation: the so-called closure hypothesis, the nature of which is best illustrated by forming moment equations on the basis of the amplitude evolution equation (1.3). The evolution equation for the moment

$\langle|\zeta_p|^2\rangle$ (the $\langle\ \rangle$ denote ensemble averaging) is obtained through multiplication of (1.3) by $\zeta_p^*$, summing the resulting equation with its conjugate, and ensemble averaging the result, yielding

$$\frac{d}{dx}\langle|\zeta_p|^2\rangle = \frac{3\omega_p}{2\sqrt{gh^3}}\sum_{n=-\infty}^{\infty}\Im\{\langle\zeta_{p-n}\zeta_n\zeta_p^*\rangle\}, \qquad (1.4)$$

where $\Im\{\ \}$ denotes 'the imaginary part of'. From (1.4) we see that the evolution of $\langle|\zeta_p|^2\rangle$ depends on the triple-moment $\langle\zeta\zeta\zeta\rangle$ through the convolution term on the *RHS*. When forming the transport equation for the triple-moment, which is obtained through similar operations, it is readily observed that it depends on the quadruple moment $\langle\zeta\zeta\zeta\zeta\rangle$; this dependency on the next higher-order moment (or cumulant) continues indefinitely, and consequently renders the set of moment equations open. Numerical evaluation of the hierarchy of stochastic equations is possible only if a closure assumption of some sort is provided such that the hierarchy is represented by a finite number of equations. In deep water, a natural asymptotic closure exists for the quartet resonances [Hasselmann, 1962; Benney & Saffman, 1966] but in shallow water, on account of the reduced dispersiveness, such a natural closure appears unavailable. Although early attempts [Abreu *et al.*, 1992] were based on a so-called semi-dispersive wave closure [Newell & Aucoin, 1971], later advances usually applied the quasi-normal closure [Herbers & Burton, 1997; Agnon & Sheremet, 1997] or modifications thereof [Eldeberky, 1996; Eldeberky *et al.*, 1996; Becq *et al.*, 1998]. In general, the quasi-normal closure, which essentially omits the fourth and higher cumulants, renders statistics that are too far from Gaussian, and is particularly inaccurate in the presence of strong nonlinearity (e.g. the surf zone). To extend modeling capability to highly nonlinear, dissipative regions, Herbers *et al.* [2003] proposed a closure approximation involving a relaxation term that allows a return to Gaussian statistics in the presence of strong nonlinear interactions, reminiscent of eddy relaxation in turbulence [Orszag, 1970].

*Stochastic modeling over topography*
Operational stochastic wave models [e.g. Komen *et al.*, 1994; Booij *et al.*, 1999] are generally based on the so-called action balance equation, which expresses the conservation of action in a slowly varying medium, with forcing (or source) terms added to account for physical processes such as e.g. wind stress on the fluid surface, nonlinear energy redistribution and dissipation on account of wave breaking. This description is an isotropic representation of the evolution of a spatially homogeneous wave field through a slowly varying medium. However, extension of this approach to include three-wave coupling from first principles is not straightforward as an isotropic evolution equation for the higher-order correlations is unavailable. Although approximations to augment the action balance equation with suitable source terms to account for near-resonant quadratic interaction have been reported [e.g. Eldeberky, 1996; Becq, 1998], later advances in nonlinear shallow-water modeling [Herbers & Burton, 1997; Agnon & Sheremet, 1997; Eldeberky & Madsen, 1999] abandoned this approach in favor of

a frequency/lateral wavenumber decomposition of the two-dimensional wave field; this so-called multi-frequency angular-spectrum decomposition [e.g. Stamnes, 1986] is a natural choice for wide-angle wave propagation over laterally uniform (one-dimensional) topography.

In the present work we follow the multi-frequency angular-spectrum approach but include two-dimensional topography through a Taylor expansion of the bottom boundary condition [Dalrymple *et al.*, 1989; Suh *et al.*, 1990]. In the coupled-mode transport equations for the (deterministic) frequency/angular components, the topographical forcing is represented through a scattering term that redistributes the angular amplitudes to correct the ray geometry in accordance with the topography. The stochastic model is based on the deterministic coupled-mode model and consists of a coupled set of transport equations for the spectrum and bi-spectrum respectively. In the stochastic framework, the scattering on submerged topography induces correlations between non-collinear wave trains; these cross-correlations capture the spatial inhomogeneity of the waves on account of the underlying topography, which is important for the modeling of e.g. crossing waves in the convergence zone of a topographical lens. Based on this stochastic angular-spectrum formalism we develop and verify a stochastic model suitable for inhomogeneous, two-dimensional, random wave fields over nearshore topography, including the surf zone.

## 1.1 Objective and outline of the present study

The integral objective of the present study is to develop and verify – both analytically and empirically – a stochastic model for surface gravity waves, suitable for application to two-dimensional random wave fields over topography in shallow water, including the surf zone, and apply it to the study of nonlinear waves over variable depth, including the forcing of long waves through quadratic difference interactions.

We first develop a deterministic evolution model suitable for nonlinear wave evolution over topography. This is achieved by means of a multi-frequency angular-spectrum decomposition applied to the governing equations for irrotational flow of an inviscid and incompressible fluid with a free surface (Chapter 2); the deterministic model accounts for quadratic and cubic interactions in a unified manner, and includes two-dimensional topography through a scattering mechanism. In Chapter 3 we present analytical and empirical verification of the unified treatment of quadratic-cubic nonlinearity and two-dimensional capability embedded in the deterministic model.

Based on the deterministic model, but omitting cubic interactions and the interaction with the wave-induced current field, a stochastic model formalism is derived in Chapter 4. In this chapter we introduce and illustrate the stochastic representation of laterally heterogeneous wave propagation. To extend the modeling capability to dissipative and strongly nonlinear regions, parameterizations for depth-induced wave breaking and a Gaussian relaxation closure are developed. Empirical verification of the stochastic model is presented in Chapter 5, including a wide range of wave conditions and topography to assess its robustness and limitations.

In Chapter 6 we study the shoaling behavior of wave-group induced long waves over variable depth, and assess the ability to model the nonlinear energy transfers and phase coupling with the stochastic model developed in Chapter 4. Detailed laboratory observations are used to examine the phase shift between wave groups and associated long wave motion over variable depth, and verify the model-predicted correlations and spectra.

Discussion of the deterministic model (Chapter 2 and Chapter 3) and stochastic model (Chapter 4 and Chapter 5) is provided in the closing sections of Chapter 3 and Chapter 5 respectively. A short discussion on our findings related to wave-group induced long waves is given in the final section of Chapter 6.

Overall conclusions of the present study are presented in Chapter 7.

# Nonlinear waves over topography: deterministic theory **2**

Since the seminal work by Stokes (1847), the nonlinear evolution of gravity waves on the surface of the oceans has received much attention and major advances have been made [e.g. Phillips, 1960; Whitham, 1974]. General formulations, without inherent limitations on spectral width, were derived for the deep ocean [Hasselmann, 1962; Zakharov, 1968], and for regions of finite depth [Herterich & Hasselmann, 1980; Stiassnie & Shemer, 1984]. These models account for cross-spectral energy transfer by cubic resonances, the lowest-order nonlinear resonances for gravity surface waves in finite depth, that involve the mutual interaction between quadruples of wave components.

As waves cross the continental shelf and propagate into shallow coastal areas, the presence of submerged topography increasingly affects the wave field evolution through refraction by large-scale depth variations [e.g. Munk & Traylor, 1947; Battjes, 1968] and Bragg-type scatter over bottom features which vary on the scale of the surface wave length [e.g. Mei, 1985; Ardhuin & Herbers, 2002; Elgar *et al.*, 2003]. The effects of slowly varying topography on the nonlinear evolution of narrow-band waves was incorporated in Chu & Mei [1970] and Djordjević & Redekopp [1978]; the work by Liu & Dingemans [1989] also accounts for rapid topographical undulations. These models describe the slow variation of the wave envelope and the concomitant wave-induced mean-flow. However, apart from the one-dimensional simulations in Dingemans *et al.* [1991], few numerical implementations have been reported. The angular-spectrum approach by Dalrymple & Kirby [1988] includes full directionality in the half plane and is suited for wide-aperture diffraction such as e.g. encountered around breakwater gaps [see e.g. Stamnes, 1986]. This approach eliminates the lateral dimension from the governing equations, describing two-dimensional wave propagation through a set of ODEs and a simple eikonal relation; it is extended to laterally varying depth, through a Taylor expansion of the bottom boundary condition, and to third-order Stokes waves by Dalrymple *et al.* [1989] and Suh *et al.* [1990]. Numerical simulations based on the nonlinear angular-spectrum approach showed good agreement with observations of finite-amplitude wave evolution over topography [Dalrymple *et al.*, 1989; Suh *et al.*, 1990].

The prevalence of cubic interactions over quadratic interactions (which are of lower order) in deeper water is due to the fact that the dispersion relation for surface waves does not support resonances between triplets of waves in finite depth. Therefore, finite-depth models with cubic interactions as the dominant nonlinear mechanism invariably assume quadratic interactions off-resonant, rendering them incompatible with shallow

water where quadratic interactions approach resonance, i.e. where the Stokes number is
$O(1)$ [e.g. Bryant, 1974].

As a consequence, in the nearshore, wave models are historically based on a different
asymptote of nonlinear wave theories. The classical uniform-depth theories of Boussinesq
[1871] and Korteweg & De Vries [1895], extended to variable depth [Mei & LeMéhauté,
1966; Peregrine, 1967], assume nonlinearity, $a/h$, and dispersion, $\mu^2$ of the same order,
i.e. the Stokes number, $(a/h)/\mu^2$, is assumed O(1) [see e.g. Dingemans 1997 Chapter 5 &
6 for an overview]. Following progress in nonlinear optics [Armstrong *et al.*, 1962] and the
work by Bretherton [1964], amplitude evolution equations based on Boussinesq theory
were developed to describe the effects of quadratic near-resonances in uniform depth
[e.g. Mei & Ünlüata, 1972; Bryant, 1973], over undulating topography [Lau & Barcilon,
1972] and over arbitrary but mildly varying depth [Freilich & Guza, 1984]. Keller [1988]
showed that similar equations are in fact derivable from fully dispersive theory. Many
models have emerged since then, either based on Boussinesq theory [e.g. Madsen &
Sørensen, 1993; Herbers & Burton, 1997] or fully dispersive theory, models that are
suitable for unidirectional waves over one-dimensional topography [e.g. Agnon *et al.*,
1993], small-angle models for two-dimensional topography [e.g. Kaihatu & Kirby, 1995;
Tang & Ouellet, 1997] and models for multi-directional wave propagation over laterally-
uniform topography [e.g. Sheremet, 1996; Eldeberky & Madsen, 1999]. In general, the
models based on fully-dispersive theory include full dispersion in the linear terms and
the non-linear interaction coefficient but retain the premise of near-resonance. The latter
restriction was removed by Bredmose *et al.* [2002, 2005] who apply suitable boundary
conditions on a general solution to the Laplace equation in the form of infinite expansions
of trigonometric functions [see also Madsen & Schäffer, 1998; Rayleigh, 1876]; based on
a conventional WKB wave field description, Janssen *et al.* [2004, 2006] derive evolution
equations that account for arbitrary resonant mismatch in quadratic interactions that –
to second-order and for unidirectional waves – can be shown identical to the expressions
in Bredmose *et al.* [2002].

In contrast to deep-water approaches, these models invariably include quadratic near-
resonances as the dominant nonlinear physics. However, they lack the ability to model
cubic near-resonances, which implicitly restricts them to relatively shallow regions where
the assumption of dominant quadratic interactions is warranted.

The following theoretical development aims at deriving generalized evolution equa-
tions suitable for surface wave propagation over two-dimensional topography, including
the transition from cubic wave-wave interactions in deep-intermediate water (Stokes
regime) to quadratic interactions in shallow water (Boussinesq regime) in a consistent
and unified manner. Our derivation is along the lines of Chu & Mei [1970], generalized to
a multi-frequency and multi-directional wave field utilizing an angular spectrum decom-
position of the wave field [e.g. Stamnes, 1986; Dalrymple *et al.*, 1989], and extended to
higher-order in the bound-wave components to support the transition to shallow water.
The effects of topographical features on the wave propagation are included through a

scattering mechanism [e.g. Suh *et al.*, 1990]. The resulting model does not break down in shallow water (where the Stokes number is $O(1)$), typical for models based on Stokes-type expansions, but instead reduces to a Boussinesq-type approximation.

In §2.1 we define the wave field and bottom decomposition, introduce notational conventions and a general treatment of secular forcing terms in the ordered boundary value problem. The finite depth solutions are given in §2.2 and extended to shallow water in §2.3. Based on these results, a uniformly valid evolution equation is presented in §2.4.

## 2.1  General theory

The starting point of our derivation is the governing set of equations for irrotational flow of an incompressible, inviscid fluid:

$$\nabla^2\Phi + \Phi_{zz} = 0, \qquad \forall z \in \mathcal{D}, \tag{2.1a}$$

$$\Phi_{tt} + g\Phi_z + \mathfrak{T}\left\{|\boldsymbol{\nabla}\Phi|^2 + (\Phi_z)^2\right\} = 0, \qquad z = \eta(x,y,t), \tag{2.1b}$$

$$\Phi_z + \boldsymbol{\nabla}h \cdot \boldsymbol{\nabla}\Phi = 0, \qquad z = -h(x,y), \tag{2.1c}$$

$$g\eta + \Phi_t + \tfrac{1}{2}\left(|\boldsymbol{\nabla}\Phi|^2 + (\Phi_z)^2\right) = 0. \qquad z = \eta(x,y,t). \tag{2.1d}$$

Here $\Phi$ is the velocity potential function, $\eta$ is the surface elevation and $g$ denotes gravitational acceleration; the operator $\mathfrak{T} = \left[\partial_t + \tfrac{1}{2}\boldsymbol{\nabla}\Phi \cdot \boldsymbol{\nabla} + \tfrac{1}{2}\Phi_z\partial_z\right]$. We use a Cartesian frame of reference with its origin at the undisturbed free surface of the fluid: $x$, $y$ denote the two horizontal coordinates and $z$ corresponds to the vertical coordinate, positive pointing upward. The operator $\boldsymbol{\nabla} \equiv (\partial_x, \partial_y)$, where $\partial_x$ is a shorthand for partial differentiation with respect to the subscripted variable. The Laplace equation (2.1a) follows from continuity. The free-surface boundary condition (2.1b) combines the kinematic and dynamic conditions while assuming a constant atmospheric pressure [see e.g. Phillips 1977 §3.1 or Dingemans 1997 §1.3]. Impermeability and immobility of the bottom is expressed by (2.1c), and the surface elevation is related to the velocity potential by the dynamic free-surface boundary condition (2.1d).

### 2.1.1 Decomposition for weak lateral depth variability

We consider weakly nonlinear surface waves propagating in finite water depth over slowly varying topography with weakly two-dimensional features. The topography is considered one-dimensional to leading order with a two-dimensional perturbation superposed, written as:

$$h(\boldsymbol{x}) = \overline{h}(x) - \widetilde{h}(\boldsymbol{x}).$$

Here $\overline{h}$ represents the lateral average of $h$; the $\widetilde{h}$ denotes the (two-dimensional) residue. Without loss of generality, we let the $x$- and $y$-axes coincide with the principal and lateral direction respectively, and since we are particularly interested in the description

of waves propagating from the deep open ocean into a shallow coastal area, we refer to the principal direction as the cross-shore direction and the lateral direction as the alongshore direction.

The magnitude of the lateral depth variations, $\widetilde{h}$, is characterized by the small parameter $\gamma$ defined as

$$O(\gamma) = O\left(\frac{\widetilde{h}_0}{\overline{h}_0}\right) \ll 1, \tag{2.2}$$

where $\widetilde{h}_0$ is a characteristic amplitude of $\widetilde{h}$ and $\overline{h}_0$ is a reference depth.

The nonlinearity of the wave field is governed by the parameter $O(\epsilon) = O(a_0/L_v) \ll 1$, where $a_0$ and $L_v$ denote a characteristic amplitude of the surface elevation and a representative vertical length scale of the wave motion respectively. Since we consider wave propagation from deep to shallow water we choose a generally applicable vertical length scale $L_v = \mu/k_0$, where $k_0$ is a representative wavenumber of the wave motion and $\mu = \tanh k_0\overline{h}_0$, which can be considered a generalized dispersion parameter varying from $O(1)$ in deep-intermediate water to $O(k_0\overline{h}_0)$ in shallow water [see also Beji, 1995; Kirby, 1998].

The depth variations are assumed small over distances $O(k_0^{-1})$, made explicit by the parameter $\beta$, where

$$O(\beta) = O\left(\frac{\partial_x \overline{h}}{k_0 \overline{h}}\right) = O\left(\frac{|\boldsymbol{\nabla}\widetilde{h}|}{k_0 \overline{h}}\right) \ll 1. \tag{2.3}$$

We set the relative magnitudes of the relevant small parameters $O(\beta) = O(\gamma^2) = O(\epsilon^2/\mu^2)$ and define multiple scales [see e.g. Chu & Mei, 1970; Liu & Dingemans, 1989; Suh $et$ $al.$, 1990]:

$$\langle t_n, x_n, y_n \rangle = \left(\frac{\epsilon}{\mu}\right)^n \langle t, x, y \rangle, \qquad n = \{1, 2\}. \tag{2.4}$$

To make the ordering of the bottom perturbation explicit in the derivation we write

$$\widetilde{h} = \gamma\widehat{h}, \qquad\qquad \boldsymbol{\nabla}\widetilde{h} = \gamma^2 \boldsymbol{\nabla}_1\widehat{h}, \tag{2.5}$$

where $\widehat{h} \sim O(1)$ and $\boldsymbol{\nabla}_1 \equiv \langle \partial_{x_1}, \partial_{y_1} \rangle$.

In the present scaling the bottom slope is $O(\epsilon^2/\mu^2)$, affecting wave evolution at $O(\epsilon^2)$ in deep-intermediate water ($O(\mu) \sim O(1)$) and $O(\epsilon)$ in shallow water ($O(\mu^2) \sim O(\epsilon)$). This approximation is well-suited to typical coastal bathymetry with a sloping beach extending onto a relatively flat continental shelf. Moreover, the relative magnitude of the lateral depth variations, $\widetilde{h}$, is introduced at lower order, $O(\epsilon/\mu)$, to accurately resolve wave propagation over shallow submerged bathymetric features such as banks and shoals that are common in coastal areas. The scaling of (2.2)–(2.4) further implies that the characteristic length scale of the two-dimensional topography is long, $O(\mu/\epsilon)$, compared with the surface wavelength and thus the back-scattering of waves (induced

by bottom undulations of about half the surface wavelength) is neglected in the present approximation, consistent with estimates of wave scattering from natural continental shelf topography presented in earlier studies [e.g. Ardhuin & Herbers, 2002].

Following Chu & Mei [1970], the set (2.1) is solved by applying a perturbation expansion of the surface elevation and velocity potential. In order to capture both the leading-order effects of cubic resonances in deep-intermediate water and quadratic resonances in shallow water, we explicitly evaluate the bound-wave components induced by quadratic wave–wave interactions

$$
\begin{bmatrix} \Phi \\ \eta \end{bmatrix} = \sum_{n=1}^{\infty} \frac{\epsilon^n}{\mu^{n-1}} \left\{ \begin{bmatrix} \Phi^{(n,0)} \\ \eta^{(n,0)} \end{bmatrix} + \begin{bmatrix} \Phi^{(n,1)} \\ \eta^{(n,1)} \end{bmatrix} + \frac{\epsilon}{\mu^2} \begin{bmatrix} \Phi^{(n+1,2)} \\ \eta^{(n+1,2)} \end{bmatrix} \right\} + \text{HBC}. \qquad (2.6)
$$

The $(n,0)$ components correspond to the wave-driven mean flow, $(n,1)$ to free waves, and $(n+1,2)$ to quadratically coupled or bound waves. Anticipating the near-resonance of quadratic nonlinear forcing terms in shallow water, these are scaled with $\epsilon/\mu^2$ which has the appropriate deep- and shallow-water asymptotes of wave steepness, $a_0 k_0$, and the Stokes number, $a_0/(k_0^2 \overline{h}_0^3)$ [Stokes, 1847], respectively. The HBC in (2.6) denotes higher-order bound components (involving cubic and higher-order, non-resonant interactions) that will not be considered in the present analysis [see also Shemer et al., 2001].

The premise of a leading-order, alongshore-uniform topography supports a frequency $(\omega)$–alongshore wavenumber $(\lambda)$ or angular-spectrum decomposition [see e.g. Suh et al., 1990]. Accordingly we write the primary wave field (lowest-order free waves) as a summation of modulated plane waves propagating at discrete angles in positive $x$ direction:

$$
\begin{bmatrix} \Phi^{(1,1)} \\ \eta^{(1,1)} \end{bmatrix} = \sum_{\substack{p,q=-\infty \\ p \neq 0}}^{\infty} \begin{bmatrix} \widetilde{\phi}_{q,p}^{(1,1)} \\ \widetilde{\zeta}_{q,p}^{(1,1)} \end{bmatrix} \exp\left[i\left(\lambda_q y - \omega_p t\right)\right] = \sum_{\boldsymbol{v}} \begin{bmatrix} \phi_{\boldsymbol{v}}^{(1,1)} \\ \zeta_{\boldsymbol{v}}^{(1,1)} \end{bmatrix} E_{\boldsymbol{v}}. \qquad (2.7)
$$

Here $\lambda_q = q\Delta\lambda$ and $\omega_p = p\Delta\omega$ in which $\Delta\lambda$ and $\Delta\omega$ represent the discrete alongshore wavenumber and angular frequency spacing respectively. The summation over $\boldsymbol{v} = (q,p)$ is a shorthand for the summation over all combinations of the discrete frequencies and alongshore wavenumbers. We exclude zero-frequency components $(p = 0)$ since these are part of the mean flow and are treated separately (Appendix C). The $\{\phi_{\boldsymbol{v}}^{(1,1)}, \zeta_{\boldsymbol{v}}^{(1,1)}\}$ are slowly varying amplitudes while the rapid phase variations are incorporated in $E_{\boldsymbol{v}}$, given as

$$
E_{\boldsymbol{v}} = \exp\left[i\left(\psi_{\boldsymbol{v}}(x) + \lambda_q y - \omega_p t\right)\right], \qquad \psi_{\boldsymbol{v}}(x) = \int^x \varkappa_{\boldsymbol{v}}(x')\,dx'. \qquad (2.8)
$$

Here $\varkappa_{\boldsymbol{v}} = \text{sgn}(p)\sqrt{k_p^2 - \lambda_q^2}$, with sgn denoting the signum function, and $k_p$ is related to the angular frequency, $\omega_p$, through the lowest-order dispersion relation. Since $\Phi$ and $\eta$ are real functions we have $\phi_{\boldsymbol{v}}^{(1,1)} = \phi_{-\boldsymbol{v}}^{(1,1)*}$ and $\zeta_{\boldsymbol{v}}^{(1,1)} = \zeta_{-\boldsymbol{v}}^{(1,1)*}$, where $*$ denotes the complex conjugate.

In the present work we consider only propagating modes. We omit exponentially decaying (evanescent) modes, such as refractively trapped waves for which $|\lambda_q| > k_p$, and vertical eigenmodes. Such non-propagating modes may e.g. be excited around bathymetric features (refractive trapping) or on steep slopes and at domain boundaries; they can be important locally, but are confined to the near field (typically a few wavelengths) of their generation source. Away from such regions, at distances much greater than $O(\varkappa_{\boldsymbol{v}}^{-1})$, the wave field is accurately represented by the propagating modes [Stamnes, 1986]. The complete solution to the linearized problem and further discussion on the validity of the present approximation is given in §19.1 of Stamnes [1986].

Using the spectral decomposition (2.7), the total wave field (2.6) can be expressed as

$$
\begin{bmatrix} \Phi \\ \eta \end{bmatrix} = \sum_{n=1}^{\infty} \frac{\epsilon^n}{\mu^{n-1}} \left\{ \begin{bmatrix} \Phi^{(n,0)} \\ \eta^{(n,0)} \end{bmatrix} + \sum_{\boldsymbol{v}_1} \begin{bmatrix} \phi_1^{(n,1)} \\ \zeta_1^{(n,1)} \end{bmatrix} E_1 + \frac{\epsilon}{\mu^2} \sum_{\boldsymbol{v}_1, \boldsymbol{v}_2} \begin{bmatrix} \phi_{12}^{(n+1,2)} \\ \zeta_{12}^{(n+1,2)} \end{bmatrix} E_{12} \right\} + \text{H.B.C.} \quad (2.9)
$$

For notational convenience, we write $E_{12\ldots n} = E_1 E_2 \ldots E_n$ and apply numerical subscripts to identify individual wave components, for example $\phi_1^{(n,1)}$ is a shorthand for $\phi_{\boldsymbol{v}_1}^{(n,1)}$ denoting the velocity potential function for free wave component $\boldsymbol{v}_1$. Double subscripts without separator always refer to the corresponding bound wave component; accordingly, $\phi_{12}^{(2,2)}$ denotes the bound wave component resulting from the quadratic interaction of $\phi_1^{(1,1)}$ and $\phi_2^{(1,1)}$.

The lateral variability of the wave field is captured by the decomposition in angular components so that the modulation of the amplitudes due to wave–wave, wave–current and wave–bottom interactions, as well as the effects of non-stationarity, take place on slow scales in $x$ and $t$ alone:

$$
\begin{bmatrix} \phi_{a_m}^{(n,m)} \\ \zeta_{a_m}^{(n,m)} \end{bmatrix} = \begin{bmatrix} \phi_{a_m}^{(n,m)}(z, x_1, t_1, x_2, t_2) \\ \zeta_{a_m}^{(n,m)}(x_1, t_1, x_2, t_2) \end{bmatrix} \qquad m = 1, 2 \quad n \geqslant m, \qquad (2.10)
$$

where the subscript $a_m = 1$ for $m = 1$ and $a_m = 12$ for $m = 2$, corresponding to components $\boldsymbol{v}_1$ and $(\boldsymbol{v}_1, \boldsymbol{v}_2)$ respectively.

The remainder of this chapter deals with the derivation of transport equations for the wave field variables that describe both the linear processes of shoaling, refraction and diffraction, and quadratic and cubic nonlinear effects. The main result of that derivation is equation (2.44) in §2.4. The order of presentation follows causality, but the reader can choose to skip ahead to §2.4 first, and read through Chapter 3, where we present both an analytical and empirical verification of the theory derived here, before returning to the details of the derivation presented in the following.

### 2.1.2 The ordered solution

Upon substituting the wave field decomposition (2.9) in the Laplace equation (2.1a), the bottom boundary condition (2.1c) and the free-surface boundary condition (2.1d), these can be written in the form [see e.g. Chu & Mei, 1970; Liu & Dingemans, 1989]:

$$\left( d_z^2 - k_{a_m}^2 \right) \phi_{a_m}^{(n,m)} = R_{a_m}^{(n,m)}, \qquad\qquad\qquad \forall z \in \mathcal{D}, \qquad (2.11a)$$

$$d_z \phi_{a_m}^{(n,m)} = F_{a_m}^{(n,m)}, \qquad\qquad\qquad z = -\overline{h}, \qquad (2.11b)$$

$$\zeta_{a_m}^{(n,m)} = \frac{1}{g} \left[ i\omega_{a_m} \phi_{a_m}^{(n,m)} - H_{a_m}^{(n,m)} \right], \qquad\qquad z = 0, \qquad (2.11c)$$

where $d_z$ denotes differentiation with respect to $z$, $n \geqslant m$ and the forcing terms $R_{a_m}^{(n,m)}, F_{a_m}^{(n,m)}$ and $H_{a_m}^{(n,m)}$ on the right-hand side (RHS) of (2.11) depend on lower-order results and are specified below as needed.

A general solution to (2.11a) and the condition (2.11b) can be found through variation of parameters [e.g. Chu & Mei, 1970]:

$$\phi_{a_m}^{(n,m)} = -\frac{\operatorname{Ch} Q_{a_m}}{k_{a_m}^2} \left[ I_1^{(n,m)}(Q_{a_m}) + \mathcal{M}_{a_m}^{(n,m)} \right] + \frac{\operatorname{Sh} Q_{a_m}}{k_{a_m}^2} \left[ I_2^{(n,m)}(Q_{a_m}) + k_{a_m} F_{a_m}^{(n,m)} \right],$$
$$(2.12)$$

where $\mathcal{M}_{a_m}^{(n,m)}$ is an integration constant,

$$Q_{a_m} = k_{a_m}(\overline{h} + z), \qquad \operatorname{Ch}\{\} = \cosh\{\}, \qquad \operatorname{Sh}\{\} = \sinh\{\}, \qquad (2.13)$$

and

$$I_1^{(n,m)}(Q_{a_m}) = \int_0^{Q_{a_m}} R_{a_m}^{(n,m)} \operatorname{Sh} Q'_{a_m} \, dQ'_{a_m}, \qquad (2.14)$$

$$I_2^{(n,m)}(Q_{a_m}) = \int_0^{Q_{a_m}} R_{a_m}^{(n,m)} \operatorname{Ch} Q'_{a_m} \, dQ'_{a_m}. \qquad (2.15)$$

Insertion of (2.12) in the combined free-surface boundary condition (2.1b) yields

$$\Delta_{a_m} \left[ I_1^{(n,m)}(q_{a_m}) + \mathcal{M}_{a_m}^{(n,m)} \right] - \Gamma_{a_m} \left[ I_2^{(n,m)}(q_{a_m}) + k_{a_m} F_{a_m}^{(n,m)} \right] = -S_{a_m}^{(n,m)} \frac{k_{a_m}}{g \operatorname{Sh} q_{a_m}}, \quad (2.16)$$

where the forcing term $S_{a_m}^{(n,m)}$ is the result of the perturbation expansion for the wave field, the expansion of the coordinates in multiple scales and the Taylor expansion of (2.1b) around $z = 0$. We have used the shorthand notation

$$\Delta_{a_m} = 1 - \frac{\omega_{a_m}^2}{gk_{a_m} T_{a_m}}, \quad \Gamma_{a_m} = \frac{1}{T_{a_m}} - \frac{\omega_{a_m}^2}{gk_{a_m}}, \quad T_{a_m} = \tanh q_{a_m}, \quad q_{a_m} = k_{a_m} \overline{h}, \quad (2.17)$$

where $\Delta_{a_m}$ can be interpreted as a measure of resonance mismatch.

Note from (2.16) that $m = 1$ is a special case in the sense that $\Delta_{a_1}$ vanishes (i.e. the forcing is secular) so that (2.16) constitutes a solvability condition on the lower-order wave field, but with $\Delta_{a_1} = 0$ it leaves the homogeneous part of $\phi_1^{(n,1)}$ (viz. $\mathcal{M}_{a_1}^{(n,1)}$) undetermined [see also Chu & Mei, 1970; Liu & Dingemans, 1989]. The derivation of the third-order evolution equations involves operations on $\phi_1^{(2,1)}$ and thus the complete solution for $\phi_1^{(2,1)}$, including the contribution from $\mathcal{M}_{a_1}^{(2,1)}$, is needed to consistently extend the derivation to this order. To this end, Chu & Mei [1970] asymptotically

matched their second-order result to the corresponding deep-water solution, whereas Liu & Dingemans [1989] derived an evolution equation for the combined first- and second-order free wave ($m = 1$) potential amplitudes. Kennedy & Kirby [2003] discarded the homogeneous contribution at second order altogether which, in their context, is equivalent to the approach of Liu & Dingemans [1989]. In the present context these approaches would either result in ambiguous results or yield modifications of the wave field due to wave–bottom interactions even in deep water, which must be rejected on physical grounds. Therefore, we pursue an explicit derivation of the second-order free wave potential from first principles that includes the contribution from $\mathcal{M}_{a_1}^{(2,1)}$ and assures a proper deep-water asymptote (i.e. vanishing contributions of wave-bottom interactions in deep water). To this end, the case $m = 1$ (free waves) is considered as the limit of a vanishing mismatch from resonance by writing

$$\omega_{a_1}^2 = \lim_{\Delta_{a_1} \to 0} g k_{a_1} T_{a_1} (1 - \Delta_{a_1}) \tag{2.18}$$

and we expand $\Gamma_{a_1}$ and $S_{a_1}^{(n,1)}$ in terms of $\Delta_{a_1}$ according to

$$\Gamma_{a_1} = \Gamma_{a_1}^{(0)} + \Delta_{a_1} \Gamma_{a_1}^{(1)}, \tag{2.19}$$

$$S_{a_1}^{(n,1)} = \sum_{j=0}^{1} \frac{\Delta_{a_1}^j}{j!} \left. \frac{d^j S_{a_1}^{(n,1)}}{d\Delta_{a_1}^j} \right|_{\Delta_{a_1}=0} + O(\Delta_{a_1}^2)$$

$$= S_{a_1}^{(n,1,0)} + \Delta_{a_1} S_{a_1}^{(n,1,1)} + O(\Delta_{a_1}^2). \tag{2.20}$$

Insertion of (2.19) and (2.20) into (2.16) yields

$$\mathcal{M}_{a_1}^{(n,1)} = \lim_{\Delta_{a_1} \to 0} \left\{ \frac{1}{\Delta_{a_1}} \left[ \Gamma_{a_1}^{(0)} \left( I_2^{(n,1)}(q_{a_1}) + k_{a_1} F_{a_1}^{(n,1)} \right) - \frac{k_{a_1}}{g \operatorname{Sh} q_{a_1}} S_{a_1}^{(n,1,0)} \right] \right.$$

$$\left. + \Gamma_{a_1}^{(1)} \left( I_2^{(n,1)}(q_{a_1}) + k_{a_1} F_{a_1}^{(n,1)} \right) - I_1^{(n,1)}(q_{a_1}) - \frac{k_{a_1}}{g \operatorname{Sh} q_{a_1}} S_{a_1}^{(n,1,1)} + O(\Delta_{a_1}) \right\} \quad (2.21)$$

and thus for vanishing $\Delta_{a_1}$ we obtain from (2.21)

$$\mathcal{M}_{a_1}^{(n,1)} = \Gamma_{a_1}^{(1)} \left( I_2^{(n,1)}(q_{a_1}) + k_{a_1} F_{a_1}^{(n,1)} \right) - I_1^{(n,1)}(q_{a_1}) - \frac{k_{a_1}^2}{\omega_{a_1}^2} \frac{S_{a_1}^{(n,1,1)}}{\operatorname{Ch} q_{a_1}}, \tag{2.22}$$

provided that the contribution between square brackets in (2.20) – multiplied by $\Delta_{a_1}^{-1}$ – cancels, yielding

$$\frac{1}{k_{a_1}} \int_0^{q_{a_1}} R_{a_1}^{(n,1)} \operatorname{Ch} Q'_{a_1} \, dQ'_{a_1} + F_{a_1}^{(n,1)} = \frac{\operatorname{Ch} q_{a_1}}{g} S_{a_1}^{(n,1,0)}. \tag{2.23}$$

Equation (2.22) unambiguously defines the homogeneous part of the velocity potential while (2.23) is the usual solvability condition. The latter is also found if the limit is not taken explicitly (as done here) but the forcing is considered secular from the outset; however, in that case the contribution given in (2.22) remains undetermined.

For $m = 2$ we have $k_{a_2} = k_{12} = |\boldsymbol{k}_1 + \boldsymbol{k}_2|$, $\omega_{a_2} = \omega_{12} = \omega_1 + \omega_2$ and the resonance mismatch is generally $O(\mu^2)$. To make the order explicit we write $\Delta_{a_2} = \mu^2 \widehat{\Delta}_{a_2}$ with $\widehat{\Delta}_{a_2} \sim O(1)$. The lowest-order forcing problem for $m = 2$ $(n = 2)$ is inhomogeneous only in the free-surface boundary condition involving the forcing term $S_{a_2}^{(2,2)}$. Since in (2.9) we expand the bound waves as $O(\epsilon^2/\mu^2)$ from the outset rather than $O(\epsilon^2)$ we correspondingly write

$$\mathcal{M}_{a_2}^{(2,2)} = -\frac{k_{a_2}}{gT_{a_2}\widehat{\Delta}_{a_2}} \frac{S_{a_2}^{(2,2)}}{\mathrm{Ch}\, q_{a_2}}. \tag{2.24}$$

In the present analysis, quadratic bound wave contributions of higher than second order $(n > 2)$ are considered only in the near-resonant shallow-water limit (see §2.3) where the Stokes number is $O(1)$.

## 2.2 Deep-intermediate water solution

In deep-intermediate water the representative vertical length scale $L_v = k_0^{-1}$ and the nonlinearity parameter, $\epsilon$, represents wave steepness. Here $\mu \sim O(1)$ and thus can be omitted, simplifying the analysis to an expansion in a single small parameter, $\epsilon$. Our expression for the second-order free wave potential differs from earlier studies (for the reasons explained in §2.1.2), leading to modifications of the $O(\epsilon^3)$ evolution equations.

### 2.2.1 First order, $O(\epsilon)$

For $m = 1$ the lowest order solution renders the boundary value problem (2.11) homogeneous ($R_{a_1}^{(1,1)} = F_{a_1}^{(1,1)} = H_{a_1}^{(1,1)} = 0$), yielding for the primary waves:

$$\phi_1^{(1,1)} = \varphi_1^{(1,1)} f_1, \qquad f_1 = \frac{\mathrm{Ch}\, Q_1}{\mathrm{Ch}\, q_1}, \qquad \varphi_1^{(1,1)} = -i\frac{g}{\omega_1}\zeta_1^{(1,1)},$$

and the dispersion relation

$$\omega_1^2 = gk_1 T_1, \tag{2.25}$$

where $\varphi_{a_m}^{(n,m)} = \phi_{a_m}^{(n,m)}|_{z=0}$ is the velocity potential amplitude evaluated at the undisturbed surface.

### 2.2.2 Second order, $O(\epsilon^2)$

At this order, for $m = 1$, the set (2.11) is inhomogeneous with secular forcing terms including a quadratic forcing term involving a product of the bottom perturbation, $\widehat{h}$, and the wave potential, $\varphi_1^{(1,1)}$, which accounts for the interaction of the wave field with the lateral depth variations:

$$R_1^{(2,1)} = -i2\varkappa_1 \phi_{1,x_1}^{(1,1)}, \tag{2.26a}$$

$$S_1^{(2,1)} = 2i\omega_1 \varphi_{1,t_1}^{(1,1)}, \tag{2.26b}$$

$$F_1^{(2,1)} = -\frac{k_1^2}{\mathrm{Ch}\, q_1}\mathcal{G}_1\{\widehat{h}, \varphi_2^{(1,1)}\}. \tag{2.26c}$$

The forcing term, $F_1^{(2,1)}$, involves the wave-bottom operator

$$\mathcal{G}_i\{a, b_j\} = \mathcal{F}_i\{a(y)\mathcal{F}^{-1}\{b_j \exp[i\psi_j]\}\} \exp[-i\psi_i], \tag{2.27}$$

where $\mathcal{F}_i$ denotes the $i$th component of the discrete Fourier transform (DFT) with respect to the lateral coordinate, and $\mathcal{F}^{-1}$ denotes the inverse Discrete fourier transform (IDFT). The interaction with the topography is thus modeled as a triad interaction between two wave components with equal frequency and a difference alongshore wavenumber matching that of the (zero-frequency) bottom component, i.e. the triad $\{\omega_1, \lambda_1; \omega_1, \lambda_2; 0, \lambda_1 - \lambda_2\}$. This scattering approach, as opposed to more conventional approaches for refraction–diffraction modeling, describes wave propagation over two-dimensional topography by a set of one-dimensional (apart from time) transport equations.

From (2.12), using (2.22), we find for the potential function $\phi_1^{(2,1)}$

$$\phi_1^{(2,1)} = \left[\mathcal{K}_1^{(1,2)} - i\left(\frac{\varkappa_1}{k_1^2}\varphi_{1,x_1}^{(1,1)}Q_1 T_{Q_1} - ik_1\mathcal{G}_1\{\widehat{h}, \varphi_2^{(1,1)}\}T_{Q_1}\right)\right]\frac{\mathrm{Ch}\,Q_1}{\mathrm{Ch}\,q_1} \tag{2.28}$$

where

$$T_{Q_1} = \frac{\mathrm{Sh}\,Q_1}{\mathrm{Ch}\,Q_1}, \qquad \mathcal{K}_1^{(2,1)} = -i\left[\frac{\varphi_{1,t_1}^{(1,1)}}{\omega_1} - \frac{\varkappa_1}{k_1^2}\varphi_{1,x_1}^{(1,1)}q_1 T_1 + ik_1 T_1\mathcal{G}_1\{\widehat{h}, \varphi_2^{(1,1)}\}\right]. \tag{2.29}$$

Setting $\mathcal{K}_1^{(2,1)} = 0$ in expression (2.28) yields the corresponding expression in Suh *et al.* [1990]. This implies a non-vanishing contribution of the lateral depth variations to both the second-order velocity potential and the corresponding second-order surface elevation, $\zeta_1^{(2,1)}$, which persists in deep water, as can be easily verified. This is unphysical. Taking $\mathcal{K}_1^{(2,1)}$ into account, as in (2.28), determines $\phi_1^{(2,1)}$ unambiguously, such that the topography has a vanishing effect on the velocity potential in deep water. The corresponding surface elevation correction at this order, $\zeta_1^{(2,1)}$, vanishes identically, which can be seen from inserting (2.28) into (2.11c).

The solvability condition (2.23) for $n = 2$ on the lowest-order wave field is

$$\mathcal{L}^{(1)}\{\varphi_1^{(1,1)}\} = \xi_1^{(2,\mathrm{wb})}\{\varphi_2^{(1,1)}\}, \tag{2.30}$$

where

$$\mathcal{L}^{(1)}\{\} = [\partial_{t_1} + V_1\partial_{x_1}], \qquad \xi_1^{(2,\mathrm{wb})}\{\varphi_2^{(1,1)}\} = i\frac{g}{2\omega_1}k_1^2\left(1 - T_1^2\right)\mathcal{G}_1\{\widehat{h}, \varphi_2^{(1,1)}\}, \tag{2.31}$$

in which $V_1 = (\varkappa_1/k_1)C_{g,1}$ is the cross-shore (principal direction) component of the linear group speed vector. The forcing term involving the operator $\xi_1^{(2,\mathrm{wb})}$ describes the lowest-order interaction between the surface waves and topography, indicated by the superscript wb. This convolution-type term redistributes the complex amplitudes over the alongshore wavenumber components, thus correcting the wave ray geometry relative

to Snel's law[†] to account for the lateral variability of the topography; lateral diffraction is accounted for implicitly by the summation of the angular wave components [see also Stamnes, 1986; Dalrymple & Kirby, 1988; Dalrymple *et al.*, 1989].

For $m = 2$ we find forcing terms quadratic in the free wave components that generally result in components that are *coupled* or *bound* to the primary waves; in fact they represent the spectral generalization of the second-order harmonic in a periodic wave train first described by Stokes [1847]. We will refer to these components with $m = 2$ as *bound* waves. The non-zero forcing term is $S_{12}^{(2,2)} = i\mathcal{D}_{1,2}\varphi_1^{(1,1)}\varphi_2^{(1,1)}$, where $\mathcal{D}_{1,2}$ is a quadratic wave–wave interaction coefficient given in Appendix A. The corresponding velocity potential is given by

$$\phi_{12}^{(2,2)} = \varphi_{12}^{(2,2)}\frac{\operatorname{Ch}Q_{12}}{\operatorname{Ch}q_{12}}, \qquad\qquad \varphi_{12}^{(2,2)} = i\frac{\mathcal{D}_{1,2}}{gk_{12}T_{12}\widehat{\Delta}_{12}}\varphi_1^{(1,1)}\varphi_2^{(1,1)}. \qquad (2.32)$$

Expressions (2.32) are in agreement with Hasselmann [1962, §4].

### 2.2.3 Third order, $O(\epsilon^3)$

At this order, for $m = 1$, we incorporate modulations due to the non-stationarity, large-scale bottom slope, cubic wave–wave and wave–bottom interactions, and the interaction with the mean flow. After some algebraic manipulation, the solvability condition (2.23) at this order yields

$$\mathcal{L}^{(2)}\{\varphi_1^{(1,1)}\} = \xi_1^{(3,\text{wb})}\{\varphi_2^{(1,1)}\} + \xi_1^{(3,\text{wbb})}\{\varphi_2^{(1,1)}\} + \xi_1^{(3,\text{wc})}\{\varphi_2^{(1,1)}\}$$
$$+ \xi_1^{(3,\text{www})}\{\varphi_2^{(1,1)}\varphi_3^{(1,1)}\varphi_4^{(1,1)}\} - \frac{1}{\omega_1}\sum_{\boldsymbol{v}_2,\boldsymbol{v}_3,\boldsymbol{v}_4}\mathcal{D}_{2,34}\varphi_2^{(1,1)}\varphi_{34}^{(2,2)}\delta_{234;1}^{\lambda,\omega}E_{234;1}, \quad (2.33)$$

where the terms involving the operators $\xi_1^{(3,j)}$ are specified below,

$$\mathcal{L}^{(2)}\{\} = \left[\partial_{t_2} + V_1\partial_{x_2} + \frac{1}{2}\partial_{x_2}V_1 - \frac{i}{2}M_1\partial_{x_1}^2\right], \qquad (2.34)$$

$$M_1 = \left(\frac{\varkappa_1}{k_1}\right)^2\frac{\partial^2\omega_1}{\partial k_1^2} + \left(1 - \left(\frac{\varkappa_1}{k_1}\right)^2\right)\frac{C_{g,1}}{k_1}, \qquad (2.35)$$

---

[†]This is sometimes spelled as 'Snell's law'. The quantitative law of refraction was named after the Dutch scientist *Willebrord Snel van Royen*. His name was latinized into *Snellius* and later incorrectly de-latinized into *Snell*. Therefore, the spelling 'Snel's law' is historically appropriate. See also Dingemans [1997, p. 67]. The discovery of the refraction law was never published by Snel but mentioned by Huygens in his 'Dioptrica', who had seen Snel's work. Although Huygens mentions that he assumes that Descartes had also seen this work, the latter makes no mention of this in his 'Dioptrices' where he presents the law in a new form and attempts to prove it with, what Mach refers to as 'a pedantic method of demonstration' [Mach, 1926]. Descartes' work led to an historic controversy with Fermat who denounced his proof; to discover what he believed to be the 'true law of refraction' Fermat devised his celebrated 'principle of least time' and – to his own astonishment – found the same refraction law as Descartes had published [Sabra, 1981]. (The least-time principle is more general and moreover correctly relates the refractive index to the ratio of velocities of propagation in the respective media.)

and we make use of the notional contractions

$$E_{ijk;l} = E_{ijk}E_l^*, \qquad \delta_{ijk;l}^{\lambda,\omega} = \delta(\lambda_i + \lambda_j + \lambda_k - \lambda_l)\delta(\omega_i + \omega_j + \omega_k - \omega_l), \qquad (2.36)$$

with $\delta$ representing a discrete Dirac delta or unit impulse function [see e.g. Oppenheim & Schafer, 1989].

Equation (2.33) is the third-order transport equation for the free-wave components. The left-hand side (*LHS*) operator in (2.33) includes the linear effects of shoaling, refraction and diffraction for waves propagating over an alongshore-uniform topography ($\overline{h}$). The forcing terms on the *RHS* of (2.33) take into account the third-order effects of the weak two-dimensional topography ($\widetilde{h}$) and nonlinearity on the wave evolution. In particular, the operators $\xi_1^{(3,\mathrm{wb})}$ and $\xi_1^{(3,\mathrm{wbb})}$ account for the interaction with the lateral depth variations; both terms are linear in the surface elevation while linear and quadratic in the bottom perturbation respectively. The terms involving the operators $\xi_1^{(3,\mathrm{wc})}$ and $\xi_1^{(3,\mathrm{www})}$ describe the interaction with the mean flow and cubic nonlinear wave interactions respectively. Note that there is no wave–wave–bottom (wwb) forcing term in (2.33) because in the present approximation the bottom wavenumbers are small relative to the wavenumber mismatch of quadratically forced bound waves such that these contributions are non-secular.

The convolution term on the *RHS* of (2.33) represents the quadratic interaction between bound and free wave components, which is given in explicit form for later use. Since (2.33) represents an intermediate result, explicit expressions for the remaining forcing terms (involving the operators $\xi_1^{(3,j)}$) are omitted for brevity. If needed they can be recovered from the final expressions in physical coordinates and variables which are included in Appendix B.

We combine (2.30) and (2.33) while absorbing the small parameters so that in physical coordinates and variables we have

$$\mathcal{L}\{\varphi_1^{(\mathrm{f})}\} = \xi_1^{(\mathrm{wb})}\{\varphi_2^{(f)}\} + \xi_1^{(\mathrm{wbb})}\{\varphi_2^{(f)}\} + \xi_1^{(\mathrm{wc})}\{\varphi_2^{(f)}\} + \xi_1^{(\mathrm{www})}\{\varphi_2^{(f)}\varphi_3^{(f)}\varphi_4^{(f)}\}$$
$$- \frac{1}{\omega_1}\sum_{\boldsymbol{v}_2,\boldsymbol{v}_3,\boldsymbol{v}_4} \mathcal{D}_{2,34}\varphi_2^{(\mathrm{f})}\varphi_{34}^{(\mathrm{b})}\delta_{234;1}^{\lambda,\omega}E_{234;1}, \qquad (2.37)$$

where $\varphi_1^{(\mathrm{f})} = \epsilon\varphi_1^{(1,1)}$ and $\varphi_{34}^{(\mathrm{b})} = \epsilon^2\varphi_{34}^{(2,2)}$ and the superscripts f and b refer to free and bound waves respectively; the operator $\mathcal{L}\{\} = \epsilon\mathcal{L}^{(1)}\{\} + \epsilon^2\mathcal{L}^{(2)}\{\}$. The forcing terms $\xi_1^{(j)}$ are given in Appendix B.

## 2.3 Extension to shallow water

The main result of §2.2, the transport equation for the $\varphi_1^{(\mathrm{f})}$ (2.37), is valid in deep-intermediate water but includes a quadratic wave-wave interaction term that involves the second-order bound waves. Closure by means of substitution of expressions (2.32) (in physical variables) for the bound wave amplitudes renders (2.37) incompatible with

the limit $O(\mu^2) \to O(\epsilon)$ where the quadratic interactions approach resonance. To include this limit with $O(\epsilon^2)$ accuracy we extend our expansion of the bound components to higher order, taking into account terms that are of $O(\epsilon^3/\mu^2)$, $O(\epsilon^4/\mu^4)$, i.e. all terms that are $O(\epsilon^2)$ or lower order as $O(\mu^2) \to O(\epsilon)$. Although this selective inclusion of higher-order terms may appear to conflict with the expansion for deep-intermediate water, the ordered expansion is merely a device to make the relative magnitude of terms explicit and is used here to identify terms that can formally be neglected in deep-intermediate depth (where they are smaller than the general order of approximation) but are essential in shallow regions where the Stokes number is $O(1)$.

Here we consider the shallow-water limit where $L_v = \overline{h}_0$, $\epsilon = a/h$ and use the Boussinesq approximation $O(\mu^2) \sim O(\epsilon)$. Secular contributions from quadratic interactions to the wave field evolution are removed by introducing the composite bound wave amplitude

$$\varphi_1^{(2,2)} = \sum_{\boldsymbol{v}_2, \boldsymbol{v}_3} \varphi_{23}^{(2,2)} \delta_{23;1}^{\lambda,\omega} E_{23;1}, \tag{2.38}$$

which can be considered the 'bound' wave contribution to spectral component $\boldsymbol{v}_1$. In shallow water, where the forcing is secular, $\varphi_1^{(2,2)}$ is a slowly varying quantity that can be described using the same WKB formalism that was used to derive the transport equations (2.30) and (2.33) for $\varphi^{(1,1)}$. Collecting terms of $O(\epsilon^3/\mu^3)$ and $O(\epsilon^4/\mu^4)$ (that become $O(\epsilon^{3/2})$ and $O(\epsilon^2)$ in shallow water respectively) yields forcing terms $R_1^{(3,2)}, S_1^{(3,2)}, F_1^{(3,2)}$ and $R_1^{(4,2)}, S_1^{(4,2)}, F_1^{(4,2)}$ that – apart from the wave–wave and wave–current interactions in $S_1^{(4,2)}$ – are identical to $R_1^{(2,1)}, S_1^{(2,1)}, F_1^{(2,1)}$ and $R_1^{(3,1)}, S_1^{(3,1)}, F_1^{(3,1)}$ respectively, with $\varphi_1^{(1,1)}$ and $\varphi_1^{(2,1)}$ consistently replaced by $\varphi_1^{(2,2)}$ and $\varphi_1^{(3,2)}$. For brevity we omit the details (which are similar to those in the analysis for deep-intermediate water) and give the resulting evolution equations for $\varphi_1^{(2,2)}$. At $O(\epsilon^3/\mu^3)$ we obtain

$$\mathcal{L}^{(1)}\{\varphi_1^{(2,2)}\} = \xi_1^{(2,\mathrm{wb})}\{\varphi_2^{(2,2)}\}. \tag{2.39}$$

At $O(\epsilon^4/\mu^4)$ we find

$$\mathcal{L}^{(2)}\{\varphi_1^{(2,2)}\} = \xi_1^{(3,\mathrm{wb})}\{\varphi_2^{(2,2)}\} + \xi_1^{(3,\mathrm{wbb})}\{\varphi_2^{(2,2)}\} - \frac{1}{2\omega_1} \sum_{\boldsymbol{v}_2, \boldsymbol{v}_3} \mathcal{D}_{2,3} \varphi_2^{(2,2)} \varphi_3^{(2,2)} \delta_{23;1}^{\lambda,\omega} E_{23;1}. \tag{2.40}$$

Equations (2.39), (2.40) are higher-order expressions describing the evolution of the $\varphi_1^{(2,2)}$ on the *slow* scales; these expressions are needed solely in the near-resonant limit (shallow water), which justifies the premise of slow variation of the component amplitudes $\varphi_1^{(2,2)}$. The similarity with (2.30), (2.33) is expected since they are obtained through a similar analysis; differences are due to the fact that we pursue only $O(\epsilon^2)$ accuracy in shallow water (in contrast to deep-intermediate water where we retain $O(\epsilon^3)$ accuracy), and the quadratic interactions in (2.40) involve a product of bound waves (as opposed to the free wave–bound wave interaction in the corresponding term in (2.33)).

It should be noted that the quadratic response may also contain fast modulations due to large resonance mismatches, even in relatively shallow water for interactions

between non-collinear wave components. The governing evolution equation, valid from deep-intermediate to shallow water, is obtained by combining (2.39) and (2.40), changing to physical coordinates while accounting for variations on the fast space scale related to the resonance mismatch, and utilizing expressions (2.32) for the bound wave amplitudes. In physical coordinates and variables we have

$$
\mathcal{L}\{\varphi_1^{(\mathrm{b})}\} = \xi_1^{(\mathrm{wb})}\{\varphi_1^{(\mathrm{b})}\} + \xi_1^{(\mathrm{wbb})}\{\varphi_1^{(\mathrm{b})}\}
$$
$$
- V_1 \sum_{\boldsymbol{v}_2,\boldsymbol{v}_3} \frac{\mathcal{D}_{2,3}}{gJ_{2,3}} \left( \varphi_2^{(\mathrm{f})}\varphi_3^{(\mathrm{f})} + \frac{gJ_{2,3}}{2\omega_1 V_1}\varphi_2^{(\mathrm{b})}\varphi_3^{(\mathrm{b})} \right) \delta_{23,1}^{\lambda,\omega} E_{23;1}, \quad (2.41)
$$

where $\varphi_1^{(\mathrm{b})} = \epsilon^2/\mu^2\varphi_1^{(2,2)}$, $J_{2,3} = k_{23}T_{23}\Delta_{23}/\Lambda_{2,3}$ and $\Lambda_{2,3} = \varkappa_2 + \varkappa_3 - \varkappa_{2+3}$. The operators $\xi_1^{(j)}$ (involving wave-bottom interaction) are given in Appendix B.

## 2.4  A generalized third-order evolution model

The evolution equations (2.37) and (2.41) represent a coupled set of equations for the free and bound wave components respectively. A transport equation for the composite amplitude $\varphi_1 = \varphi_1^{(\mathrm{f})} + \varphi_1^{(\mathrm{b})}$ is obtained by summing (2.37) and (2.41):

$$
\mathcal{L}\{\varphi_1\} = \xi_1^{(\mathrm{wb})}\{\varphi_2\} + \xi_1^{(\mathrm{wbb})}\{\varphi_2\} + \xi_1^{(\mathrm{wc})}\{\varphi_2\}
$$
$$
+ \xi_1^{(\mathrm{www})}\{\varphi_2\varphi_3\varphi_4\} - V_1 \sum_{\boldsymbol{v}_2,\boldsymbol{v}_3} \frac{\mathcal{D}_{2,3}}{gJ_{2,3}} \left( \varphi_2^{(\mathrm{f})}\varphi_3^{(\mathrm{f})} + \frac{gJ_{2,3}}{2\omega_1 V_1}\varphi_2^{(\mathrm{b})}\varphi_3^{(\mathrm{b})} \right) \delta_{23,1}^{\lambda,\omega} E_{23;1}
$$
$$
- \frac{1}{\omega_1} \sum_{\boldsymbol{v}_2,\boldsymbol{v}_3,\boldsymbol{v}_4} \mathcal{D}_{2,34}\varphi_2^{(\mathrm{f})}\varphi_{34}^{(\mathrm{b})} \delta_{234;1}^{\lambda,\omega} E_{234;1}. \qquad (2.42)
$$

The forcing terms $\xi_1^{(j)}$ are given in explicit form in Appendix B. Note that

$$
\lim_{\mu^2 \to \epsilon} \frac{gJ_{2,3}}{2\omega_{2+3}V_{2+3}} = 1 + O(\epsilon) \qquad (2.43)
$$

so that, upon substituting $\varphi_1$ in the products in the first convolution sum on the RHS of (2.42), we can replace $\varphi_1^{(\mathrm{f})}$ by $\varphi_1$ and substitute the second-order bound wave solution (2.32) for $\varphi_{34}^{(\mathrm{b})}$ in the remaining terms. These operations result in the closed-form equation

$$
\mathcal{L}\{\varphi_1\} = \xi_1^{(\mathrm{wb})}\{\varphi_2\} + \xi_1^{(\mathrm{wbb})}\{\varphi_2\} + \xi_1^{(\mathrm{wc})}\{\varphi_2\}
$$
$$
+ \xi_1^{(\mathrm{M,www})}\{\varphi_2\varphi_3\varphi_4\} + \xi_1^{(\mathrm{ww})}\{\varphi_2\varphi_3\}, \qquad (2.44)
$$

which retains $O(\epsilon^2)$ accuracy in the limit $O(\mu^2) \to O(\epsilon)$. Here $\xi^{(\mathrm{ww})}$ and $\xi^{(\mathrm{M,www})}$ account for quadratic and cubic interactions in $\varphi_1$; the latter is modified with respect to the finite depth result, indicated by the M in the superscript (explicit expressions are given in Appendix B); it ensures proper cubic nonlinearity in finite depth while retaining $O(\epsilon^2)$

accuracy in shallow water. Equation (2.44), the main result of the present analysis, is a one-dimensional (in space) evolution equation for weakly nonlinear waves propagating from deep to shallow water over weakly two-dimensional topography. Although (2.44) does not consider bound and free wave components explicitly, it fully accounts for near-resonant cubic interactions in deep-intermediate depth and near-resonant quadratic interactions in shallow water; also, quadratic non-secular contributions (off-resonant bound waves) are accounted for (see §3.1). It is a closed set of equations, apart from the term involving the mean-flow quantities, for which expressions are given in Appendix C. Since the mean flow is modeled without $z$-dependence the model is suitable for intermediate depths ($k_0\overline{h}_0 \sim O(1)$) and shallow water where waves 'feel the bottom'. In deeper water ($\epsilon k_0\overline{h}_0 \geq O(1)$) more general expressions for the mean flow are needed, which is considered in Peregrine [1983$b$].

Equation (2.44) describes the evolution of the velocity potential amplitude. The corresponding spectral amplitudes for the surface elevation function can be readily obtained from

$$\zeta_1 = i\frac{\omega_1}{g}\varphi_1 - \frac{1}{g}\sum_{\boldsymbol{v}_2,\boldsymbol{v}_3} \mathcal{R}_{2,3}\varphi_2\varphi_3\delta_{2,3;1}^{\lambda,\omega}E_{2,3;1}, \qquad (2.45)$$

where the nonlinear term is a second-order correction required to accurately include second-order bound waves in the free surface elevation. This term is $O(\epsilon^2)$ and thus a genuine second-order term irrespective of the resonance mismatch. In contrast, the contribution to $\varphi_1$ due to quadratic interactions is $O(\epsilon^2/\mu^2)$ and becomes an $O(\epsilon)$ secular forcing term in shallow water with leading-order contributions over distances $O(\epsilon^{-1})$. In view of this, the nonlinear term in (2.45) – contributing a local, second-order correction without affecting the wave field evolution – is usually neglected in models for near-resonant quadratic interactions [e.g. Agnon $et\ al.$, 1993; Kaihatu & Kirby, 1995], which is consistent with the premise of that derivation. Since the present model allows for arbitrary resonance mismatch (and thus includes off-resonant, second-order bound waves), the inclusion of the nonlinear term in (2.45) is necessary to obtain second-order accuracy in the surface elevation matching Stokes' second-order theory.

In the following chapter (Chapter 3) the theory presented here is verified, both analytically – through comparison to expressions in the literature – and through comparison of numerical simulations to laboratory observations.

# Analysis and verification deterministic theory **3**

The main result of Chapter 2 is a set of evolution equations for the angular spectrum components (viz. (2.44)), suitable for wave propagation from deep-intermediate to shallow water over weakly two-dimensional topography.

We verify the uniform validity of the nonlinearity embedded in the model propagation, through analytical comparison to well-established expressions in the literature (§3.1) and empirical verification for one-dimensional wave propagation is presented (§3.2). In the analytical comparison we address both the deep-water (§3.1.1) and shallow-water asymptotes (§3.1.2). With respect to the latter, various approximations exist in the literature; their mutual (dis-)similarities are considered and their relation, as special cases, to the more general expression in eq. (2.44) is shown. We empirically verify the model through comparison of numerical simulations with a reduction of eq. (2.44), appropriate for one-dimensional wave propagation, to laboratory observations of unidirectional waves (§3.2).

The two-dimensional capability of the model is assessed in §3.3 and §3.4, where we primarily focus on the concomitant modeling of the effects of quadratic interactions and refraction; the third-order nonlinear physics is omitted. In particular we address the (linear) properties of the two-dimensional approximation, its inherent limitations, and relation to more general, two-dimensional formulations of waves over varying depth (§3.3). The robustness of the approximation with respect to lateral depth variability, in the presence of shallow-water nonlinearity, is empirically verified (§3.4) through comparison of model-predicted wave evolution to observations of waves over weakly non-uniform topography (§3.4.1), and over submerged two-dimensional obstacles (§3.4.2).

The inherent limitations and potential of the present approach, both from a deterministic viewpoint (Chapters 2 and 3) and with an outlook to stochastic modeling (Chapters 4 and 5) are discussed in §3.5.

## 3.1 Asymptotic limits of the nonlinear model

### 3.1.1 Deep-intermediate water: cubic nonlinearity

We consider wave propagation in sufficiently deep water such that second-order bound waves do not affect the wave field evolution and nonlinear resonances are accounted for through the cubic forcing term $\xi^{(\mathrm{www})}$ given in Appendix B. It can be shown (Appendix D) through some algebraic manipulation that the interaction coefficient $\mathcal{H}_{1,2,3}$ in $\xi^{(\mathrm{www})}$ is equivalent to that of Herterich & Hasselmann [1980] [a corrected version of the

interaction term given in Hasselmann, 1962]. Furthermore, it can be shown (Appendix D) that expressions for the dispersion corrections from the pairwise, third-order interaction of a bichromatic, directional wave train in deep water agree with expressions derived by Longuet-Higgins & Phillips [1962] (when accounting for the misprint in that paper previously pointed out by Hogan *et al.* [1988] and Willebrand [1973, 1975]).

If we further restrict the wave field to a single angular component

$$\eta = \zeta \exp\left[i\left(\int^x \varkappa\, dx + \lambda y - \omega t\right)\right] + * \tag{3.1}$$

then (2.44) reduces to

$$\left[\partial_t + V\partial_x + \frac{1}{2}\partial_x V - \frac{i}{2}\left[\left(\frac{\varkappa}{k}\right)^2 \frac{\partial^2 \omega}{\partial k^2} + \left(1 - \left(\frac{\varkappa}{k}\right)^2\right)\frac{C_g}{k}\right]\partial_x^2\right]\zeta$$

$$= -i\frac{k^2\omega}{4T^2}\left(9T^{-2} - 12 + 13T^2 - 2T^4\right)|\zeta|^2\zeta + i\zeta\left[\frac{k^2}{2\omega}\left(1 - T^2\right)\partial_t - \boldsymbol{k}\cdot\boldsymbol{\nabla}\right]\overline{\overline{\Phi}}. \tag{3.2}$$

This expression, coupled to the mean-flow equations in Appendix C, agrees with corresponding expressions given by e.g. Liu & Dingemans [1989] if likewise lateral modulation of the wave amplitude is omitted and higher-order refraction corrections [included in Liu & Dingemans, 1989] are excluded.

Alternatively, if we consider a wave train, propagating along $x$ with slow modulations in both horizontal dimensions we may write the surface elevation as

$$\eta = a(x, y) \exp\left[i\left(\int^x k\, dx - \omega t\right)\right] + *,$$

where we decompose the amplitude $a$ as

$$a(x, y) = \sum_\lambda \zeta_\lambda \exp\left[i\left(\int^x (\varkappa_\lambda - k)\, dx + \lambda y\right)\right]. \tag{3.3}$$

For small-angle propagation ($\lambda \ll k$) the eikonal $\varkappa_\lambda = \sqrt{k^2 - \lambda^2}$ can be approximated by $\varkappa_\lambda - k \approx -\lambda^2/(2k)$, and we can write

$$d_x a(x, y) \approx \sum_\lambda \left(d_x \zeta_\lambda - i\frac{\lambda^2}{2k}\zeta_\lambda\right)\exp\left[i\left(\int^x (-\frac{\lambda^2}{2k})\, dx + \lambda y\right)\right]. \tag{3.4}$$

We rewrite (2.44) using (3.4), assuming uniform depth and deep-intermediate water, and transform to coordinates of a frame moving with the envelope, $\xi = x - C_g t$ so that the evolution of $a$ may be written as

$$\left[\partial_t - \frac{i}{2}\frac{\partial^2 \omega}{\partial k^2}\partial_\xi^2 - \frac{i}{2}\frac{C_g}{k}\partial_y^2\right]a = -i\frac{k^2\omega}{4T^2}\left(9T^{-2} - 12 + 13T^2 - 2T^4\right)|a|^2 a$$

$$- i\frac{k^2}{2\omega}C_g\left[2\frac{C}{C_g} + \left(1 - T^2\right)\right]\overline{\overline{\Phi}}_\xi a. \tag{3.5}$$

Here we have made use of the identity $d_y^n a = \sum_\lambda (i\lambda)^n \zeta_\lambda \exp[i\lambda y]$. For the mean flow (Appendix C) we obtain

$$\left(gH - C_g^2\right)\overline{\overline{\Phi}}_{\xi\xi} + gH\overline{\overline{\Phi}}_{yy} = -\frac{gk}{T}C_g\left[2\frac{C}{C_g} + \left(1 - T^2\right)\right]\left(|a|^2\right)_\xi. \tag{3.6}$$

The equations (3.5) and (3.6) constitute a coupled set for the wave envelope evolution and the concomitant wave-induced mean flow; it can be shown that they are equivalent to the eq.'s (2.15) and (2.14) in Davey & Stewartson [1974] respectively.

For unidirectional wave propagation (no lateral modulations), the mean-flow equations can be integrated once with respect to $\xi$, and back-substituted into the envelope equations so that the result can be written in the cubic Schrödinger form [see e.g Mei, 1983; Griffiths, 1994]

$$i\partial_t \widetilde{a} + \frac{1}{2}\frac{\partial^2 \omega}{\partial k^2}\partial_\xi^2 \widetilde{a} - \mathcal{J}|\widetilde{a}|^2\widetilde{a} = 0 \tag{3.7}$$

with

$$\mathcal{J} = \frac{k^2\omega}{4T^4}\left[\left(9 - 12T^2 + 13T^4 - 2T^6\right) - 2\frac{\left(2\frac{C}{C_g} + \left(1 - T^2\right)\right)^2}{\left(\frac{gH}{C_g^2} - 1\right)}\right] \tag{3.8}$$

$$\widetilde{a} = a\exp\left[i\int^t C_g \frac{k^2}{2\omega}\left(2\frac{C}{C_g} + \left(1 - T^2\right)\right)N(t')\,dt'\right] \tag{3.9}$$

and $N(t)$ an integration constant. These expressions agree with Mei (1983, §12). For one-dimensional wave propagation ($\varkappa_i = k_i$) over variable depth, (3.2) can be shown to agree with expression (2.14) in Djordjević & Redekopp [1978] (if the last $\sigma$ in their expression (2.17) for $\nu$ is replaced by $\sigma^2$).

Amplitude dispersion embedded in our model is evaluated for the reduced case of Stokes waves, i.e. one-dimensional, periodic waves of permanent shape in uniform depth. Therefore we omit terms involving non-stationarity of the wave field and the topographical variations from (2.44). To make analytical comparison to Stokes theory we assume zero net mass flux (the appropriate choice for wave flume experiments), which determines current and set-down terms unambiguously. The resulting transport equation for a single primary wave component reads

$$\frac{1}{\varphi_p}\frac{d}{dx}\varphi_p = i\frac{|\varphi_p|^2}{2\omega_p C_{g,p}}\left[3\mathcal{D}_{p,p,-p} - 2\mathcal{D}_{p+p,-p}\frac{\mathcal{D}_{p,p}}{gk_{pp}T_{pp}\Delta_{pp}} + 4k_p^3\frac{T_p}{h} - k_p^4(1 - T_p^2)^2\right], \tag{3.10}$$

where the secular forcing terms are due to cubic self-self interaction and quadratic interaction with its harmonic. The last two terms between brackets on the *RHS* of (3.10) account for the effects of the wave-induced return current and set-down respectively (see Appendix C); since the mean surface elevation corrections must vanish identically, the last term in brackets *counters* the water level corrections that are implicitly included in the third-order interaction coefficient $\mathcal{D}_{p,p,-p}$. The forcing terms in (3.10), in quadrature

with $\varphi_p$, cannot transfer energy but result in (amplitude) dispersion corrections. Seeking a permanent-shape solution, we insert $\varphi_p(x) = -ig a_p/(2\omega_p) \exp i\theta_p(x)$ into (3.10) with $a_p$ the (constant) surface elevation amplitude, and evaluate the nonlinear wavenumber correction $\widetilde{k}_p = d_x \theta_p$:

$$\widetilde{k}_p = -\frac{1}{2}(k_p a_p)^2 k_p \frac{C_p}{C_{g,p}} \left[ \frac{\left(9 - 10T_p^2 + 9T_p^4\right)}{8T_p^4} - \frac{1}{q_p T_p} \right]. \tag{3.11}$$

Here $C_p$ and $C_{g,p}$ are the linear phase and group speeds respectively. Eq. (3.11) corresponds to the expressions in Stokes [1880] apart from the last term between square brackets. The latter term accounts for the wave-induced current [see e.g. Isobe & Kraus, 1983; Fenton, 1985], such that the resulting wave celerity is in accordance with Stokes' second definition [see Stokes, 1847]. Note that, although expression (3.11) includes the effects of amplitude dispersion by correcting the wavenumber rather than the frequency, as is typical for a frequency-domain model, the corresponding frequency correction $\widetilde{\omega}_p = -(d\omega_p/dk_p)\widetilde{k}_p$ can be shown to agree to third order in wave steepness with eq. (26) of Fenton [1985] for zero mass flux.

### 3.1.2 Shallow water: quadratic interactions

In this section the wording 'shallow-water' is not used to imply explicit restrictions on water depth from the outset (i.e. $kh \ll 1$), but rather the region where quadratic interactions are dynamically important to the wave field evolution. The evolution equations considered here, generally do not have explicit restrictions on water depth (i.e. $kh \ll 1$), neither in the linear terms nor in the interaction coefficient [Agnon et al., 1993; Kaihatu & Kirby, 1995]. The absence of such explicit restrictions on water depth has focused much of the discussion in the literature on the matching to Stokes second-order theory [e.g. Eldeberky & Madsen, 1999] which, given the second-order accuracy retained in the models, seems a reasonable demand. Nevertheless, the fundamental motivation for deriving evolution-type models is to include dynamical effects on the propagation, effective over asymptotically large distances [see e.g. Armstrong et al., 1962; Bretherton, 1964; Mei & Ünlüata, 1972]. Even with an exact match to Stokes second-order theory in deeper water (where these interactions constitute non-secular, local corrections), the omission of cubic nonlinear terms, the prevalent nonlinear mechanism in deep-intermediate water, implicitly restricts models that account for quadratic but not cubic interactions to fairly shallow water or relatively short propagation distances. Hence the title.

When considering the propagation of steady waves over alongshore-uniform bathymetry while momentarily omitting interaction with the mean flow and cubic wave–wave interactions, the general equations (2.44) and (2.45) reduce to the form

$$\left[ \frac{d}{dx} + \frac{1}{2V_1} \frac{dV_1}{dx} \right] \varphi_1 = i \sum_{\boldsymbol{v}_2, \boldsymbol{v}_3} \frac{\mathcal{D}_{2,3}}{g J_{2,3}} \varphi_2 \varphi_3 \delta_{23;1}^{\lambda, \omega} E_{23;1}, \tag{3.12}$$

$$\zeta_1 = i \frac{\omega_1}{g} \varphi_1 - \frac{1}{g} \sum_{\boldsymbol{v}_2, \boldsymbol{v}_3} \mathcal{R}_{2,3} \varphi_2 \varphi_3 \delta_{2,3;1}^{\lambda, \omega} E_{2,3;1}, \tag{3.13}$$

which can be solved as a coupled set to obtain the surface elevation amplitudes [Kaihatu, 2001]. Alternatively, the coupled set can be combined into a single evolution equation, describing the spatial variation of surface elevation amplitudes by eliminating the velocity potential amplitude. Through substitution we have

$$\left[ \frac{d}{dx} + \frac{1}{2V_1} \frac{dV_1}{dx} \right] \zeta_1 = i \sum_{\boldsymbol{v}_2, \boldsymbol{v}_3} \mathcal{Z}_{2,3}^{(\mathrm{g})} \zeta_2 \zeta_3 \delta_{23;1}^{\lambda, \omega} E_{23;1}, \tag{3.14}$$

where

$$\mathcal{Z}_{2,3}^{(\mathrm{g})} = \frac{\omega_{2+3}}{\omega_2 \omega_3 J_{2,3}} \mathcal{D}_{2,3} + \frac{g}{\omega_2 \omega_3} \Lambda_{2,3} \mathcal{R}_{2,3}. \tag{3.15}$$

The coupling coefficient $\mathcal{Z}_{2,3}^{(\mathrm{g})}$ in (3.14) is equivalent to the nonlinear coupling coefficient derived in Bredmose *et al.* [2005]; in fact, the evolution equation (3.14) reduces to the corresponding equation in Bredmose *et al.* [2002] for unidirectional waves. The eq. (3.14) represents a generalization with respect to the treatment of the quadratic interactions of the earlier, resonant models by Agnon *et al.* [1993], Kaihatu & Kirby [1995], Sheremet [1996], and the 'quasi-resonant' model by Eldeberky & Madsen [1999], in the sense that it is valid for arbitrary resonance mismatch; the generalized form of the coupling coefficient is identified by the (g) in the superscript for later use. We refer to the present interaction coefficient as 'generalized' since both the resonant and quasi-resonant coefficients are special cases which can, with the appropriate restriction on resonance mismatch instated, be derived from the interaction coefficient $\mathcal{Z}_{2,3}^{(\mathrm{g})}$. We use the wording 'quasi-resonant' to indicate the fact that, although the model by Eldeberky & Madsen [1999] assumes resonance from the outset, it does include the nonlinear contribution in the relation between the velocity potential and the surface elevation as present in (3.13); essentially this approximation is found by assuming resonance in the first term of (3.15) while retaining the second term in that expression[†]. If the latter term is omitted, which is consistent with the assumption of quadratic resonance (see also §2.4, following eq. (2.45)), we refer to the model as 'resonant' [Agnon *et al.*, 1993; Kaihatu & Kirby, 1995; Sheremet, 1996].

Taking the shallow-water limit of (2.44) by setting $O(\epsilon/\mu^2) = O(1)$ and expanding all contributions explicitly in terms of $\mu^2$, yields to order $O(\epsilon^2, \epsilon\mu^2)$ the transport equation:

---

[†]If resonance is consistently assumed, the second term in (3.13) would also vanish since $\Lambda_{1,2}$ is of the order of the resonance mismatch. The wording 'quasi-resonant' is inspired by the semantics 'quasi-normal', commonly used to indicate an inconsistent use of the premise of Gaussianity with respect to the closure of the hierarchy of statistical moments [see e.g. Lesieur, 1997; Salmon, 1998, and Chapter 4 of this thesis].

$$\left[\frac{d}{dx} + \frac{1}{4h}\frac{dh}{dx} - i\frac{\omega_1}{\sqrt{gh}}\left(1 + \frac{\omega_1^2 h}{6g} - \frac{\lambda_1^2}{2\omega_1^2}gh\right)\right]\eta_1 =$$

$$-i\frac{3\omega_1}{4h\sqrt{gh}}\sum_{\boldsymbol{v}_2,\boldsymbol{v}_3}\eta_2\eta_3\delta_{23;1}^{\lambda,\omega} + O(\epsilon^2\mu^2, \mu^4\epsilon, \epsilon^3), \quad (3.16)$$

where $\eta_1\exp\{i(\lambda_1 y - \omega_1 t)\} = \zeta_1 E_1$. Equation (3.16) is a lowest order Boussinesq approximation in agreement with Herbers & Burton [1997] and (for unidirectional waves) Freilich & Guza [1984, the 'consistent shoaling model']. Evolution equations based on Boussinesq equations with improved dispersion characteristics [e.g. Madsen & Sørensen, 1993] are detailed in Bredmose [2002] and Bredmose *et al.* [2004], and not further considered here. Instead we will refer to the 'Boussinesq' approximation only where it applies to the interaction kernel, not the linear properties of the model such as frequency dispersion and shoaling; this is similar to the so-called 'dispersive' model by Freilich & Guza [1984], an approach later also considered by Becq [1998]. In the following we will make use of the archetype evolution equation for the surface elevation spectral amplitudes, written as

$$\frac{d}{dx}A_1 = i\sum_{\boldsymbol{v}_2,\boldsymbol{v}_3}\sqrt{\frac{V_1}{V_2 V_3}}\mathcal{Z}_{2,3}^{(j)}A_2 A_3\delta_{23;1}^{\lambda,\omega}E_{23;1}, \quad (3.17)$$

where $A_1 = \sqrt{V_1}\zeta_1$ and various forms of the coupling coefficient $\mathcal{Z}_{2,3}^{(j)}$ for generalized, resonant and Boussinesq approximations are listed in Table 3.1. This list is by no means exhaustive, and certainly within the context of e.g. higher-order (in the dispersion parameter) Boussinesq approximations many more approximate forms can be conceived. However this set includes both a lowest-order Boussinesq form [Freilich & Guza, 1984; Herbers & Burton, 1997], the most general form [Bredmose *et al.*, 2005; Janssen *et al.*, 2006], the resonant approximation [Agnon *et al.*, 1993; Kaihatu & Kirby, 1995] and quasi-resonant expressions [Eldeberky & Madsen, 1999], which more than suffices for the purpose of discussion.

*Superharmonics and amplitude dispersion*
It is well known [Stokes, 1847] that the appearance of quadratic terms in the boundary value problem for small but finite-amplitude, oscillatory wave motion in finite depth results in forced wave motion at harmonic frequencies. From a spectral point of view this can be regarded as a self-self interaction: the interaction of component $(\omega, k)$ with itself forces a wave at $(2\omega, 2k)$. In turn, the (difference) interaction of the harmonic component at $(2\omega, 2k)$ with the primary train $(\omega, k)$ produces a resonance at the third order in wave steepness, in quadrature with the primary wave, resulting in a dispersion correction of the latter. In the coupled-mode models these effects are also present. Surely, it comes as no surprise that harmonic modes are excited which is, after all, the prime motivation to include the nonlinear coupling term in the first place. However, perhaps less conspicuous is the fact that the nonlinear coupling also induces third (and higher) order amplitude

| Model | Coupling coefficient |
|---|---|
| Generalized  <br> *Bredmose* et al. *[2005]* <br> *Janssen* et al. *[2006], this thesis* | $\mathcal{Z}_{1,2}^{(\mathrm{g})} = \dfrac{\omega_{1+2}}{\omega_1\omega_2 J_{1,2}}\mathcal{D}_{1,2} + \dfrac{g}{\omega_1\omega_2}\Lambda_{1,2}\mathcal{R}_{1,2}$ |
| Quasi-resonant  <br> *Eldeberky & Madsen [1999]* | $\mathcal{Z}_{1,2}^{(\mathrm{qr})} = \dfrac{g}{2\omega_1\omega_2 V_{1+2}}\mathcal{D}_{1,2} + \dfrac{g}{\omega_1\omega_2}\Lambda_{1,2}\mathcal{R}_{1,2}$ |
| Resonant  <br> *Agnon* et al. *[1993]* <br> *Kaihatu & Kirby [1995]* | $\mathcal{Z}_{1,2}^{(\mathrm{r})} = \dfrac{g}{2\omega_1\omega_2 V_{1+2}}\mathcal{D}_{1,2}$ |
| Boussinesq  <br> *Freilich & Guza [1984]* <br> *Herbers & Burton [1997]* | $\mathcal{Z}_{1,2}^{(\mathrm{b})} = -\dfrac{3\omega_{1+2}}{4h\sqrt{gh}}$ |

**Table 3.1:** Coupling coefficients quadratic wave–wave interactions. Co-efficients $\mathcal{D}_{1,2}$ and $\mathcal{R}_{1,2}$ are given in Appendix A. The $\Lambda_{1,2}$ and $V_1$ denote resonant mismatch and the principal component of the group speed vector. The $J_{1,2}$ and $\Lambda_{1,2}$ are given on pp. 22 below (2.41). We remark that the numeral subscripts are used as running counters, related to the frequency/lateral wavenumber pairs $(\omega_{p_1},\lambda_{q_1})$ and $(\omega_{p_2},\lambda_{q_2})$.

dispersion effects. After all, the convolution sum, which governs the nonlinear evolution of component $(\omega,k)$, includes all contributions for which the frequencies add up to $\omega$, including the difference interactions between $(2\omega,2k)$ and $(\omega,k)$. However, the nonlinear coupling term is derived on the premise that the interacting modes are 'free' WKB waves, an assumption clearly not applicable to the bound component $(2\omega,2k)$, rendering the weighting of the (third-order) interaction inaccurate. Given these considerations with respect to the harmonic-primary interactions, augmented with the fact that cubic terms (primary-primary-primary interactions) are lacking entirely in the quadratic models, we do not anticipate amplitude dispersion predictions by these models to agree with third-order theory (if this is the case then the second-order model would have third-order accuracy for this class of interactions). Nevertheless, it is useful to understand the amplitude dependency in the dispersion characteristics of these types of models (see Table 3.1) and their mutual differences. Thereto, and to investigate the forcing of bound superharmonics in unidirectional waves, we substitute a convenient surface elevation function into the governing evolution equation (3.17), written as

$$\eta = \sum_{p=1}^{2} \zeta_p \exp\left[i\left[(k_p x - \omega_p t)\right]\right] + *, \tag{3.18}$$

where

$$\zeta_p = \epsilon^p \frac{a'_p}{2k_1} \exp\left[ i \left( p(k_1 + \epsilon^2 \widetilde{k}x) - k_p \right) \right]. \tag{3.19}$$

The $\epsilon \ll 1$ denotes a measure of wave steepness, the $a'_p$ are constant (non-dimensional) amplitudes of $O(1)$, and $\widetilde{k}$ is the wavenumber correction due to the nonlinear interactions. Inserting this decomposition into (3.17) we readily find

$$a'_2 = \frac{\mathcal{Z}_{1,1}^{(j)}}{2k_1 \left( 2k_1 - k_2 \right)} (a'_1)^2, \tag{3.20}$$

$$\widetilde{k} = \frac{\mathcal{Z}_{2,-1}^{(j)}}{k_1} a'_2 = \frac{\mathcal{Z}_{1,1}^{(j)} \mathcal{Z}_{2,-1}^{(j)}}{2k_1^2 \left( 2k_1 - k_2 \right)} (a'_1)^2. \tag{3.21}$$

If we substitute the expression for the generalized interaction coefficient $\mathcal{Z}_{1,1}^{(g)}$ (see Table 3.1) into eq. (3.20) for the first harmonic it reads (in physical variables)

$$\zeta_2 = k_1 \frac{3 - T_1^2}{2T_1^3} \zeta_1^2, \tag{3.22}$$

which agrees with Stokes' second-order theory [see e.g. Stokes 1847; Dingemans 1997 §2.8]. If instead we substitute the interaction coefficient corresponding to the quasi-resonant model the result is but slightly different (see Figure 3.1). In fact, for one-dimensional wave propagation, the quasi-resonant model is equivalent to the generalized model in deep water ($kh \rightarrow \infty$), which can also be readily seen from the algebraic expressions for the coupling coefficients (Table 3.1). In contrast, in deep water, differences with the resonant and Boussinesq approximation are most prominent. This can be understood from the fact that in deep water, quadratic forcing is entirely due to the nonlinear contribution to the relation between velocity potential and surface elevation: this contribution is absent in the resonant and Boussinesq approximation.

As we argued before, it is unreasonable to expect these second-order models to accurately predict amplitude dispersion, a third-order phenomenon. As it turns out: neither of them does. In fact, when compared to the exact expression in (3.10) for zero net mass flux (Stokes' second definition Stokes 1847, §3) we find that the generalized model typically overestimates the amplitude dispersion strongest (Figure 3.2); the quasi-resonant model performs slightly better overall but has much the same dispersion characteristics as the generalized model (strong overestimation). The behavior in deep water for the resonant and Boussinesq model is quite distinct. On account of the vanishing of their coupling coefficient, essentially rendering the model linear in the wave-field variable, amplitude dispersion effects are absent for these models in deep water.

Although it comes as no surprise that the second-order models are incapable of accurately predicting a *third-order* effect, it is somewhat disappointing that the most general second-order model, being 'exact' at the second-order, seems to be the most inaccurate
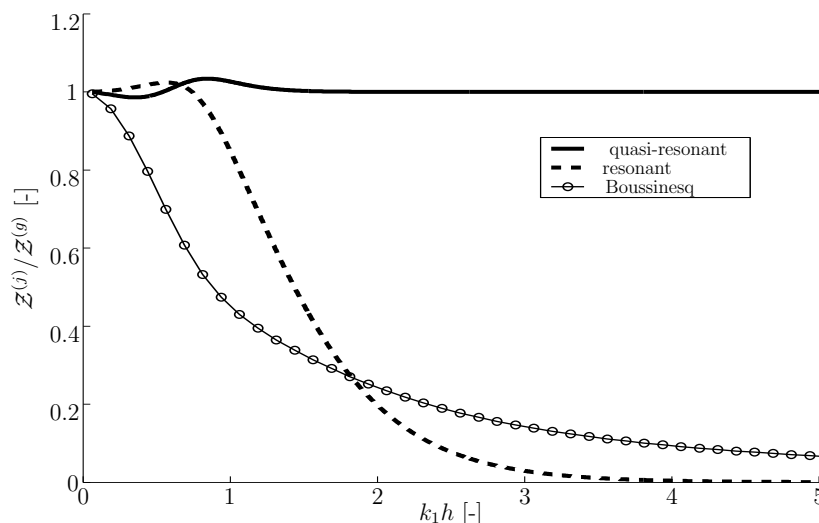
**Figure 3.1:** Self-self interaction coefficients for Stokes harmonic normalized with generalized formulation as a function of $k_1 h$.

model in terms of amplitude dispersion; however, a more accurate representation of a lower order does not imply an improvement at the next (and it turns out it does not). The magnitude of the mismatch found for the generalized and (quasi-)resonant model (Figure 3.2) suggests that for intermediate depth ($kh \approx 1.5$) these models can be expected to significantly overestimate wave celerity, and in terms of dispersion may perform even worse than linear models (that account for frequency dispersion) in such regions [see also Bredmose *et al.*, 2005].

*Narrow-band difference interactions: surfbeat*
Another well-known phenomenon induced by quadratic nonlinearities in modulated wave trains is the forcing of a secondary wave train at the beat frequency. This class of wave motion was theoretically predicted by Biésel [1952] and related to the concept of 'radiation stress' by Longuet-Higgins & Stewart [1962]. To compare beat motion as predicted by the coupled-mode models to the theory by Longuet-Higgins & Stewart [1962] for narrow-band forcing and uniform depth (in Chapter 6 bound-wave evolution in shoaling waves is discussed), we consider the surface elevation as the sum of a bichromatic primary wave field and a low-frequency component at the beat frequency (momentarily omitting forced super-harmonics) written as

$$\eta = \sum_{p=1}^{2} \zeta_p \exp\left[i\left(k_p x - \omega_t\right)\right] + \zeta_\Delta \exp\left[i\left(k_\Delta x - \Delta\omega t\right)\right] + *,$$

where the $\zeta_p$ and $\zeta_\Delta$ denote the primary wave and forced wave amplitudes respectively. Further, we write

PSfrag replacements
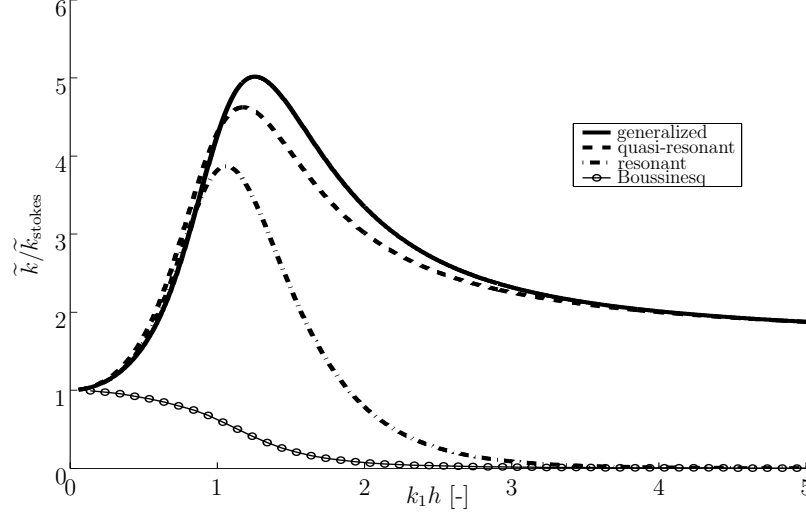


**Figure 3.2:** Amplitude dispersion normalized by Stokes amplitude dispersion (viz. eq. (3.10)). Values larger than 1 indicate an *overestimation* of the wave propagation velocity with respect to Stokes theory (Stokes' second definition).

$$\zeta_p = \epsilon \frac{a_p'}{2k_0}, \qquad\qquad \zeta_\Delta = \epsilon^2 \frac{a_\Delta'}{2k_0}. \qquad (3.23)$$

The $k_\Delta$ denotes the wavenumber related to $\Delta\omega$ through the linear dispersion relation. We assume $\Delta\omega \ll \omega_0$ so that

$$\begin{bmatrix} \omega_1 \\ \omega_2 \end{bmatrix} = \omega_0 - \frac{\Delta\omega}{2} \begin{bmatrix} 1 \\ -1 \end{bmatrix}, \quad \begin{bmatrix} k_1 \\ k_2 \end{bmatrix} = k_0 - \frac{\Delta\omega}{2C_{g,0}} \begin{bmatrix} 1 \\ -1 \end{bmatrix}, \quad C_{g,0} = \frac{d\omega}{dk}\big|_{\omega=\omega_0}. \quad (3.24)$$

Further, we anticipate the water depth such that the low-frequency component is a long wave, viz. $k_\Delta h \ll 1 \Rightarrow \Delta\omega/k_\Delta \approx \sqrt{gh}$.

Through substitution of the decomposition (3.23) in the general form (3.17) we can show that for the generalized model we obtain

$$a_\Delta' = -\frac{g}{k_0\left(gh - C_{g,0}^2\right)} \left[2\frac{C_{g,0}}{C_0} - \frac{1}{2}\right] a_2'(a_1')^* \exp\left[i(k_2 - k_1 - k_\Delta)x\right]. \qquad (3.25)$$

In physical variables, the low-frequency surface elevation can thus be written as

$$\eta_{\mathrm{lf}} = 2\Re\{\zeta_\Delta \exp\left[i\left(k_\Delta x - \Delta\omega t\right)\right]\} = -\frac{RS(x,t)}{\rho\left(gh - C_{g,0}^2\right)}, \qquad (3.26)$$

where $\rho$ is the fluid density and $RS(x,t)$ is the radiation stress function written as

$$RS(x,t) = 4\rho g \left[2\frac{C_{g,0}}{C_0} - \frac{1}{2}\right] \Re\{\zeta_1\zeta_2^* \exp\left[i\left((k_1 - k_2)x - \Delta\omega t\right)\right]\}. \qquad (3.27)$$
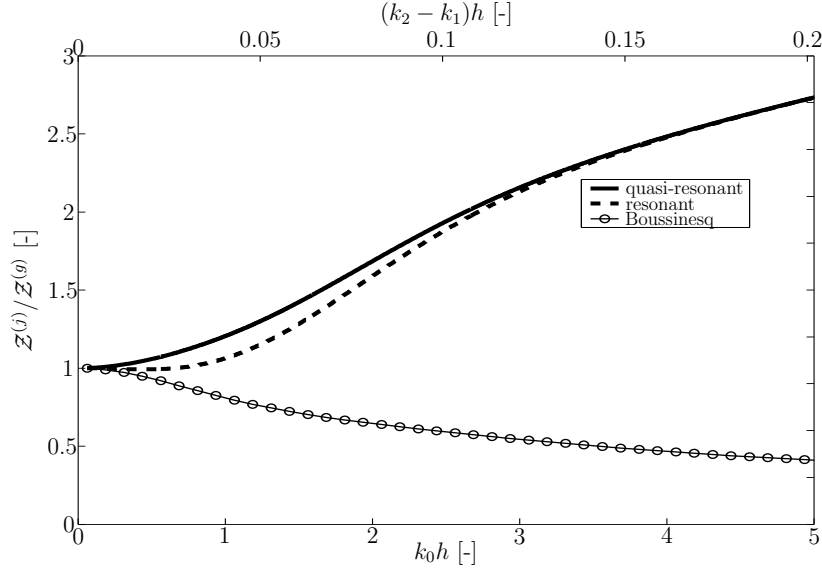
**Figure 3.3:** Difference interaction, $\Delta\omega = 0.02\omega_0$. Coupling coefficient for difference interactions for different approximations normalized with expression generalized model (viz. (3.26)), as a function of $k_0 h$ (bottom axes) and $(k_2 - k_1)h$ (top axes).

The eq. (3.26) is the well-known expression for the long-wave response due to radiation stress forcing in water of uniform depth [Longuet-Higgins & Stewart, 1962]. This is a forced response, consequently of small magnitude, propagating with the primary wave group at the (linear) group speed $C_{g,0}$. Note that this is not a valid description in the limit of near-resonance where the denominator in (3.26) diminishes. The equivalence with Longuet-Higgins & Stewart [1962] is only for the generalized model; the quasi-resonant and resonant coupling coefficients generally predict higher values for the bound wave amplitude (Figure 3.3) whereas the Boussinesq approximation predicts bound-wave amplitudes that are lower than the equilibrium solution (3.26).

*Interactions over finite bandwidth*

The quadratic narrow-band sum and difference interactions are but special cases of the interaction configurations in a spectrum of arbitrary bandwidth. Since analytical expressions for forced modes in a spectrum of arbitrary shape are not readily available, we resort to inter-comparison of the coupling coefficients (for unidirectional waves), utilizing the generalized coupling coefficient $\mathcal{Z}_{2,3}^{(g)}$ as a benchmark. We have verified the latter with the second-order expressions in Hasselmann (1962) §4, which can be regarded as a spectral generalization of Stokes second-order theory.

In Figure 3.4, 3.5 and 3.6 we show contour lines in the $(k_1 h, k_2 h)$-plane for the quasi-resonant, resonant and Boussinesq coupling coefficients respectively, normalized by the generalized coefficient, for both sum and difference interactions. For the quasi-resonant model (Figure 3.4), the contour lines are close to unity in most of the domain, in particular for the sum-interactions. Notable exception are the interaction configurations

**Figure 3.4:** Quasi-resonant coupling coefficient $\mathcal{Z}^{(qr)}$ normalized by generalized coefficient $\mathcal{Z}^{(g)}$ for sum-interactions (upper-left) and difference interactions (lower-right). Shaded area indicates $\delta_{1,2}^{(r)} < 0.5$.

corresponding to fairly narrow-band difference interactions (region near diagonal in lower pane), where values considerably larger than unity are observed (lower pane of Figure 3.4). For the resonant model (Figure 3.5) and Boussinesq model (Figure 3.6) the differences in interaction coefficients are more pronounced. In particular, coupling through sum-interactions is generally underestimated by the resonant and Boussinesq approximations. The forcing of difference interactions is overestimated by the resonant coefficient and underestimated by the Boussinesq coefficient for the ranges shown.

However, differences in the coupling coefficient do not necessarily reflect a distinct dynamical behavior of the nonlinear wave system. Away from resonance the quadratic response is a forced, non-secular, contribution and inherently of small magnitude; it is only when interaction configurations approach resonance that they have a dynamical effect on the wave evolution. A measure for the proximity to resonance is[†]

$$\delta_{1,2}^{(r)} = \left| \frac{\varkappa_1 + \varkappa_2 - \varkappa_{1+2}}{\min\left(\varkappa_1, \varkappa_2, \varkappa_{1+2}\right)} \right|. \tag{3.28}$$

Small values of $\delta_{1,2}^{(r)}$ indicate that the interaction is near-secular, whereas $\delta_{1,2}^{(r)} \sim O(1)$ indicate a departure from resonance. The shaded areas in Figures 3.4, 3.5 and 3.6 represent the regions where $\delta^{(r)} < 0.5$. It can be seen that in these regions, apart maybe from the Boussinesq model, the coupling coefficients are very nearly the same. Thus, in

---

[†]Differing from measures proposed by Agnon *et al.* [1993] and Eldeberky & Madsen [1999] in that the denominator is the minimum wavenumber in the interaction.

**Figure 3.5:** Resonant coupling coefficient $\mathcal{Z}^{(r)}$ normalized by generalized coefficient $\mathcal{Z}^{(g)}$ for sum-interactions (upper-left) and difference interactions (lower-right). Shaded area indicates $\delta_{1,2}^{(r)} < 0.5$.



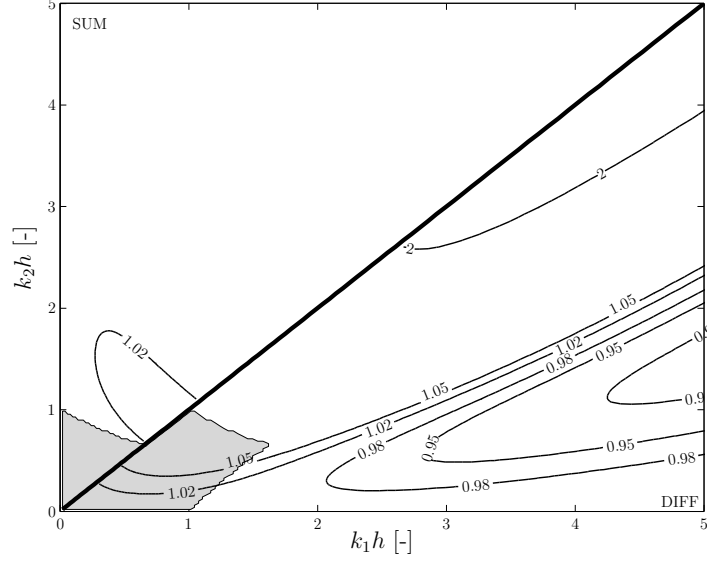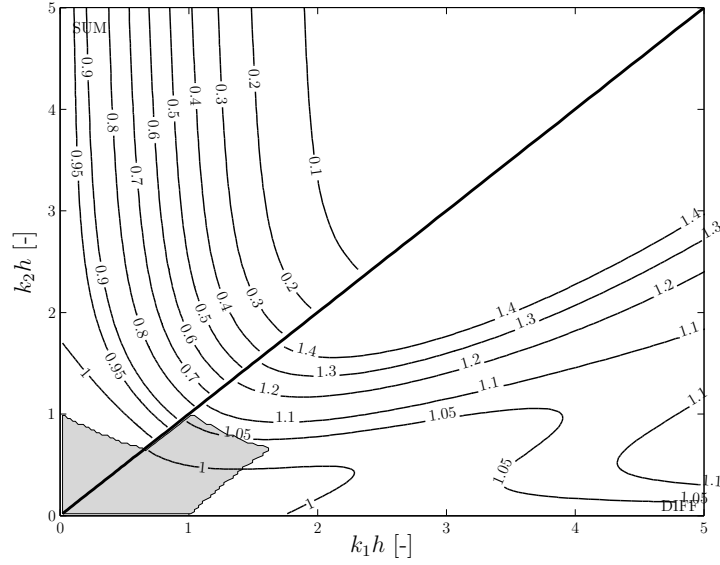**Figure 3.6:** Boussinesq coupling coefficient $\mathcal{Z}^{(b)}$ normalized by generalized coefficient $\mathcal{Z}^{(g)}$ for sum-interactions (upper-left) and difference interactions (lower-right). Shaded area indicates $\delta_{1,2}^{(r)} < 0.5$.
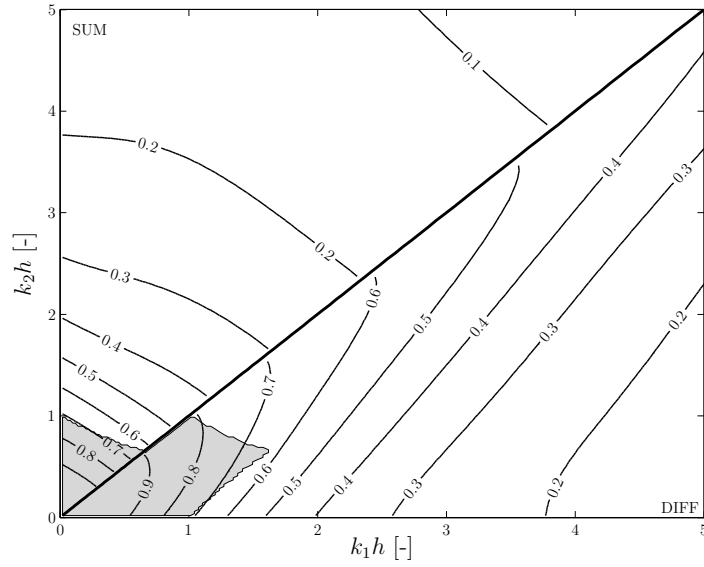
$|\lambda_1 - \lambda_2| > k_{1-2}$

$\varkappa$ $\qquad$ $\varkappa$

$\Delta\varkappa_1$ $\qquad$ $\Delta \boldsymbol{k}$

$k_{1-2}$ $\qquad$ $k_{1+2}$ $\qquad$ $\boldsymbol{k}_1$

$k_{1+2}$ $\qquad$ $\boldsymbol{k}_1 + \boldsymbol{k}_2$ $\qquad$ $k_1$ $\qquad$ $\boldsymbol{k}_2$

$k_1$ $\qquad$ $\Delta\varkappa_1$ $\qquad$ $k_1$ $\qquad$ $k_2$

$k_2$ $\qquad$ $\boldsymbol{k}_2$ $\qquad$ $k_{1-2}$

$\lambda$ $\qquad$ $\lambda$

$|\lambda_1 - \lambda_2| > k_{1-2}$
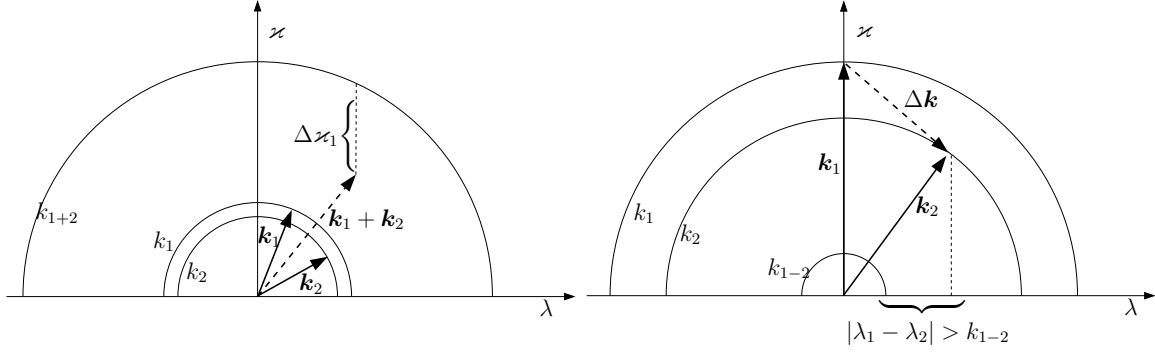
**Figure 3.7:** Sketches of interaction configurations; solid arrows indicate wavenumber vectors of primary waves; dashed arrows indicate sum/difference wavenumber vector. Left panel: non-collinear sum interaction, $\Delta\varkappa_1$ indicates resonance mismatch. Right panel: non-collinear difference interaction, illustrating angle limitation for this class of interactions.

the vicinity of resonance, the dynamically most interesting region, the models are nearly equivalent, implying that their nonlinear dynamical response is very similar; it is only in the bound wave representation, and then mostly in the low-frequency bound waves, that the models are at variance.

*Non-collinear interactions in the angular-spectrum representation*
Noteworthy is the fact that, although the angular spectrum description forms a natural basis for directional wave fields, and most of the considerations for unidirectional waves readily apply to the shoaling of directional wave fields in the presence of nonlinearity, this is not the case for non-collinear difference interactions. Although non-collinear interactions are generally further from resonance than their collinear counterparts [Newell & Aucoin, 1971, even proposed to use directionality in shallow water as a source of 'dispersion'], these interactions can contribute to the dynamics of the nearshore wave field [see e.g. Elgar *et al.*, 1993]. In the present approximation, non-collinear difference interactions are only partially represented. Consider for instance the difference interaction between component $(\omega_1, \lambda_1)$ and $(\omega_2, \lambda_2)$ forcing a component $(\omega_1 - \omega_2, \lambda_1 - \lambda_2)$, which is schematically sketched in the right panel of Figure 3.7. On account of the fact that we model such forced modes as modulations of *propagating* free modes we implicitly impose the condition $\lambda_1 - \lambda_2 \leq k_{1-2}$, with $k_{1-2}$ denoting the wavenumber related to $\omega_1 - \omega_2$ through the linear dispersion relation. However, from that dispersion relation we have $k_1 - k_2 > k_{1-2}$ such that we exclude forced waves for which the lateral wavenumber is $k_{1-2} < \lambda_1 - \lambda_2 \leq k_1 - k_2$, since for these components the corresponding free mode $(\omega_1 - \omega_2, \lambda_1 - \lambda_2)$ is evanescent. Thus, on account of the fact that we model the presence of bound waves through the modulation of propagating free modes we implicitly introduce an aperture restriction on bound wave motion forced by non-collinear difference interactions. Since non-collinear interactions are generally further from resonance than their (near-)collinear counterparts, the dynamical consequences of their omission are most likely indirect, through excitation (or lack thereof) of trapped

modes [edge waves, see e.g Bowen & Guza, 1978]. No such implicit restrictions apply to superharmonic interactions in directional wave fields; for these components $k_1 + k_2 \leq k_{1+2}$, so that they are fully represented in the angular spectrum description (left panel Figure 3.7).

## 3.2 Comparison to observations: unidirectional waves in deep and shallow water

In this section we compare model results with laboratory observations of steady, unidirectional waves to verify the generalized validity of the nonlinear interaction terms that account for cubic resonances in deep-intermediate water and quadratic resonances in shallow water.

For a steady wave field (2.44) reduces to

$$\left( \frac{d}{dx} + \frac{1}{2V_1} \frac{dV_1}{dx} \right) \varphi_1 = \widetilde{\Xi}_1^{(\text{wb})} \{\varphi_2\} + \widetilde{\Xi}_1^{(\text{wbb})} \{\varphi_2\} + \widetilde{\Xi}_1^{(\text{wc})} \{\varphi_2\}$$
$$+ \widetilde{\Xi}_1^{(\text{ww})} \{\varphi_2 \varphi_3\} + \widetilde{\Xi}_1^{(\text{www})} \{\varphi_2 \varphi_3 \varphi_4\}, \quad (3.29)$$

where $\widetilde{\Xi}_1^{(\text{ww})} = \xi_1^{(\text{ww})}/V_1$, $\widetilde{\Xi}_1^{(\text{www})} = \xi_1^{(\text{M,www})}/V_1$ and the remaining forcing terms are given in Appendix B. The corresponding surface elevation amplitudes, $\zeta_1$, are found through (2.45).

For unidirectional wave propagation over one-dimensional topography we numerically evaluate (3.29) for $\lambda = 0$ (thus unidirectional waves propagating along $x$) and omit the terms involving the lateral depth variability. For that case, the wave–current forcing term $\widetilde{\Xi}_1^{(\text{wc})}\{\varphi_1\}$ for $\lambda = 0$ is given as

$$\widetilde{\Xi}_{p_1}^{(\text{wc})}\{\varphi_{p_1}\} = i \frac{k_{p_1}}{C_{g,p_1}} \varphi_{p_1} \sum_{p_2} \frac{\omega_{p_2} k_{p_2}}{gh} |\varphi_{p_2}|^2. \quad (3.30)$$

and accounts for the effects of the attendant return current – to ensure zero net mass flux – on the wave propagation. The predicted wave-induced water level changes (i.e. set-down) were found to be everywhere smaller than 0.1% of the undisturbed water depth, and are neglected here.

The model is initialized at the up-wave boundary with the observed primary spectral component(s) obtained from a Fourier-transformed time series at that location with added (theoretical) second-order harmonics. This boundary condition was chosen, instead of simply utilizing the full observed spectrum, to minimize spurious modulations in the computations induced by spectral leakage effects as a result of small imperfections in e.g. wave generation or recording devices [see also Shemer et al., 2001].

The ordinary differential equations (3.29) are integrated using a standard fourth-order, fixed-step-size, Runge–Kutta scheme.

### 3.2.1 Evolution of wave groups in intermediate water depth

The third-order model (3.29) is compared to observations of periodic wave groups propagating in relatively deep water reported by Shemer *et al.* [2001], to verify the model's representation of the deep-water nonlinear physics (i.e. near-resonant cubic interactions). The experiments were conducted in a wave flume, 18 m long and 1.2 m wide, with a uniform water depth of 0.60 m. The positive $x$-axis is in the direction of propagation with the origin at the wave generator. For more detailed information on the experimental set-up and the complete set of experiments conducted we refer to Shemer *et al.* [1998, 2001].

The wave field consists of a periodically modulated carrier wave with period $T_0 = 0.9$ s. The wave board is driven by a signal of the form

$$s(t) = s_0|\cos{(\Omega_0 t)}|\cos{(\omega_0 t)}, \qquad\qquad \Omega_0 = \frac{\omega_0}{20}, \qquad\qquad (3.31)$$

where $\omega_0 = 2\pi/T_0$. The spectrum of this signal is characterized by a maximum at $\omega_0$ and sidebands at integer multiples of $2\Omega_0$ with the two nearest to $\omega_0$ being most significant. For the case considered here $k_0 a_0 \approx 0.21$, where $k_0$ is related to $\omega_0$ through the linear dispersion relation and $a_0$ is taken (after Shemer *et al.*, 1998) as the maximum amplitude of the carrier wave in a group close to the wave generator.

The model is initialized with the spectral components at $\omega_0$ and $\omega_0 \pm 2\Omega_0$ of a time series of 18 s (i.e. 20 wave periods) duration observed at $x = 0.245$ m (re-sampled with $N = 1024$ points and $\Delta t = 0.0176$ s). Second-order components are computed using Stokes' second-order theory (equation (2.32)) and included in the up-wave boundary condition. We compute the evolution of an equidistant array of 65 frequencies with $\Delta\omega = 2\pi/(N\Delta t)$. The integration is performed using a step size, $\Delta x$, of 0.1 m.

In Figure 3.8 we compare the observed (circles) and predicted (solid line) time series at five positions: $x = \{0.245, 1.845, 5.78, 6.98, 8.425\}$ m. The initially near-symmetrical wave groups develop strong left–right asymmetry of the envelope with steep fronts and gently sloping rears as also observed in the experiments reported by e.g. Feir [1967]. The asymmetry can be explained heuristically by the combined effects of amplitude and frequency dispersion (Lighthill 1978, p. 462). Initially the larger waves in the group propagate fastest under the effects of amplitude dispersion, reducing wavelengths in the front of the group and increasing those in the rear; the associated group speed variation further enhances the localization of energy in the front of the groups, resulting in increasingly forward leaning of the wave groups as observed in the experimental data.

In Figure 3.9 observed and predicted amplitudes of the spectral components are compared for the same locations as in Figure 3.8. The initially narrow spectrum widens by energy transfers mostly to higher frequencies and an increase of the energy level just below the main peak, apparently at the expense of the spectral components just above the peak (Figure 3.9). The agreement with the model results is excellent (as implied by the level of agreement in the time domain).
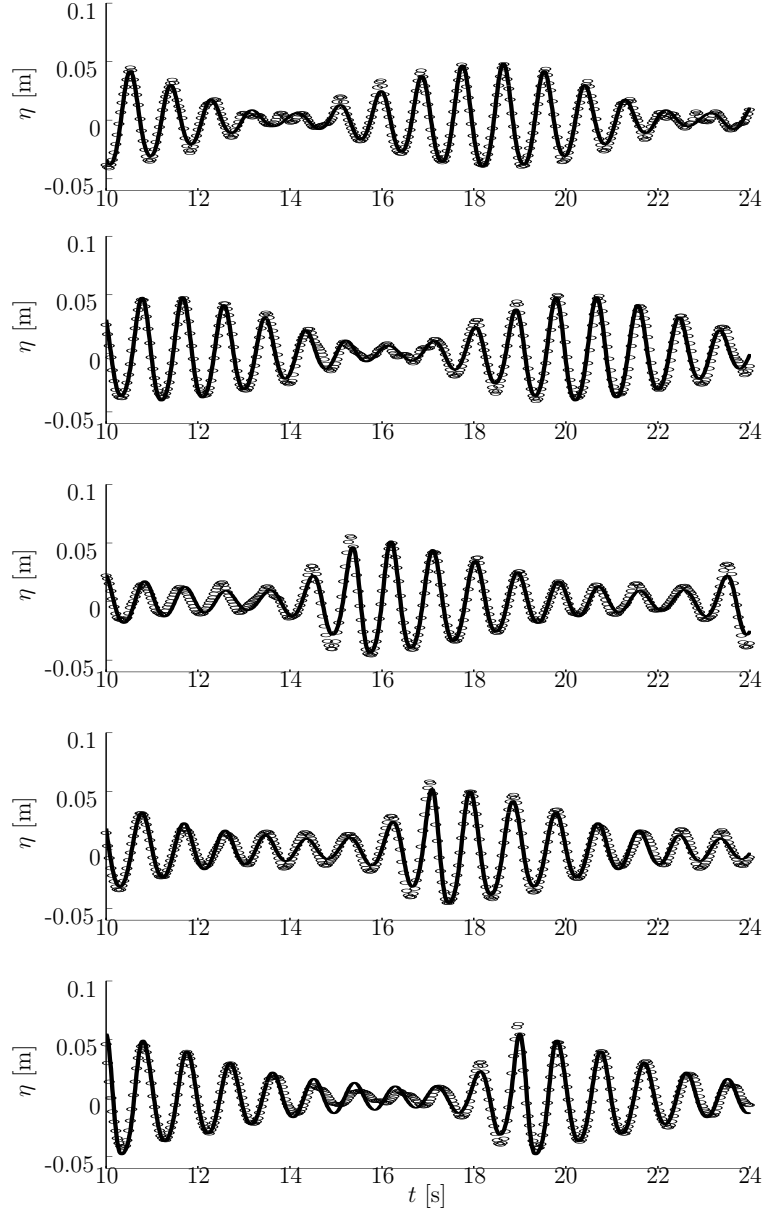
**Figure 3.8:** Time series comparison of observed and predicted nonlinear wave group evolution in uniform depth. The carrier frequency $\omega_0 = 2\pi/(0.9\,\mathrm{s})$, water depth $= 0.6\,\mathrm{m}$, $\epsilon \approx 0.21$. Circles denote observed surface elevations from Shemer *et al.* [1998, 2001]; solid line denotes model result. Panels (from top to bottom) correspond to positions $\{0.245, 1.845, 5.78, 6.98, 8.425\}\,\mathrm{m}$.
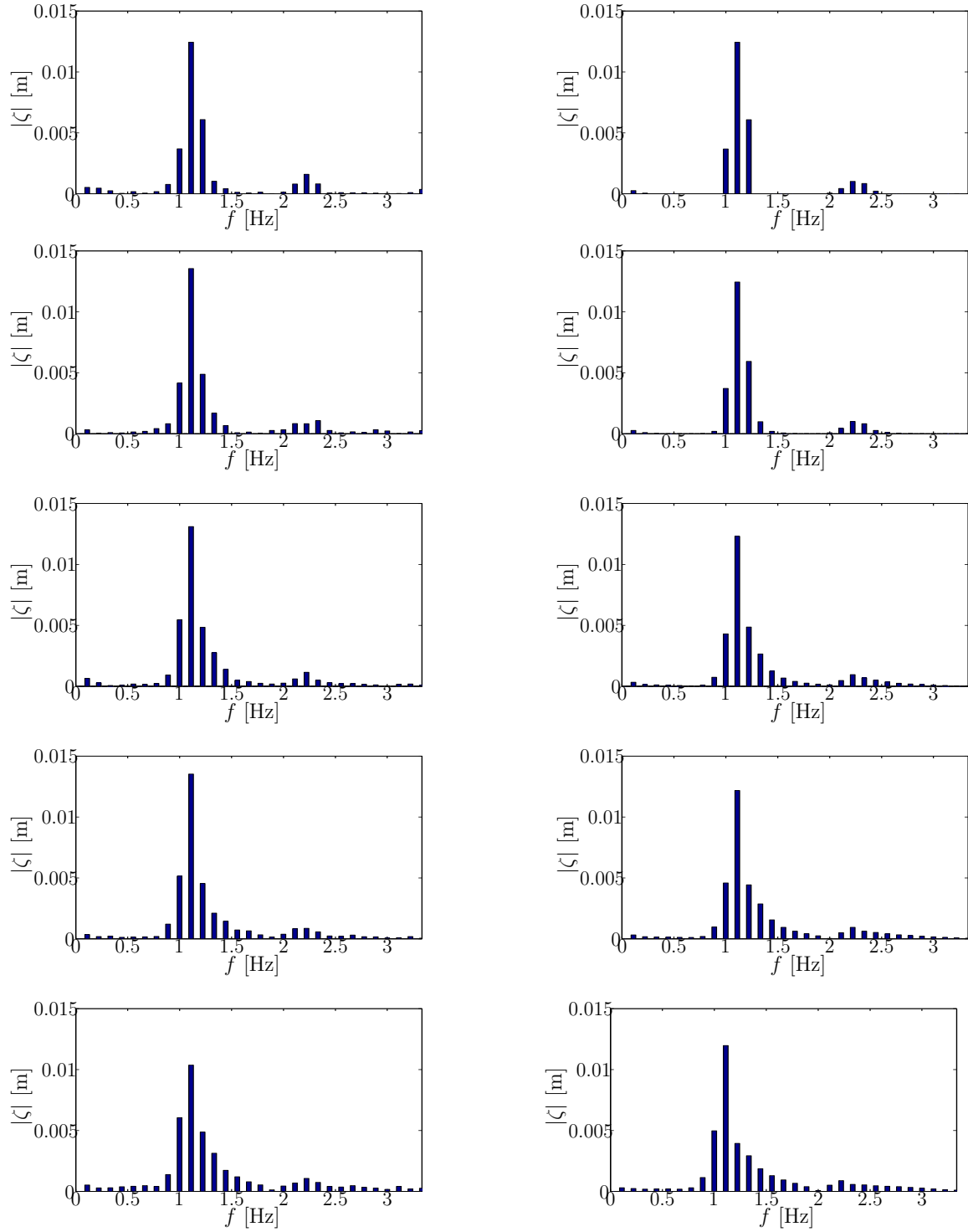
**Figure 3.9:** Comparison of observed and predicted spectral amplitudes of nonlinear wave groups in uniform depth. The carrier frequency $\omega_0 = 2\pi/(0.9\,\text{s})$, water depth $= 0.6\,\text{m}$, $\epsilon \approx 0.21$. Left panels: observed amplitudes from Shemer *et al.* [1998, 2001]. Right panels: model predictions. Rows (from top to bottom) correspond to positions $\{0.245, 1.845, 5.78, 6.98, 8.425\}\,\text{m}$. Following Shemer *et al.* [2001], amplitudes of the observed spectra at frequencies other than intervals of integer multiples of $2\Omega_0$ separated from $\omega_0$ are set to zero. These amplitudes are small for all positions and attributed mainly to spectral leakage.
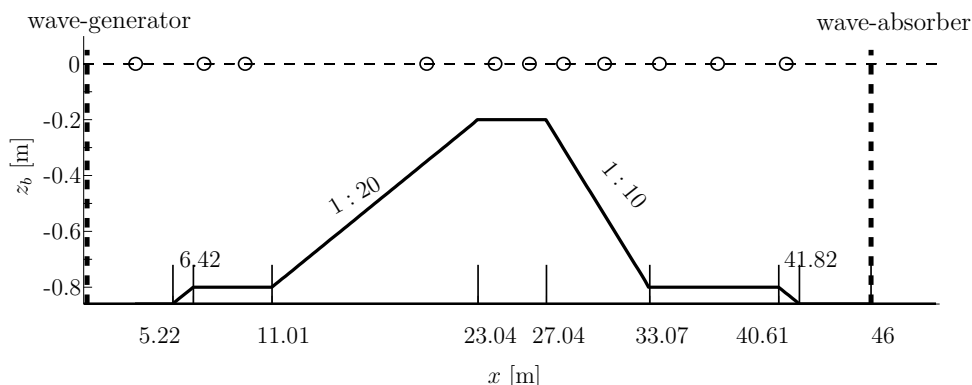
**Figure 3.10:** Schematic representation of the trapezoidal bottom profile of Luth *et al.* [1994]; circles at $z = 0$ m denote wave gauge positions.

The model predictions accurately reproduce both the increasing asymmetry of the envelope and the evolution of the individual waves. Apart from some discrepancies in the less energetic region between groups, the agreement is excellent. This demonstrates the model's ability to accurately predict wave group evolution resulting from near-resonant cubic wave–wave interactions in deep-intermediate water depth.

Model simulations (not shown here) extended to larger distances from the wavemaker than for which observations were available in the experimental data, indicate that the groups eventually split into a group consisting of the higher waves and one with the lower waves. The higher-wave group leads and eventually coalesces with the preceding low-wave group followed by recurrence-type behavior qualitatively similar to that observed and discussed in Lo & Mei [1985]. Intermittent wave breaking due to increased steepness ($k_0 a \approx 0.34$ was observed in the numerical simulations) will probably result in only partial recurrence.

### 3.2.2 Wave propagation over a submerged obstacle

To test the model's ability to predict harmonic generation due to near-resonant quadratic interactions over variable depth in relatively shallow water, we consider the propagation of waves over a trapezoidal shoal in a laboratory flume [Luth *et al.*, 1994; Beji & Battjes, 1993], a schematic representation of which is shown in Figure 3.10. The up- and downslope of the shoal are 1:20 and 1:10 respectively. Away from the shoal the uniform water depth is 0.80 m, and the minimum depth over the shoal is 0.20 m. The wave generator is positioned at $x = 0$. At $x = 46$ m a wave absorber is installed to ensure unidirectional wave propagation in the area of interest; circular markers in the figure denote wave gauge positions. The bathymetrical dimensions are those reported by Luth *et al.* [1994], which is a scaled, enlarged version (by a factor of 2) of the set-up used by Beji & Battjes [1993]. The wave field characteristics were scaled accordingly to reproduce cases reported by Beji & Battjes [1993].
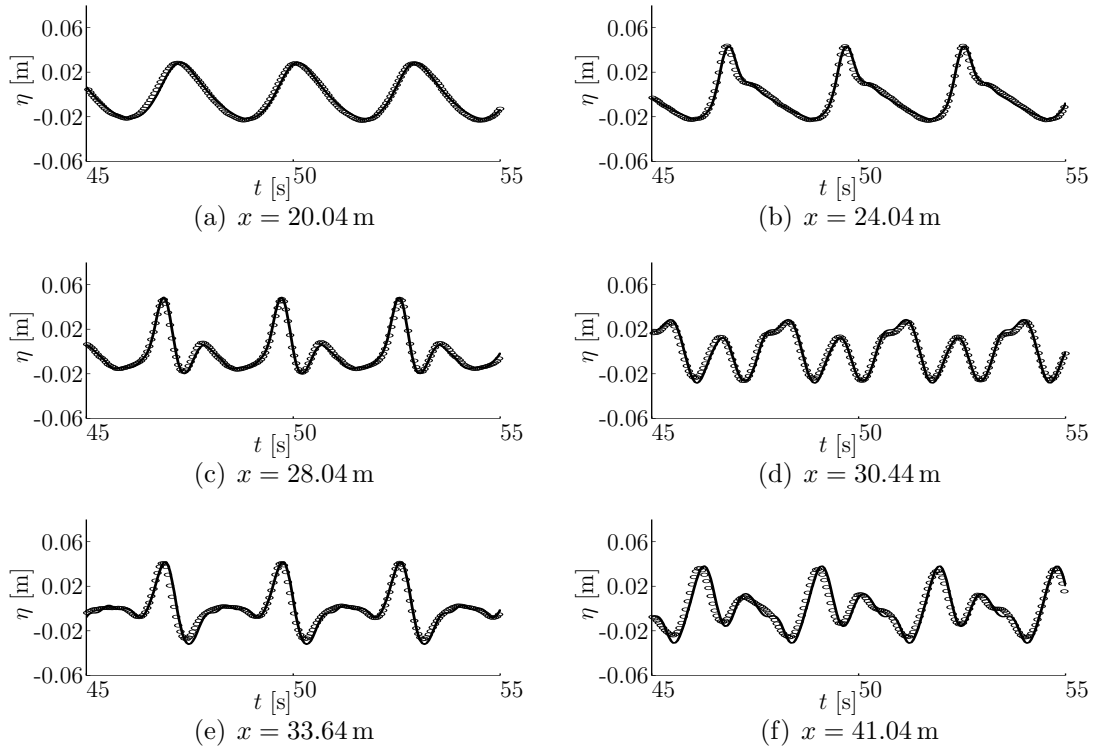
**Figure 3.11:** Comparison of observed and predicted time series for wave propagation over a shoal. Incident waves have wave period 2.86 s and amplitude 0.02 m. Circles denote laboratory observations by Luth *et al.* [1994], solid line represents model predictions.

The incident wave train is monochromatic with period $T_0 = 2.86$ s and amplitude 0.02 m. The model is initialized with the spectral component at $\omega_0$ of a (re-sampled) time series of 25.71 s duration (512 points at 0.0502 s intervals) observed at $x = 3.04$ m. The first harmonic is computed using Stokes' second-order theory (viz. (2.32)) and included in the up-wave boundary condition.

The numerical integration is performed for 60 equidistant frequency components with $\Delta\omega = 2\pi/(N\Delta t)$ with a spatial step size of 0.1 m.

Figure 3.11 shows a comparison of observed and predicted surface elevation time series for positions $x = \{20.04, 24.04, 28.04, 30.44, 33.64, 41.04\}$ m. The model successfully captures both the initial steepening and forward leaning of the waves on the up-slope and the release of higher harmonics over the shoal and down-slope; the agreement between observed and predicted time series is excellent, even at the farthest location $x = 41.04m$ (Figure 3.11). Similar agreement with somewhat larger discrepancies in the details of the wave profile was reported by Beji & Battjes [1994], who compared simulations of a Boussinesq model with improved dispersion characteristics [Madsen & Sørensen, 1992] to the earlier dataset of Beji & Battjes [1993] in a more restricted domain. These authors also illustrated that improved dispersion is crucial to predict the wave evolution accurately by including a comparison to simulations with Boussinesq equations with
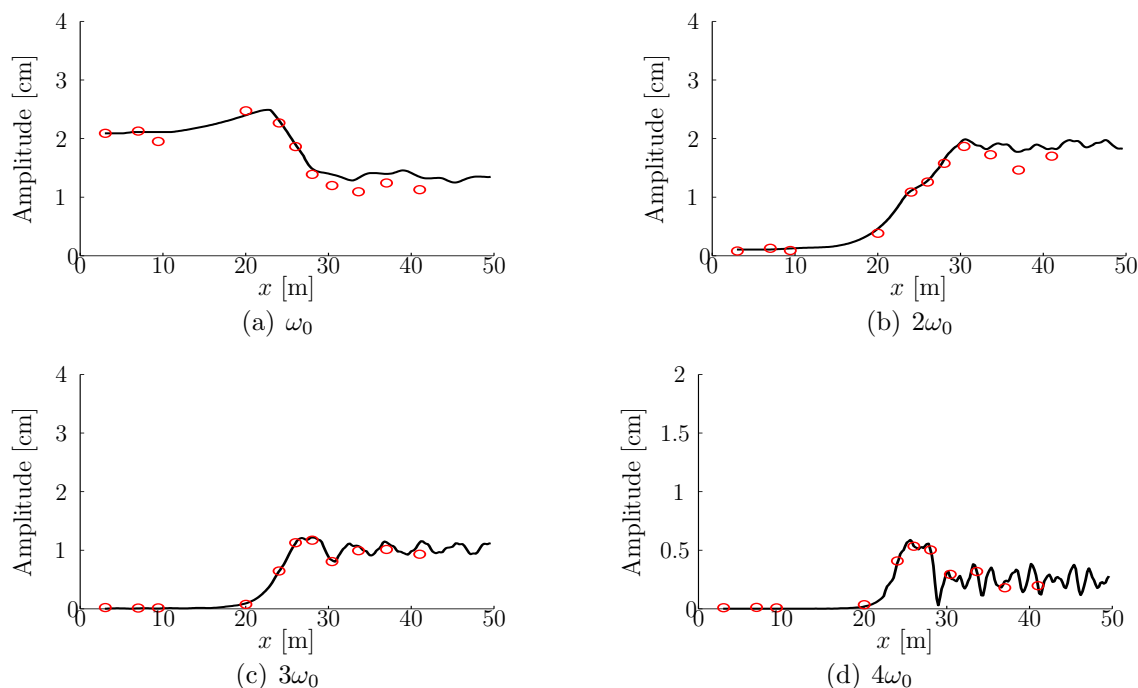
**Figure 3.12:** Evolution of amplitude of the primary wave component and three harmonics for a periodic incident wave with period $2.86\,\mathrm{s}$ and initial amplitude $0.02\,\mathrm{m}$ propagating over a shoal. Circles denote observed values from Luth *et al.* [1994], solid line represents model result. Note different scale vertical axis for $4\omega_0$.

lowest-order dispersion [Peregrine, 1967], which compared considerably less favorably with the observations than the dispersion-enhanced formulation by Madsen & Sørensen [1992]. Dingemans (1997, §5.9) showed that even the predictions with the enhanced Boussinesq formulation deteriorate for positions far behind the shoal ($x = 33.64\,\mathrm{m}$ and $x = 41.04\,\mathrm{m}$, no measurements were available at these positions in the set-up used by Beji & Battjes), suggesting that taking full account of dispersion (as in the present work) or a high-order approximation [e.g. Agnon *et al.*, 1999; Madsen *et al.*, 2003] is essential to resolve wave phases over larger distances [see also Stelling & Zijlema, 2003].

A comparison between predicted and observed amplitudes of the primary wave component and three harmonics as a function of the horizontal coordinate is shown in Figure 3.12. The model slightly overestimates the amplitude of the primary wave and its first harmonic for all positions behind the shoal; overall the computed evolution is in very good agreement with the observations.

Although the depth variations over the shoal are fairly rapid, the observations at locations between the generator and the trapezoid (not shown here) did not indicate the presence of significant wave reflections; moreover, the level of agreement between observations and predictions supports the assumptions of unidirectionality and slowly varying depth as implicit in the model.

## 3.3  Wave-bottom interactions in the angular-spectrum approximation

In this paragraph we address the properties of the approximation with respect to the lateral variability, its limitations and relation to more general, two-dimensional, formulations.

In the linear approximation, the angular spectrum description is, apart from the omission of local evanescent modes, an 'exact' description of the wave field evolution over an alongshore-uniform topography [e.g. Stamnes, 1986]. However, the inclusion of the effects of lateral depth variability on the wave evolution, contained in the convolution-type forcing terms on the evolution equations involving the depth perturbation $\widetilde{h}$, is more approximate. Essentially, through these terms, the waves 'feel' the perturbation of the bottom boundary condition. Their contribution to the wave evolution or, equivalently, the sensitivity of the wave field to perturbations at the bottom, is attenuated with increasing depth and vanishes in deep water. These wave–bottom operators are rather long expressions and, apart from the fact that they vanish in deep water, a causal prerequisite, they are not readily interpretable in physically meaningful terms.

We illustrate the nature of the approximation and its inherent limitations by means of a reduced case example of waves over uniform depth. However, we write the (uniform) depth, somewhat arbitrarily, as the sum of a (constant) reference depth $\overline{h}$ and a (small, and uniform) perturbation $\widetilde{h}$ such that $h = \overline{h} - \widetilde{h}$, and $\widetilde{h} \ll \overline{h}$. The attendant wave field is represented by a temporally and laterally periodic potential function written as

$$\Phi = \widetilde{\varphi}\frac{\operatorname{Ch} Q}{\operatorname{Ch} q} \exp\left[i\left(\lambda y - \omega t\right)\right] + *, \tag{3.32}$$

with $\widetilde{\varphi}$ governed by the Helmholtz equation

$$\left[\frac{d^2}{dx^2} + (k^2 - \lambda^2)\right]\widetilde{\varphi}(x) = 0, \tag{3.33}$$

and $k$ is related to the frequency $\omega$ through the dispersion relation. We omit evanescent modes and consider only waves propagating into the half plane of positive $x$. The associated principal wavenumber $\widetilde{\varkappa} = (k^2 - \lambda^2)^{1/2}$ is expanded in a Taylor expansion around the reference depth $\overline{h}$ as in

$$\widetilde{\varkappa}(h) = \sum_{j=0}^{\infty} \frac{(-\widetilde{h})^j}{j!} \left.\frac{d^j\widetilde{\varkappa}}{dh^j}\right|_{h=\overline{h}} = \sum_{j=0}^{\infty} \frac{(-\widetilde{h})^j}{j!} \frac{d^j\varkappa}{dh^j}. \tag{3.34}$$

In the following, for convenience of notation, we use $\varkappa = \widetilde{\varkappa}|_{h=\overline{h}}$ and $d_h^n\varkappa = d_h^n\widetilde{\varkappa}|_{h=\overline{h}}$. The potential amplitude $\widetilde{\varphi}$, governed by (3.33), is subsequently written as

$$\widetilde{\varphi} = \varphi \exp\left[i\varkappa x\right], \tag{3.35}$$

where $\varphi$ is a slowly varying amplitude that incorporates the difference between the 'actual' cross-shore wavenumber $\widetilde{\varkappa}$ and $\varkappa$, evaluated at the reference depth. In essence,

the modulation of $\varphi$ accounts for all the remaining terms ($j > 0$) in the expansion (3.34) which, in differential form, may be written as

$$\frac{d}{dx}\varphi = i\varphi \sum_{j=1}^{\infty} \frac{(-\widetilde{h})^j}{j!} \frac{d^j \varkappa_1}{dh^j}. \tag{3.36}$$

To relate (3.36) to the angular-spectrum approximation we consider the transport equation eq. (3.29), in the linear approximation for a topography consisting of a two-dimensional perturbation $\widetilde{h}$ on an otherwise horizontal bottom ($\overline{h}$):

$$d_x\varphi_1 = \widetilde{\Xi}_1^{(\mathrm{wb})}\{\varphi_2\} + \widetilde{\Xi}_1^{(\mathrm{wbb})}\{\varphi_2\}. \tag{3.37}$$

If, as in the reduced case above, we assume the perturbation $\widetilde{h}$ to be spatially uniform we can show (after some manipulation) that eq. (3.37) reads

$$\frac{d}{dx}\varphi_1 = -i\left[\widetilde{h}\frac{d\varkappa_1}{dh}\varphi_1 - \frac{1}{2}\widetilde{h}^2\frac{d^2\varkappa_1}{dh^2}\right]\varphi_1. \tag{3.38}$$

The *RHS* of (3.38) is identically the first two terms of the expansion in (3.36), which shows that the wave–bottom terms in (3.29) in fact represent the first few terms of a series expansion of the eikonal relation around a reference depth. Therefore, to ensure accuracy of the approximation we require

$$O(\frac{\widetilde{h}^j}{\varkappa_1}\frac{d^j\varkappa_1}{dh^j}) \ll 1, \tag{3.39}$$

which becomes increasingly restrictive on $\widetilde{h}$ with decreasing $\varkappa_1$ (thus increasing angle of wave incidence). Thus, although the angular-spectrum approximation derived here is isotropic for the discrete angular components incident into the half plane of positive $x$ over a laterally uniform topography, it is an anisotropic approximation with respect to the wave interaction with the laterally varying depth; the approximation is increasingly restrictive on the magnitude of the lateral depth variation for increasing angle of wave incidence.

If we consider a more general setting, allowing for spatial variability of the (one-dimensional) reference depth $\overline{h}$, we can (after some manipulations) write the linear forcing terms involving the two-dimensional perturbation $\widetilde{h}$ as

$$\widetilde{\Xi}_1^{(\mathrm{wb})}\{\varphi_2\} = -i\frac{d\varkappa_1}{dh}\mathcal{G}_1\{\widetilde{h}, \varphi_2\} - \frac{1}{2V_1}\frac{dV_1}{dh}\mathcal{G}_1\{\widetilde{h}_x, \varphi_2\} - \frac{\lambda_1}{2k_1V_1}\frac{\partial C_{g,1}}{\partial h}\mathcal{G}_1\{\widetilde{h}_y, \varphi_2\}, \tag{3.40}$$

$$\widetilde{\Xi}_1^{(\mathrm{wbb})}\{\varphi_2\} = \frac{i}{2}\frac{d^2\varkappa_1}{dh^2}\mathcal{G}_1\{\widetilde{h}^2, \varphi_2\}. \tag{3.41}$$

The bottom slope terms represent a lowest-order (in terms of $\widetilde{h}$) approximation of the more general two-dimensional evolution equations for WKB waves [e.g. Mei, 1983], apart from the fact that they are anisotropic. In particular, in the third term on the *RHS* of

(3.40) the derivation with respect to the depth is a partial derivative $(\partial/\partial h)$, while in the second term, accounting for variation in the principal direction, a total derivative $(d/dh)$ operates on the principal group speed component $V_1$. This anisotropy in the bottom slope terms can be brought back to the disparate treatment of variations in the principal and lateral direction. In the principal direction multiple scales were defined, and used in the WKB formalism, while in the lateral direction variations are implicit in the summation of the angular components, without distinction of slow and fast scales.

Although the expressions (3.40) and (3.41) are physically meaningful and surprisingly simple in appearance, they are obtained through *a posteriori* analysis, motivated by heuristic considerations. Nevertheless, the result suggests that the wave–bottom approximation can indeed quite simply be related to the lowest-order terms of more general, two-dimensional formulations, which in turn leads us to hypothesize that the algebraic effort required to derive the higher-order approximations for the wave–bottom interactions – which in the formalism adopted in Chapter 2 becomes quite exhaustive at the order presently retained – may be circumvented when a more heuristic approach is followed from the outset. Although a more efficient derivation may bring even higher-order approximations within reach, the approximation in the wave–bottom interactions remains inherently restricted to relatively small incident wave angles, even with a larger – but finite – number of terms included.

## 3.4 Comparison to observations: waves over topography

To asses the model's performance over complex topography in the presence of nonlinearity, and verify empirically the robustness of the approximation, we compare model simulations to observations of wave propagation over two-dimensional topography. The emphasis is on the modeling of lateral depth variability in the presence of shallow-water nonlinearity. Since the cases we consider either involve wave propagation over relatively short length scales or exhibit very weak nonlinearity, we tentatively discard third-order effects (cubic interactions and wave–current interaction) in the simulations. Numerical simulations are performed with a slightly modified form of the governing equations for stationary wave fields (viz. (3.29)). A convenient form for the governing set is obtained upon combining (3.29) and (2.45) into a single equations for $A_1 = \sqrt{V_1}\zeta_1$ (more detail on the form of the quadratic nonlinear term is given in §3.1.2)

$$\frac{dA_1}{dx} = \Xi_1^{(\mathrm{wb})}\{A_2\} + \Xi_1^{(\mathrm{wbb})}\{A_2\} + i\sum_{\boldsymbol{v}_2,\boldsymbol{v}_3} \mathcal{W}_{2,3}A_2A_3\delta_{23;1}^{\lambda,\omega}E_{23;1}, \qquad (3.42)$$

where the operators $\Xi_1^{(\mathrm{j})}$ are modified with respect to the $\widetilde{\Xi}_1^{(\mathrm{j})}$ in (3.29) only to account for the 'shoaling factor' $\sqrt{V_1}$

$$\Xi_1^{(\mathrm{j})}\{A_2\} = \sqrt{V_1}\widetilde{\Xi}_1^{(\mathrm{j})}\{\frac{A_2}{\sqrt{V_2}}\}, \qquad (3.43)$$

and

$$\mathcal{W}_{2,3} = \sqrt{\frac{V_{2+3}}{V_2 V_3}} \, \mathcal{Z}_{2,3}^{(\mathrm{g})}. \tag{3.44}$$

The $\mathcal{Z}_{2,3}^{(\mathrm{g})}$ is the generalized form of the interaction coefficient defined in §3.1.2, eq. (3.15).

In all the numerical evaluations of (3.42) for two-dimensional cases, evanescent modes ($|\lambda| > k_\omega$) are excluded from the computations, including those modes that are evanescent at $x = 0$ but become propagating inside the computational domain on account of the variable depth. The set of ordinary differential equations (viz. eq. (3.42)) are integrated with a fourth-order, fixed-step-size, Runge–Kutta scheme.

### 3.4.1 Harmonic generation on a convex beach: weak lateral depth variability

To validate the model representation of wave propagation over weakly two-dimensional topography in the presence of strong harmonic enhancement, we compare model predictions to observations reported by Whalin [1971, 1972] who performed experiments on a laterally convex-shaped beach, shown in Figure 3.13, with monochromatic, normally incident waves. The experiments were performed in a wide flume (6.1 m wide, 25.6 m long). The two-dimensional topography consists of circular bottom contours with equal radii (half the flume width), centered along the centerline of the flume. The topography can be approximated by [Whalin, 1972]

$$h(x,y) = \begin{cases} 0.457\,\mathrm{m}, & \text{if } 0 \le x < 7.62\,\mathrm{m} + \tfrac{1}{2}W_f - G(y) \\ 0.457\,\mathrm{m} + \tfrac{1}{25}\left(7.62\,\mathrm{m} + \tfrac{1}{2}W_f - G - x\right), & \text{if } 7.62\,\mathrm{m} + \tfrac{1}{2}W_f - G(y) \le x \\ & \qquad\qquad \le 15.24\,\mathrm{m} + \tfrac{1}{2}W_f - G(y) \\ 0.152\,\mathrm{m}, & \text{if } 15.24\,\mathrm{m} + \tfrac{1}{2}W_f - G(y) < x \le 21.34\,\mathrm{m} \end{cases} \tag{3.45}$$

where $W_f$ denotes the width of the flume (6.1 m) and

$$G(y) = \sqrt{y\left(W_f - y\right)}, \qquad\qquad 0 \le y \le W_f. \tag{3.46}$$

The principal and lateral coordinates, $x$ and $y$ respectively, are defined as in Figure 3.13. The wave generator was positioned in the deeper part of the wave tank at $x = 1.615\,\mathrm{m}$. The observations by Whalin [1971, 1972] indicate significant enhancement of harmonics in the focal region where the combined effects of refraction, diffraction and nonlinear wave–wave interactions are important.

We compare model simulations (viz. a numerical implementation of (3.42)) to observations for four cases; periods and amplitudes are listed in Table 3.2 for each experiment. A snapshot of the model-predicted surface elevation over the topography for the case with 2.0 s period and 1.06 cm amplitude is shown in the lower panel of Figure 3.13. For each of the cases considered, the model is initialized with a single spectral component with the appropriate amplitude, frequency and alongshore wavenumber at $x = 0$, and
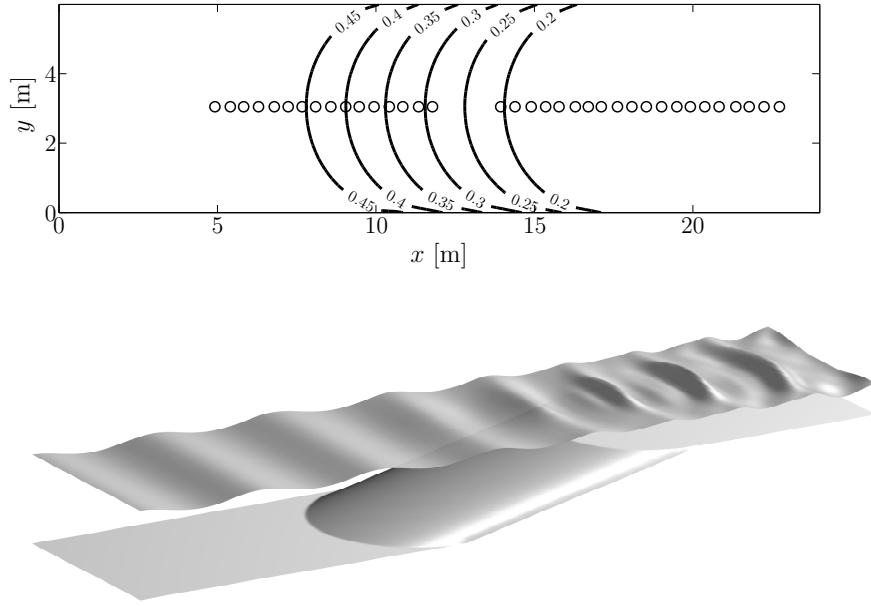
**Figure 3.13:** Top panel: depth contours experimental set-up of Whalin [1971] (units m), circles denote wave gauge positions along the centerline. Lower panel: model-predicted surface elevation (viz. eq. (3.29)) for incident wave period $2.0\,$s and initial amplitude $1.06\,$cm.

the corresponding (theoretical) first harmonic (Stokes second-order theory). The spatial domain is discretized with $\Delta x$ and $\Delta y$ both equal to $0.1\,$m; we numerically evaluate the evolution of the primary wave ($\omega_0$) and its three harmonics ($2\omega_0, 3\omega_0, 4\omega_0$).

| Period [s] | Amplitude [cm] |
|:---:|:---:|
| 2.0 | 0.75 |
| 2.0 | 1.06 |
| 1.0 | 0.97 |
| 1.0 | 1.95 |

**Table 3.2:** Wave periods and amplitudes for cases selected from Whalin [1971], for model-data comparison.

Figure 3.14 shows the evolution of the spectral amplitudes of the primary, first and second harmonic for the $2.0\,$s cases considered. As the waves propagate from the deep end of the flume over the topography into shallow water, the primary wave component initially increases predominantly due to shoaling and wave convergence until quadratic interactions approach resonance, resulting in the observed rapid growth of the first and second harmonic at the expense of the primary wave component, followed by partial recurrence.

For the 1.0 s cases, waves are in relatively deeper water and the quadratic interactions are considerably further from resonance. This results in relatively small first harmonic amplitudes (see Figure 3.15) and practically negligible second harmonics (not shown, no observations available). The large resonance mismatch results in rapid oscillations in the harmonic amplitude at the shallow end of the flume. These rapid recurrences can be understood as follows. At $x = 0$ the model is initialized with second-order, uniform-depth boundary conditions so that in the uniform-depth, deep end of the flume the amplitudes are constant (waves of permanent shape). Over the slope the interactions result in the excitement of 'free' motion at the harmonic frequency; in this region and in the shallow end of the flume, the harmonic wave train is then the superposition of free and forced waves (forced waves according to the local equilibrium) which, due to the large resonance mismatch, results in the oscillatory-type behavior observed in the predicted harmonic amplitude. Although we expect similar oscillations present also in the observations, the spatial resolution in the observations is insufficient to conclusively resolve such variations.

The agreement between model predictions and the observations is generally good. The large spread in observed wave amplitudes in the uniform-depth, deep-end of the flume is unexplained, and not seen in the simulation result; it is expected that these are in part due to inaccuracies in the wave generation (Whalin remarks that the plunger-type wave generator does not produce perfect sinusoidal waves, suggesting spurious wave excitation even at the lowest order). For the larger-wave 2.0 s case, the model predicts spatial oscillations of the primary harmonic in the down-wave region of the flume (Figure 3.14 panel $b$), which is absent in the observations; a similar discrepancy was invariably found by other authors [e.g. Liu $et\ al.$, 1985; Kaihatu & Kirby, 1995; Tang & Ouellet, 1997].

**Figure 3.14:** Evolution of amplitudes of primary wave component and harmonics for a periodic incident wave with period 2.0 s propagating over two-dimensional bathymetry. Amplitudes incident waves are 0.75 cm (left panels) and 1.06 cm (right panels) respectively. Circles denote observed values by Whalin [1971], solid line represents model results. Note differences in amplitude scales.
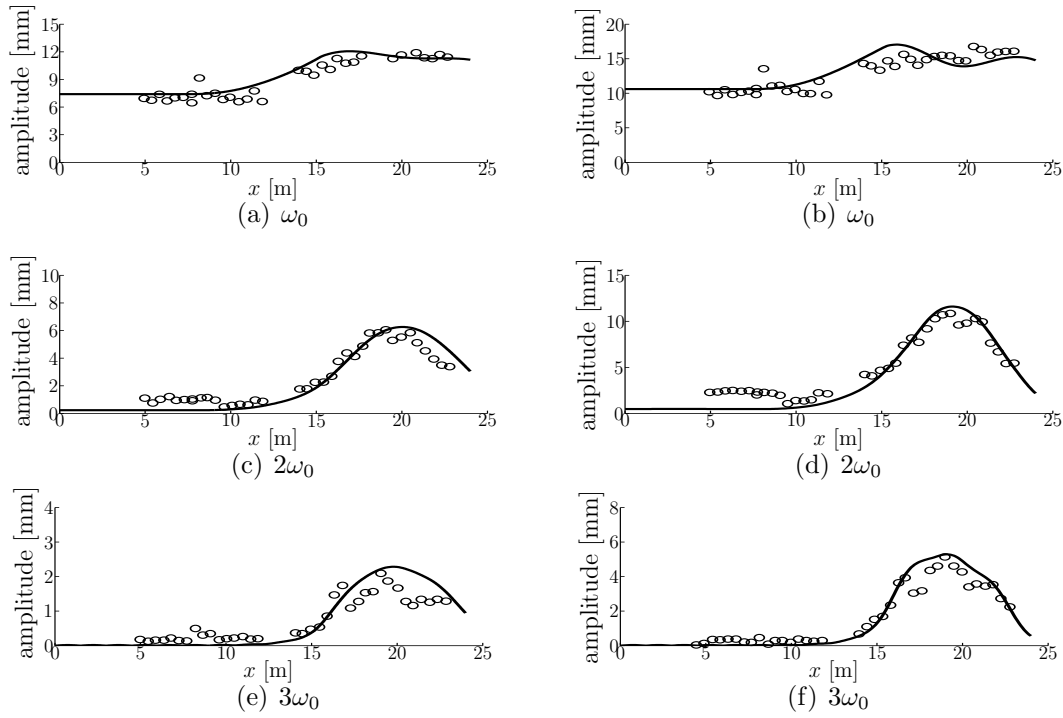


**Figure 3.15:** Evolution of amplitudes of primary wave component and harmonics for a periodic incident wave with period 1.0 s propagating over two-dimensional bathymetry. Amplitudes incident waves are 0.97 cm (left panels) and 1.95 cm (right panels) respectively. Circles denote observed values by Whalin [1971], solid line represents model results. Note differences in amplitude scales.
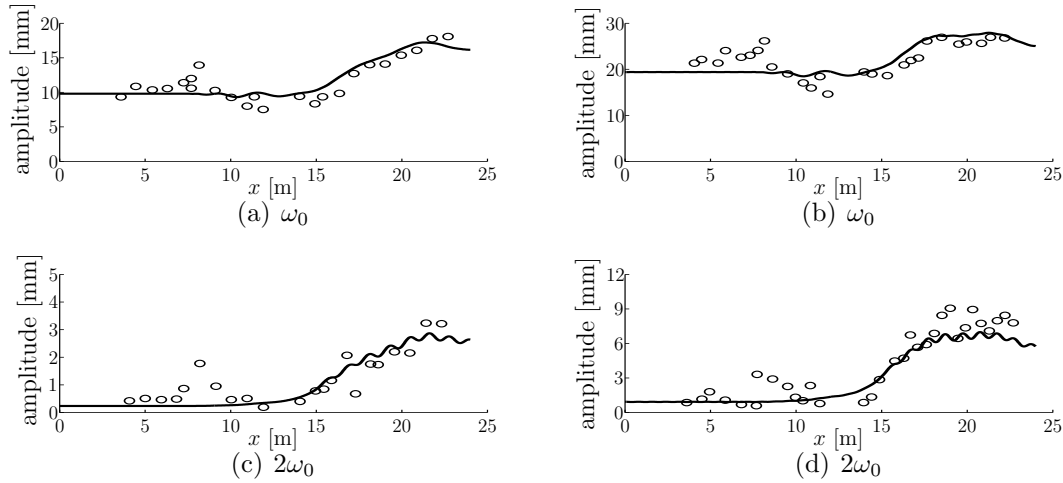
### 3.4.2 Waves over topography: submerged two-dimensional obstacles

The premise of weak lateral depth variations appears a reasonable one for the topography in the experiments by Whalin [1971]. However, less idealized topography can (and most likely will) be present on most natural beaches (e.g. nearshore sandbars or irregular reef shapes). In any case, if pronounced two-dimensional topography is present, the angular-spectrum model should generally be applied with caution. Here we empirically assess the limits of applicability of the model by comparing predictions to observations of waves traversing localized two-dimensional topography.

In the presence of fairly localized (in the lateral sense) obstacles, a practical difficulty occurs in the definition of the reference depth $\overline{h}$. In the derivation we have chosen the laterally averaged depth as the reference depth, as this appears a natural choice for cases where the lateral depth perturbation is fairly homogeneous (thus lateral homogeneity of the topography in the statistical sense is implied). However, since the reference depth is the key determining factor for the sensitivity of the model to the lateral depth variations (the model essentially 'picks up' the perturbation at the reference depth) this is probably not the best choice for more localized topographical variability. The most conspicuous difficulty with using a laterally averaged depth as a reference depth for cases with fairly local (in the lateral sense) depth variability, is the fact that the model's sensitivity to bottom perturbation depends on the lateral extent of the domain. For instance, consider the sketch in Figure 3.16. If we extend the uniform-depth area laterally, the mean water depth diminishes, rendering the model less sensitive to the same obstacle. This behavior is clearly unphysical and highly undesirable from a practical point of view, for obvious reasons.

To ameliorate this, instead of using the lateral average, we propose to use half the depth range as in

$$h_m(x) = \frac{1}{2} \left( \max\left[h(x,y)\right] + \min\left[h(x,y)\right] \right).$$
(3.47)

where $\max\left[h(x,y)\right]$ and $\min\left[h(x,y)\right]$ are the maximum and minimum depth respectively over the lateral section at $x$. This measure does not depend on the lateral extent of the domain; moreover, since for laterally homogeneous perturbations this definition is practically equivalent to a lateral average, the $h_m$ can generally be used (re-computations of the Whalin cases utilizing $h_m$ instead of $\overline{h}$ yielded similar results, not shown).

PSfrag replacements



**Figure 3.16:** Principle sketch of definition reference depth for submerged two-dimensional obstacle. The sketch shows the actual bottom profile (dashed line) the laterally averaged depth $\overline{h}$ (thick solid line), and half the depth range $h_m$ (dash-dot).

Although $h_m$ is generally more applicable than $\overline{h}$ for use as a reference depth, since it does not depend on the lateral extent of the domain, situations are conceivable were even $h_m$ is not very well suited. For instance, consider the case where a localized obstacle (as shown in Figure 3.16) stands out from on otherwise (very) deep area. If the depth-attenuated, wave-induced fluid motions are confined to an upper region of the fluid, above $h_m$ say, then by placing the reference at $h_m$ the model is not affected by the topographical features, i.e. although the topography physically interferes with the wave-induced fluid motions, the model, on account of the reference depth being too deep, cannot correct the wave motion accordingly. This can occur for instance for wave fields traversing nearshore canyons and troughs. To improve the model's sensitivity to topographical variations in such regions, a modification of the depth function is needed; essentially it requires placing a 'false bottom' at the depth where wave motion is practically no longer felt, say where $k_r h = \alpha$, with $k_r$ denoting a characteristic wave number for the waves. We propose, somewhat arbitrarily, $\alpha = 3$, which we will use throughout the remainder of this thesis. The modified depth function reads

$$h^* = \begin{cases} h, & \text{if } h \leq \alpha/k_r \\ \alpha/k_r, & \text{if } h > \alpha/k_r \end{cases} \tag{3.48}$$

and accordingly

$$h_m^*(x) = \frac{1}{2}\left(\max\left[h^*(x,y)\right] + \min\left[h^*(x,y)\right]\right). \tag{3.49}$$

The $h_m^*$ is a modification of the definition of $h_m$ to account for such extreme cases where local topography stands out from a deep surrounding area; if the bottom is everywhere felt by the waves $h_m^*$ is equivalent to $h_m$. In the numerical simulations of waves over localized two-dimensional topography in the present work, we have everywhere used $h_m^*$ as a reference depth. However, for the cases considered, the maximum $kh$ equals 2.35 thus for $\alpha = 3$ this implies $h_m = h_m^*$.

For each of the cases considered in the following, two simulations are performed: one including quadratic nonlinearity (viz. eq. (3.42)) and a linear run where the quadratic term in (3.42) is omitted. The model runs are initialized with the spectral component with the appropriate amplitude, frequency and alongshore wavenumber ($\lambda = 0$) at $x = 0$; for the nonlinear model the corresponding (theoretical) first harmonic (Stokes second-order theory) is added.

To verify model predictions with experimental observations, we compare predicted and observed normalized wave heights along instrumented transects. To quantify the level of agreement between observations and model predictions along these transects we utilize the index of agreement proposed by Willmott [1981]:

$$d = 1 - \frac{\sum_i |y_i - x_i|^2}{\sum_i \left(|y_i - \overline{y}| + |x_i - \overline{x}|\right)^2}, \tag{3.50}$$

where $x_i$ and $y_i$ are the measured and predicted values respectively; the $\overline{x}$ and $\overline{y}$ denote their mean values [the present notation follows Dingemans, 1997, §4.7].

*Ito & Tanimoto 1972*

Ito & Tanimoto [1972] performed experiments over a topography where a shoal with concentric circular contours is placed on an otherwise horizontal bottom (see Figure 3.17). The submerged shoal acts like a lens which, when described by the wave rays of geometrical optics, results in a cusped caustic. It is well known that in the region of ray convergence, the theory of rectilinear wave propagation is not a proper presentation of the physics, and a diffraction theory (present model) is needed [see e.g. Mach, 1926; Stamnes, 1986].

In the experimental set-up used by Ito & Tanimoto [1972], the water depth surrounding the shoal is $h_0 = 0.15\,\mathrm{m}$, and in the shoal area the depth is given by

$$h(x,y) = 0.05\,\mathrm{m} + (0.15625\,\mathrm{m}^{-1})\left[(x-x_c)^2 + (y-y_c)^2\right]. \qquad (3.51)$$

The minimum depth over the shoal is $0.05\,\mathrm{m}$, and the shoal center coordinates are $(x_c, y_c) = (1.2, 1.2)\,\mathrm{m}$. Monochromatic waves are normally incident at $x = 0$ (Figure 3.17) with wave height and period equal to $1.04\,\mathrm{cm}$ and $0.511\,\mathrm{s}$ respectively. Observations are available along three transects, indicated in Figure 3.17.
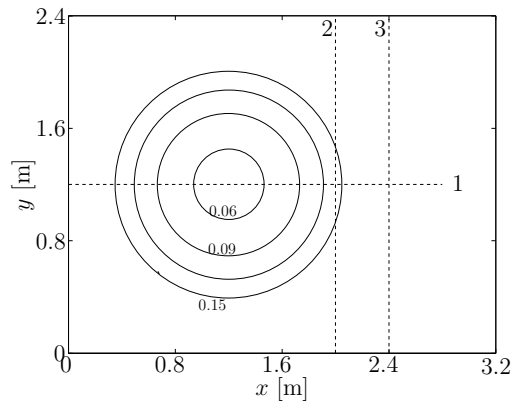


**Figure 3.17:** Bottom lay-out experimental set-up Ito & Tanimoto [1972], depth in meters. Waves incident from the left. Dashed lines indicate instrumented transects.

For the numerical simulations the spatial domain is discretized with $\Delta x$ and $\Delta y$ equal to $4.0\,\mathrm{cm}$ and $3.8\,\mathrm{cm}$ respectively; the evolution of the primary wave ($\omega_0$) and its first harmonic ($2\omega_0$) is computed.

Along the center of the shoal, wave heights are amplified as the waves are refractively focused (top panel Figure 3.18). Due to the refraction of the incident waves and the associated bending of the rays, crossing wave trains occur in the area behind the shoal, which is visible from the wave height patterns observed (and predicted) at the cross-sectional transects 2 & 3 (middle and lower panel Figure 3.18).

Overall, the agreement between predictions and observations is fairly good (Figure 3.18), also substantiated by the high Willmott-index values listed in Table 3.3. A few notable differences remain. At transect 2, the model-predicted lateral wave height variability, away from the center region of strong refractive focus ($1.0\,\mathrm{m} < y < 1.4\,\mathrm{m}$),

is not as pronounced as in the observations. The observations along Transect 3 exhibit lateral asymmetry (with respect to the shoal center); this is at variance with the laterally symmetrical conditions imposed on the numerical model, and therefore not found in the simulation results.

PSfrag replacements

| Transect no. | Nonlinear | Linear |
|:---:|:---:|:---:|
| 1 | 0.962 | 0.964 |
| 2 | 0.960 | 0.962 |
| 3 | 0.961 | 0.960 |

PSfrag replacements

$x$ [m]

**Table 3.3:** Willmott index values for angular spectrum model predictions and observations by Ito & Tanimoto [1972]; normally incident waves with 1.04 cm amplitude and
PSfrag replacements 0.511 s period. (Transects indicated in Figure 3.17.)

$x$ [m]

The effect of nonlinearity is minimal for the case considered (Figure 3.18) on account of the fact that the waves are of fairly low steepness, and propagate over a relative short distance (few wavelengths) in relatively deep water.

0.2
3
1.6
1
2.4



(a) Transect 1

(b) Transect 2
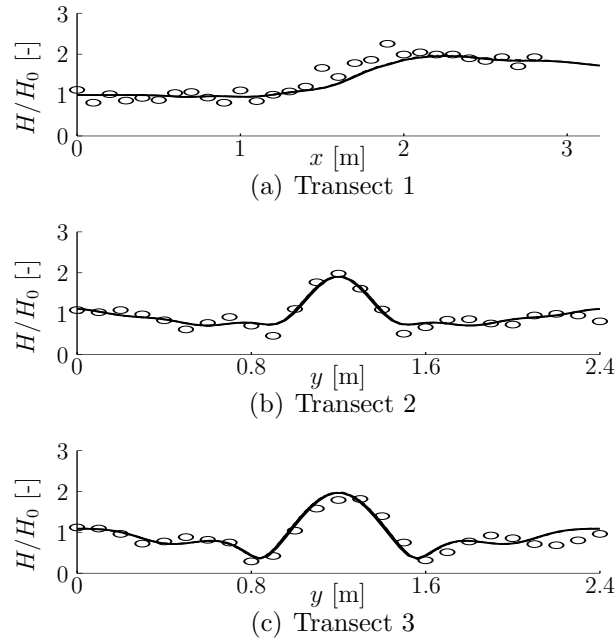
(c) Transect 3

**Figure 3.18:** Comparison predicted and observed [Ito & Tanimoto, 1972] normalized wave heights; normally incident waves with 1.04 cm wave height and 0.511 s period. Thick solid line represents nonlinear model prediction (eq. (3.42)); dashed line is linear model prediction (same equation without nonlinear coupling).

*Berkhoff, Booij & Radder 1982*

The experimental study by Berkhoff *et al.* [1982] was specifically designed to test the performance of approximate numerical models in regions of combined refraction-diffraction. The topography consists of an elliptic shoal situated on a plane, 1:50, sloping beach, rotated over $20^0$ with respect to the (straight) wave generator. Depth contours and measurement transects are shown in Figure 3.19. At the deep end of the basin, water depth measures $0.45\,\text{m}$; the minimum depth over the shoal is $0.1332\,\text{m}$. The $x$ and $y$ axis for the computational domain are defined as in Figure 3.19, but the topography is best described in coordinates $(x', y')$ with the origin at the shoal center $((x_c, y_c) = (10.5, 10)\,\text{m})$ and oriented along the slope-normal (Figure 3.19). In that coordinate frame, the area occupied by the shoal is defined as

$$\left(\frac{x'}{3\,\text{m}}\right)^2 + \left(\frac{y'}{4\,\text{m}}\right)^2 \leq 1 \tag{3.52}$$

with the depth in this region given by

$$h = 0.75\,\text{m} - 0.02\,(5.84\,\text{m} + x') - \frac{1}{2}\left[1 - \left(\frac{x'}{3.75\,\text{m}}\right)^2 - \left(\frac{y'}{5\,\text{m}}\right)^2\right]^{1/2}. \tag{3.53}$$

Outside of the shoal area the depth is given by

$$h = \begin{cases} 0.45\,\text{m}, & \text{if } x' < -5.84\,\text{m} \\ 0.45\,\text{m} - 0.02\,(5.84\,\text{m} + x'), & \text{if } x' \geq -5.84\,\text{m} \end{cases} \tag{3.54}$$

These shoal-coordinates are related to the computational coordinates through

$$x' = (x - 10.5\,\text{m})\cos 20^o + (y - 10\,\text{m})\sin 20^o, \tag{3.55}$$

$$y' = (x - 10.5\,\text{m})\sin 20^o - (y - 10\,\text{m})\cos 20^o. \tag{3.56}$$

This topography will clearly violate the lateral periodicity assumption implied in the angular-spectrum model, which results in modeling errors originating from the lateral boundaries. However, for the case considered the observational area is well away from the lateral model boundaries (Figure 3.19) and we tentatively assume boundary effects negligible in the area of interest. Comparison is made to observations of an incident wave field with $1.0\,\text{s}$ period and $2.32\,\text{cm}$ amplitude. The spatial domain is discretized with $\Delta x = 0.1\,\text{m}$ and $\Delta y = 0.078\,\text{m}$. The evolution of the primary wave $(\omega_0)$ and its first harmonic $(2\omega_0)$ is computed.

We compare normalized wave heights along the transects 1–8 (Figure 3.20 & 3.21). Overall, we observe that the inclusion of the nonlinear terms in the simulation results in much better agreement with the observations. Table 3.4 confirms the generally good agreement between predictions and observations (values close to 1.0); also it indicates that the inclusion of quadratic nonlinear interactions results in improvements at all

0.4

0.45

0.35
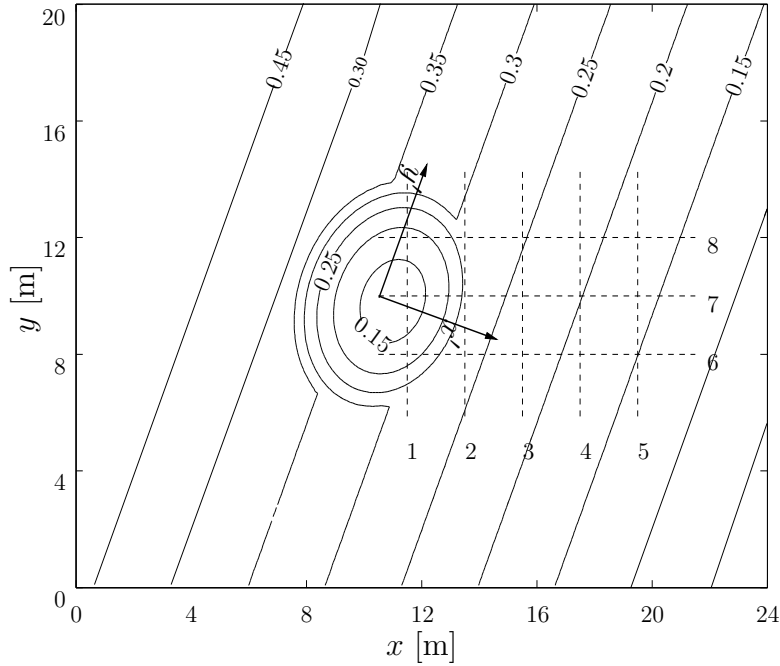


**Figure 3.19:** Bottom lay-out experimental set-up Berkhoff *et al.* [1982], depth in meters. Dashed lines indicate instrumented transects.

| Transect no. | Nonlinear | Linear |
|:---:|:---:|:---:|
| 1 | 0.902 | 0.924 |
| 2 | 0.961 | 0.955 |
| 3 | 0.987 | 0.986 |
| 4 | 0.994 | 0.975 |
| 5 | 0.987 | 0.942 |
| 6 | 0.987 | 0.864 |
| 7 | 0.981 | 0.952 |
| 8 | 0.915 | 0.928 |

**Table 3.4:** Willmott index values for angular spectrum predictions and observations by Berkhoff *et al.* [1982]; normally incident waves with 2.32 cm amplitude and 1.0 s period. (Transects indicated in Figure 3.19.)

transects except no. 8 and 1 where the linear model scores slightly better (note that wave height variability is relatively small over these transects and therefore small deviations are heavily penalized by the Willmott index).

It is instructive to consider the differences in the wave field prediction between the linear and nonlinear model in a more qualitative sense (Figure 3.22). The inclusion of the nonlinear term results in the well-known elongation of the troughs and sharpening of the crests (Stokes waves), an effect most pronounced in the refractive focus area

(a) Transect 6

(b) Transect 7

(c) Transect 8

(d) Transect 1
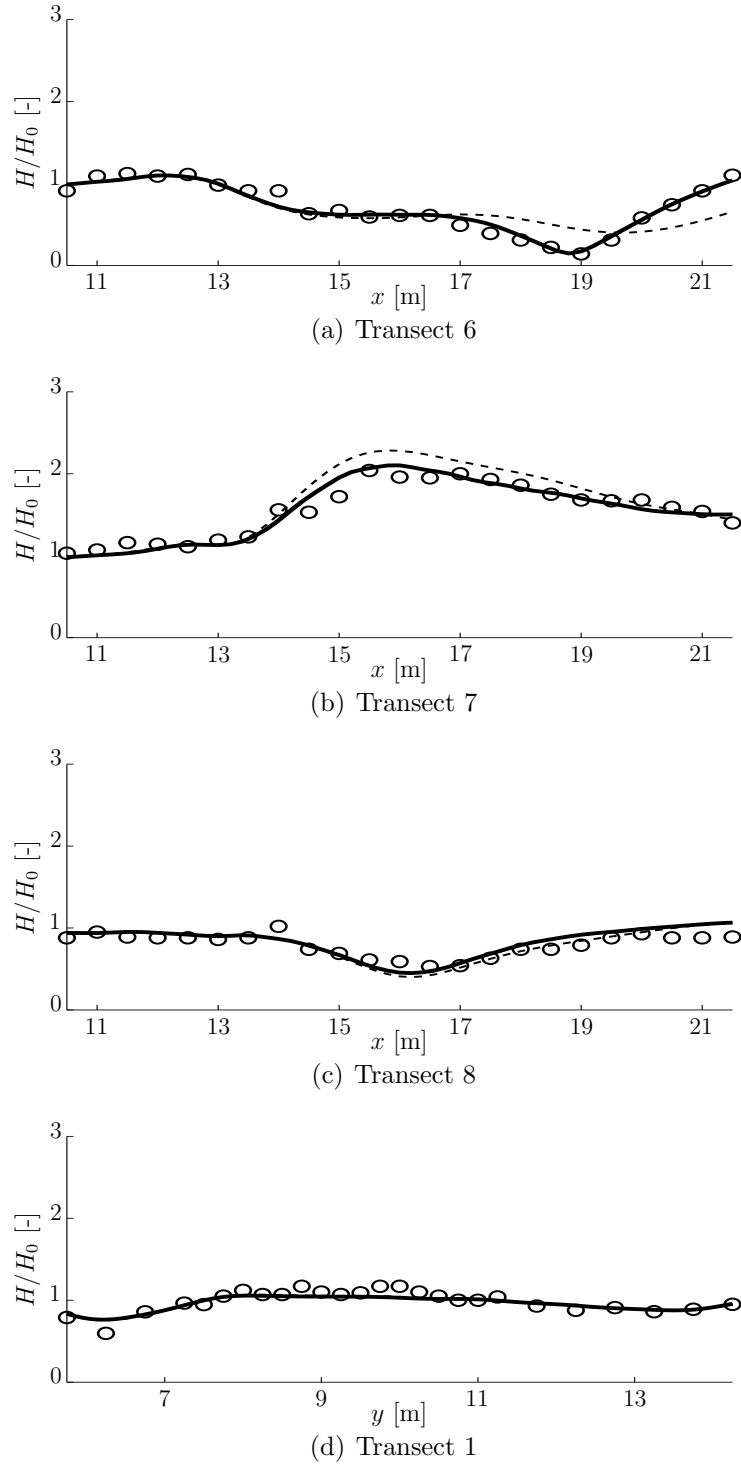
**Figure 3.20:** Comparison of predicted and observed [Berkhoff *et al.*, 1982] normalized wave heights; normally incident waves with 2.32 cm amplitude and 1.0 s period. Thick solid line represents nonlinear model predictions (eq. (3.42)); dashed line is linear model predictions (same equation without nonlinear coupling).

(a) Transect 2

(b) Transect 3

(c) Transect 4

(d) Transect 5
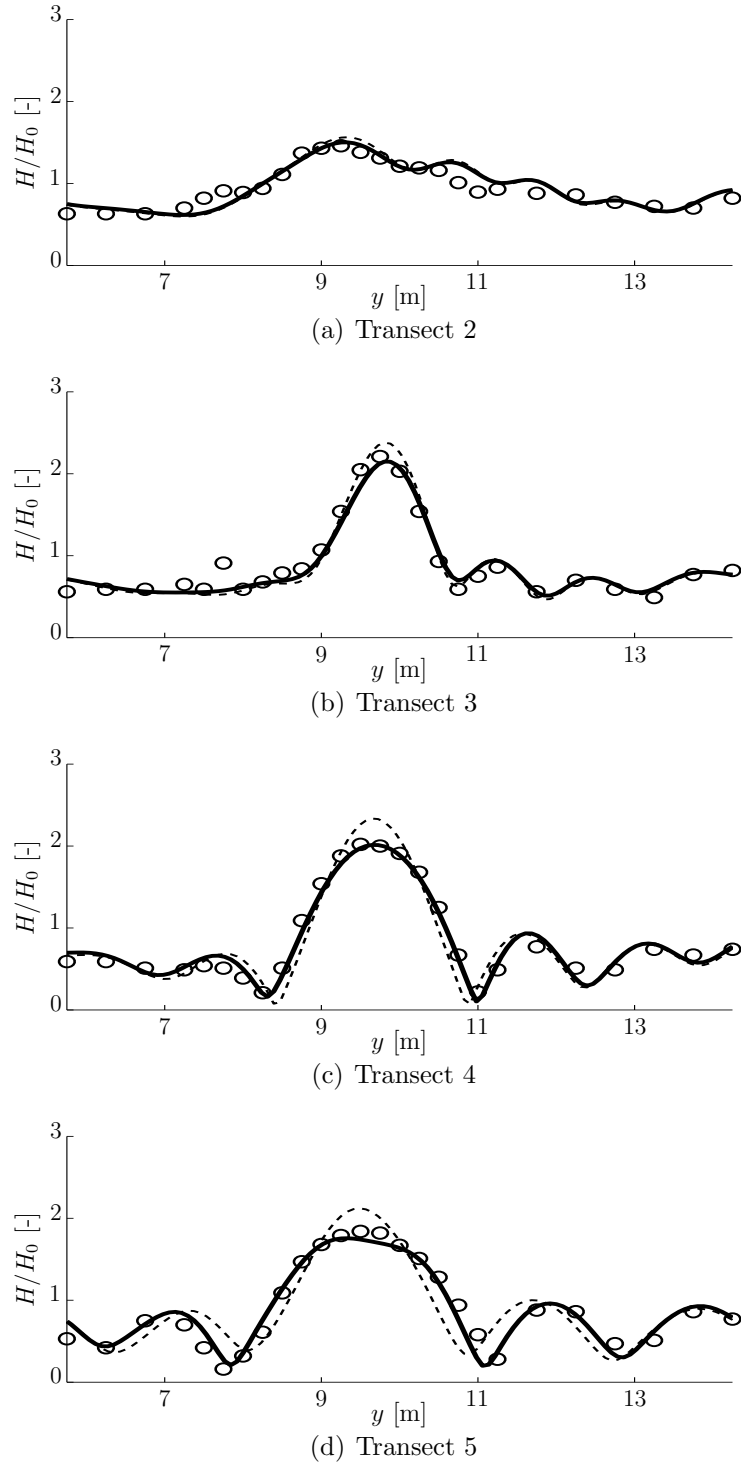
**Figure 3.21:** Comparison of predicted and observed [Berkhoff *et al.*, 1982] normalized wave heights; normally incident waves with $2.32\,\mathrm{cm}$ amplitude and $1.0\,\mathrm{s}$ period. Thick solid line represents nonlinear model predictions (eq. (3.42)); dashed line is linear model predictions (same equation without nonlinear coupling).
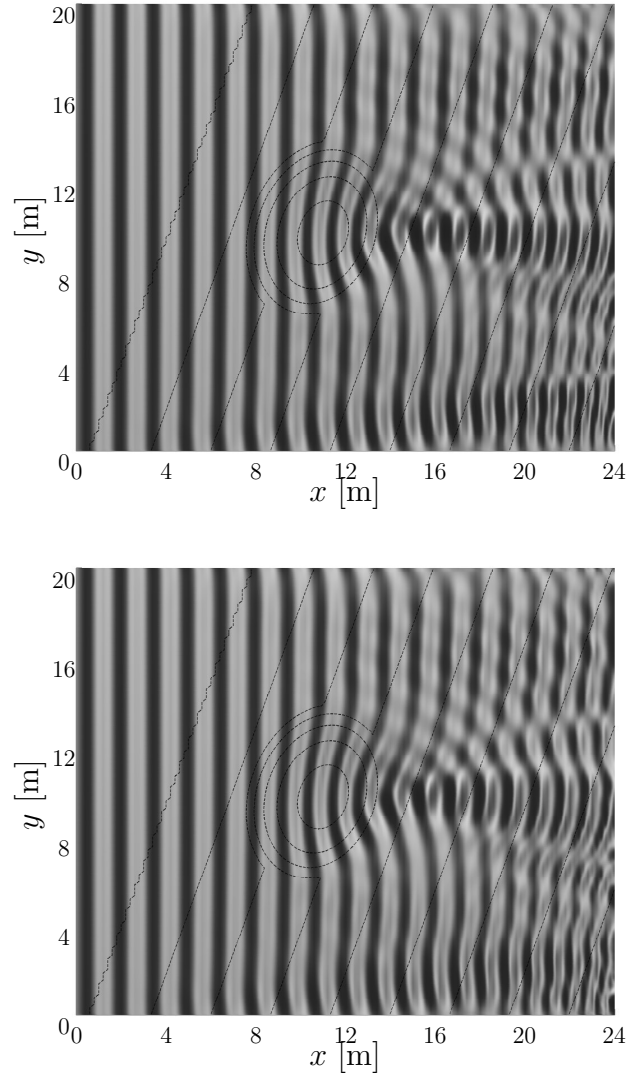
**Figure 3.22:** Model-predicted surface elevation (viz. eq. (3.42)) for incident wave period 1.0 s and 2.32 cm amplitude. Top panel: linear model. Lower panel: nonlinear model.

and the shallower part of the basin. More importantly perhaps is the fact that the nonlinearity is seen (Figure 3.22) to induce a widening of the aperture of the refractive focus (de-focusing effect). The quantitative comparisons in Figures 3.20 & 3.21 indicate that the linear model predicts a focal region slightly too narrow and overestimates wave height amplification in that region (notably transect 4 in Figure 3.21). The inclusion of nonlinearity causes a de-focusing of the waves in the focal region behind the shoal, resulting in wave height values that are in closer agreement with the observations along transects in that region.

Remarkable is the fact that the improvement due to the inclusion of quadratic nonlinearity is qualitatively similar to the improvements observed by e.g. Kirby & Dalrymple

[1983] and Suh *et al.* [1990] who included amplitude dispersion through a cubic self-self-self interaction term. It is surprising to find that such disparate formulations for nonlinear wave propagation result in very similar effects/improvements in the model predictions. However, the disparity is but apparent and the physical phenomenon in both cases is believed the same, namely amplitude dispersion. Although the harmonic amplitudes in the observational area remain relatively small (compare upper and lower panel Figure 3.22), it is indirectly through the dispersion corrections on the primary wave train that the nonlinearity affects the refractive focus. We recall from the discussion in §3.1.2 that the quadratic interaction term generally overestimates such effects in these water depths, nevertheless, when compared to the linear estimate, the nonlinear model is notably more accurate.

Then, on the premise that the improvements in the model predictions are due to amplitude dispersion, the argument can be made that this invalidates the omission of cubic terms from the equation, amplitude dispersion being a third-order effect; an argument strengthened by the fact that the second-order model strongly overestimates such effects in unidirectional waves (§3.1.2). The conclusive answer needs to await numerical evaluation of the complete model, including such terms. However, although amplitude dispersion in unidirectional waves is strongly overestimated by the quadratic models in deeper water, the nonlinear de-focusing effect is due to amplitude-induced, *relative* phase changes of the directional components in the focal region. Therefore, although the wave field as a whole can be expected to propagate too fast, a deduction that can be verified by comparing time series at locations in and beyond the focal region (not available for the present case), the relative phase modification of directional components inside a narrow aperture is weighted approximately proportional to the square of the wave amplitude, as one would also expect in a third-order theory. Although this is an a posteriori argument, inspired foremost by the notable improved agreement in wave height evolution due to the inclusion of nonlinear terms, it provides some rationale to qualitatively explain the undeniable improvements in the model result with an incomplete description of the third-order nonlinear physics.

*Chawla 1995*

Chawla [1995] performed laboratory experiments over a topography [see also Chawla *et al.*, 1996, 1998] consisting of a circular shoal (radius $r = 2.57\,\mathrm{m}$), with its center at $(x_c, y_c) = (5.0, 8.98)\,\mathrm{m}$ placed on an otherwise uniform bottom ($x$ and $y$ as in top panel of Figure (3.23)). Within the shoal perimeter the depth is given as

$$h = h_0 - \sqrt{R_s^2 - (x - x_c)^2 - (y - y_c)^2} + 8.73\,\mathrm{m}, \qquad (3.57)$$

where $h_0 = 0.45\,\mathrm{m}$ is the depth away from the shoal and $R_s = 9.1\,\mathrm{m}$ is the radius of the sphere defining the shoal geometry. Model simulations are compared to observations of normally incident waves (along $x$) with $1.0\,\mathrm{s}$ period and $1.165\,\mathrm{cm}$ amplitude. The computational domain is discretized with $\Delta x = 0.1\,\mathrm{m}$ and $\Delta y = 0.0706\,\mathrm{m}$.
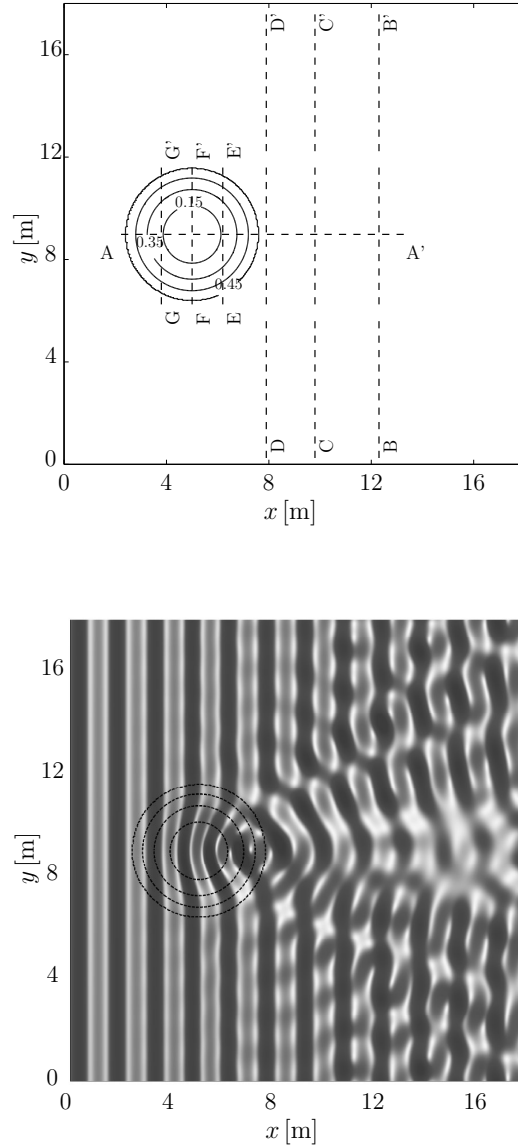
**Figure 3.23:** Bottom lay-out (top panel) experimental set-up Chawla [1995], depth in meters; dashed lines indicate instrumented transects. Model-predicted surface elevation (bottom panel, viz. eq. (3.42)); incident wave period 1.0 s and 1.165 cm amplitude.

This is the most extreme of the cases considered for two-dimensional wave propagation in terms of the lateral depth variations in the topography. With the depth varying from 45 cm away from the shoal to 8 cm over the top of the shoal this topography exhibits considerable lateral depth variability and thus represents a severe test on the model's two-dimensional capability.

The incident wave field experiences strong refractive focusing as it traverses the shoal area, indicated by the wide-angle scattering in the surface elevation (bottom panel Figure 3.23), and the rapid increase in wave height along the center-line of the basin (Figure

3.24, transect $A$). Although model-predicted amplitude variation over the shoal along $A$ is in fair agreement with the observed variability, the predictions spatially lag behind the observations; moreover, the model predictions show wave height oscillations for $x > 10\,\mathrm{m}$ which are not present in the observations. Along the cross-basin transects $G$ & $F$ (Figure 3.24) wave height variations are minimal, but strong lateral wave height variations, with a pronounced maximum near the shoal-center along transects $B$–$E$ (Figure 3.25), indicate the presence of a distinct focal region and considerable cross-basin standing wave motion associated with the crossing of wave trains behind the shoal.

The agreement between observations and predictions is notably less than for the other cases considered (observations by Ito & Tanimoto and Berkhoff *et al.*), also indicated by the markedly lower Willmott index values (Table 3.5). This is not surprising given the fact that the fundamental assumption of weak lateral variations in water depth is strained to it limits and perhaps well beyond. Taking that into account, the agreement between model predictions and observations is actually remarkable. Prominent features such as the rapid increase in wave height over the shoal, and the laterally standing wave height patterns behind the shoal are all faithfully predicted by the model. Even at a more quantitative level, the agreement is generally favorable. In particular, good agreement is found for the transects $D$–$B$ (located behind the shoal, Figure 3.25), away from the primary focusing region. These (strong) lateral variations in wave height outside the primary focal region (near $y_c$) are due to crossing waves scattered at relative large angles in the refraction-diffraction process over the shoal and in the refractive focus area; the observed level of agreement is attributed to the wide-angle ability of the model. Good agreement in these regions was also found by Kaihatu [2001] with a wide-aperture approximation to the mild-slope equation (see also discussion in §3.5).

| Transect | Nonlinear | Linear |
|:---:|:---:|:---:|
| A | 0.889 | 0.913 |
| B | 0.842 | 0.837 |
| C | 0.688 | 0.674 |
| D | 0.829 | 0.832 |
| E | 0.937 | 0.947 |
| F | 0.736 | 0.769 |
| G | 0.5 | 0.504 |

**Table 3.5:** Willmott index values for angular spectrum model and observations by Chawla [1995]; normally incident waves with $1.165\,\mathrm{cm}$ amplitude and $1.0\,\mathrm{s}$ period. (Transects indicated in Figure 3.23.)

However, some distinct quantitative disagreement remains. The most conspicuous data-model disagreement is the erroneous wave height variation along the center transect $A$; although approximately correct in magnitude range, the predicted wave height

variations are spatially lagging. This lag is also reflected in the lesser agreement between predicted and observed wave heights over the cross-basin transects $B-G$ in the focal area near $y_c$. Consistent with the spatial lagging of the model-predicted wave height observed along transect $A$, the wave height along transects $E-G$, near $y_c$, is underestimated by the model; at transects $D-B$ the model consistently overestimates wave heights in that area.

The cases considered exhibit very low wave steepness and consequently nonlinear effects are very weak. However, in general, over strongly two-dimensional topography the quadratic nonlinear coupling term is inaccurate; the lateral heterogeneity of the topography only affects the nonlinear coupling indirectly though the lateral variation of the amplitude, not through the varying depth directly since the coupling coefficient depends on the reference depth, not the laterally varying part. It is clear that nonlinearity is enhanced locally, over the shallow part of the shoal even if, hypothetically, the wave height would be laterally uniform. This laterally global nature of the coupling coefficient results in underestimation of the ensuing nonlinear couplings in the vicinity of two-dimensional shoal and over-prediction in the surrounding area.

PSfrag replacements



(a) Transect A

(b) Transect G

(c) Transect F
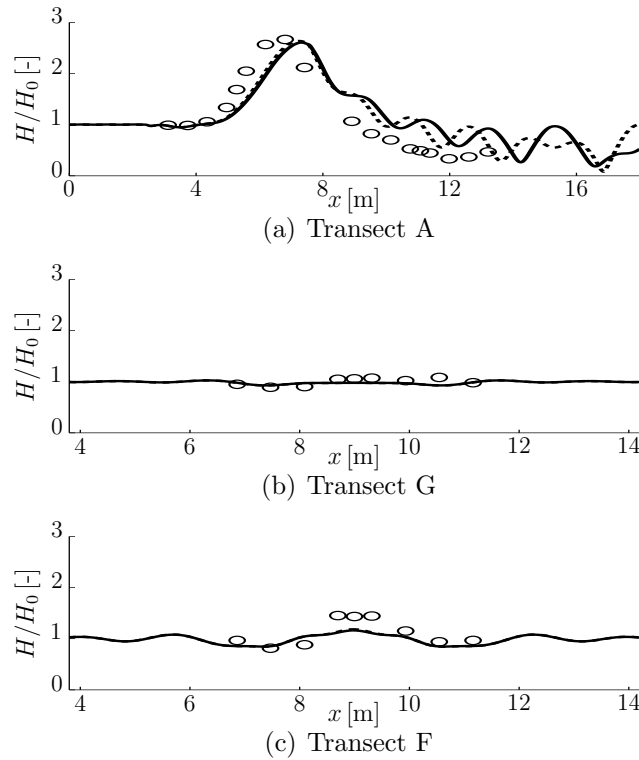
**Figure 3.24:** Comparison of predicted and observed [Chawla, 1995] normalized wave heights; normally incident waves with $1.65\,\mathrm{cm}$ amplitude and $1.0\,\mathrm{s}$ period. Thick solid line represents nonlinear model predictions (eq. (3.42)); dashed line is linear model prediction (same equation without nonlinear coupling).
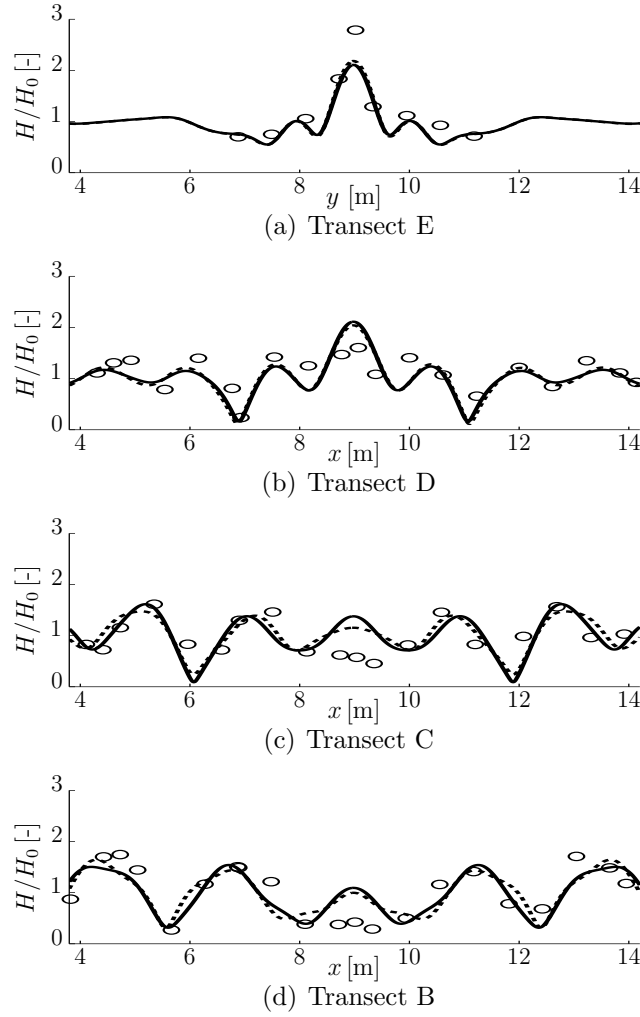
**Figure 3.25:** Comparison of predicted and observed [Chawla, 1995] normalized wave heights; normally incident waves with $1.165\,\mathrm{cm}$ amplitude and $1.0\,\mathrm{s}$ period. Thick solid line represents nonlinear model predictions (eq. (3.42)); dashed line is linear model prediction (same equation without nonlinear coupling).

## 3.5  Discussion deterministic model

*Outlook on approach and numerical feasibility*

The application of a multi-frequency angular-spectrum decomposition results in a dimensional reduction of the governing equation (a set of ODEs describes the evolution of stationary, two-dimensional wave fields over two-dimensional topography) at the expense of convolution-type forcing terms for the wave–wave and wave–bottom interaction, which is typical for spectral Galerkin-type methods.

Direct evaluation of the convolution-type forcing terms is straightforward, but in particular for the cubic interaction terms the number of operations is $O(N^3)$ ($N$ being the number of spectral components), which becomes prohibitive for larger-scale applications. Such terms can be implemented by utilizing standard pseudospectral methods [see

e.g. Orszag, 1972] so that the number of operations scale as $O(N \log_2 N)$ [see also e.g. Bredmose *et al.*, 2002, 2004, 2005; Canuto *et al.*, 1987]; this renders the approach suitable for application to wave fields with realistic spectra and spatial scales as encountered in typical (nearshore) oceanographic applications. Pseudo-spectral approaches are possible for resonant formulations only, not for the generalized forms of the coupling coefficient; the dissimilarities in dynamic response between resonant and generalized models are very minor [see also Bredmose *et al.*, 2005, and discussion in §3.1.2] so that for practical application it is preferable to use a resonant formulation with the convolutions efficiently evaluated through the use of a pseudospectral implementation. Practical considerations for such implementations are discussed in detail in Bredmose *et al.* [2005]. No such (or other) efficiency improvements were pursued for the numerical evaluations presented here, but we remark that on a standard desktop (P4) computer the computations for the unidirectional cases with cubic nonlinearity take a few minutes, not hours; the two-dimensional model runs (cubic terms omitted and maximal four harmonics computed), require less than a minute of CPU time.

For waves of moderate amplitude over mildly varying depth with weak lateral variations, the multi-frequency angular-spectrum approach presented here is efficient and applicable to scales covering hundreds of wavelengths (e.g. wave propagation over the continental shelf onto beaches); in particular, it has the potential to investigate the effects and relative importance of competing nonlinear processes in random ocean waves over shoals and banks. More general time-domain models such as boundary-integral methods and field approximations of the Laplace equation [e.g Westhuis, 2001] or even recent developments in extended Boussinesq theory [e.g Madsen *et al.*, 2003] are potentially more accurate, in particular over steep topography or in the presence of strong nonlinearity, but are computationally intensive which generally restricts their application to smaller areas. Furthermore, such models do not explicitly describe the wave interaction mechanisms, which, since Stokes [1847], are so deeply rooted in our conceptual understanding of nonlinear wave physics and at the basis of widely used, operational wave models [e.g. Hasselmann, 1962].

*Angular spectrum and small-angle approximation*
The model derivation is based on the premise of weak lateral depth variability. Comparison to observations of waves over two-dimensional topography indicate that this approximation is applicable to realistic beach topographies (§3.4.2, observations by Berkhoff, Booij & Radder) but should be applied with caution over topographies with pronounced and localized two-dimensional features (see e.g. §3.4.2, observations by Chawla). Moreover, it was noted that the nature of the approximation impairs the accuracy of the nonlinear coupling in regimes with pronounced two-dimensional topography.

Notwithstanding the apparent robustness of the approach, for wave fields impinging on strongly two-dimensional topography the underlying premises of the angular-

spectrum model are clearly violated, and may not be the most suitable in the first place. In particular, if the incident wave field is characterized by a narrow-aperture propagation along a principal direction, say $x$, then a so-called 'small-angle' approximation, which assumes small-aperture wave propagation along a principal direction but retains two-dimensionality in the topographical forcing, appears a more realistic approximation.

To illustrate the differences between the angular-spectrum description and small-angle approximation, we consider time-periodic waves propagating over laterally uniform topography governed by the mild-slope equation [Berkhoff, 1976]

$$\nabla \left[ CC_g \nabla \eta \right] + k^2 CC_g \eta = 0, \tag{3.58}$$

where $k$ is related to the wave frequency through the dispersion relation. We consider solely waves propagating into the half plane of positive $x$ and insert the angular-spectrum expansion for the wave field variable

$$\eta = \sum_\lambda \zeta_\lambda(x) \exp\left[ i(\varkappa_\lambda x + \lambda y) \right] \exp\left[ -i\omega t \right] + *. \tag{3.59}$$

Further, we assume the angular amplitudes $\zeta_\lambda$ sufficiently slowly varying in $x$ so that we may ignore $\partial_x^2 \zeta_\lambda$ and accordingly write (3.58) as

$$i \left[ 2V_\lambda \frac{d}{dx} + \frac{dV_\lambda}{dx} - i\frac{C_g}{k}\left( k^2 - \varkappa_\lambda^2 - \lambda^2 \right) \right] \zeta_\lambda = 0, \tag{3.60}$$

where, as before, $V_\lambda = (\varkappa_\lambda/k)C_g$ denotes the cross-shore component of the group speed vector. Equating imaginary and real parts gives

$$\sum_\lambda \frac{dA_\lambda}{dx} = 0, \tag{3.61}$$

where $A_\lambda = \sqrt{V_\lambda}\zeta_\lambda$, and the simple eikonal

$$\varkappa_\lambda = \sqrt{k^2 - \lambda^2}. \tag{3.62}$$

Eq.'s (3.61) & (3.62) constitute the angular-spectrum description of waves shoaling on a laterally uniform beach.

A similar reasoning can be extended to, what we refer to as, the 'small-angle' approximation. Instead of allowing the waves to propagate at arbitrary angles in the half plane, we assume their propagation direction confined to a narrow aperture along the principal direction $(x)$. On the basis of this assumption we write the surface elevation as

$$\eta = a \exp\left[ i\left( kx - \omega t \right) \right] + * = \sum_\lambda \zeta_\lambda^{(\mathrm{sa})} \exp\left[ i\lambda y \right] \exp\left[ i\left( kx - \omega t \right) \right] + *, \tag{3.63}$$

where the (sa) in the superscript is an abbreviation of 'small-angle'. The aperture width is incorporated through the (slow) variation of the amplitude $a$. Insertion into (3.58),

assuming again a laterally uniform depth and the amplitudes $\zeta_\lambda^{(sa)}(x)$ slowly varying along the principal direction, yields the expression

$$\sum_\lambda \left[ \frac{d}{dx} + i\frac{\lambda^2}{2k} \right] A_\lambda^{(sa)} = 0, \tag{3.64}$$

with $A_\lambda^{(sa)} = \sqrt{C_g}\zeta_\lambda^{(sa)}$. From (3.64) we see that the small-angle[†] approximation implies the eikonal relation

$$\varkappa_\lambda = k - \frac{\lambda^2}{2k}, \tag{3.66}$$

which is the first two terms of a Taylor expansion of (3.62) for small angles ($\lambda \ll k$). Based on the small-angle approximation Kaihatu & Kirby [1995] derived evolution equations including quadratic nonlinearity. To further illustrate the differences in the approximation, by means of a numerical comparison to the experimental data by Chawla [1995], we evaluate the governing equations in Kaihatu [2001] (modifying the nonlinear term for compatibility with the present model) utilizing a spectral method in the lateral direction. In that way the models can be evaluated with the same numerical scheme (one-dimensional, $4^{th}$-order Runge-Kutta), thus minimizing differences from a numerical origin. Thereto we write the surface elevation associated with a narrow-aperture wave field propagating along $x$ as

$$\eta = \sum_{p=-\infty}^{\infty} a_p(x,y) \exp\left[i\left(\int^x \overline{k}_p\, dx - \omega_p t\right)\right]$$

$$= \sum_{p,q=-\infty}^{\infty} \zeta_{p,q}(x) \exp\left[i\lambda_q y\right] \exp\left[i\left(\int^x \overline{k}_p\, dx - \omega_p t\right)\right], \quad (3.67)$$

where $\lambda_q$ are again the discrete lateral wavenumbers; the laterally averaged wavenumber $\overline{k}_p(x) = 1/L_y \int_0^{L_y} k_p(x,y')\, dy'$, where $k_p$ is related to $\omega_p$ through the linear relation dispersion and $L_y$ is the lateral extent of the domain. Note that the $\zeta_{p,q}$ represent the lateral Fourier coefficients of the amplitude $a_p(x,y)$, which is distinct from the angular-spectrum model; here the lateral wavenumber decomposition is introduced merely as a means to numerically evaluate the evolution equations as a set of ODEs rather than the parabolic-form partial differential equation in Kaihatu & Kirby [1995] and Kaihatu [2001]. Inserting the decomposition (3.67) into the linear part of eq. (4) in Kaihatu [2001]

---

[†]Upon inverse Fourier transforming (3.64) with respect to $\lambda$ we obtain the relation

$$\frac{\partial \widetilde{A}^{(sa)}}{\partial x} = \frac{i}{2k} \frac{\partial^2 \widetilde{A}^{(sa)}}{\partial y^2}, \tag{3.65}$$

where the $\widetilde{A}^{(sa)} = \sum_\lambda A_\lambda^{(sa)} \exp[i\lambda y]$. Thus the small-angle approximation changes the governing equation (3.58) from being essentially elliptic, utilizing semantics borrowed from analytical geometry, to the parabolic form of (3.65); therefore the small-angle approximation is also often referred to as the 'parabolic' approximation. In the present context, we prefer the wording 'small-angle', which is more inclined toward the physical significance of the approximation.

and augmenting it with the generalized nonlinear coupling term[†] discussed in §3.1.2, we obtain in terms of the surface elevation

$$\frac{d\zeta_{p,q}}{dx} = -i\overline{k}_p\zeta_{p,q} + \mathcal{F}_q\{f_p^{(1)}(y), \mathcal{F}_{q'}^{-1}\{\zeta_{p,q'}\}\} + \mathcal{F}_q\{f_p^{(2)}(y), \mathcal{F}_{q'}^{-1}\{i\lambda_q\zeta_{p,q'}\}\}$$
$$- \mathcal{F}_q\{f_p^{(3)}(y), \mathcal{F}_{q'}^{-1}\{\lambda_q^2\zeta_{p,q'}\}\}$$
$$+ \mathcal{F}_q\left\{i\sum_{n,m}\mathcal{Z}_{n,m}^{\lambda=0}(y)\mathcal{F}_{q'}^{-1}\{\zeta_{n,q'}\}\,\mathcal{F}_{q''}^{-1}\{\zeta_{m,q''}\}\,\delta_{nm;p}^\omega\overline{E}_{nm;p}\right\}. \quad (3.68)$$

Here the operator $\mathcal{F}_q\{\,\}$ denotes the $q^{th}$ component of the Fourier transform with respect to the lateral coordinate; the $\mathcal{F}_q^{-1}\{\,\}$ is the inverse Fourier transform with respect to the lateral wavenumbers associated with the subscript. The interaction coefficient $\mathcal{Z}_{n,m}^{\lambda=0}(y)$ is the generalized interaction coefficient $\mathcal{Z}_{1,2}^{(g)}$ defined in §3.1.2 (Table 3.1), for $\lambda = 0$ (thus unidirectional waves) but a function of the lateral coordinate $y$; the $\overline{E}_{nm;p} = \exp\left[i\int^x(\overline{k}_n + \overline{k}_m - \overline{k}_p)\right]dx\}$, and the $f_p$'s are given as

$$f_p^{(1)}(y) = -\frac{C_{g,p}}{2C_{g,p}(y)} + ik_p, \quad (3.69)$$

$$f_p^{(2)}(y) = i\frac{\partial_y\left(C_{g,p}/k_p\right)}{2C_{g,p}}, \quad (3.70)$$

$$f_p^{(3)}(y) = \frac{i}{2k_p}. \quad (3.71)$$

Note that here the $k_p$ and $C_{g,p}$ are functions of the lateral coordinate. The equation (3.68) describes the nonlinear wave evolution on the premise of small-angle propagation relative to the principal direction $(x)$, but without explicit restrictions on the slowly varying topography. The model is accurate only for $(\lambda_q/k_p)^2 \ll 1$ and for reasons of numerical stability we explicitly exclude lateral wavenumber components for which $|\lambda_q| > \sqrt{2}k_p$; these components are well beyond the validity of the model and very high lateral wavenumbers render the numerical integration unstable.

The experimental observations by Chawla (see §3.4.2), given the fairly extreme topography, are well-suited to illustrate the differences between the small-angle model (viz. eq. (3.68)) and the angular-spectrum model (viz. eq. (3.42)). The models are initialized as in §3.4.2 and computations are performed with the same spatial discretization as before; computed surface elevations are shown in Figure 3.26.

In a qualitative sense, the most conspicuous difference in the surface elevation predictions by the two models is the directional spreading predicted behind the shoal. Compared to the angular-spectrum model prediction (bottom panel), the small-angle model (eq. (3.68)) predicts a wave field in the refractive region with a somewhat narrower aperture[‡]. Also, the cancellation of wave motion due to directional interference along

---

[†]The nonlinear term in Kaihatu [2001] is equivalent to the quasi-resonant model by Eldeberky & Madsen [1999] (see §3.1.2).

[‡]This is not due to the computational cut-off for $|\lambda_q| > \sqrt{2}k_p$; simulations with cut-offs at much higher wavenumbers (not shown) rendered identical results.

PSfrag replacements

$x$ [m]

$y$ [m]



PSfrag replacements

$x$ [m]

$y$ [m]
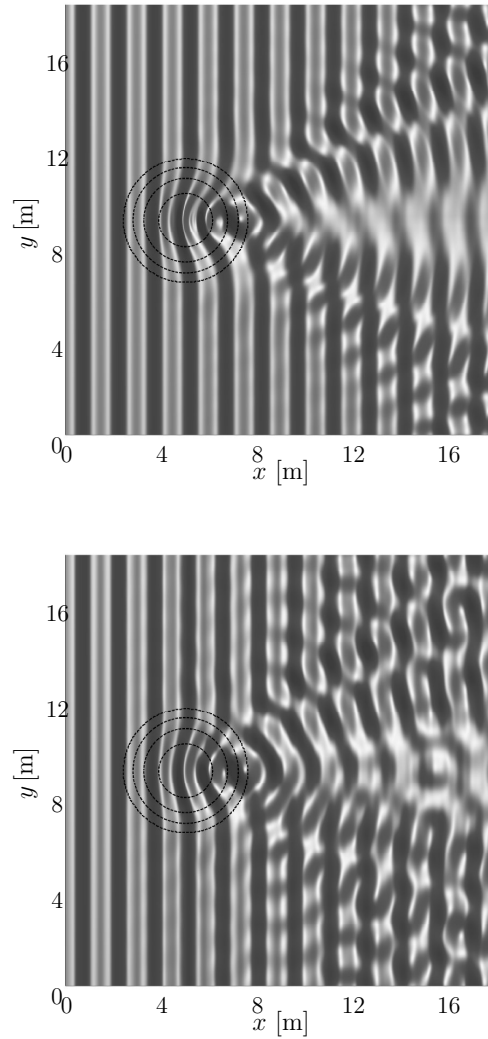


**Figure 3.26:** Inter-comparison model-predicted surface elevation for incident wave period 1.0 s and 1.165 cm amplitude over topography as in Chawla [1995]. Top panel: small-angle model (viz. eq. (3.68)). Bottom panel: angular-spectrum model (viz. eq. (3.42)). The lateral asymmetries in surface elevation are on account of the of the (artificial) lighting of the plot.

the center line of the tank in the focal region is stronger in the small-angle model than in the angular-spectrum model.

In a more quantitative sense the differences are quite distinct (Figure 3.27). The small-angle model predictions are generally in very good agreement with the observations at locations well inside the main focal region (sections $B$ and $C$, near the center line); the agreement is certainly better than that found for the angular-spectrum predictions in that region. However, for these sections ($B$ and $C$), and away from the center line, we note that the angular-spectrum model appears more accurate, i.e. the wide-angle spreading behind the shoal appears better captured by the angular-spectrum model

than by the small-angle model. This wave motion, propagating at large relative angles with the principal direction, is the result of strong refraction effects and diffractive scattering in the focal region. The angular-spectrum model includes the topographical forcing only approximately, but wide-angle diffraction is fully accounted for [in the far field approximation, see e.g. Stamnes, 1986; Dalrymple *et al.*, 1989].



(a) Transect A

(b) Transect B

(c) Transect C

(d) Transect E

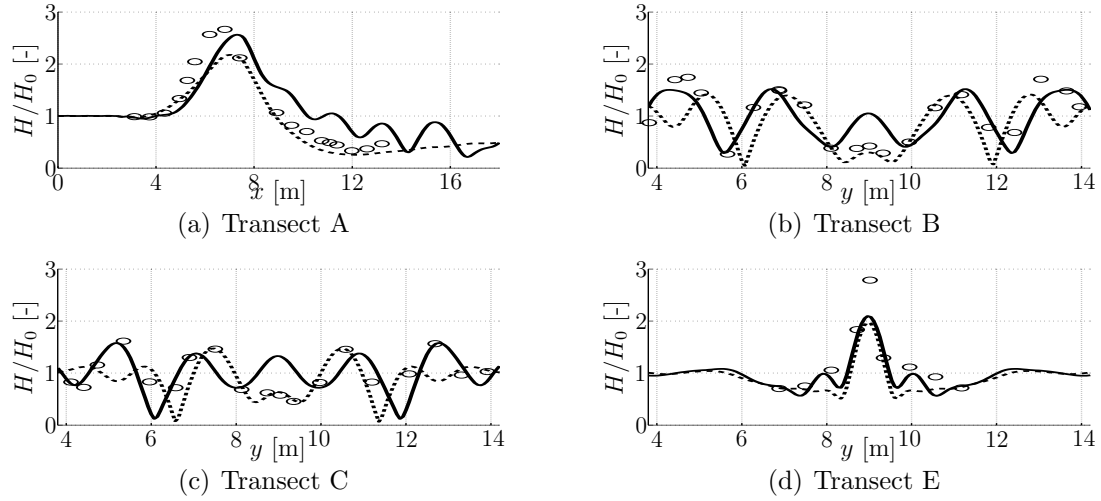**Figure 3.27:** Comparison of predicted and observed [Chawla, 1995] normalized wave heights; normally incident waves with $1.165\,\mathrm{cm}$ amplitude and $1.0\,\mathrm{s}$ period. Thick solid line represents angular spectrum model (eq. (3.42)); dashed line is small-angle model (eq. (3.68)).

It turns out that the small-angle model does not generally produce much higher Willmott index values (Table 3.6), and despite its markedly better agreement at some locations, even scores slightly lower along some transects. As the Willmott index measures the performance over the transect as a whole it penalizes the small-angle model for its limited representation of wide-angle components, deteriorating its overall performance in terms of the index values. We remark that the underestimation by the small-angle model of wave height increase over the shoal as seen along transect $A$ was not found by Kaihatu [2001]. Although we use the same small-angle model, the difference may be on account of our use of the spectral method in the lateral direction (differences on account of the different nonlinear term are minimal, not shown). Nevertheless, the small-angle model scores much better along this transect than the angular-spectrum model.

We noted in §3.4.2 that the description of nonlinearity in the angular-spectrum model results in underestimation of nonlinear couplings in localized shallow regions; the nonlinear coupling in the small-angle model does not have directional dependency but is a function of the local (not the global) depth and is therefore expected more sensitive to two-dimensional topographical features, and more accurate for near-collinear wave propagation. In Table 3.6 the Willmott index values for the linear models are also shown; along transect $B$ and $D$ the small-angle model predictions improve considerably through the inclusion of nonlinearity but the effects of nonlinear corrections are small

| Transect | Angular Spectrum | | Small-angle | |
| :---: | :---: | :---: | :---: | :---: |
| | Nonlinear | Linear | Nonlinear | Linear |
| A | 0.889 | 0.913 | 0.965 | 0.948 |
| B | 0.842 | 0.837 | 0.769 | 0.634 |
| C | 0.688 | 0.674 | 0.705 | 0.683 |
| D | 0.829 | 0.832 | 0.736 | 0.534 |
| E | 0.937 | 0.947 | 0.892 | 0.922 |
| F | 0.736 | 0.769 | 0.902 | 0.919 |
| G | 0.500 | 0.504 | 0.638 | 0.658 |

**Table 3.6:** Willmott index values for angular spectrum and small-angle model predictions and observations by Chawla [1995]; normally incident waves with $1.165\,\mathrm{cm}$ amplitude and $1.0\,\mathrm{s}$ period.

at other transects, the nonlinear simulation being generally – but not everywhere – the more accurate.

Thus the restriction on two-dimensionality of the topography, as implied in the angular-spectrum approach, can be removed at the expense of aperture limitations on the wave propagation (small-angle model). Both approaches are approximate over fully two-dimensional topography; the angular-spectrum explicitly, due to its assumption of weak lateral variation; the small-angle model implicitly, since the presence of two-dimensional depth variations will result in wide-angle refraction and scattering of the wave field. We have not discussed wider-angle approximations [Kirby, 1986; Kaihatu, 2001] that ameliorate the aperture limitation of the small-angle model, neither is the comparison intended to claim the 'better' approximation. This discussion and comparison serve to illustrate how these models are inter-related and how the differences in the premises, on which the derivations are based, reflect on model performance when predicting wave evolution over complex topography. It generally depends on the nature of the physical reality, of which the model is supposed to be a fair representation, which approximation is the better suited.

*Stochastic evolution equations*

For random ocean wave fields, understanding of the evolution of the wave field statistics is often more useful than detailed, deterministic knowledge of individual realizations. For applications on scales typically encountered in coastal areas, a stochastic modeling approach, despite its approximate closure, is generally preferred over Monte Carlo simulations, for reasons of efficiency. The multi-frequency angular-spectrum approach, developed in Chapter 2 and verified in the present chapter, is particularly well suited as a basis for the latter approach, which is further detailed in Chapter 4.

# A stochastic model for nonlinear waves over topography

**4**

The spatial and temporal irregularity of ocean waves, visible even from casual observation, presents great difficulty for deterministic modeling approaches as it requires detailed, phase-resolving knowledge of the wave field along the model boundary. In practice, such detailed information is not available. However, most engineering applications (e.g. the modeling of morpho-dynamic evolution, structural fatigue & design criteria) require statistical properties of the wave field as input, such that the intrinsic deterministic details of the wave field are usually of little interest. Instead, prediction of the wave field characteristics in a statistical sense suffices.

From a stochastic viewpoint, the instantaneous surface elevation is but a realization of an underlying random process, which – from a loose use of the central limit theorem – is generally regarded weakly non-Gaussian, with deviations from normality anticipated owing to the nonlinearity of the governing equations. The description of ocean waves as a stochastic rather than deterministic process, and the anticipation of near-Gaussianity, has lead to great advances, both in our theoretical and conceptual understanding of ocean wave physics [Hasselmann, 1962; Kinsman, 1965; Benney & Saffman, 1966], and in the operational wave modeling capability [see e.g. Komen *et al.*, 1994].

If a deterministic model exists, the properties of the underlying random process can – in principle – be estimated by computing an ensemble of realizations through repeated simulations [Tucker *et al.*, 1984], and subsequently ensemble-average the moments of the wave field variable [Freilich & Guza, 1984]. However, to accurately estimate the statistical moments with such a Monte-Carlo approach (in particular the higher-order moments such as the sea surface skewness) large ensembles are needed, rendering the technique computationally intensive. Alternatively, the governing equations can be recast into evolution equations for the ensemble-averaged spectral moments, describing the evolution of the wave field statistics directly, i.e. without the need for repeated simulations. However, this is achieved at the expense of an additional approximation or a so-called closure hypothesis.

To substantiate the discussion somewhat, which is central to much of the following, consider the one-dimensional transport equation for the Fourier components, $\zeta_p$, of a random wave field

$$\frac{d}{dx}\zeta_p = ik_p\zeta_p + i\sum_{n+m=p}\mathcal{W}_{nm}\zeta_n\zeta_m, \tag{4.1}$$

where the linear term represents dispersion, and the convolution is the quadratic nonlinearity originating from the free surface, with $\mathcal{W}_{nm} = \mathcal{W}_{mn}$. The details of these terms

are of no particular concern at this point. In the present context, the eq. (4.1) describes evolution of nonlinear surface waves, but similar equations can be conceived e.g. in the context of turbulence, with the linear term then accounting for viscous damping (instead of dispersion) and nonlinearity originating from the advective term in the Navier-Stokes equation [see e.g. Leslie, 1973]. By forming the evolution equations for the ensemble-averaged spectral moments, and if, after Holloway & Hendershott [1977], we temporarily drop all subscripts, summations and coefficients, the moment-hierachy is symbolically represented by

$$d_x \langle \zeta\zeta \rangle = \langle \zeta\zeta \rangle + \langle \zeta\zeta\zeta \rangle \tag{4.2a}$$

$$d_x \langle \zeta\zeta\zeta \rangle = \langle \zeta\zeta\zeta \rangle + \langle \zeta\zeta \rangle \langle \zeta\zeta \rangle + \langle \zeta\zeta\zeta\zeta \rangle^C \tag{4.2b}$$

$$d_x \langle \zeta\zeta\zeta\zeta \rangle^C = \langle \zeta\zeta\zeta\zeta \rangle^C + \langle \zeta\zeta \rangle \langle \zeta\zeta\zeta \rangle + \langle \zeta\zeta\zeta\zeta\zeta \rangle^C \tag{4.2c}$$

$$\vdots$$

where the superscript $C$ denotes the so-called cumulant, the residue after decomposing the moment in products of lower-order moments [e.g. Kim & Powers, 1979; Priestley, 1981]. The set (4.2) is open. After all, in order to compute the evolution of a moment of order $n$, we require knowledge of the next higher-order moment (cumulant). This problem of closure has been studied extensively in turbulence modeling [see e.g. Proudman & Reid, 1954; Orszag, 1970; Leslie, 1973; Lesieur, 1997; Salmon, 1998, and many others].

For surface gravity waves in deep water, in marked contrast to turbulence, a natural asymptotic closure for the hierarchy of stochastic equations exists. Based on heuristic considerations, Hasselmann [1962] first derived evolution equations for the wave spectrum in closed form by assuming normality and filtering non-resonant contributions by integrating the moment equations over an asymptotic large time. Using formal multiple scales, Benney & Saffman [1966] showed that the closure implied in Hasselmann's work is valid, without the necessity of assuming the wave field to be Gaussian [see also Benney & Newell, 1969; Benney, 1971]. This natural asymptotic closure is the result of the coexistence of isolated nonlinear resonances and strong dispersive effects; the former generating correlations over asymptotic length scales, governed by the prevalent nonlinear mechanism; the latter represents a de-correlating mechanism, effective on much shorter scales and enforcing a return to the Gaussian state. After Holloway [1979] we refer to this form of asymptotic closure as 'resonant interaction' (RI) closure.

In shallow water, due to lack of frequency dispersion, the RI closure is invalidated. Abreu *et al.* [1992] developed a stochastic wave model for shallow water based on the asymptotic closure proposed by Newell & Aucoin [1971]; the latter closure substitutes directionality of the waves as a de-correlation mechanism, while assuming exact resonance among collinear waves. This approach is suitable for what is coined 'semi-dispersive' wave systems by Newell & Aucoin [1971]. However, it is doubtful that surface gravity waves, even in the shallow-water limit, actually belong to this sub-class of wave systems. Apart even from the fact that the closure excludes energy transfers between non-collinear

wave components, which is at variance with empirical evidence [Elgar *et al.*, 1993], the resonance mismatch due to frequency dispersion is, in shallow water, of the same order as the directional effects, which invalidates a fundamental premise of the closure used in Abreu *et al.* [1992].

After this first attempt at the stochastic modeling of shallow-water wave propagation, a multitude of approaches emerged, either based on the so-called Zakharov kinetic integral [Eldeberky, 1996; Eldeberky *et al.*, 1996; Becq *et al.*, 1998], Boussinesq-type amplitude equations [Herbers & Burton, 1997; Kofoed-Hanssen & Rasmussen, 1998] or amplitude evolution equations including full dispersion in the linear terms and the coupling coefficient [Agnon & Sheremet, 1997; Eldeberky & Madsen, 1999]. Invariably these models apply a so-called quasi-normal closure, a semantics borrowed from turbulence literature, with either full discard of the fourth cumulant or a heuristic approximation [see Rasmussen, 1998, for a review]. Generally, these stochastic models either solve a coupled set of equations for the spectrum and bi-spectrum equations [Herbers & Burton, 1997; Kofoed-Hanssen & Rasmussen, 1998; Eldeberky & Madsen, 1999] or explicitly integrate the bispectral evolution equation – at the expense of additional assumptions – to obtain a single transport equation for the energy spectrum [e.g. Eldeberky, 1996; Eldeberky *et al.*, 1996; Becq *et al.*, 1998].

The stochastic models by e.g. Agnon & Sheremet [1997] and Herbers & Burton [1997] compare favorably to observations up to Ursell numbers around 1.5 [Kofoed-Hanssen & Rasmussen, 1998; Agnon & Sheremet, 1997; Norheim *et al.*, 1998]. At the shallow end of the beach and the surf zone, a region typified by strong concomitant dissipative and nonlinear effects [Chen *et al.*, 1997; Herbers *et al.*, 2000], modeling capability is greatly hampered by the quasi-normal closure approximation, to the extent that predictions become entirely unreasonable and even unphysical [occurrence of negative 'energies', see e.g. Ogura, 1962]. Herbers *et al.* [2003] extend the predictive capability to the surf zone through modification of the closure approximation by means of a heuristic relaxation term, inducing a return to Gaussian statistics in the presence of dissipation. Comparison to observations of waves propagating across a beach, including the surf zone, show good agreement, even through regions involving strong dissipation and high Ursell numbers.

State-of-the-art shallow-water nonlinear stochastic models [Agnon & Sheremet, 1997; Eldeberky & Madsen, 1999; Herbers *et al.*, 2003] are based on an angular-spectrum decomposition of the wave field, assuming a one-dimensional topography. In the present chapter we aim at deriving a stochastic nonlinear wave model for shallow regions including the surf zone, without inherent limitations on (linear) frequency dispersion, and suitable for two-dimensional topography. The stochastic model development is based on the deterministic model derived in Chapter 2, which accounts for interaction with two-dimensional topography through a scattering mechanism. To illustrate the stochastic representation of two-dimensional wave-bottom interaction, we consider the angular-spectrum decomposition of a time-periodic surface elevation function

$$\eta(x, y, t) = \sum_{q=-\infty}^{\infty} \widetilde{\zeta}_q \exp\left[i\left(\lambda_q y - \omega t\right)\right], \tag{4.3}$$

where the $q$ denotes the lateral wavenumber counter. Assuming the waves to propagate over two-dimensional topography, represented as a superposition of a uniform reference depth and a two-dimensional perturbation, the linear evolution along the principal direction of the spectral amplitudes $\widetilde{\zeta}_q$, is governed by a transport equation of the form (see e.g. §3.4)

$$\left[\frac{d}{dx} - i\varkappa_q\right]\widetilde{\zeta}_q = \sum_{q_b+q'=q} \widetilde{f}_{q_b}(x)\widetilde{\zeta}_{q'}, \tag{4.4}$$

where $\varkappa_q = \sqrt{k^2 - \lambda_q^2}$ is the principal wavenumber component ($k$ is related to $\omega$ through the linear dispersion relation at the reference depth); the $\widetilde{f}_{q_b}$ symbolically denotes the Fourier amplitude associated with the lateral wavenumber $\lambda_{q_b}$ of the topographical forcing, the details of which do not concern us here. For purpose of illustration we have written the interaction with the laterally varying depth as a spectral convolution, rather than the more implicit pseudo-spectral operator notation used elsewhere. In essence the wave-bottom interaction in the deterministic model (viz. (4.4)) is thus described as a triad interaction between two wave components with a difference wavenumber matching that of the bottom component, i.e. $\lambda_q = \lambda_{q'} + \lambda_{q_b}$.

From (4.4) we derive evolution equations for the statistical moments $\langle\widetilde{\zeta}_q\widetilde{\zeta}_{q''}^*\rangle$ (the $\langle\ \rangle$ denote ensemble averaging) through multiplication by $\widetilde{\zeta}_{q''}^*$, summing with the evolution equation for $\widetilde{\zeta}_{q''}^*$ multiplied by $\widetilde{\zeta}_q$, and ensemble averaging the result. These operations yield

$$\left[\frac{d}{dx} - i\left(\varkappa_q - \varkappa_{q''}\right)\right]\langle\widetilde{\zeta}_q\widetilde{\zeta}_{q''}^*\rangle = \sum_{q_b+q'=q}\widetilde{f}_{q_b}\langle\widetilde{\zeta}_{q'}\widetilde{\zeta}_{q''}^*\rangle + \left(\sum_{q_b+q'=q''}\widetilde{f}_{q_b}\langle\widetilde{\zeta}_{q'}\widetilde{\zeta}_q^*\rangle\right)^*. \tag{4.5}$$

The set of transport equations (4.5) constitute a stochastic model representation of the wave field evolution over topography. Note that the scattering term that accounts for the wave bottom interactions, induces correlations between non-collinear wave components – represented here by the cross-spectrum terms $\langle\widetilde{\zeta}_{p,q}\widetilde{\zeta}_{p,q''}^*\rangle$ with $q \neq q''$. Consequently, on account of the anticipated lateral heterogeneity, the spectral description in the stochastic framework is dimensionally extended from one-dimensional (for a homogeneous wave field) to two-dimensional in the lateral wavenumber space. This reflects the fact that the covariance function in a heterogeneous wave field depends on location *and* separation, whereas for homogeneous conditions it is a function of the separation alone (thus likewise a dimensional extension by one). Consider the covariance function of the surface elevation function at $(x, y + \upsilon/2, t)$ and $(x, y - \upsilon/2, t)$ which can be written as

$$\langle\eta(x, y + \upsilon/2, t)\eta(x, y - \upsilon/2, t)\rangle = \text{Cov}(x, y, \upsilon)$$
$$= \sum_{q,q''}\langle\widetilde{\zeta}_q\widetilde{\zeta}_{q''}^*\rangle \exp\left[i\left(\tfrac{1}{2}\left(\lambda_q + \lambda_{q''}\right)\upsilon + (\lambda_q - \lambda_{q''})y\right)\right]. \tag{4.6}$$

The spatial variation of the wave field statistics results from the off-diagonal moments ($\langle \widetilde{\zeta_q} \widetilde{\zeta}^*_{q''} \rangle$ with $q \neq q''$). For instance, if a laterally homogeneous wave field ($\langle \widetilde{\zeta_q} \widetilde{\zeta}^*_{q''} \rangle = 0$ for $q \neq q''$) impinges on two-dimensional topography ($\widetilde{f}_{q_b} \neq 0$) then the interaction with $\widetilde{f}_{q_b}$ causes the off-diagonal moments to develop (see eq. (4.5)). In the stochastic framework, the effects of the lateral depth variability and associated heterogeneity of the wave field are thus accounted for through the evolution of the averaged moments $\langle \widetilde{\zeta_q} \widetilde{\zeta}^*_{q''} \rangle$, $q \neq q''$; conceptually we can think of these off-diagonal moments as forced by triads involving two wave components and a bottom wavenumber component (viz. $\langle f \zeta \zeta \rangle$), but since the topography is considered deterministic, the bottom component can be taken outside of the averaging operation. Physically this can be understood as follows. Submerged topography in shallow water scatters waves in different directions. These scattered components are mutually correlated through the interaction with the topography, and exactly this correlation is captured through the cross-spectrum terms. As such, this stochastic formalism resolves the spatial inhomogeneity of the wave field, including the (linear) phase coupling of topography-induced non-collinearity (e.g. in the focal region of a topographical lens).

Since the stochastic model is closed in the linear sense, the (linear) processes of shoaling, refraction and diffraction are accounted for with the same accuracy as the deterministic model (see Chapter 3). Since phase coupling between non-collinear waves is fully resolved, this approach is potentially more accurate than conventional spectral models such as SWAN [Booij *et al.*, 1999], which assume homogeneity from the outset, in regions where such heterogeneous effects are important (for instance in focal regions behind topographical lenses or wave propagation around breakwater heads). We will return to the heterogeneous effects and interpretation in terms of geometrical optics in more detail in §4.2.

With respect to the nonlinear processes the stochastic model is more approximate than the underlying deterministic model since the stochastic hierarchy of moment equations is closed utilizing a heuristic modification of the quasi-normal closure. Moreover, since the anticipated domain of operation is the inner shelf and shallow coastal areas, we omit cubic nonlinear interactions from the model; they are assumed negligible over the typical length scales over which waves propagate in such regions. Also the wave-driven mean flow and its effect on the attendant wave field evolution is omitted; there is no fundamental (or even practical) difficulty with including the flow-induced forcing on the wave field [see also Kennedy & Kirby, 2003], however, the computation of the near-shore wave-induced current field on a natural beach is certainly not trivial [e.g. Reniers *et al.*, 2002; Van Dongeren *et al.*, 2003] and well outside the scope of the present work.

The resulting stochastic model describes directionally spread waves over topography, including the effects of quadratic nonlinearity and is accurate over distances $O(\epsilon^{-1})$. Depth-induced wave breaking is parameterized and a heuristic closure modification is included to support wave propagation through dissipative and strongly nonlinear regions, thus including the surf zone. Additional forcing terms that account for the

processes of e.g. wind forcing and dissipation due to steepness instability can be added; such extensions are not pursued in the present work. Instead, we focus on the linear and nonlinear wave processes over two-dimensional topography, including the spatial structure and correlations in heterogeous wave fields.

This chapter is organized as follows. In §4.1 we derive stochastic model equations based on the deterministic model presented in Chapter 2. In §4.2 we discuss interpretation of the model-predicted spectra in terms of geometrical optics. Parameterizations of closure relaxation and surf zone dissipation are given in §4.3 and §4.4.

Empirical verification through comparison with laboratory and field observations, is presented in Chapter 5.

## 4.1  Derivation of the stochastic model

The starting point of the derivation is the deterministic angular-spectrum model presented in Chapter 2, without terms accounting for cubic interactions and wave-induced mean flow, written here as

$$
\left[\frac{d}{dx} - i\varkappa_1^1\right]\widetilde{A}_1^1 = \frac{1}{L_y}\int_{-L_y/2}^{L_y/2}\sum_{\lambda_2}\frac{S_1^1(x,y)}{\sqrt{V_1^2}}\widetilde{A}_1^2\exp\left[i\left(\lambda_2 - \lambda_1\right)\right]dy
$$

$$
- \frac{1}{2L_y}\int_{-L_y/2}^{L_y/2}\sum_{\lambda_2}\sqrt{\frac{V_1^1}{V_1^2}}D_1(x,y)\widetilde{A}_1^2\exp\left[i\left(\lambda_2 - \lambda_1\right)\right]dy
$$

$$
+ i\sum_{\boldsymbol{v_2}}\mathcal{W}_{(1-2)2}^{(1-2)2}\widetilde{A}_{(1-2)}^{(1-2)}\widetilde{A}_2^2. \tag{4.7}
$$

For the purpose of presentation, instead of using a single-index notation as in Chapter 2, we choose to split up the numeric subscripts into sub- and superscripts, denoting the frequency and alongshore wavenumber index respectively; this is done in anticipation of lateral heterogeneity of the wave field for which, in the stochastic description, a single index would be ambiguous. Further, we have introduced the wave field variable $\widetilde{A}_1^1 = A_1^1\exp\left[i\int^x\varkappa_1^1\,dx\right]^\dagger$. The numeral superscripts on variables should not be confused with an exponent; thus $\widetilde{A}_1^2$ denotes the amplitude $\widetilde{A}$ pertinent to the frequency/wavenumber pair $(\omega_{p_1},\lambda_{q_2})$, while operations on such variables that are usually placed in the superscript position are preceded by brackets, e.g. the conjugate of $\widetilde{A}_1^2$ is denoted as $(\widetilde{A}_1^2)^*$, and likewise its square reads $(\widetilde{A}_1^2)^2$. We will omit commas separating numeral subscripts on the interaction coefficients, such that $\mathcal{W}_{12}^{12}$ denotes the weighting coefficient of the product $\widetilde{A}_1^1\widetilde{A}_2^2$; the coefficient $\mathcal{W}_{12} = \sqrt{V_1^1/(V_2^2 V_3^3)}\mathcal{Z}_{12}^{(\mathrm{g})}$ with $\mathcal{Z}_{12}^{(\mathrm{g})}$ given in Table 3.1. For brevity we have gathered the (linear) terms accounting for the lateral depth variations

---

†Recall that the (complex) spectral amplitudes, $A_1^1$ are related to the surface elevation, $\eta$, through

$$
\eta(x,y,t) = \sum_{p_1,q_1=-\infty}^{\infty}\frac{A_1^1}{\sqrt{V_1^1}}\exp\left[i\left(\int^x\varkappa_1^1\,dx + \lambda_1 y - \omega_1 t\right)\right],
$$

with $V_1^1 = (\varkappa_1^1/k_1)C_{g,1}$, $\lambda_1 = q_1\Delta\lambda$ and $\omega_1 = p_1\Delta\omega$. See also §2.1.1 and §3.1.2.

in a single forcing term, denoted by the $S_1^1(x, y)$, which can accordingly be decomposed as

$$S_1^1(x, y) = S_1^{1,(\text{wb})}(x, y) + S_1^{1,(\text{wbb})}(x, y). \tag{4.8}$$

Here the wb and wbb superscripts denote the forcing due to interaction with the laterally varying depth, linear and quadratic in the bottom perturbation respectively. The expressions for $S_1^{1,(\text{wb})}$ and $S_1^{1,(\text{wbb})}$ can be derived from the expressions given in the Appendix B and read

$$S_1^{1,(\text{wb})}(x, y) = i \frac{g}{2\omega_1 \sqrt{V_1^1}} \left(1 - T_1^2\right) \left[k_1^2 \widetilde{h} + i\varkappa_1^1 P_1^1 \widetilde{h}_x + i\lambda_1 \left(q_1 T_1 - 1\right) \widetilde{h}_y\right], \tag{4.9a}$$

$$S_1^{1,(\text{wbb})}(x, y) = i \frac{g}{2\omega_1 \sqrt{V_1^1}} \left(1 - T_1^2\right) k_1^3 \frac{C_1}{2C_{g,1}} \frac{\left(1 - T_1^2\right)^2}{T_1} \left[\frac{1}{\left(1 - T_1^2\right)} - P_1^1\right] \widetilde{h}^2. \tag{4.9b}$$

Here the $C_1$ and $C_{g,1}$ represent phase and group speed respectively for frequency $\omega_1$; the $V_1^1 = (\varkappa_1^1/k_1)C_{g,1}$ is the principal (cross-shore) component of the group speed vector, and $T_1 = \tanh(k_1 h)$; the $P_1^1$ is given in Appendix B. The $D_1(x, y)$ in the second term on the *RHS* of (4.7) represents a sink term associated with dissipation due to depth-limited wave breaking; it is considered here a (real) function of frequency (through the subscript) in anticipation of a frequency weighting of the dissipation distribution over the spectrum [see e.g. Chen *et al.*, 1997; Herbers *et al.*, 2000]; details and rationale for the $D_1$ are deferred to §4.3.

Through multiplying (4.7) by $(\widetilde{A}_1^2)^*$, summing with the transport equation for $(\widetilde{A}_1^2)^*$ multiplied by $\widetilde{A}_1^1$, applying the ensemble averaging operator and letting $\Delta\lambda, \Delta\omega \to 0$, we obtain the evolution equation

$$\left[\frac{d}{dx} - i\Lambda_1^{1;2}\right] \mathcal{E}_1^{12}$$

$$= \frac{1}{2\pi} \iint dy \, d\lambda_3 \left[\frac{S_1^1}{\sqrt{V_1^3}} \mathcal{E}_1^{32} \exp\left[i\left(\lambda_3 - \lambda_1\right) y\right] + \left(\frac{S_1^2}{\sqrt{V_1^3}} \mathcal{E}_1^{31}\right)^* \exp\left[-i\left(\lambda_3 - \lambda_2\right) y\right]\right]$$

$$- \frac{1}{4\pi} \iint dy \, d\lambda_3 \, D_1 \sqrt{\frac{V_1^1}{V_1^3}} \left[\sqrt{\frac{V_1^2}{V_1^1}} \mathcal{E}_1^{32} \exp\left[i\left(\lambda_3 - \lambda_1\right) y\right] + \left(\mathcal{E}_1^{31}\right)^* \exp\left[-i\left(\lambda_3 - \lambda_2\right) y\right]\right]$$

$$+ i \iint d\lambda_3 d\omega_3 \left[\mathcal{W}_{(1-3)3}^{(1-3)3} \mathcal{C}_{(1-3)3}^{(1-3)32} - \mathcal{W}_{(1-3)3}^{(2-3)3} \left(\mathcal{C}_{(1-3)3}^{(2-3)31}\right)^*\right]. \tag{4.10}$$

Here the integrals should be taken from $-\infty$ to $\infty$, the wavenumber mismatch is denoted by the shorthand $\Lambda_{1..N}^{1..N;M} = \varkappa_1^1 + \ldots + \varkappa_N^N - \varkappa_{\sum_1^N}^M$, and the spectral and bi-spectral density functions are defined as

$$\mathcal{E}_1^{12}(x) = \mathcal{E}(\omega_1, \lambda_1, \lambda_2, x) = \lim_{\Delta\lambda, \Delta\omega \to 0} \frac{\langle \widetilde{A}_1^1 (\widetilde{A}_1^2)^* \rangle}{\Delta\lambda^2 \Delta\omega}, \tag{4.11}$$

$$\mathcal{C}_{12}^{123}(x) = \mathcal{C}(\omega_1, \omega_2, \lambda_1, \lambda_2, \lambda_3, x) = \lim_{\Delta\lambda, \Delta\omega \to 0} \frac{\langle \widetilde{A}_1^1 \widetilde{A}_2^2 (\widetilde{A}_{(1+2)}^3)^* \rangle}{\Delta\lambda^3 \Delta\omega^2}. \tag{4.12}$$

Note that the spectrum $\mathcal{E}_1^{12}$ and bi-spectrum $\mathcal{C}_{12}^{123}$ are two- and three dimensional in lateral wavenumber space respectively. The dimensional extension by one (with respect to the laterally homogeneous case) reflects the dimensional extension of the wave co-variance function (of which the spectrum is the Fourier transform) in a heterogeneous wave field. After all, the covariance function for an inhomogeneous (or non-stationary, if the heterogeneity is in time) process depends on the separation *and* location, whereas for homogeneous/stationary processes it is merely a function of the separation (or lag). The dimensional extension of the (bi-)spectrum accounts for the phase coupling (or directional coherence) between couples of non-collinear wave components and the topography, thus resolving the interference patterns of e.g. crossing wave trains in topography-induced caustic regions. We return to this in §4.2 where we relate the heterogeneous description of the wave evolution and the associated dimensional extension of the spectral density functions to the concepts of geometrical optics.

Through similar operations that lead to eq. (4.10) we obtain the evolution equation for the bi-spectrum:

$$\left[\frac{d}{dx} - i\left(\Lambda_{12}^{12;3} + i\mu_{12}^{123}\right)\right]\mathcal{C}_{12}^{123} = \frac{1}{2\pi}\iint dy\,d\lambda_4 \left[\frac{S_1^1}{\sqrt{V_1^4}}\mathcal{C}_{12}^{423}\exp\left[i\left(\lambda_4 - \lambda_1\right)y\right]\right.$$

$$\left.+\frac{S_2^2}{\sqrt{V_2^4}}\mathcal{C}_{12}^{143}\exp\left[i\left(\lambda_4 - \lambda_2\right)y\right] + \frac{S_{(1+2)}^{3*}}{\sqrt{V_{(1+2)}^4}}\mathcal{C}_{12}^{124}\exp\left[-i\left(\lambda_4 - \lambda_2\right)y\right]\right]$$

$$-\frac{1}{4\pi}\iint dy\,d\lambda_4 \left[D_1\sqrt{\frac{V_1^1}{V_1^4}}\mathcal{C}_{12}^{423}\exp\left[i\left(\lambda_4 - \lambda_1\right)y\right]\right.$$

$$+D_2\sqrt{\frac{V_2^2}{V_2^4}}\mathcal{C}_{12}^{143}\exp\left[i\left(\lambda_4 - \lambda_2\right)y\right] + D_{(1+2)}\sqrt{\frac{V_{(1+2)}^3}{V_{(1+2)}^4}}\mathcal{C}_{12}^{124}\exp\left[-i\left(\lambda_4 - \lambda_2\right)y\right]\right]$$

$$+2i\int d\lambda_4 \left[\mathcal{W}_{(1+2)(-2)}^{(1+4)(-4)}\mathcal{E}_2^{24}\mathcal{E}_{(1+2)}^{(1+4)3} + \mathcal{W}_{(1+2)(-1)}^{(2+4)(-4)}\mathcal{E}_1^{14}\mathcal{E}_{(1+2)}^{(2+4)3} - \mathcal{W}_{12}^{(3-4)(4)}\mathcal{E}_1^{14}\mathcal{E}_2^{2(3-4)}\right]$$

$$(4.13)$$

where – following Holloway & Hendershott [1977]; Holloway [1979]; Herbers *et al.* [2003] – the fourth cumulant contribution is tentatively written as a linear damping term $\mathcal{C}^{(4)} = -\mu_{12}^{123}C_{12}^{123}$; expressions and rationale for this heuristic damping term are given in §4.4. Suffice it to remark here that this contribution provides a means of relaxation toward Gaussian statistics in regions of strong nonlinearity, where the quasi-normal closure ($\mathcal{C}^{(4)} = 0$) generally predicts statistics too far from Gaussian [e.g. Orszag, 1970].

The stochastic evolution equations (4.10) and (4.13) are the main result of this section. They represent a set of coupled evolution equations for the spectrum $\mathcal{E}_1^{12}$ and bi-spectrum $\mathcal{C}_{12}^{123}$. In the linear approximation, the stochastic model equations are closed (i.e. no additional assumptions are required), so that the set (4.10) describes the linear effects of shoaling, refraction and diffraction with the same accuracy as the underlying

deterministic theory; we return to this in §4.2. To extend modeling capability to the surf zone, dissipation due to depth-induced wave breaking is accounted for through a parameterization of the associated macro effects (the details of which are presented in §4.3). The moment hierarchy is closed by means of a modification of quasi-normal closure hypothesis; a heuristic relaxation is proposed to support a return to Gaussian statistics in strongly nonlinear regions (see §4.4 for discussion and details).

## 4.2 Lateral inhomogeneity and geometrical optics

In the deterministic model (eq. (4.7)), laterally heterogeneous topography is accounted for through a scattering term that redistributes the (complex) amplitudes across the angular components. The stochastic formalism accounts for the topography-induced coupling through the evolution of the correlations between non-collinear wave components, which resolves the lateral heterogeneity of the wave field. The spectral quantities evolved in the stochastic model are not 'local' in the lateral sense and as such not readily interpretable in terms of geometrical optics. However, these spectra can in fact be readily brought into a geometrically interpretable form; this is discussed in §4.2.1. Although the present stochastic formalism is not uncommon in other fields such as e.g. optics [Papoulis, 1968; Bastiaans, 1979], it has – to the author's knowledge – not been applied before in the context of gravity wave propagation over topography. A numerical example in §4.2.2 illustrates the embedded modeling capability of random, directionally spread waves over topography, including a caustic region. The stochastic model predictions are compared to Monte-Carlo simulations with the deterministic model.

### 4.2.1 A local spectrum: the Wigner distribution

The spectrum $\mathcal{E}_1^{12}$ and bi-spectrum $\mathcal{C}_{12}^{123}$ are two- and three-dimensional in the lateral wavenumber space respectively, but they are not a function of the lateral coordinate. However, a geometrically interpretable 'local' (in the lateral sense) spectrum takes the form of a Wigner distribution [e.g. Wigner, 1932; Alber, 1978; Bastiaans, 1979; Mallat, 1998] and is related to $\mathcal{E}(\omega_1, \lambda_1, \lambda_2, x)$ through the Fourier transform relation

$$\widehat{\mathcal{E}}(\omega, \lambda, x, y) = \int \mathcal{E}(\omega, \lambda + \lambda'/2, \lambda - \lambda'/2, x) \exp\left[i\lambda' y\right] d\lambda'. \tag{4.14}$$

The quantity $\widehat{\mathcal{E}}(\omega, \lambda, x, y)\, d\omega d\lambda$ can then be given the usual interpretation of a contribution to the variance at the location $(x, y)$ for the 'ray' pertinent to component $(\omega, \lambda)$ with vector wavenumber $(\sqrt{k_\omega^2 - \lambda^2}, \lambda)$. However, as such it does not constitute the contribution to the variance associated with the surface elevation; after all, $\widehat{\mathcal{E}}(\omega, \lambda, x, y)$ carries dimensions $[(\mathrm{m}^3/\mathrm{s})/(\mathrm{rad}^2/(\mathrm{s\,m}))]$ and is best regarded as a 'flux-spectrum'. The transformation to a flux-spectrum was pursued with the purpose of simplifying the governing equations. Of course the back-transformation to a surface elevation variance spectrum is readily obtained by substituting $\mathcal{E}_1^{12}/\sqrt{V_1^1 V_1^2}$ for $\mathcal{E}_1^{12}$ in (4.14). However,

to elucidate the notion of the 'local' spectrum and its relation to the spectrum $\mathcal{E}_1^{12}$ we consider the surface elevation, $\eta(x, y, t)$, as a realization of a zero-mean, stationary random process such that the corresponding correlation function reads

$$
\begin{aligned}
&\langle \eta(x, y + \upsilon/2, t + \tau/2)\eta(x, y - \upsilon/2, t - \tau/2)\rangle \\
&= \iiint d\lambda \, d\lambda' \, d\omega \frac{\mathcal{E}(\omega, \lambda + \lambda'/2, \lambda - \lambda'/2, x)}{\sqrt{V_\omega^{\lambda+\lambda'/2} V_\omega^{\lambda-\lambda'/2}}} \exp\left[i\left(\lambda\upsilon + \lambda'y - \omega\tau\right)\right], \quad (4.15)
\end{aligned}
$$

where $\tau$ and $\upsilon$ denote the temporal and lateral separation. The variance at location $(x, y)$, denoted by $\langle |\eta(x, y)|^2\rangle$, is obtained by setting $\tau = 0$ and $\upsilon = 0$ so that

$$
\langle |\eta(x, y)|^2\rangle = \iint d\lambda \, d\omega \left( \int \frac{\mathcal{E}(\omega, \lambda + \lambda'/2, \lambda - \lambda'/2, x)}{\sqrt{V_\omega^{\lambda+\lambda'/2} V_\omega^{\lambda-\lambda'/2}}} \exp\left[i\lambda'y\right]d\lambda' \right)
$$

$$
= \iint S(\omega, \lambda, x, y) \, d\lambda d\omega \quad (4.16)
$$

and the quantity

$$
\mathcal{S}(\omega, \lambda, x, y) = \int \frac{\mathcal{E}(\omega, \lambda + \lambda'/2, \lambda - \lambda'/2, x)}{\sqrt{V_\omega^{\lambda+\lambda'/2} V_\omega^{\lambda-\lambda'/2}}} \exp\left[i\lambda'y\right]d\lambda' \quad (4.17)
$$

is thus interpretable in the usual sense as the surface elevation variance density spectrum of spectral component $(\omega, \lambda)$ passing through location $(x, y)$. The spectrum $\mathcal{S}(\omega, \lambda, x, y)$ is a density function in angular frequency and lateral wavenumber space. A more commonly used representation of the directional wave spectrum is in frequency-directional space, which is readily obtained through the appropriate Jacobian transformations; for later use we note

$$
\mathcal{S}(f, \theta, x, y) = 2\pi k_\omega \cos\theta \, \mathcal{S}(\omega, \lambda, x, y). \quad (4.18)
$$

This reasoning can be extended to the bi-spectral density function. Consider the triple correlation

$$
\langle \eta(x, y + \upsilon_1, t + \tau_1)\eta(x, y + \upsilon_2, t + \tau_2)\eta(x, y - \upsilon_1 - \upsilon_2, t - \tau_1 - \tau_2)\rangle =
$$

$$
\int \cdots \int d\lambda_1 \, d\lambda_2 \, d\lambda' \, d\omega_1 \, d\omega_2 \left[ \frac{\mathcal{C}(\omega_1, \omega_2, \lambda_1 + \lambda'/3, \lambda_2 + \lambda'/3, \lambda_1 + \lambda_2 - \lambda'/3, x)}{\sqrt{V_{\omega_1}^{\lambda_1+\lambda'/3} V_{\omega_2}^{\lambda_2+\lambda'/3} V_{\omega_1+\omega_2}^{\lambda_1+\lambda_2-\lambda'/3}}} \right.
$$

$$
\left. \cdot \exp\left[i\left(\lambda_1\left(2\upsilon_1 + \upsilon_2\right) + \lambda_2\left(2\upsilon_2 + \upsilon_1\right) + \lambda'y - \omega_1\left(2\tau_1 + \tau_2\right) - \omega_2\left(2\tau_2 + \tau_1\right)\right)\right] \right]. \quad (4.19)
$$

For zero separation ($\tau_1 = \tau_2 = \upsilon_1 = \upsilon_2 = 0$), the expected value of the surface elevation cubed $\langle \eta(x, y)^3\rangle$ reads

$$\langle \eta(x,y)^3 \rangle = \iiiint \mathcal{B}(\omega_1, \omega_2, \lambda_1, \lambda_2, y, x) \, d\lambda_1 \, d\lambda_2 \, d\omega_1 \, d\omega_2 \qquad (4.20)$$

with

$$\mathcal{B}(\omega_1, \omega_2, \lambda_1, \lambda_2, y, x) = \int d\lambda' \frac{\mathcal{C}(\omega_1, \omega_2, \lambda_1 + \lambda'/3, \lambda_2 + \lambda'/3, \lambda_1 + \lambda_2 - \lambda'/3, x)}{\sqrt{V_{\omega_1}^{\lambda_1 + \lambda'/3} V_{\omega_2}^{\lambda_2 + \lambda'/3} V_{\omega_1 + \omega_2}^{\lambda_1 + \lambda_2 - \lambda'/3}}} \exp\left[i\left(\lambda' y\right)\right].$$
$$(4.21)$$

### 4.2.2 Linear waves over topography: a numerical example

To illustrate the representation of lateral heterogeneity in the stochastic formalism derived in §4.1, and the associated spectral transformations over topography, we consider simulations with a numerical implementation of the stochastic model which – in the linear approximation – is written as

$$\left[\frac{d}{dx} - i\Lambda_1^{1;2}\right] \mathcal{E}_1^{12}$$
$$= \frac{1}{2\pi} \iint dy \, d\lambda_3 \left[\frac{S_1^1}{\sqrt{V_1^3}} \mathcal{E}_1^{32} \exp\left[i\left(\lambda_3 - \lambda_1\right)y\right] + \left(\frac{S_1^2}{\sqrt{V_1^3}} \mathcal{E}_1^{31}\right)^* \exp\left[-i\left(\lambda_3 - \lambda_2\right)y\right]\right].$$
$$(4.22)$$

Here the *RHS* accounts for the lateral depth variability (see eq. 4.9). For our present purpose we omit the effects of depth-induced breaking.

We consider wave propagation over a topography as described in §3.4.2, consisting of a shoal placed on an otherwise horizontal bottom (see Figure 3.23). As in §3.4.2, the model domain (basin) measures 18 m by 18 m; $x$ and $y$ coordinates are defined as in Figure 3.23, with $x$ positive along the mean incident wave direction and $y$ representing the lateral coordinate. The depth at the center of the shoal measures 0.11 m; away from the shoal the water depth is 0.50 m. Shoal center coordinates are $x_c = 5$ m and $y_c = 9.14$ m respectively. The spatial coordinates are discretized with $\Delta x = 0.2$ m and $\Delta y = 0.2857$ m. The frequency array consists of 20 (positive) frequencies with $\Delta \omega = 0.2\pi$ rad/s; the discrete lateral wavenumber increment is $\Delta \lambda = 2\pi / L_y$ and the lateral wavenumber array is $\Delta \lambda \left[-M \ldots M\right]$, with $M = L_y / (2\Delta y) = 32$; in the computations evanescent modes $(\lambda_1 > k_1)$ are omitted.

We parameterize the incident, directionally spread random wave field as

$$\mathcal{S}(\omega, \theta) = \mathcal{S}(\omega) D(\theta) \qquad (4.23)$$

with a (double-sided) Gaussian variance density spectrum $\mathcal{S}(\omega)$ given for positive frequencies as

$$\mathcal{S}(\omega) = \frac{H_{m0}^2}{32\sigma\sqrt{2\pi}} \exp\left[-\frac{(\omega - \omega_p)^2}{2\sigma^2}\right]. \qquad (4.24)$$

Here $H_{m0}$ denotes the zeroth-moment significant wave height of the incident waves $(H_{m0} = 4\sqrt{m_0})$, and $\omega_p$ is the peak (angular) frequency. The directional spreading is

parameterized as a wrapped normal distribution [e.g. Vincent & Briggs, 1989; Mardia & Jupp, 2000]

$$D(\theta) = \frac{1}{2\pi} + \frac{1}{\pi} \sum_{n=1}^{N} \exp\left[-\frac{1}{2}(n\sigma_D)^2\right] \cos n\left(\theta - \theta_m\right). \tag{4.25}$$

Here $\theta$ represents the wave angle, $\theta_m$ is the mean wave angle, $N$ is the number of harmonics in the series (set at 100 in the present example), and $\sigma_D$ is the directional spreading parameter in radians. Waves are incident with $\theta_m = 0$ and frequency spectra defined by $H_{m0} = 1\,\mathrm{cm}$, $\omega_p = 1.2\pi\,\mathrm{rad/s}$, and $\sigma = 1/2\sqrt{2}\,\mathrm{rad/s}$. We consider two directional distributions: a relatively narrow and wide aperture, parameterized with $\sigma_D = 0.05\,\mathrm{rad}$ and $\sigma_D = 0.25\,\mathrm{rad}$ respectively[†].

In Figure 4.1 we show the variance density spectra $\mathcal{S}$ at discrete locations along a transect across the center of the shoal ($y = 9.14\,\mathrm{m}$). These local spectra are obtained though the relation (4.17). The spectral evolution along this transect shows a directional broadening over the shoal, i.e. the scattering on the topography results in energy at large angles.

To validate the stochastic model, we compare wave height estimates obtained from Monte-Carlo simulations with the deterministic model to those computed with the stochastic model; the wave heights from the respective models are derived through

$$H_{m0}^2(x,y) = \begin{cases} 32 \sum_{p_1} \left\langle \left| \sum_{q_1} \frac{\widetilde{A}_1^1(x)}{\sqrt{V_1^1}} \exp\left[i\lambda_1 y\right] \right|^2 \right\rangle, & \text{Deterministic model} \\ 32 \sum_{p_1,q_1} \mathcal{S}_1^1(x,y)\Delta\omega\Delta\lambda, & \text{Stochastic model} \end{cases} \tag{4.26}$$

where the $\langle\,\rangle$ indicate averaging over the ensemble of realizations. Summations are over the longshore wavenumber array ($q_1 \in [-M \dots M]$) and the positive frequencies ($p_1 \in [1 \dots 20]$).

The wave height patterns (Figure 4.2) predicted by the stochastic model for the narrow- and wide-aperture incident wave field are quite distinct. The narrow-aperture case features rather strong lateral wave height variations (associated with laterally standing waves) in the refractive focus behind the shoal, which are sustained over long distances. In contrast, for the wide-aperture incident wave field, the wave heights are primarily affected in the direct vicinity of the shoal whereas in the far-field they are fairly homogeneous. The wave height predicted by the Monte-Carlo simulations (64 realizations) with the deterministic model are nearly identical to the stochastic model (Figure 4.2 and Figure 4.3), particularly so for the narrow directional spreading. Generally, for a given aperture, the level of agreement between stochastic and Monte-Carlo predicted wave height variations increases with increasing number of realizations, consistent with the fact that the stochastic model is closed in the linear sense. In the limit

[†]Note that $\sigma_D$ carries dimensions radians, not degrees as e.g. in Vincent & Briggs [1989] and Chawla et al. [1998].
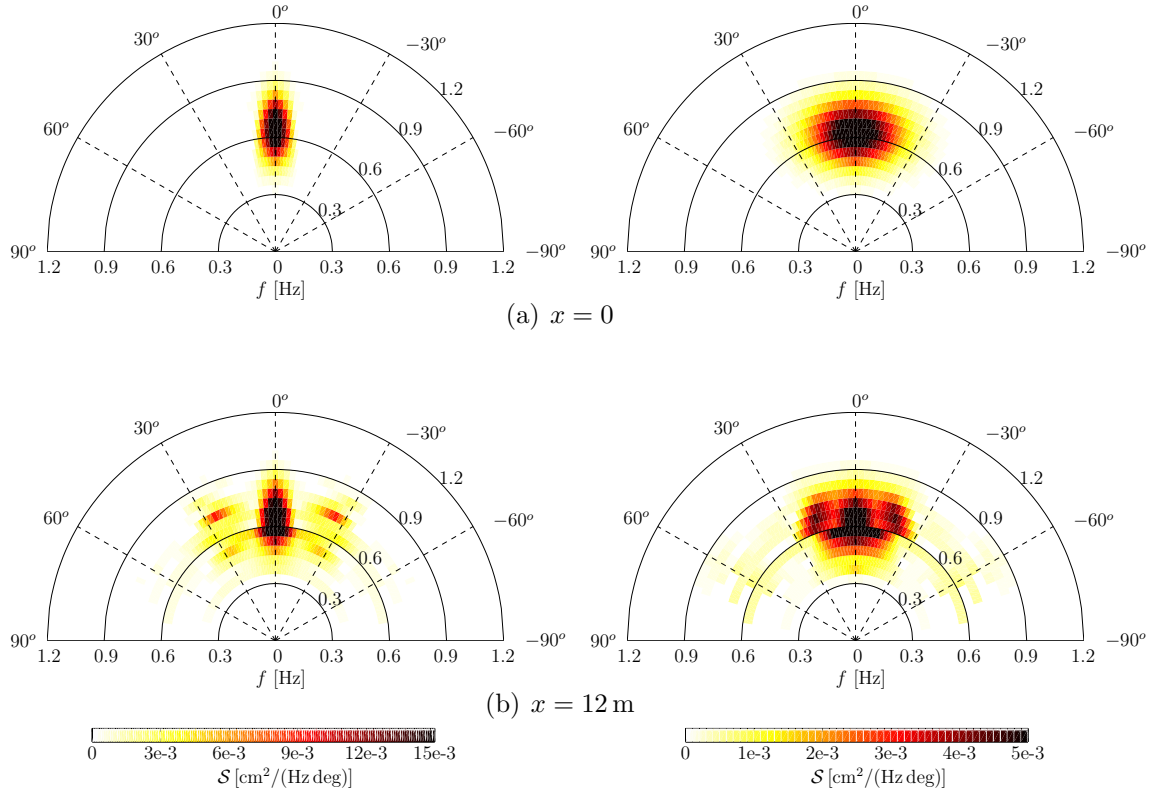
**Figure 4.1:** Wave spectrum evolution over submerged mound. Incident wave field $H_{m0} = 1.0\,\text{cm}$ and $\omega_p = 1.2\pi\,\text{rad/s}$. Spectra shown at discrete $x$-locations (see sub-captions) along $y = y_c = 9.14\,\text{m}$. Left panel: narrow directional distribution ($\sigma_D = 0.05\,\text{rad}$). Right panel: wide directional distribution ($\sigma_D = 0.25\,\text{rad}$).

of unidirectional wave incidence, the lateral wave height variability is entirely depth-controlled and, as a consequence, the normalized wave height variability predicted by the stochastic model is exactly equivalent to that predicted by a single realization of its deterministic counterpart [Papoulis, 1968].

The present stochastic formalism inherits the diffraction capability embedded in the deterministic model (Chapter 3), and fully accounts for phase-coupling in laterally crossing wave trains and strong lateral diffractive effects in the half-plane without aperture limitation [e.g. Stamnes, 1986; Dalrymple & Kirby, 1988]. This is in marked contrast to conventional spectral models [Komen *et al.*, 1994; Booij *et al.*, 1999] where directional components are treated as statistically independent. Although phase-decoupled diffraction approximations have been implemented for such models [Holthuijsen *et al.*, 2003], the premise of statistical independence of directional components eradicates phase-coupling information between non-collinear components from the model and therewith its ability to accurately resolve wave height variations in heterogenous wave fields, such as those associated with the crossing wave trains in a refractive focus [see O'Reilly & Guza, 1991, who present a detailed comparison between refraction-diffraction and refraction approximation in focal regions]. The present formalism, with its inherent
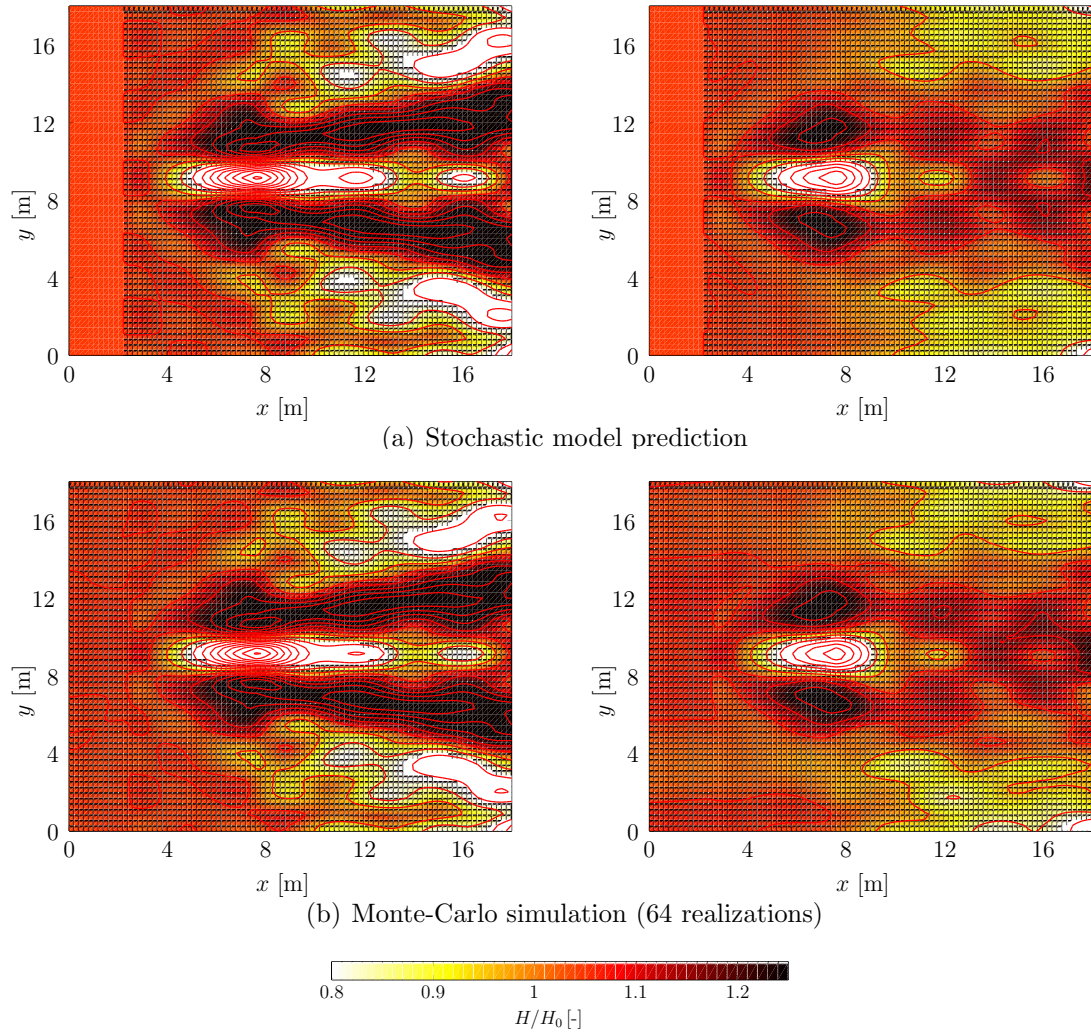
(a) Stochastic model prediction



(b) Monte-Carlo simulation (64 realizations)

**Figure 4.2:** Comparison of normalized wave heights ($H/H_0$, $H$ is zeroth-moment wave height) predicted by stochastic model (top panels) and Monte-Carlo simulation with deterministic model (bottom panels). Contours drawn at $\Delta H/H_0 = 0.1$. Left panels: narrow-aperture incident wave field ($\sigma_D = 0.05\,\text{rad}$). Right panels: wide-aperture incident wave field ($\sigma_D = 0.25\,\text{rad}$).

ability to account for strong diffraction and lateral heterogeneity, appears also well suited to model spectral evolution around breakwater tips and harbor entrances; an application hereof is presented and discussed in §5.5.
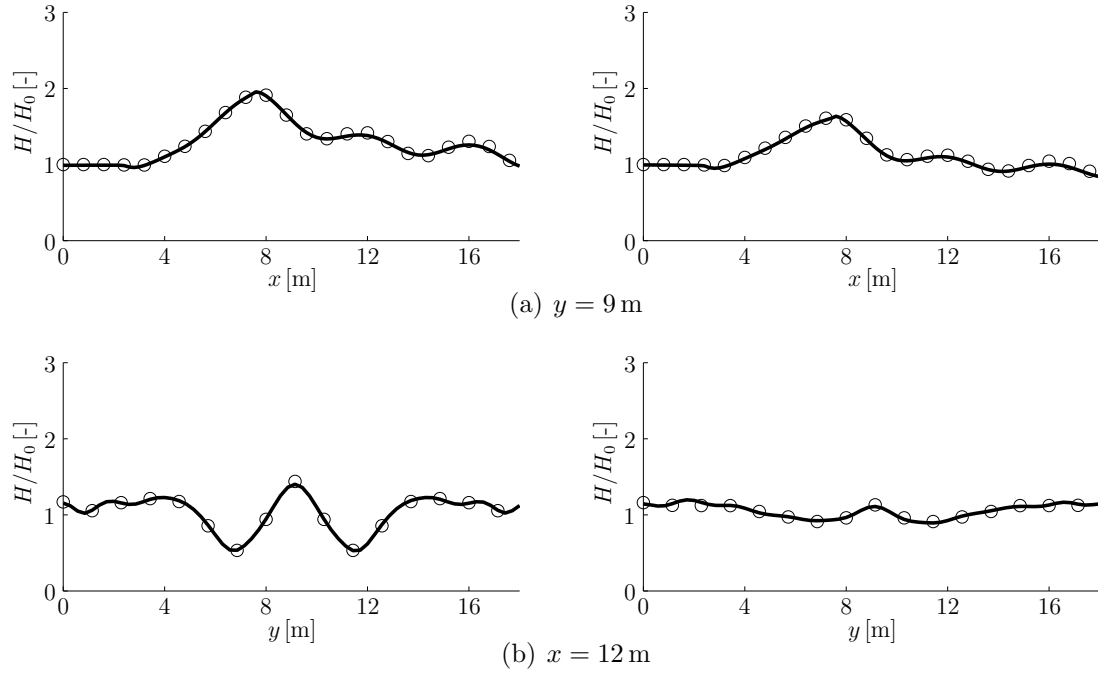
(a) $y = 9\,\mathrm{m}$

(b) $x = 12\,\mathrm{m}$

**Figure 4.3:** Comparison of normalized wave heights ($H/H_0$, $H$ is zeroth-moment wave height) along transects indicated in sub-captions for stochastic model (circles), and Monte-Carlo simulation (thick solid line). Left panels: narrow-aperture incident wave field ($\sigma_D = 0.05\,\mathrm{rad}$). Right panels: wide-aperture incident wave field ($\sigma_D = 0.25\,\mathrm{rad}$).

## 4.3 Parameterization depth-induced wave breaking

Of all the processes affecting waves propagating in the nearshore across a surf zone, the instability process, generally referred to as the 'breaking' of the wave, is cumulatively by far the most important, and at the same time probably least understood. The wide variety of appearances of breaking waves, from the gentle 'spilling' breaker on mildly sloping beaches to the violent 'shore-break' on steep slopes, and the sheer complexity involved in a detailed description of the transition from smooth-surfaced macro-scale motion to one that is increasingly chaotic and involves micro-scale turbulent motions [see e.g. Peregrine, 1983a], hampers a first-principle-based modeling on any operational scale. Instead, a parametrization of the processes, accounting for the macro-scale effects of the instability, is pursued.

Assuming all the waves above a certain height to be broken, Battjes & Janssen [1978] describe surf zone wave height statistics by a clipped Rayleigh-type distribution, from which the fraction of breaking waves is derived. Utilizing the analogy with dissipation in turbulent bores [e.g. Lamb, 1932, article 187], these authors estimate the bulk rate of energy dissipation per unit area for a random wave field, which is subsequently included as a sink term in the energy balance equation for shoaling waves. By considering the evolution of the wave field's energy, Battjes & Janssen [1978] account for the history of the shoaling process, thus relaxing an overly strong dependence on local bed variations as

inherently present in previous approaches [that consider the wave height as algebraically dependent on the local depth alone, see e.g. Battjes, 1972; Goda, 1975], and extending application to topography involving non-monotonically decreasing depth.

The model by Thornton & Guza [1983] follows much the same reasoning but instead of the clipped Rayleigh distribution, an empirically motivated distribution function for the heights of the broken waves is proposed. Their model is algebraically simpler, since it does not involve a transcendental equation for the portion of broken waves as in Battjes & Janssen [1978], but the distribution function is induced from observations and – in contrast to the Rayleigh distribution – lacks a theoretical basis. Baldock *et al.* [1998] (BHBW hereafter), motivated by empirical evidence that wave height statistics – even in the surf zone – are generally well described by a Rayleigh distribution [e.g. Thornton & Guza, 1983], propose a Rayleigh distribution for the wave heights in the surf zone, regardless whether they are smaller or larger than some breaker height, above which height we consider the wave broken. The resulting model is thus based on a well-established and theoretically founded distribution function, is supported by empirical evidence, and has the convenience of providing an explicit expression for the bulk dissipation rate. Here we derive a dissipation function following BHBW's approach, while correcting for an inconsistency in their derivation.

### 4.3.1 An alternative parameterization
Following the reasoning of BHBW we assume the probability of wave heights, regardless whether the waves are broken or unbroken, described by a single Rayleigh-type distribution, expressed as

$$p(H) = \frac{2H}{H_{\mathrm{rms}}^2} \exp\left[-\left(\frac{H}{H_{\mathrm{rms}}}\right)^2\right], \qquad (4.27)$$

where $H$ and $H_{\mathrm{rms}}$ represent the wave height and its root-mean-square value respectively. After Battjes & Janssen [1978], based on a bore analogy, the power dissipated per unit area in the breaking process for a wave of height $H$ is written as

$$\wp = \frac{B}{8\pi} \omega \rho g \frac{H^3}{h}, \qquad (4.28)$$

where $\omega$ is the angular frequency of the wave, $\rho$ represents the fluid density, and $B$ is a (tunable) parameter that controls the intensity of the dissipation. For application to random waves, the $\omega$ is replaced by a representative measure such as a mean or peak frequency [Battjes & Janssen, 1978; Battjes & Stive, 1985], denoted in the following by $\overline{\omega}$. The expected value of $\wp$ is obtained from $\langle\wp\rangle = \int_{H_b}^{\infty} \wp\, p\, dH$, where $H_b$ represents the wave height above which the waves are assumed to break. However, prior to taking the expected value of $\wp$, BHBW substitute $H^2$ for $H^3/h$, for which they seek justification in Battjes & Janssen [1978]. The result is an explicit expression for $\langle\wp\rangle$ reading

$$\langle\wp\rangle^{(\mathrm{BHBW})} = \frac{B}{8\pi}\overline{\omega}\rho g \int_{H_b}^{\infty} H^2 p(H)\, dH = \frac{B}{8\pi}\overline{\omega}\rho g H_{\mathrm{rms}}^2 \left(1 + H_r^2\right) \exp\left[-H_r^2\right], \qquad (4.29)$$

where $H_r = H_b/H_{rms}$. However, substituting $H^2$ for $H^3/h$ is inconsistent and no justification is given in Battjes & Janssen [1978]. Although these authors do assert $H_b^3/h \sim H_b^2$ (b in the subscript designating the height above which waves are assumed broken) as 'an order-of-magnitude relationship', which – in the deterministic context of determining the dissipation rate in a shallow-water wave of a given height – is entirely reasonable, a similar reasoning does not apply if $H$ is a stochastic variable, which is the case in Baldock *et al.* [1998]. In the latter case this substitution implies that $\langle H^3/h \rangle$ equals $\langle H^2 \rangle$, which is generally incorrect. Although algebraically convenient, this simplification is wholly unnecessary, and for our present purpose we thus derive the average power dissipated, $\langle \wp \rangle$, from

$$
\begin{aligned}
\langle \wp \rangle^{\text{(CRAD)}} &= \frac{B}{8\pi} \frac{\overline{\omega} \rho g}{h} \int_{H_b}^{\infty} H^3 p(H)\, dH \\
&= \frac{B}{8\pi} \frac{\overline{\omega} \rho g}{h} H_{rms}^3 \left[ \left( H_r^3 + \frac{3}{2} H_r \right) \exp\left[ -H_r^2 \right] + \frac{3}{4}\sqrt{\pi} \left( 1 - \text{erf}\left( H_r \right) \right) \right].
\end{aligned} \quad (4.30)
$$

The erf represents the error function, a contribution due to the odd power of the wave height in the dissipation function; for even powers no such contribution is present [as in BHBW]. In what follows, we refer to the present formulation as the Consistent Rayleigh Dissipation (CRAD) model. Collectively the CRAD and BHBW formulation constitute what we will refer to as Rayleigh-type dissipation models, reflecting the underlying premise of a Rayleigh distribution to describe the wave heights for all waves in the surf zone, irrespective of the fact that they are breaking or not. Note that for these formulations, the fraction of breaking waves, $Q$, is simply given as

$$
Q = \exp\left[ -\left( \frac{H_b}{H_{rms}} \right)^2 \right]. \quad (4.31)
$$

The average dissipation is then determined, apart from a value for $H_b$ and $B$. Unless explicitly stated otherwise we set $B = 1$ and obtain the ratio $\gamma = H_b/h$ from [Battjes & Stive, 1985]

$$
\gamma = \frac{H_b}{h} = 0.5 + 0.4 \tanh\left( 33 S_0 \right). \quad (4.32)
$$

Here $S_0$ denotes the offshore wave steepness, defined as $H_{rms}^d/L^d$, the superscript d indicating that the deep-water value is implied.

For saturated surf zone conditions ($H_{rms} = H_b$), the present formulation predicts a dissipation rate of around $3\gamma/2$ times the BHBW-predicted dissipation rate; for common $\gamma$ values (say $\gamma \sim 0.7$) predictions of dissipation rates are thus of comparable magnitude. However, on steep beaches – where the inner surf zone is generally over-saturated ($H_{rms} > H_b$) – there are differences. The CRAD model formulation consistently includes the dissipation due to the breaking of waves that are considerably higher than the saturation height, resulting in enhanced dissipation under such conditions; this effect is only partially accounted for in BHBW. Generally, over-saturated surf zone conditions

occur in the very nearshore (or on steep slopes) and it is illustrative to consider the shallow-water asymptote of the dissipation formulation. In order to relate this to the wave height evolution in the inner surf zone we consider the one-dimensional energy balance equation with the parameterization of dissipation due to depth-induced wave breaking included as a sink term

$$\frac{d}{dx}\left(\frac{1}{8}\overline{C}_g \rho g H_{\text{rms}}^2\right) = -\langle \wp \rangle. \tag{4.33}$$

Here $\overline{C}_g$ is the group speed corresponding to $\overline{\omega}$, in the linear approximation. For breaking waves on a plane slope in shallow water ($\overline{k}h \ll 1$) and over-saturated surf zone conditions ($H_r \ll 1$), the $H_{\text{rms}}$ evolution can be expressed analytically as

$$H_{\text{rms}} = H_{\text{rms},0}\left(\frac{h_0}{h}\right)^{1/4}\exp\left[-\frac{\overline{\omega}B}{\pi\sqrt{g}h_x}\left(\sqrt{h}-\sqrt{h_0}\right)\right] \qquad \text{(BHBW)} \tag{4.34}$$

for the BHBW dissipation formulation and

$$H_{\text{rms}} = h^{-1/4}\left[(h_0^{1/4}H_{\text{rms},0})^{-1}-\frac{\overline{\omega}B}{2\sqrt{g}\pi h_x}\left(h^{(-3/4)}-h_0^{(-3/4)}\right)\right]^{-1} \qquad \text{(CRAD)} \tag{4.35}$$

for the CRAD formulation proposed in the present work. Here the 0 as a subscript indicates the value at the offshore boundary and, in order for (4.34) & (4.35) to represent proper asymptotes of the wave evolution predicted by the more general eq. (4.33), this boundary needs to be chosen such that the premises for the analytical description (viz. $\overline{k}h \ll 1$ and $H_r \ll 1$) are warranted. From (4.34) & (4.35) we can observe that for an over-saturated inner surf zone the CRAD formulation (viz. (4.30)) predicts wave heights varying according to the proportionality $H_{\text{rms}} \sim h^{1/2}$, thus diminishing wave height as $h \to 0$. In marked contrast, the shallow-water asymptote of the BHBW shallow-water expression (viz. (4.34)) implies $H_{\text{rms}} \sim h^{-1/4}$, which is Green's shoaling law. This indicates that for the latter model, dissipation is insufficient to counter shoaling effects so that in the limit of shallow water, shoaling governs the wave height variations (Green's law). Clearly, this implies – as noted by Battjes & Janssen [1978] – a shoreline singularity reminiscent of the classical breakdown of conservative WKB theory. The normalized wave height and $Q$ evolution over a 1 : 10 slope predicted by eq. (4.33) is shown in Figure 4.4, along with the shallow-water asymptotes (4.34) & (4.35). It can be seen that in shallow water the predictions diverge, with the BHBW model predicting a wave height increasing with decreasing depth. In fact the shallow-water limit for over-saturated surf zone conditions for this model predicts increasing wave heights wherever

$$\frac{|dh/dx|}{\overline{\omega}}\sqrt{\frac{g}{h}} > 2\frac{B}{\pi}, \tag{4.36}$$

where the *LHS* is recognized as a normalized bed slope.

PSfrag replacements

$H_{\mathrm{rms}}/H_{\mathrm{rms},0}$ [-]

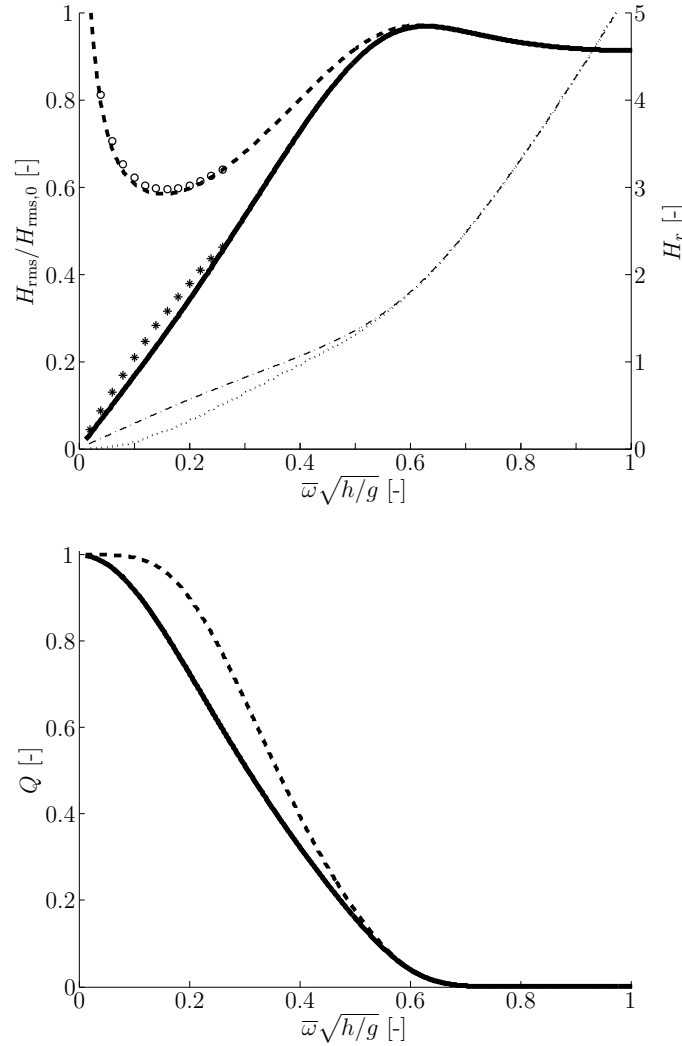$H_r$ [-]

1.2

1.4

0

1

2

3

4

5

1.2

1.4

**Figure 4.4:** Comparison of predicted wave height (top panel) and fraction of breaking waves $Q$ (bottom panel) by CRAD model (thick solid line) and BHBW formulation (thick dashed line) for waves with $H_{\mathrm{rms}}^{\mathrm{d}} = 1.0\,\mathrm{m}$, $\overline{\omega} = 0.4\pi\,\mathrm{rad/s}$ ($\gamma = 0.78$ from (4.32)) incident on a $1:10$ slope. Dash-dot and dotted line in top panel represent $H_r$ values for CRAD and BHBW model respectively (right axis). The circles (o) and asterices (*) denote the wave height predictions according to the asymptotes (4.34) & (4.35) respectively, initiated at $H_r = 0.75$.

Clearly, the argument can be made that this shallow-water limit is well outside the validity of the physical principles implied in the derivation of the dissipation model (among others: uni-directional, linear WKB-type wave propagation) in the first place, and therefore the unphysical behavior in that region certainly need not be disqualifying. However, no first-principle modeling of the surf zone physics is pursued. Instead we seek a *parameterization* of the nearshore wave height statistics, that predicts wave heights in agreement with what is invariably observed in reality. The occurrence of a nearshore singularity *is* disqualifying for such a parameterization and needs amelioration [see

Battjes & Janssen, 1978]. The fact that the present CRAD formulation is internally consistent *and* predicts a vanishing wave height in the very nearshore as $h \to 0$, makes it a suitable candidate for parameterization of the dissipation due to depth-induced breaking.

Although the models are quite disparate in the nearshore for steep beaches, for typical field conditions of waves incident on gently sloping sandy beaches, the differences are less conspicuous. In general, for such conditions, dissipation rates implied by the present Rayleigh formulations are similar to that predicted by the Battjes-Janssen model [not shown here, see Baldock *et al.*, 1998]. For instance, for waves impinging on a plane $1:20$ slope (left panels Figure 4.5) wave height and $Q$ variations are very similar throughout the surf zone except for the very nearshore, where the predictions diverge. For the $1:100$ slope, considered in the right panels of that figure, predictions are similar for the BHBW and CRAD model, throughout the surf zone and including the very nearshore.
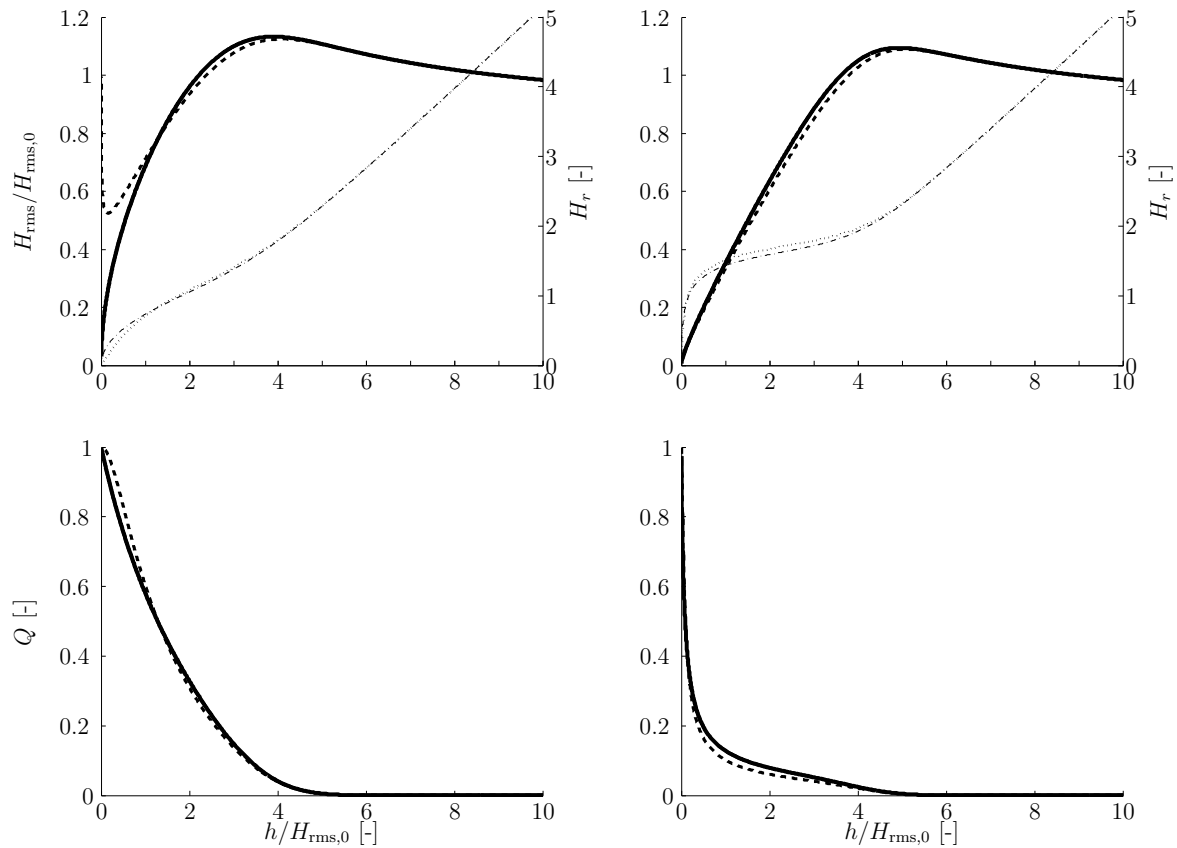


**Figure 4.5:** Comparison of predictions of wave height (top panels) and fraction of breaking waves $Q$ (bottom panels) by CRAD model (thick solid line) and BHBW formulation (thick dashed line) for waves with $H_{\mathrm{rms}}^{\mathrm{d}} = 1.0\,\mathrm{m}$, $\overline{\omega} = 0.2\pi\,\mathrm{rad/s}$ ($\gamma \approx 0.5$ from (4.32)) incident on a $1:20$ (left panels) and $1:100$ (right panels) slope. Dash-dot and dotted line in top panels represent $H_r$ values for CRAD and BHBW model respectively (right axis).

### 4.3.2 A quasi-homogeneous approximation

Although the analogy with dissipation in turbulent bores, combined with a reasonable assertion with respect to statistics of wave heights in the surf zone, provides a measure of bulk dissipation rate for random waves, it provides no information on how this dissipation is distributed across the spectrum; nor is it clear how such a spectral distribution can be deduced from physical principles. As a consequence the spectral distribution of dissipation due to depth-induced wave breaking is induced from observations.

Based on laboratory observations and simulations with a KdV-type model, Mase & Kirby [1992] suggested that the dissipation rate is proportional to the local energy density weighted by the square of the frequencies. In contrast, induced from observations by Battjes & Beji [1992] who compare spectral evolution for breaking and non-breaking waves, Eldeberky & Battjes [1996] propose a spectral distribution of the bulk dissipation proportional to the local spectral density. The finding that the dissipation in random waves exhibits a preference toward higher frequencies [Mase & Kirby, 1992] is further consolidated by empirical evidence reported by Chen *et al.* [1997]. These authors find that, although the frequency-weighting of the dissipation distribution does not greatly affect the spectral shape – a finding consistent with the inference by Eldeberky & Battjes [1996] – it does strongly affect the intricate balance between nonlinearity and dissipation in the shallow nearshore [see also Elgar *et al.*, 1997]. As a consequence, the non-uniform weighting of the dissipation across the spectrum is reflected in the higher-order bulk statistics such as skewness and asymmetry, which are generally in much better agreement with observations when frequency-squared weighting of the dissipation is applied [Chen *et al.*, 1997]. These findings are further substantiated by Herbers *et al.* [2000] who analyze observations along a closely spaced cross-shore array, relating the observed cross-shore energy flux gradient to the spectral redistribution due to nonlinear interactions (based on a Boussinesq model), which demonstrates the concomitant action of wave breaking and (conservative) nonlinear processes in the surf zone.

The remaining task is to relate the dissipation term $D_1(x, y)$ in (4.10) to the bulk average rate of energy dissipation $\langle \wp \rangle$. For a two-dimensional, heterogeneous wave field this is not trivial. Given the overall crudeness of the present representation of the dissipation processes, and the fact that directionality of the wave field is generally very limited in the surf zone [see e.g. Elgar *et al.*, 1993], we propose what is best referred to as a 'quasi-homogeneous' approximation. It consists of treating the 'local' spectra $\widehat{\mathcal{E}}(\omega_1, \lambda_1, x, y)$ (see §4.2) as mutually (laterally) independent, thus evolving them as

$$\frac{d\widehat{\mathcal{E}}_1^1}{dx} = -D_1(x, y)\widehat{\mathcal{E}}_1^1 + R.T. \tag{4.37}$$

essentially considering the wave field 'locally' as if it was laterally homogeneous. The *R.T.* symbolically denotes the remaining terms accounting for the quadratic nonlinearities (that are cumulatively conservative). We omit the interaction with the lateral depth variability here; as such, relating the $D_1$ to $\langle \wp \rangle$ through (4.37) ignores the (two-dimensional) divergence/convergence of the wave field. We stress that we solely make

this approximation to relate $D_1(y)$ to $\langle \wp \rangle$, whereas no such simplification is implied in the remaining model equations. For laterally homogeneous wave conditions (4.37) is not an approximation but is similar – in form – to the dissipation formulation in Herbers *et al.* [2003] (although the underlying models differ).

The dissipation factor $D_1$ is decomposed in a frequency weighted and a frequency-independent part

$$D_1(x,y) = \left( \sum_n \frac{r_n}{\widetilde{m}_n} |\omega_1|^n \right) D(x,y), \tag{4.38}$$

where the $r_n$ are positive fractions, included to keep the frequency weighting fairly general, provided that $\sum_n r_n = 1$; the $\widetilde{m}_n$ represent the spectral moments defined as

$$\widetilde{m}_n(x,y) = \iint |\omega_1|^n \widehat{\mathcal{E}}_1^1(x,y)\, d\lambda_1 d\omega_1. \tag{4.39}$$

The cross-shore gradient of the bulk energy flux is obtained by integrating (4.37) over all frequencies and alongshore wavenumbers, and multiplying the result by $\rho g$ which yields

$$\frac{d}{dx}\rho g \widetilde{m}_0 = -\rho g D = -\langle \wp \rangle. \tag{4.40}$$

Thus from the expression for the averaged bulk dissipation $\langle \wp \rangle$ (viz. (4.30)) we obtain

$$D = \frac{2B}{\pi}\frac{m_1}{h}\sqrt{2m_0}\left[ \left( H_r^3 + \frac{3}{2}H_r \right) \exp\left[ -H_r^2 \right] + \frac{3}{4}\sqrt{\pi}\left( 1 - \mathrm{erf}\left( H_r \right) \right) \right]. \tag{4.41}$$

Here we substituted $\overline{\omega} = m_1/m_0$ and $H_{\mathrm{rms}} = \sqrt{8m_0}$. The moments $m_n$ are given as

$$m_n(x,y) = \iint |\omega_1|^n \mathcal{S}_1^1(x,y)\, d\lambda_1 d\omega_1, \tag{4.42}$$

with $\mathcal{S}_1^1(x,y)$ the surface elevation variance density spectrum defined in §4.2. Upon back-substituting into (4.10), the evolution of the spectral density is described by

$$\left[ \frac{d}{dx} - i\Lambda_1^{1;2} \right] \mathcal{E}_1^{12} = -\frac{1}{4\pi}\iint dy d\lambda_3 \left( \sum_n \frac{r_n}{\widetilde{m}_n} |\omega_1|^n \right) D \sqrt{\frac{V_1^1}{V_1^3}} \left[ \sqrt{\frac{V_1^2}{V_1^1}} \mathcal{E}_1^{32} \exp\left[ i\left( \lambda_3 - \lambda_1 \right) y \right] \right.$$
$$\left. + \left( \mathcal{E}_1^{31} \right)^* \exp\left[ -i\left( \lambda_3 - \lambda_2 \right) y \right] \right] + R.T. \tag{4.43}$$

with $D$ given in (4.41). The dissipation terms in the bi-spectral evolution equation can likewise be written as

$$\left[\frac{d}{dx} - i\left(\Lambda_{12}^{12;3} + i\mu_{12}^{123}\right)\right]\mathcal{C}_{12}^{123}$$

$$= -\frac{1}{4\pi}\iint dy\,d\lambda_4\,D\left[\sqrt{\frac{V_1^1}{V_1^4}}\left(\sum_n \frac{r_n}{\widetilde{m}_n}|\omega_1|^n\right)\mathcal{C}_{12}^{423}\exp\left[i\left(\lambda_4 - \lambda_1\right)y\right]\right.$$

$$+\sqrt{\frac{V_2^2}{V_2^4}}\left(\sum_n \frac{r_n}{\widetilde{m}_n}|\omega_2|^n\right)\mathcal{C}_{12}^{143}\exp\left[i\left(\lambda_4 - \lambda_2\right)y\right]$$

$$\left.+\sqrt{\frac{V_{(1+2)}^3}{V_{(1+2)}^4}}\left(\sum_n \frac{r_n}{\widetilde{m}_n}|\omega_{(1+2)}|^n\right)\mathcal{C}_{12}^{124}\exp\left[-i\left(\lambda_4 - \lambda_3\right)y\right]\right] + R.T. \quad (4.44)$$

## 4.4 Cumulant-discard parameterization

For surface gravity waves in shallow water, the lack of frequency dispersion and the non-isolated occurrence of near-resonances, precludes a natural asymptotic stochastic closure. The stochastic description thus requires a suitable closure approximation, reminiscent of the closure problem in turbulence [Orszag, 1970; Lesieur, 1997; Salmon, 1998].

It is evidently impossible to model wave propagation with the full infinity of moment (or cumulant) equations, and at some order the cumulants need to be discarded or approximated in terms of the lower-order results. A common closure is the so-called quasi-normal (QN)[†] closure which essentially discards the fourth and higher cumulants. The wording *quasi*-normal indicates that the closure implies an inconsistent use of the assumption of normality (Gaussianity). After all, when we strictly adhere to the Gaussian assumption, the triple moment (or third cumulant) must also vanish, rendering the set closed but eradicating any form of nonlinear re-distribution of the energy in the system.

The neglect of the fourth and higher cumulants generally results in wave field statistics that are, somewhat counterintuitively, too far from Gaussian [Orszag, 1970], implying nonlinear couplings that are unrealistically strong. This results in overshoot behavior in regions of strong nonlinearity, in turn causing a rapid deterioration of the predictive capability of the model. To ameliorate the unsatisfactory performance of the QN closure in such regions we propose a relaxation term (§4.4.3) for the bi-spectral evolution equation, allowing a return to Gaussian statistics when the wave field encounters regions of enhanced nonlinearity. From the outset we emphasize that, although the general form of this relaxation is inspired by considerations of the relevant physics, the parameterization of the de-correlation effect is based on heuristic arguments. The relaxation allows the nonlinear couplings to develop locally, while attenuating the system's memory over long distances and in regions of strong nonlinearity, with the aim to prevent the breakdown of the QN approximation in shallow water (the surf zone). We first discuss the nature of the quasi-normal approximation, its idiosyncrasies and limitations, and outline some

---

[†]Also referred to as 'quasi-Gaussian' or 'cumulant-discard' closure for obvious reasons.

of the prevalent approaches in the literature to provide context and rationale for our modeling choices.

### 4.4.1 Quasi-normal closure and relaxation

To substantiate the discussion we will consider the one-dimensional 'prototype' set

$$\frac{dE_1}{dx} = -2 \sum_{p_2, p_3} \mathcal{W}_{23} \Im\{C_{23}\} \delta_{23;1}^{\omega}, \tag{4.45a}$$

$$\frac{dC_{12}}{dx} = i\Lambda_{12}C_{12} + 2i\mathrm{Q}_{12} + C_{12}^{(4)}, \tag{4.45b}$$

where the $E_1$ and the $C_{12}$ are the discrete spectrum and bi-spectrum defined as

$$E_1 = \langle |\widetilde{A}_1|^2 \rangle, \qquad\qquad C_{12} = \langle \widetilde{A}_1 \widetilde{A}_2 (\widetilde{A}_{(1+2)})^* \rangle, \tag{4.46}$$

and $\mathrm{Q}_{12} = E_{(1+2)}\left(\mathcal{W}_{(1+2)(-2)}E_2 + \mathcal{W}_{(1+2)(-1)}E_1\right) - \mathcal{W}_{12}E_1E_2$; the $C_{12}^{(4)}$ denotes the fourth cumulant contribution. For ease of discussion we restrict ourselves to unidirectional wave propagation and momentarily discard effects of dissipation; we consider discrete, rather than continuous, spectral variables to facilitate comparison to (discrete) expressions from the literature. The one-dimensional, discrete considerations with respect to the closure approximation are believed, mutatis mutandis, to apply to the more general description of the evolution of continuous spectral variables over two-dimensional topography.

We refer to (4.45) as a 'prototype' set since we will use it as a basis for discussing the closure approximations without giving too much thought about the details of the coefficients, which merely reflect the nature of the underlying deterministic model and are of little concern here. In fact, where we refer to approaches presented in the literature, we refer to the form of the solution, rather than the details of coefficients as they appear in the governing equations themselves, which may differ on account of the deterministic framework.

Formally, the 'closure' implies simply the act of replacing the (unknown) $C_{12}^{(4)}$, by a known value or variable, thus 'closing' the set. Closure by means of setting $C_{12}^{(4)} = 0$, generally referred to as the *quasi-normal* (QN) approximation, leaves the set (4.45) in the form of models by e.g. Herbers & Burton [1997]; Kofoed-Hanssen & Rasmussen [1998] and Eldeberky & Madsen [1999]. To illustrate the characteristics of this closure the spectral evolution implied in (4.45) with $C_{12}^{(4)} = 0$ is written as

$$\frac{dE_1}{dx} = -4 \sum_{p_2, p_3} \mathcal{W}_{23} \Re\{ \int_0^x \mathrm{Q}_{23}(x') \exp\left[ \int_{x'}^x i\Lambda_{23}\, dx'' \right] dx' \}. \tag{4.47}$$

The integral on the *RHS* of (4.47) can be viewed upon as a 'memory' integral through which past states of the spectrum affect its evolution. In the off-resonant case ($\Lambda \sim O(1)$), past states are unimportant due to the scrambling effect of the rapidly varying exponential function, inducing rapid loss of memory. However, if the system approaches
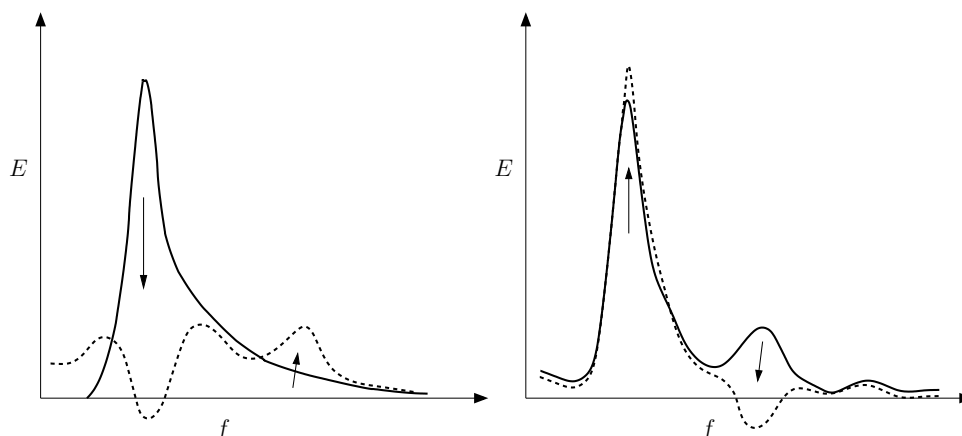
PSfrag replacements                                    PSfrag replacements

**Figure 4.6:** Sketch of slingshot effect. Solid line initial spectrum; dashed line, resulting spectrum with negative 'energies' due to exaggeration of nonlinear couplings. Left panel: anticipated spectral evolution on a beach. Right panel: anticipated spectral evolution of waves on the down-slope of a submerged obstacle.

resonance ($\Lambda \to 0$) the system's memory increases and initial tendencies tend to persist. The exaggeration of this persistence is an idiosyncrasy of the quasi-normal closure [see e.g. Orszag, 1970] and causes what is sometimes referred to as the 'slingshot effect' [Salmon, 1998]. Consider for instance a fairly narrow-band wave field incident onto a sloping beach. As the water depth decreases, nonlinear interactions are enhanced and at some point, for small $\Lambda$, the primary peak will start feeding energy to harmonic frequencies causing the main peak to decrease. The unrealistic persistence of this initial tendency can cause the main peak to plunge through zero, resulting in the occurrence of negative 'energy' (see left panel Figure 4.6). When traversing a submerged shoal similar effects can cause the spectrum at harmonic frequencies to plunge through zero on the down-slope where energy is fed back into the primary peak (right panel Figure 4.6). Although the occurrence of negative 'energies' violates the so-called realizability of the model and is clearly unphysical ($E_1 = \langle |\widetilde{A}_1|^2 \rangle$ is non-negative by definition), it need not disqualify the approach as a whole. After all, the QN model is an approximation. Would such negative energies exclusively occur in spectral regions with low energy levels, far away from the spectral regions of primary interest, the closure may have been tenable. However, this is not the case [e.g. Orszag, 1970]. In regions of strong nonlinearity the shortcomings of the QN closure generally result in a complete breakdown of the modeling capability through the exaggeration of nonlinear couplings (this will be substantiated in §4.4.3 and Chapter 5).

   In turbulence literature the poor behavior of QN closure, in particular for high Reynolds numbers where viscous damping is weak, has led to relaxation modifications – sometimes referred to as eddy-relaxation [Orszag, 1970] – that attenuate initial tendencies. Such relaxation, or damping terms, can be physically motivated on the grounds that by discarding the higher-order cumulants we are isolating the triple correlations

from their environment. The interaction with the background (eddies in turbulence) is represented, in the (un-closed) hierarchy, by the (omitted) higher-order cumulants, resulting in a loss of coherence for the triple moments and a relaxation toward a Gaussian state [Orszag, 1970]. The damping term thus represents a parameterization of this scrambling effect, which checks the triple moments.

Applying a similar reasoning to shallow-water waves, where the triple moments reside on a background of random, nonlinear waves, we tentatively write $C_{12}^{(4)} = -\mu_{12}C_{12}$, with $\mu_{12}$ positive and real, thus introducing a linear damping term to the *RHS* of the bi-spectral evolution equation (4.45b). For this closure the spectral evolution reads

$$\frac{dE_1}{dx} = -4 \sum_{p_2,p_3} \mathcal{W}_{23} \Re\{ \int_0^x Q_{23}(x') \exp\left[ \int_{x'}^x (i\Lambda_{23} - \mu_{23}) \ dx'' \right] dx' \}. \qquad (4.48)$$

We anticipate that $\mu_{23}$ is very small compared to $\Lambda_{23}$ in off-resonant regimes ($\Lambda_{23} \sim 0(1)$), while increasing if the interaction approaches resonance ($\Lambda_{23} \to 0$). Thus if resonance is approached ($\Lambda_{23} \to 0$), the real and positive $\mu_{23}$ attenuates the effect of past states on the local evolution, thus suppressing the slingshot effect illustrated in Figure 4.6. In the modified closure hypothesis by Herbers *et al.* [2003] $\mu_{23}$ is governed by the intensity of dissipation due to depth-induced wave breaking. The use of the attendant dissipation as an (indirect) measure for the strength of nonlinear couplings appears quite suitable for fairly monotonic, natural sandy beaches where strong nonlinearity usually coincides with intense dissipation (surf zone); this is substantiated in Herbers *et al.* [2003]. However, for waves propagating in relatively shallow water over a (near–)uniform bottom, strong nonlinear coupling may occur in absence of dissipation; for such a case, energy loss due to wave breaking is not a suitable measure of the length scale that governs the stochastic relaxation. An alternative approach is considered in §4.4.3.

### 4.4.2 Markovian approximation

On the premise that $\mu_{23}$ is sufficiently large, so that only very recent states contribute to the integral on the *RHS* of (4.48) and assuming, which is not without controversy – alike in turbulence and shallow-water waves – that over such recent states the $Q_{23}$ are approximately invariant, the latter can be taken from under the integral as in

$$\frac{dE_1}{dx} = -4 \sum_{p_2,p_3} \mathcal{W}_{23} Q_{23}(x) \Re\{ \int_0^x \exp\left[ \int_{x'}^x (i\Lambda_{23} - \mu_{23}) \ dx'' \right] dx' \} \qquad (4.49)$$

which, borrowing semantics from turbulence, is a so-called *Markovian* form, indicating that the wave field's future states depend only on the present, not its past states [Salmon, 1998].

In the surface gravity wave context, Markov-type forms were pursued by e.g. Elde-berky [1996], Eldeberky *et al.* [1996] and Becq *et al.* [1998]. Their approaches follow a suggestion by Holloway [1979] who, in the context of mixed RI-turbulence[†] closure

---

[†]RI stands for Resonant Interaction, see pp. 76 for definition.

for Rossby waves, proposed a modification of the RI-closure to account for frequency uncertainty, originating from the presence of the background wave field. In line with the RI closure formalism, these shallow-water wave models consider the *asymptotic* response of the modified closure by evaluating the integral over the exponential function in (4.49) for large $x$ yielding approximately

$$\frac{dE_1}{dx} \approx \lim_{x \to \infty} -4 \sum_{p_2,p_3} \mathcal{W}_{23} Q_{23}(x) \Re\{ \int_0^x \exp\left[ \int_{x'}^x (i\Lambda_{23} - \mu_{23})\ dx'' \right] dx' \}$$

$$\approx -4 \sum_{p_2,p_3} \mathcal{W}_{23} Q_{23}(x) \left[ \frac{\mu_{23}}{\Lambda_{23}^2 + \mu_{23}^2} \right], \quad (4.50)$$

where $\mu_{23}$ is assumed a tuneable (and – unfortunately – dimensional) constant [Eldeberky, 1996; Eldeberky *et al.*, 1996; Becq *et al.*, 1998]. From a numerical point of view, the form eq. (4.50) is much preferred over e.g. (4.48) since it requires only a single integration and, moreover, the grid size restrictions can be relaxed since the resonance mismatch ($\Lambda_{12}$) need not be resolved. However, the closure assumes separable length scales for the evolution of the wave energy terms in $Q_{23}$ and the wavenumber mismatch $\Lambda_{23}$, which – although a proper deep-water closure assumption [see e.g. Benney & Saffman, 1966] – is not valid in shallow water. As the water depth decreases, and the interactions approach resonance, substantial energy exchanges can occur over a single recurrence length, such that the $Q_{23}$ and $\Lambda_{23}$ must necessarily vary on the same length scale, i.e. there appears no justification for the asymptotic treatment of the integral [e.g. Bryant, 1973; Elgar *et al.*, 1990].

The Markovian form pursued by Agnon & Sheremet [1997] is distinct in that they do not invoke the asymptotic limit as in (4.50). However, they also do not introduce any form of relaxation (viz. $\mu_{12} = 0$), and instead simply *postulate* the slow variation of $Q_{12}$ relative to the phase variations on account of the resonance mismatch $\Lambda_{12}$. On the basis of that assumption the governing equation (4.48) can be reduced to

$$\frac{dE_1}{dx} = -4 \sum_{p_2,p_3} \mathcal{W}_{23} Q_{23}(x) \Re\{\mathcal{P}_{12}\}, \quad (4.51)$$

where

$$\mathcal{P}_{12} = \int_0^x \exp\left[ \int_{x'}^x i\Lambda_{12}\, dx'' \right] dx'. \quad (4.52)$$

The integral representation of (4.52) can equivalently be written in differential form

$$\frac{d\mathcal{P}_{12}}{dx} = i\Lambda_{12}\mathcal{P}_{12} + 1. \quad (4.53)$$

The set (4.51) and (4.53) represents a one-way coupled set. Although (4.51) involves $\mathcal{P}_{12}$, the eq. (4.53) can be solved independent from (4.51). This partial decoupling is on account of the Markovanization. From a numerical point of view, the set (4.51) & (4.53)

is very similar to the original set (4.45). The decoupling of eq. (4.53) can be advantageous if e.g. the model is applied on a given domain multiple times with varying incident wave fields, in which case $\mathcal{P}_{12}$ needs only be computed once. Although Agnon & Sheremet [1997] suggest that this modeling approach also eases grid restrictions, this is unlikely. After all, the evolution of $\mathcal{P}_{12}$ is typified by the same rapid oscillations due to resonance mismatch as the bi-spectral equation and therefore similar grid size restrictions must be anticipated.

Arguably, $\mathcal{P}_{12}$ can be initialized as $\mathcal{P}_{12} = i/\Lambda_{12}$ which, for a horizontal bottom, will result in $d_x\mathcal{P}_{12} = 0$ and – on account of the $\mathcal{P}_{12}$ being imaginary – no spectral energy transfers occur; consequently, grid restrictions are practically absent. However, this is a special (and trivial) case. Moreover, this trivial case can likewise be modeled with the set (4.45) (for $C_{12}^{(4)} = 0$) by simply initializing $C_{12} = -2Q_{12}/\Lambda_{12}$. These initializations are entirely equivalent and correspond to second-order Stokes theory, implying symmetrical, skewed wave profiles of permanent shape and interactions in quadrature (no energy transfers). In general however, these are merely initial conditions; over variable depth the interactions will be forced away from exact quadrature, which induces – for interactions far from resonance – rapid oscillations that reflect the mixed free/bound wave character of the wave field, and restrict grid sizes (see also discussion in §5.5).

The assumed slow variation of $Q_{23}$ with respect to the exponential function is reasonable where the interactions are off-resonant but cannot be expected to hold in regions where quadratic interactions are nearly secular, in which case the anticipated separation of scales is not tenable; a limitation also noted by Agnon & Sheremet. This is unfortunate for two reasons. Firstly, it excludes the dynamically most interesting region, where these interactions result in leading-order cross-spectral energy transfers over relatively short distances. Secondly, it contradicts the basic premise in the derivation of the underlying deterministic model, namely the assumption that the quadratic interactions are in fact close to resonance. This Markovian approach is further expanded upon in Agnon & Sheremet [2000], but without altering the fundamental approach outlined here.

It is noteworthy that the Markovian approaches do not suffer from what we described as the 'slingshot' effect. In fact, by definition, the Markovian closure completely rids the system of its dependency on past states. Although it is clear that the QN closure exaggerates the persistence of initial tendencies, it is questionable whether a complete memory loss at each integration step, for which there appears no theoretical justification, provides a better description of the ensuing physics.

### 4.4.3 A cumulant-relaxation parameterization

The propagation of surface gravity waves across a surf zone is generally typified by strong dissipation on account of depth-induced wave breaking, and enhanced nonlinear effects (high Ursell numbers). Modeling capability in this region thus particularly depends on both the robustness of the breaking parameterization, and the stochastic closure. The most commonly applied closure approximation is the QN closure, which

– unfortunately – has proven unreliable at Ursell numbers typically encountered close to and inside the surf zone. Herbers *et al.* [2003] propose a modified closure with a dissipation-controlled de-correlating mechanism to check the triple-correlations, and enforce a return to Gaussian statistics. To account for nonlinear surf-zone dynamics and provide statistical relaxation even when breaking is absent but nonlinearity is strong, we propose a similar damping term that is controlled by the strength of both the nonlinear coupling and the dissipation.

For ease of presentation we present the closure modification in the context of a one-dimensional stochastic model. The same reasoning is then applied to the more general laterally heterogeneous case, for which the results are given later.

The one-dimensional (in frequency space) reduction of the set (4.10) and (4.13) reads

$$\frac{d\mathcal{E}_1}{dx} = -D_1\mathcal{E}_1 - 2\int \mathcal{W}_{(1-2)2}\Im\{\mathcal{C}_{(1-2)2}\}\,d\omega_2, \tag{4.54a}$$

$$\frac{d\mathcal{C}_{12}}{dx} = -\frac{1}{2}\left(D_1 + D_2 + D_{(1+2)}\right)\mathcal{C}_{12} + i\left(\Lambda_{12} + i\mu_{12}\right)\mathcal{C}_{12} + 2i\mathcal{Q}_{12}, \tag{4.54b}$$

where $\mathcal{Q}_{12} = \mathcal{E}_{(1+2)}\left(\mathcal{W}_{(1+2)(-2)}\mathcal{E}_2 + \mathcal{W}_{(1+2)(-1)}\mathcal{E}_1\right) - \mathcal{W}_{12}\mathcal{E}_1\mathcal{E}_2$. For the linear damping term $\mu_{12}$ we propose

$$\mu_{12} = \beta\left[\frac{|\mathcal{N}_1^{(\mathrm{D})} + \mathcal{N}_2^{(\mathrm{D})} + \mathcal{N}_{(1+2)}^{(\mathrm{D})}| + |\mathcal{N}_1^{(\mathrm{NL})} + \mathcal{N}_2^{(\mathrm{NL})} + \mathcal{N}_{(1+2)}^{(\mathrm{NL})}|}{\mathcal{E}_1 + \mathcal{E}_2 + \mathcal{E}_{(1+2)}}\right] \tag{4.55}$$

with $\beta$ a tuneable non-dimensional constant, anticipated real and positive. The

$$\mathcal{N}_i^{(\mathrm{D})} = -D_i\mathcal{E}_i, \qquad\qquad \mathcal{N}_i^{(\mathrm{NL})} = -2\int \mathcal{W}_{(i-j)j}\Im\{\mathcal{C}_{(i-j)j}\}\,d\omega_j, \tag{4.56}$$

and represent the net energy loss rates of component $i$ resulting from dissipation and nonlinear interactions respectively. The relaxation term in (4.55) is of a composite nature. It measures the strength of the random-wave background through the non-linearly driven net flux of energy across a triad, and losses through dissipation. With respect to the former, if the background wave field is sufficiently weak then a triad can in fact be considered in isolation from it (as implied by the QN closure), and the $|\mathcal{N}_1^{(\mathrm{NL})} + \mathcal{N}_2^{(\mathrm{NL})} + \mathcal{N}_{(1+2)}^{(\mathrm{NL})}|$ is very small. However, in shallow water, where the quadratic interactions approach resonance and strong nonlinear transfers occur, generally $|\mathcal{N}_1^{(\mathrm{NL})} + \mathcal{N}_2^{(\mathrm{NL})} + \mathcal{N}_{(1+2)}^{(\mathrm{NL})}|$ increases, i.e. there is a net gain/loss of energy over the triad (although cumulatively over the spectrum energy is still conserved). Through $\mu_{12}$ this then provides a means to check triple correlations and enforce a return to Gaussianity.

Whereas the nonlinearly-driven part of the relaxation is motivated by the truncation of the hierarchy of moment-equations, the dissipative contribution to the statistical relaxation is based on the notion that the breaking-associated increase of chaos in the fluid mass provides a background of turbulent eddies; the anticipated de-correlation

effect of this chaotic background on the wave field is parameterized by weighting cumulative energy losses over the triad. The latter contribution is thus external to the inviscid theory on which the model is based and results from heuristic, macro-scale considerations of the ensuing physical phenomena anticipated in breaking waves.

The relaxation is normalized by the total density content in the triad. This in effect implies that, if $\beta \sim O(1)$, the length scale on which relaxation takes place is of the same order as the length scale over which the triad exchanges energy with its environment, either through the interaction with the random background field or through losses to wave breaking.

The complex interaction with a random background – which is lacking in the model due to the truncation of the hierarchy – is thus modeled through a heuristic damping term. In what follows we refer to this closure approximation ($\beta > 0$) as the Relaxed Quasi-Normal (RQN) closure.

In order to asses the effect of the proposed stochastic closure modification we compare the QN and RQN model to Monte-Carlo (MC) simulations of the underlying deterministic model over long evolution distances ($O(100)$ peak wavelengths). In this comparison the effects of dissipation are momentarily omitted since the anticipated turbulent background in the surf zone is external to the inviscid deterministic theory considered here. The MC simulation serves as a benchmark, with – for sufficiently large ensembles – a 'perfect' closure implying convergence of the stochastic model-predicted wave field statistics to the MC predictions.

Stochastic simulations are performed with the set (4.54), with $\beta = 0$ (QN) and $\beta = 1.5$ (RQN) respectively. The Monte-Carlo simulations are performed with the one-dimensional version of (4.7), viz.

$$\frac{d}{dx}\widetilde{A}_1^1 = i\varkappa_1^1 \widetilde{A}_1^1 + i\sum_{\boldsymbol{v}_2} \mathcal{W}_{(1-2)2}\widetilde{A}_{(1-2)}\widetilde{A}_2. \tag{4.57}$$

The (double-sided) variance spectrum at $x = 0$ for positive frequencies is given by

$$\mathcal{S}(\omega, x = 0) = \frac{H_{\mathrm{m0}}^2}{32\sigma\sqrt{2\pi}} \exp\left[-\frac{(\omega - \omega_p)^2}{2\sigma^2}\right], \tag{4.58}$$

with $\sigma = \sqrt{0.2}\,\mathrm{rad/s}$. The initial flux spectrum is $\mathcal{E}(\omega) = C_g(\omega)\mathcal{S}(\omega)$, which is discretized into 64 equidistant, positive frequencies with $\Delta\omega = 0.05\pi$ rad/s; the bi-spectrum is initialized with $\mathcal{C}_{12} = 0$. The Monte-Carlo ensemble consists of 128 realizations initialized with phases selected from a uniform distribution and appropriate Rayleigh-distributed amplitudes [see Tucker et al., 1984].

We consider three cases. Two cases involve waves over uniform depth with $k_p h = 0.3$ ($k_p$ being the peak wavenumber), with incident wave heights $H_{m0} = 0.25\,\mathrm{cm}$ and $H_{m0} = 1.25\,\mathrm{cm}$, and corresponding Stokes numbers (defined here as $H_{m0}/(2k_p^2 h^3)$) 0.15 and 0.75 respectively. Additionally we consider a case involving waves traversing a submerged bar as sketched in Figure 4.7, with the depth varying from 0.7 m ($k_p h = 0.84$)

in the deep part of the profile to $0.1\,\mathrm{m}$ ($k_p h = 0.3$) over the bar. With incident wave height $H_{m0} = 0.63\,\mathrm{cm}$, the Stokes number varies approximately from 0.006 at $x = 0$ to 0.54 over the bar.
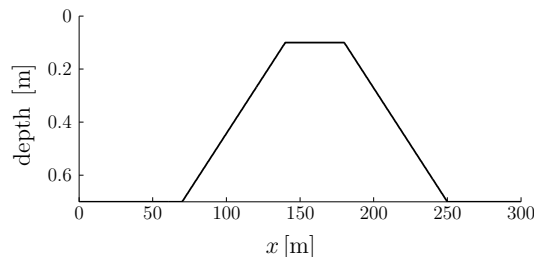


**Figure 4.7:** Submerged bar profile used in numerical bar-experiment. Depth away from bar is $0.7\,\mathrm{m}$, whereas over the top of the bar it measures $0.1\,\mathrm{m}$. The up-slope starts at $x = 70\,\mathrm{m}$ ending at $x = 140\,\mathrm{m}$; the down-slope starts at $x = 180\,\mathrm{m}$ and extends to $x = 250\,\mathrm{m}$.

The MC simulations of the uniform-depth cases, show rapid initial amplification of harmonics (Figure 4.8). For the lower-Stokes-number case (left panel) harmonic peaks are sustained over the distances considered here, whereas the stronger nonlinear case (center panels) exhibits a rapid evolution toward a near-featureless spectral shape. For the case involving the submerged bar, MC-predicted spectra show harmonic amplification on the up-slope, strong nonlinear evolution over the bar, and a partial feedback of energy to the primary peak on the down-slope and region behind the bar.

In general, the QN model tends to over-predict nonlinear coupling strength and associated energy transfers, resulting in quite erratic spectral shapes, in particular in the harmonic ranges, which become highly irregular and at considerable variance with the – much smoother – MC predictions. This loss of agreement is aggravated with increasing nonlinearity as seen from the higher-nonlinear, uniform-depth case, and the submerged bar case (where the nonlinear couplings are enhanced in the shallow area). In contrast, the RQN model predicts much smoother spectra, generally in much better agreement with the MC predictions; however, nonlinear couplings appear underestimated (over-damping) such that feedback of energy at higher harmonics to the primary peak is hampered; this is particularly noted behind the submerged bar, where energy levels at harmonic ranges are overestimated by the RQN model; also, with the added damping of triad coupling in the RQN model, the drop-off of the high-frequency tail toward higher frequencies is systematically less than found from the Monte-Carlo predictions.

In Figure 4.9 we compare – for each of the cases considered – the model-predicted third-order bulk statistics of skewness and asymmetry defined as [see e.g. Elgar & Guza, 1985]

$$\text{Skewness} = \frac{6 \iint_0^\infty d\omega_1 d\omega_2 \, \Re\{\mathcal{B}(\omega_1, \omega_2)\}}{\left(\int_{-\infty}^\infty \mathcal{S}(\omega)\, d\omega\right)^{3/2}} \tag{4.59}$$

and

(a) $x = 10\,\mathrm{m}$

(b) $x = 140\,\mathrm{m}$

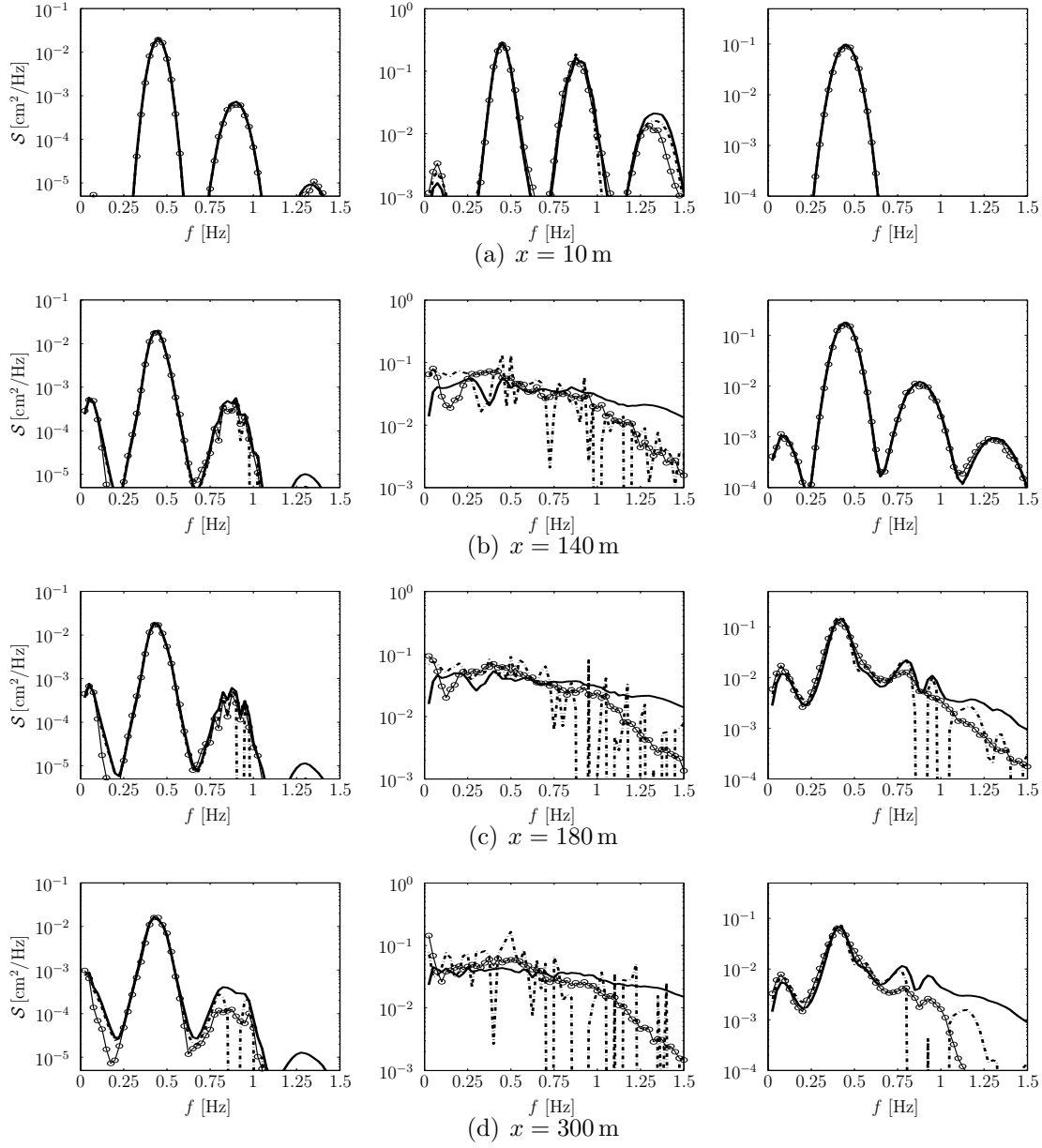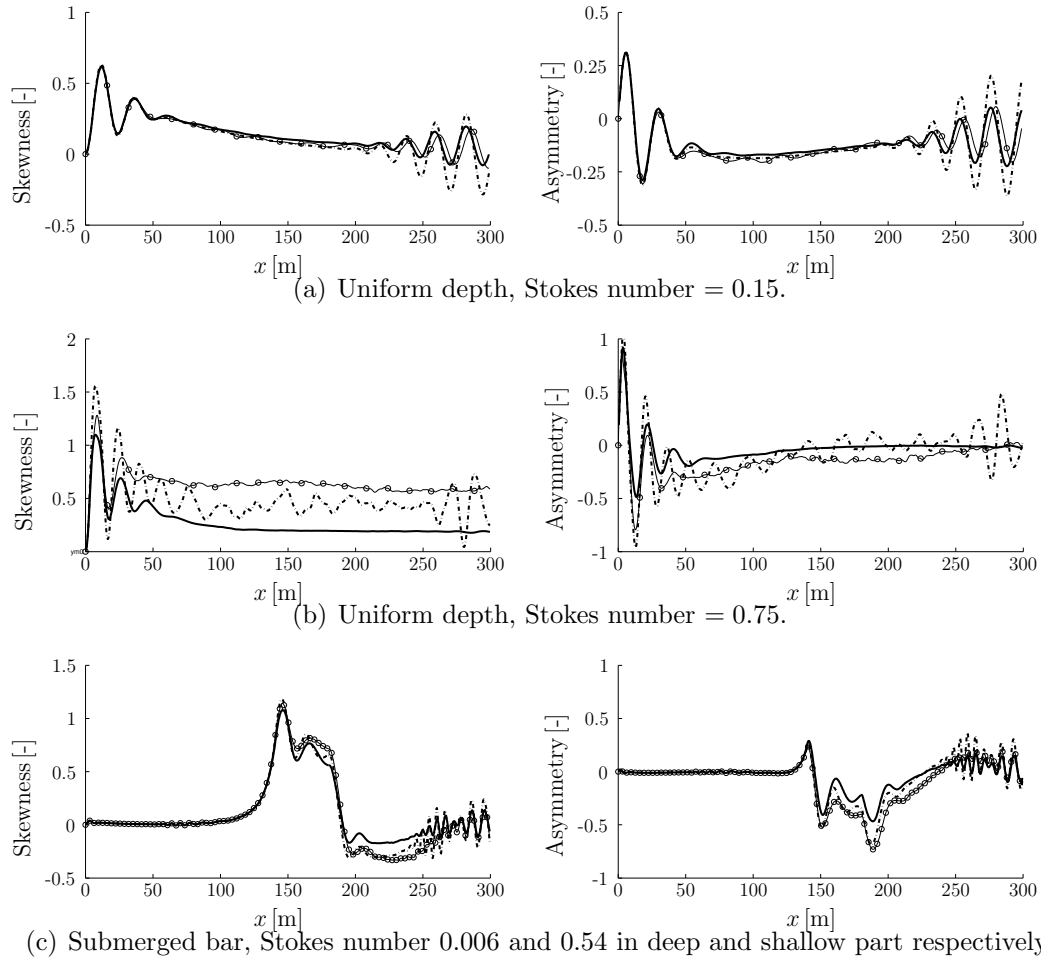(c) $x = 180\,\mathrm{m}$

(d) $x = 300\,\mathrm{m}$

**Figure 4.8:** Comparison of predictions of spectral evolution over long evolution distances for Monte-Carlo simulation (circles), quasi-normal (QN) closure (dash-dot line, $\beta = 0$) and relaxed quasi-normal (RQN) closure (solid line, $\beta = 1.5$). The spectra, $\mathcal{S}$, are given at discrete locations indicated in the sub-captions. Left panels: uniform depth, $k_p h = 0.3$ (Stokes number 0.15). Middle panels: uniform depth, $k_p h = 0.3$ (Stokes number 0.75). Right panels: submerged bar bottom profile $k_p h|_{\mathrm{deep}} = 0.84$, $k_p h|_{\mathrm{shallow}} = 0.36$ (Stokes number 0.006 and 0.54 in deep and shallow part respectively).

$$\mathrm{Asymmetry} = \frac{6 \iint_0^\infty d\omega_1 d\omega_2 \,\Im\{\mathcal{B}(\omega_1, \omega_2)\}}{\left(\int_{-\infty}^\infty \mathcal{S}(\omega)\, d\omega\right)^{3/2}}, \tag{4.60}$$

(a) Uniform depth, Stokes number = 0.15.

(b) Uniform depth, Stokes number = 0.75.

(c) Submerged bar, Stokes number 0.006 and 0.54 in deep and shallow part respectively.

**Figure 4.9:** Comparison of predictions of skewness and asymmetry over long evolution distances for Monte-Carlo simulation (circles), quasi-normal (QN) closure (dash-dot line, $\beta = 0$) and relaxed quasi-normal (RQN) closure (solid line, $\beta = 1.5$). Top and middle panels: uniform depth. Bottom panels: submerged bar profile.

where $\mathcal{B}(\omega_1, \omega_2) = \mathcal{C}(\omega_1, \omega_2)/\sqrt{C_{g,1} C_{g,2} C_{g,(1+2)}}$. These third-order bulk quantities measure 'peakedness' and 'pitching forward/backward' of the waves respectively.

The MC, QN and RQN models predict quite similar evolution of the third-order bulk statistics in weakly nonlinear waves (Figure 4.9, top panels), although over long distances, spatial variations in the QN predictions are somewhat stronger than the MC and RQN model. In the presence of stronger nonlinearity, the damping in the RQN model causes the model-predicted asymmetry to reduce to zero faster than predicted by the MC model, and converge to a skewness that is lower than the MC-predicted values.

In the present simulations we have chosen $\beta = 1.5$ (on the basis of a few trial runs) such that the development of the highly irregular spectral shapes as seen in the QN model predictions are suppressed. Larger $\beta$-values result in a more rapid damping, a smaller steady-state skewness and a further reduction of nonlinear feedback.

The present closure modification thus allows the stochastic model to smoothly traverse regions of strong nonlinearity without the unrealistic strong cross-spectral energy transfers as present in the QN model. The damping in the RQN model appears exaggerated in these idealized tests; although over short distances the evolution of the third-order statistics is in fair agreement with the MC predictions, over long distances it results in underestimation of skewness values. Further verification of the closure approximation over variable depth and for less idealized conditions, by means of comparison to observational data, is considered in Chapter 5.

Although for the sake of clarity the discussion so far was limited to unidirectional wave propagation, the same reasoning can be extended to the more general case of directional wave propagation over cylindrical beaches and over laterally heterogeneous topography. For the latter case, the proposed relaxation term reads

$$\mu_{12}^{123} = \beta \left[ \frac{|\mathcal{N}_1^{11,(D)} + \mathcal{N}_2^{22,(D)} + \mathcal{N}_{(1+2)}^{33,(D)}| + |\mathcal{N}_1^{11,(NL)} + \mathcal{N}_2^{22,(NL)} + \mathcal{N}_{(1+2)}^{33,(NL)}|}{\mathcal{E}_1^{11} + \mathcal{E}_2^{22} + \mathcal{E}_{(1+2)}^{33}} \right], \quad (4.61)$$

with

$$\mathcal{N}_i^{jj,(D)} = -\frac{1}{2\pi} \iint dy \, d\lambda_n \, D_i \sqrt{\frac{V_i^j}{V_i^n}} \Re\{\, \mathcal{E}_i^{nj} \exp\left[i\left(\lambda_n - \lambda_j\right) y\right] \},$$

$$\mathcal{N}_i^{jj,(NL)} = -2 \iint d\lambda_n \, d\omega_m \, \mathcal{W}_{(i-m)m}^{(j-n)n} \Im\{\, \mathcal{C}_{(i-m)m}^{(j-n)nj} \}, \quad (4.62)$$

and $\beta$, as before, a (dimensionless) tuning constant.

The stochastic model equations derived in §4.1, augmented with the expressions for dissipation due to depth-induced wave breaking presented in §4.3 and the cumulant-relaxation closure modification discussed here, present a closed set of evolution equations for the propagation of random wave fields over topography, including the surf zone. The robustness and limitations of the present model are assessed through comparison to observational data in Chapter 5.

# Random waves over topography: empirical verification **5**

In Chapter 4 a set of stochastic evolution equations is derived (§4.1), suitable for prediction of the evolution of the statistics of random, directionally spread wave fields propagating over topography. These equations account for quadratic (triadic) nonlinearities and, through parameterization of the effects of depth-induced wave breaking (§4.3) and a heuristic relaxation of the quasi-normal closure (§4.4), are made suitable for shallow, dissipative regions, such as the surf zone. In the present chapter these formulations are verified through the comparison of model predictions to both laboratory and field observations.

The evolution of unidirectional waves over variable depth, including localized nonlinearity enhancement and dissipation, is considered in §5.2. Directionally spread, random waves over two-dimensional topography are modeled in §5.3, and comparison is made to laboratory observations. The latter observations encompass (very) weakly nonlinear wave fields and the comparison mostly assesses the two-dimensional capability of the model and its inherent limitations. Lastly, the model is compared to observations of directional waves incident on a natural beach with nearly shore-parallel depth contours, at Duck (NC) (§5.4). Comparison is made to observations from two campaigns (fall of 1994 and of 1997), with incident wave conditions ranging from low-energetic, narrow-band swell to strongly dissipative conditions with wide-aperture wave incidence. Detailed comparison is made to spectra and bulk statistics derived from measurements across the beach. Through comparison of predictions to observations for a wide range of wave conditions, we assess the model's robustness and its potential for application to the scale of a typical coastal zone or inner shelf, including the surf zone.

The observations are compared to numerical implementations of reduced forms of the general equations presented in Chapter 4. These comparisons provide insight in the model performance for a wide range of scales and conditions, and verifies its robustness and suitability for application in typical coastal areas. Details of the numerical implementation are given in the following.

## 5.1 Numerical implementation and initialization

Numerical simulations are performed with implementations of the nonlinear stochastic angular-spectrum model derived in Chapter 4. The model equations for directional waves over topography (see §5.3) on a finite domain in space and time are

$$
\left[\frac{d}{dx} - i\Lambda_1^{1;2}\right]\mathcal{E}_1^{12} = \frac{1}{L_y}\int\,dy\sum_{\lambda_3}\left[\frac{S_1^1(y)}{\sqrt{V_1^3}}\mathcal{E}_1^{32}\exp\left[i\left(\lambda_3 - \lambda_1\right)y\right]\right.
$$

$$
\left.+ \left(\frac{S_1^2(y)}{\sqrt{V_1^3}}\mathcal{E}_1^{31}\right)^*\exp\left[-i\left(\lambda_3 - \lambda_2\right)y\right]\right]
$$

$$
- \frac{1}{2L_y}\int\,dy\sum_{\lambda_3}D_1\sqrt{\frac{V_1^1}{V_1^3}}\left[\sqrt{\frac{V_1^2}{V_1^1}}\mathcal{E}_1^{32}\exp\left[i\left(\lambda_3 - \lambda_1\right)y\right] + \left(\mathcal{E}_1^{31}\right)^*\exp\left[-i\left(\lambda_3 - \lambda_2\right)y\right]\right]
$$

$$
+ i\sum_{\boldsymbol{v}_3}\left[\mathcal{W}_{(1-3)3}^{(1-3)3}\mathcal{C}_{(1-3)3}^{(1-3)32} - \mathcal{W}_{(1-3)3}^{(2-3)3}\left(\mathcal{C}_{(1-3)3}^{(2-3)31}\right)^*\right]\Delta\omega\Delta\lambda,
$$

$$
(5.1a)
$$

$$
\left[\frac{d}{dx} - i\left(\Lambda_{12}^{12;3} + i\mu_{12}^{123}\right)\right]\mathcal{C}_{12}^{123} = \left[\frac{\overline{S}_1^1}{\sqrt{V_1^1}} + \frac{\overline{S}_2^2}{\sqrt{V_2^2}} + \frac{\overline{S}_{(1+2)}^{3*}}{\sqrt{V_{(1+2)}^3}}\right]\mathcal{C}_{12}^{123}
$$

$$
- \tfrac{1}{2}\left[\overline{D}_1 + \overline{D}_2 + \overline{D}_{1+2}\right]\mathcal{C}_{12}^{123} + 2i\sum_{\lambda_4}\left[\mathcal{W}_{(1+2)(-2)}^{(1+4)(-4)}\mathcal{E}_2^{24}\mathcal{E}_{(1+2)}^{(1+4)3}\right.
$$

$$
\left.+ \mathcal{W}_{(1+2)(-1)}^{(2+4)(-4)}\mathcal{E}_1^{14}\mathcal{E}_{(1+2)}^{(2+4)3} - \mathcal{W}_{12}^{(3-4)(4)}\mathcal{E}_1^{14}\mathcal{E}_2^{2(3-4)}\right]\Delta\lambda,\qquad(5.1b)
$$

where the overbar denotes the lateral average $(1/L_y\int\,dy)$ and the $S_1^1$ given in §4.1 (eq. 4.9). The spectrum $\mathcal{E}_1^{12}$ and bi-spectrum $\mathcal{C}_{12}^{123}$ are density functions (see §4.1), discretely sampled on an equidistant grid with spacing $\Delta\omega$ and $\Delta\lambda$.

Note that (5.1b) is a simplified form of the governing equation for the bi-spectral density function derived in Chapter 4 (eq. (4.13)), in the sense that the convolution of the bi-spectrum with the laterally varying depth and dissipation function is replaced by a multiplication with the lateral average of these contributions. This approximation implies the assumption that the lateral heterogeneity of the bi-spectral density function is primarily caused by the laterally heterogeneous spectrum; we ignore the interaction with the lateral depth variations, and lateral variability of the dissipation function as sources of heterogeneity in the description of the bi-spectrum evolution. This approximation simplifies the numerical implementation, without depriving the model of its principal source of heterogeneity for the triple moments, namely the laterally inhomogeneous energy density function. Although the simplified model is shown here to agree well with observations, a thorough evaluation of the neglected terms awaits a numerical implementation of the complete model.

This implementation, suitable for laterally heterogeneous wave fields and topographies, is refered to by the acronym *SAM2D*[†]. For a cylindrical topography (see §5.4) the spectral and bi-spectral density are two- and four-dimensional in spectral space respectively; a dimensional reduction by one with respect to the heterogeneous case. This implies a substantial simplification of the governing equations, yielding

$$\frac{d\mathcal{E}_1^1}{dx} = -D_1 \mathcal{E}_1^1 - 2 \sum_{\boldsymbol{v}_2} \mathcal{W}_{(1-2)2}^{(1-2)2} \mathcal{C}_{(1-2)2}^{(1-2)2} \Delta\omega \Delta\lambda, \tag{5.2a}$$

$$\frac{d\mathcal{C}_{12}^{12}}{dx} = i \left( \Lambda_{12}^{12} + i\mu_{12}^{12} \right) \mathcal{C}_{12}^{12} - \frac{1}{2} \left( D_1 + D_2 + D_{(1+2)} \right) \mathcal{C}_{12}^{12}$$
$$+ 2i \left[ \mathcal{W}_{(1+2)(-2)}^{(1+2)(-2)} \mathcal{E}_2^2 \mathcal{E}_{(1+2)}^{(1+2)} + \mathcal{W}_{(1+2)(-1)}^{(1+2)(-1)} \mathcal{E}_1^1 \mathcal{E}_{(1+2)}^{(1+2)} - \mathcal{W}_{12}^{12} \mathcal{E}_1^1 \mathcal{E}_2^2 \right]. \tag{5.2b}$$

This implementation, suitable for directional waves over one-dimensional depth variations, is referred to as the *SAM1D* model implementation. For unidirectional wave propagation the model reduces to the model of §4.4.3, which, repeated here for completeness, in the present, semi-discrete notation reads

$$\frac{d\mathcal{E}_1}{dx} = -D_1 \mathcal{E}_1 - 2 \sum_{p_2} \mathcal{W}_{(1-2)2} \mathcal{C}_{(1-2)2} \Delta\omega, \tag{5.3a}$$

$$\frac{d\mathcal{C}_{12}}{dx} = i \left( \Lambda_{12} + i\mu_{12} \right) \mathcal{C}_{12} - \frac{1}{2} \left( D_1 + D_2 + D_{(1+2)} \right) \mathcal{C}_{12}$$
$$+ 2i \left[ \mathcal{W}_{(1+2)(-2)} \mathcal{E}_2 \mathcal{E}_{(1+2)} + \mathcal{W}_{(1+2)(-1)} \mathcal{E}_1 \mathcal{E}_{(1+2)} - \mathcal{W}_{12} \mathcal{E}_1 \mathcal{E}_2 \right], \tag{5.3b}$$

which will be referred to as the *SAMuD* model.

The parameterization of the closure relaxation and depth-induced breaking dissipation involve a number of free parameters for which sensible choices need to be made. Moreover, with the objective of assessing the robustness of the parameterizations involved, we choose a single set of parameters which is kept constant for all cases considered. The parameter values are determined ad hoc, and no systematic optimization of these empirical coefficients is pursued here.

Based on inspection of a few trial numerical experiments we have set the free parameter $\beta$, controlling the closure relaxation, at 1.5 throughout. Depth-induced breaking is modeled utilizing $B = 1$ (a measure of breaker intensity) and $\gamma$ values are derived from eq. (4.32) after Battjes & Stive [1985]. Lastly, the frequency weighting of the dissipation function is predominantly quadratic with a small uniformly weighted contribution

$$D_1 = \frac{1}{m_0} \left( r_0 + r_2 \omega_1^2 \frac{m_0}{m_2} \right) D, \tag{5.4}$$

with the weights $r_0 = 1/10$ and $r_2 = 1 - r_0 = 9/10$ respectively. The frequency-independent dissipation function $D$ is given in (4.41).

---

[†]SAM: Stochastic Angular-spectrum Model

Although it is possible to initialize the SAM2D model with a laterally inhomogeneous wave field (see e.g. discussion in §5.5), here we assume the wavefield initially laterally homogeneous, with the heterogeneity developing through interaction with the topography as the waves propagate through the domain. The energy equation is initialized with a discretized flux spectrum at the offshore boundary ($\mathcal{E}_1^1 = V_1^1 \mathcal{S}_1^1$, with $\mathcal{S}_1^1$ the discretized surface elevation variance density spectrum), either available from observations or in parameterized form. The corresponding initial bi-spectral density function is obtained from considering the SAM1D bi-spectral equation (eq. (5.2b))

$$\frac{d}{dx}\mathcal{C}_{12}^{12} = i\Lambda_{12}^{12}\left[\mathcal{C}_{12}^{12} + 2\frac{\mathcal{Q}_{12}^{12}}{\Lambda_{12}^{12}}\right], \tag{5.5}$$

with

$$\mathcal{Q}_{12}^{12} = \mathcal{W}_{(1+2)(-2)}^{(1+2)(-2)}\mathcal{E}_2^2\mathcal{E}_{(1+2)}^{(1+2)} + \mathcal{W}_{(1+2)(-1)}^{(1+2)(-1)}\mathcal{E}_1^1\mathcal{E}_{(1+2)}^{(1+2)} - \mathcal{W}_{12}^{12}\mathcal{E}_1^1\mathcal{E}_2^2. \tag{5.6}$$

It is readily seen that

$$\mathcal{C}_{12}^{12} = -2\frac{\mathcal{Q}_{12}^{12}}{\Lambda_{12}^{12}} \tag{5.7}$$

is a steady solution for the laterally homogeneous case and is used here to initialize the bi-spectral integration both for the SAM2D and SAM1D model (since lateral homogeneity was assumed at the offshore boundary, the SAM1D and SAM2D can be initialized with the same – homogeneous – boundary conditions). Likewise (5.7) is used as an initial condition for the bi-spectral evolution equation pertinent to the SAMuD model, where the omission of the lateral wavenumber space is understood.

The bi-spectral initialization (5.7) corresponds to Stokes' second-order theory [see e.g. Hasselmann *et al.*, 1963; Herbers & Burton, 1997] and implies a skewed, symmetrical wave field at the offshore location. This initialization is reasonable if the offshore boundary is in sufficiently deep water and the depth is (near-)uniform, so that uniform-depth second-order wave theory is a good approximation.

For a given computational domain, with lateral extent $L_y$ and discretization $\Delta y$, the alongshore wavenumber array is given as $\Delta\lambda\left[-L_y/(2\Delta y)\dots L_y/(2\Delta y)\right]$, with $\Delta\lambda = 2\pi/L_y$. Since the derivation does not include evanescent modes ($|\lambda| > k_\omega$), these are consistently omitted from the computation, including such modes that are evanescent at the offshore boundary but become propagating inside the domain on account of the variable depth. The spatial and spectral discretizations differ for the various cases considered, and are specified were needed.

The constituent ordinary differential equations of the SAM2D, SAM1D and SAMuD implementations (viz. (5.1), (5.2) and (5.3)) are integrated utilizing a standard, fixed step-size, fourth-order Runge-Kutta scheme.

## 5.2  One-dimensional wave propagation

The occurrence of multiple crests (or 'frequency-doubling') behind submerged obstacles is a common phenomenon in shallow coastal waters [Munk & Traylor, 1947; Johnson

*et al.*, 1951]. From laboratory observations, Jolas [1960]<sup>†</sup> deduced that the shorter waves appearing on the lee side of the obstacle were due to the the amplification of harmonics over the shallow part of the obstacle; an hypothesis consistent with later advances in near-resonant interaction theory [Mei & Ünlüata, 1972; Bryant, 1973].
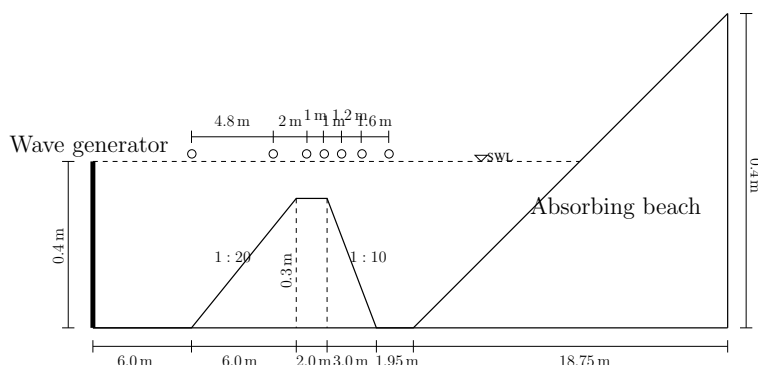


**Figure 5.1:** Bottom profile experiments Beji & Battjes [1993]. Circles indicate wave gauge locations.

However, harmonic generation over obstacles in regular, unbroken waves (see e.g. Chapter 3, §3.2.2) is the exception rather than the rule. In most field situations, (random) wave propagation over shallow sandbars, and the associated amplification of harmonic motion, is accompanied by wave breaking [Byrne, 1969; Young, 1989; Elgar *et al.*, 1997]. With the purpose of empirically investigating the concomitant action of nonlinear harmonic generation and dissipation in breaking waves over a localized obstacle, Beji & Battjes [1993] performed laboratory experiments including random waves impinging on a submerged, trapezoidal obstacle (Figure 5.1). The experiments were performed in a 37.5 m long flume, 0.8 m wide and 0.75 m deep (Figure 5.1). Observations are available at 7 locations over the shoal as indicated in the figure. The wave generation is first-order accurate (thus second-order spurious waves must be anticipated); reflections are minimized through the presence of an absorbing beach at the far end of the flume (Figure 5.1). The incident wave field has a Jonswap spectral shape, peak frequency $f_p = 0.5 \, \text{Hz}$ and $H_{m0} = 4\sqrt{m_0} = 2.3 \, \text{cm}$.

Simulations are performed with the SAMuD model (viz. the set (5.3)). The observed frequency spectrum at $x = 6 \, \text{m}$ at the toe of the up-slope (with $x = 0$ at the wave generator, and $x$ positive in the direction of wave propagation) is discretized into an equidistant frequency array consisting of 135 frequencies with $\Delta\omega = 0.05\pi \, \text{rad/s}$ and used to initialize the model. The initial bi-spectrum is obtained from second-order wave theory (see §5.1). The spatial step size $\Delta x = 0.10 \, \text{m}$.

---

<sup>†</sup>Jolas [1960] derives an N-point least-squares algorithm (*N* being an integer $\leq 2$) for the directional decomposition of one-dimensional wave trains. Such a least-squares approach has been advanced much later by Mansard & Funke [1980], as a three-point method, improving the earlier 2-point method by Goda & Suzuki [1976]. The more general *N*-point approach described by Jolas [1960] was later presented by Zelt & Skjelbreia [1992], who were presumably unaware of the work by Jolas that appeared in French.
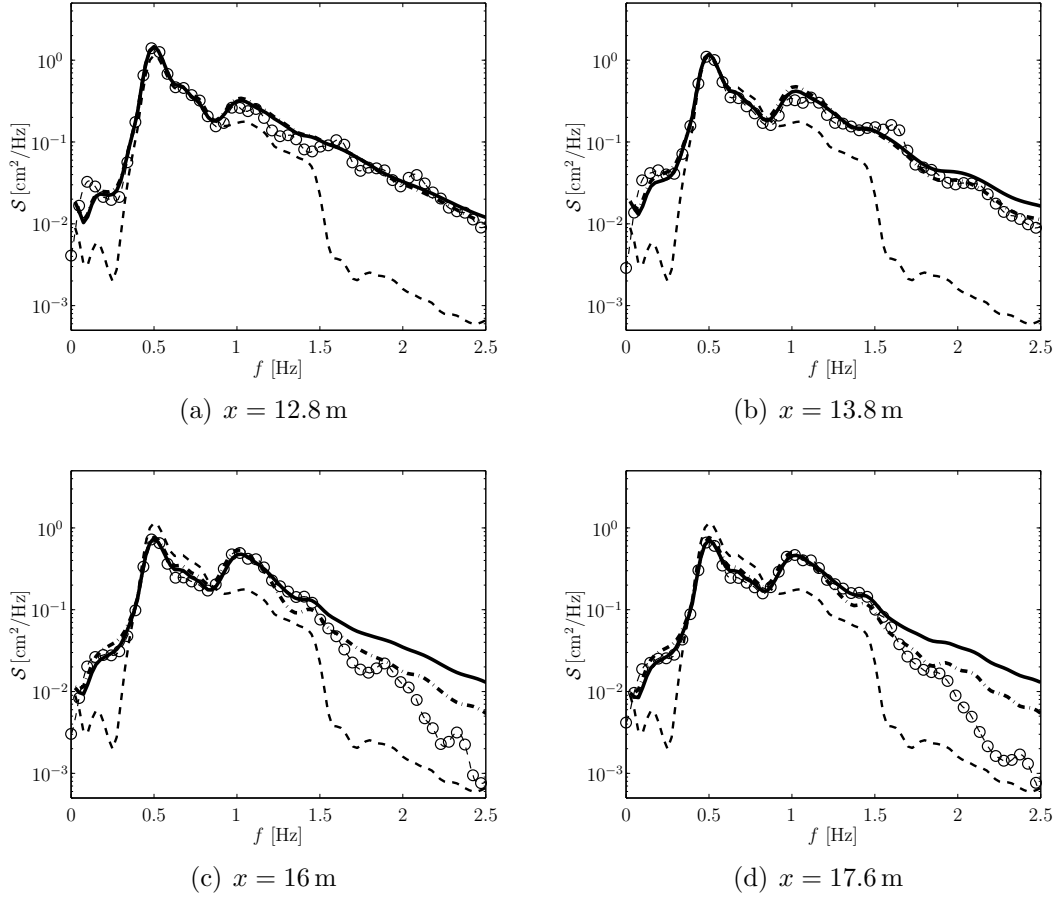
(a) $x = 12.8\,\mathrm{m}$

(b) $x = 13.8\,\mathrm{m}$

(c) $x = 16\,\mathrm{m}$

(d) $x = 17.6\,\mathrm{m}$

**Figure 5.2:** Comparison of observed (circles) [Beji & Battjes, 1993], RQN-predicted (solid line) and QN-predicted (dash-dotted line) frequency spectra at four observation locations (sub-captions); dashed line indicates the initial wave spectrum at $x = 6\,\mathrm{m}$. Incident wave field with Jonswap spectrum ($f_p = 0.5\,\mathrm{Hz}$, $H_{m0} = 2.3\,\mathrm{cm}$).

As the wave field propagates on the up-slope and over the obstacle, energy is transported from the initial peak to harmonic frequency ranges (Figure 5.2); on the down-slope some of this energy is subsequently returned to the main peak through a phase reversal of the nonlinear coupling. Overall the model predictions are in very good agreement with the observations. A notable exception is a systematic overestimation of energy levels beyond $f \approx 1.5\,\mathrm{Hz}$ for locations $x = 16\,\mathrm{m}$ and $x = 17.6\,\mathrm{m}$, in particular for the simulation including relaxation (RQN). This is consistent with the finding in Chapter 4 (§4.4.3) that the relaxation of the bi-spectrum tends to under-predict the spectral slope of the high-frequency tail. In contrast, the evolution of the low-frequency regions of the spectrum (beat frequencies) are very well predicted throughout the interval of propagation (note that the assumed unidirectionality is not necessarily warranted for the low-frequency waves in the spectrum; see Chapter 6).

PSfrag replacements
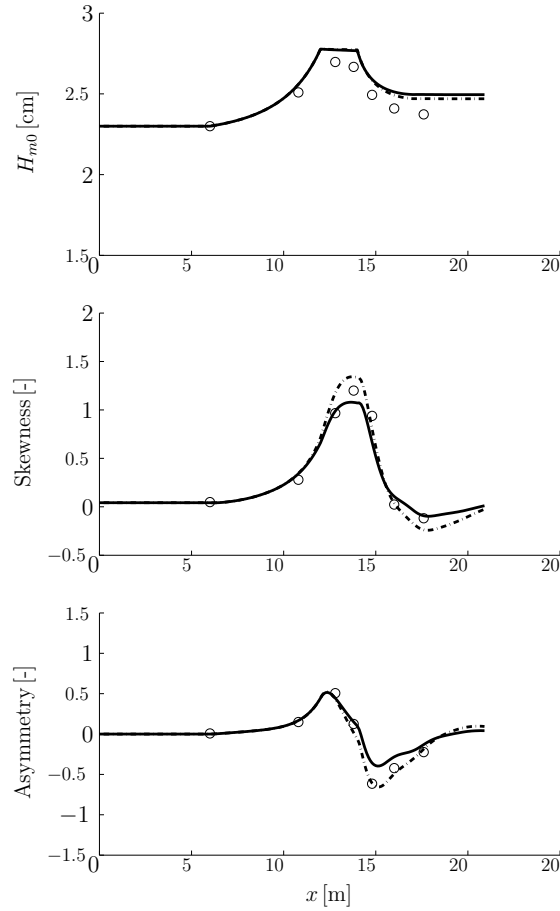


**Figure 5.3:** Comparison of observed (circles), RQN-predicted (solid line) and QN-predicted (dash-dotted line) wave height (top panel), skewness (middle panel), and asymmetry (bottom panel). Incident wave field with Jonswap spectrum ($f_p = 0.5\,\text{Hz}$, $H_{m0} = 2.3\,\text{cm}$).

The model-predicted bulk statistics for the wave height, skewness and asymmetry (see eq.'s (5.14) and (5.15) for definitions) are in good agreement with the observed values (Figure 5.3). The RQN model underestimates skewness levels slightly over the bar, and the negative asymmetry occurring on the down-slope is not resolved entirely accurate. In contrast, the QN model over-predicts skewness in the shallow part of the flume, but the predicted asymmetry is in better agreement than RQN-predicted values.

Overall, for this case, involving only localized (over the obstacle) enhancement of nonlinearity and dissipation, agreement between predictions and observations is good; the QN model predictions are overall in slightly better agreement but predictions from the RQN en QN model differ only in details. The similarity between RQN- and QN-predicted spectral evolution is consistent with the anticipated behavior of the RQN closure modification. After all, these closure modifications should only be operative where the QN model, on account of high Ursell numbers and intense dissipation over extended regions, becomes highly inaccurate (see e.g. §5.4). Since the latter does not

occur in the present case, relaxation should be rather ineffective and consequently result in minor modifications of the wave field evolution.

## 5.3  Directional waves over topography

Vincent & Briggs [1989] performed experiments including random, directionally spread waves over a submerged, elliptic shoal. These experiments were performed with the primary aim to assess the adequacy of modeling refraction-diffraction effects in random waves through representation of the wave field by a characteristic monochromatic wave train, a common practice in many engineering applications.
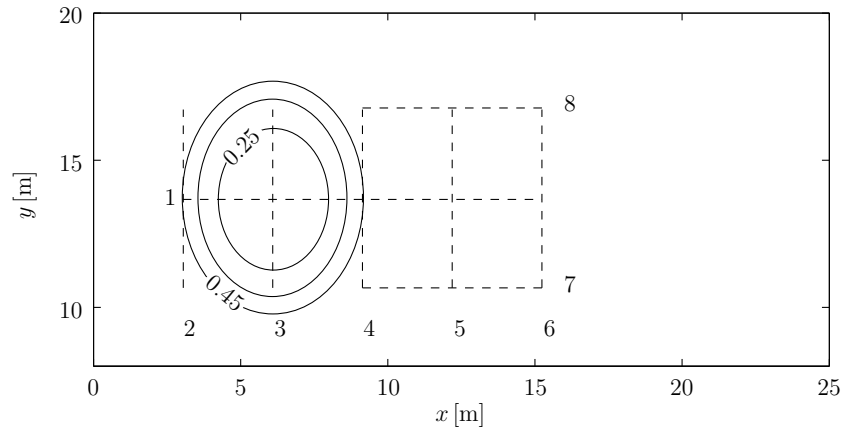


**Figure 5.4:** Bottom profile experimental set-up Vincent & Briggs [1989]. Depth is in meters; instrumented transects are indicated by dashed lines.

The experiments were performed in a wave basin, 35 m wide and 29 m long. The topography consists of an elliptic shoal (moulded after Berkhoff *et al.* [1982]), placed on an otherwise horizontal bottom (Figure 5.4). The shoal area is conveniently described in shoal-coordinates $(x', y')$ with the origin at the shoal center, which – in computational coordinates $(x, y)$ – is located at $(x_c, y_c) = (6.10, 13.72)$ m. The area occupied by the shoal is

$$\left(\frac{x'}{3.05\,\text{m}}\right)^2 + \left(\frac{y'}{3.96\,\text{m}}\right)^2 \leq 1, \tag{5.8}$$

where the depth is given by

$$h = 0.914\,\text{m} - 0.762\,\text{m}\left[1 - \left(\frac{x'}{3.81\,\text{m}}\right)^2 - \left(\frac{y'}{4.95\,\text{m}}\right)^2\right]^{1/2}. \tag{5.9}$$

The depth at the shoal center is 15.24 cm; outside the shoal area the water depth is $h = 45.72$ cm. The shoal-coordinates are related to the computational coordinates ($x$ and $y$ in Figure 5.4) through

$$x' = x - x_c, \qquad\qquad y' = y - y_c. \tag{5.10}$$

Waves are generated with a 27.43 m long, segmented wave generator, situated along the line $x = 0$. To suppress adverse reflections, wave absorbers are installed along the perimeter of the basin.

For the cases considered, the computational domain measures $L_y = 30$ m by $L_x = 20$ m in lateral and principal direction respectively. Consequently, the alongshore wavenumber spacing is $\Delta\lambda = 2\pi/L_y = 1/15\pi$ rad/m. Comparison is made to wave heights observed along the instrumented transects 1-8 that are indicated in Figure 5.4; transects 1, 7 and 8 are longitudinal, whereas transects 2-6 extend in the lateral direction.

### 5.3.1 Monochromatic unidirectional waves

To illustrate the diffraction modeling capability embedded in the SAM2D model, we compare observations of a normally incident monochromatic wave train to simulation results. Although the stochastic angular-spectrum modeling approach is particularly well suited for the modeling of the propagation of directionally-spread random waves, there is no fundamental difficulty in modeling unidirectional, monochromatic waves as the limit of a narrow-band incident wave field. The topography acts as a lens, causing strong cross-directional correlations (standing waves in the lateral direction) in the refractive convergence zone behind the shoal.

The incident wave field has angular frequency $\omega = 1.45\pi$ rad/s and waveheight $H_{m0} = 4.4$ cm. The model is initialized with

$$\mathcal{E}(\omega_1, \lambda_1, \lambda_2, 0) = \delta(\omega_1 - \omega)\delta(\lambda_1)\delta(\lambda_2)C_{g,1}\frac{H_{m0}^2}{32\Delta\omega\Delta\lambda^2} \tag{5.11}$$

and the appropriate bi-spectral density (viz. §5.1). The spatial domain is discretized with $\Delta x = 0.1$ m, $\Delta y = 0.24$ m; the spectral discretization consists of three, equidistant frequency components with $\Delta\omega = 1.45\pi$ rad/s.

| Transect | Index values |
|:--------:|:------------:|
| 1 | 0.93869 |
| 7 | 0.97414 |
| 8 | 0.88327 |
| 2 | 0.44531 |
| 3 | 0.59936 |
| 4 | 0.96234 |
| 5 | 0.98548 |
| 6 | 0.94567 |

**Table 5.1:** Willmott index values for monochromatic wave [Vincent & Briggs, 1989] with $H_{m0} = 4.4$ cm, and $\omega = 1.45\pi$ rad/s; transects are indicated in Figure 5.4.

The observed and computed wave height evolution are in close agreement (Figure 5.5), quantitatively confirmed by the high Willmott-index values (definition: see §3.4.2, eq. (3.50); values in Table 5.1). The low Willmott score for transect 2 & 3 (not shown in figure) is on account of the (very) small variations along these transects, both in the observations and predictions, resulting in heavily penalized mismatches (see also §3.4.2). The stochastic model, apart from local details, faithfully resolves the refraction-diffraction wave height patterns, including the refractive focus behind the shoal. The latter illustrates that the combined refraction-diffraction effect on the wave field transformation can be accurately described utilizing the SAM formalism, which captures the lateral heterogeneity through evolving – in one-dimensional physical space – the off-diagonal spectral components, which represent the correlations between non-collinear wave components (see also §5.5).
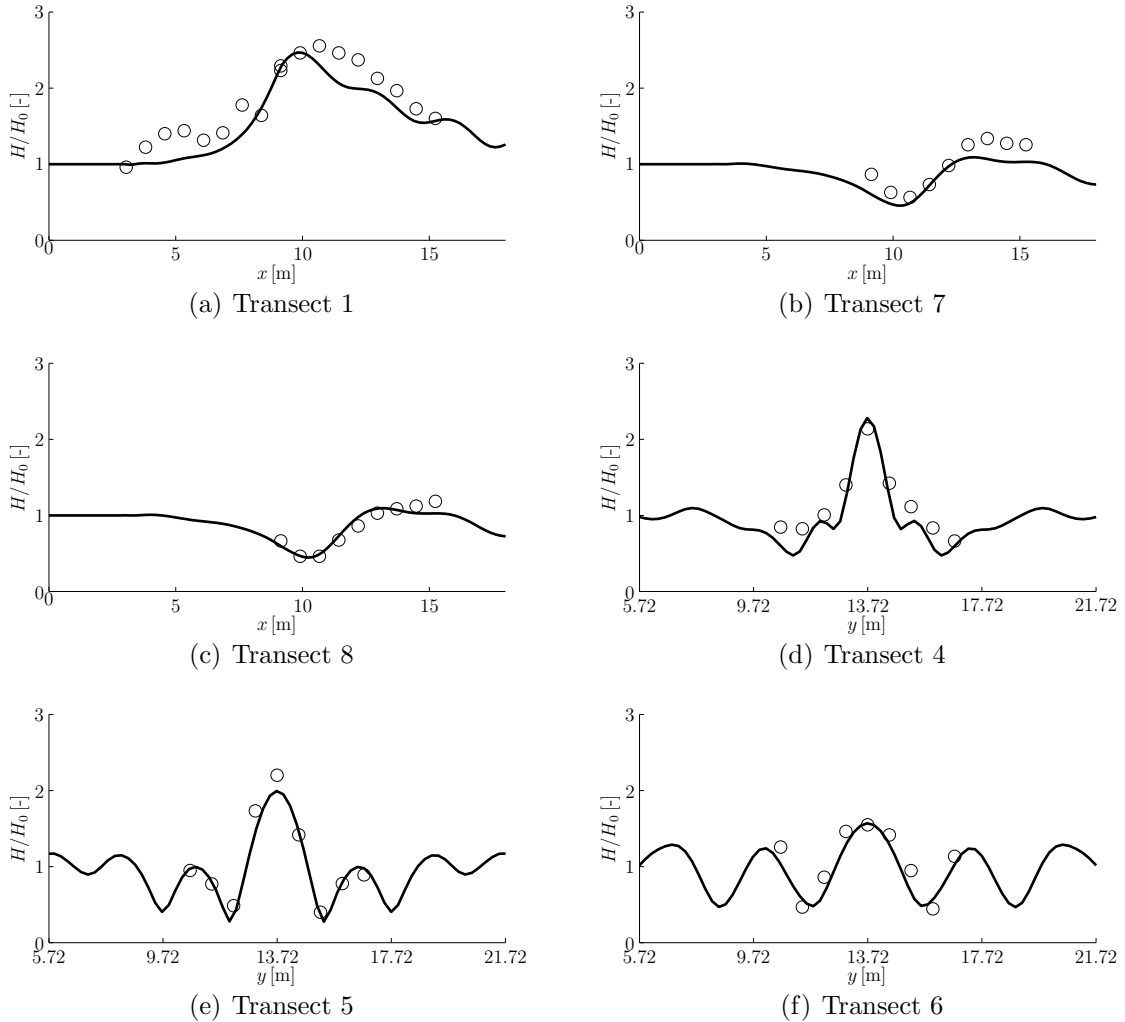


**Figure 5.5:** Comparison of observed (circles) [Vincent & Briggs, 1989] and predicted (solid line) wave heights; monochromatic, normally incident waves with $H_{m0} = 4.4$ cm and frequency $\omega = 1.45\pi$ rad/s.

### 5.3.2 Directionally spread waves over topography

The experiments with random, directionally-spread waves by Vincent & Briggs [1989] were performed utilizing frequency spectra of the TMA-type [Bouws *et al.*, 1985] and a wrapped-normal spreading function [Mardia & Jupp, 2000]. The two-dimensional spectra are written as

$$\mathcal{S}(\omega, \theta) = \mathcal{S}(\omega)D(\theta), \tag{5.12}$$

with the TMA frequency spectrum $\mathcal{S}(\omega)$ defined by the free parameters: peak frequency $f_{\text{tma}}$, $\alpha_{\text{tma}}$ constant, and peak enhancement factor $\gamma_{\text{tma}}$. The directional distribution, $D(\theta)$, is parameterized by a wrapped normal spreading function (see eq. (4.25)) with the mean wave direction $\theta_m = 0$ and $N = 100$, which is the (arbitrary) number of terms in the series (see eq. (4.25)).

We consider two cases, labeled as in Vincent & Briggs [1989]. The values for the parameters defining the incident wave field are listed in Table 5.2 (wave heights are taken from observations). Both cases have the same frequency distribution but case B1 exhibits a wider directional distribution than N1.

| Case | $f_{\text{tma}}$ [Hz] | $\alpha_{\text{tma}}$ [-] | $\gamma_{\text{tma}}$ [-] | $\sigma_{\text{D}}$ [rad] | $H_{m0}$ [cm] |
|------|------|------|------|------|------|
| N1 | 0.77 | 0.01440 | 2 | 0.175 | 7.5 |
| B1 | 0.77 | 0.01440 | 2 | 0.5236 | 7.1 |

**Table 5.2:** Parameters for target spectra directionally spread incident waves [Vincent & Briggs, 1989]. Parameters listed as as in Vincent & Briggs [1989] but wave heights from observations.

The computational domain is discretized with $\Delta x = 0.1\,\text{m}$ and $\Delta y = 0.48\,\text{m}$. The frequency spectrum is discretized into 20 equidistant positive frequencies, with $\Delta \omega = 0.2\pi\,\text{rad/s}$. Directional spectra are generated using the parameters listed in Table 5.2, interpolated onto the frequency-lateral wavenumber grid at $x = 0$, and converted to the flux spectrum $\mathcal{E}$ to initialize the SAM2D model (§5.1). The bi-spectrum according to Stokes' second-order theory is used to initialize the bi-spectral evolution equations (viz. §5.1).

On account of the finite bandwidth of the wave field, in particular the directional aperture [Vincent & Briggs, 1989], correlation between directional components in the refractive focus are sustained over much shorter distances than for unidirectional incident waves (§5.3.1), and the characteristic standing wave height pattern throughout the refractive focus is suppressed owing to directional phase mixing (Figure 5.6 & Figure 5.7), in particular for B1 (widest aperture). The model faithfully captures the wave height evolution, including the enhanced attenuation of phase coupling with increasing directional spreading of the incident wave field. Overall, the agreement between model-predicted wave height evolution and observations is good.
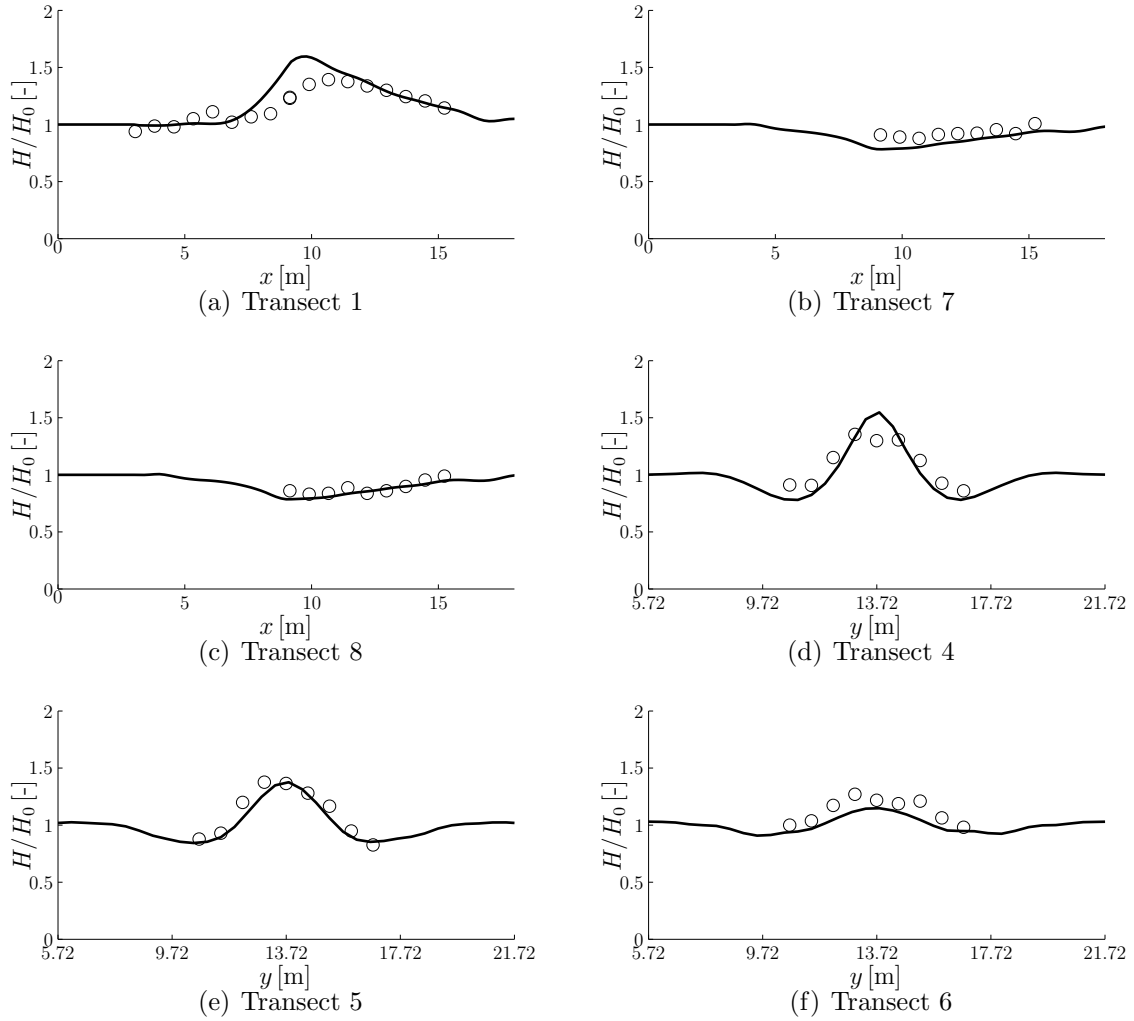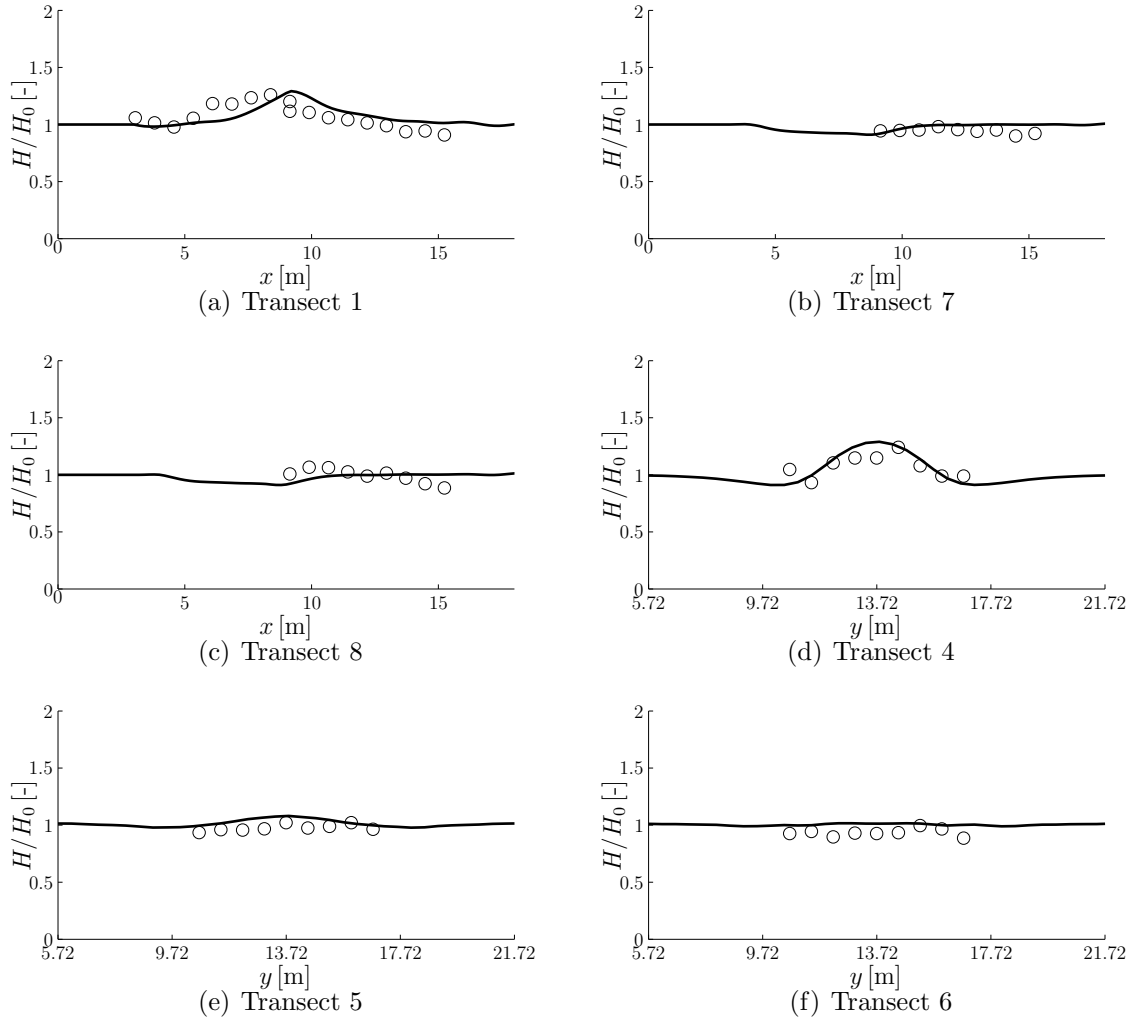
**Figure 5.6:** Comparison of observed (circles) [Vincent & Briggs, 1989] and predicted (solid line) normalized zeroth-moment significant wave heights for case N1 (see Table 5.2).

The spectral evolution for case N1 (Figure 5.8) shows an initial directional widening, primarily on account of the interaction with the lateral depth variations and to a lesser extent related to the effects of laterally varying dissipation. After the initial widening, the spectrum narrows somewhat again and evolves toward what could be considered a tri-modal shape (in directional space), consisting of main center lobe and two side-lobes. Apart from the wider initial shape, the computed spectral evolution for B1 exhibits qualitatively similar characteristics (not shown).

The spectra in Figure 5.8 are local spectra along $y = 13.8\,\mathrm{m}$ approximately crossing the shoal center ($y = 13.72\,\mathrm{m}$), obtained through a discrete approximation of the transform relations detailed in §4.2 (eq. (4.17)). It is seen from Figure 5.8 that enhancement of energy levels at harmonic ranges is not visible, indicating that nonlinear effects, at least in the numerical simulations (no observations of spectra were available), are weak.

$x$ [m]

$y$ [m]



(a) Transect 1

(b) Transect 7

(c) Transect 8

(d) Transect 4

(e) Transect 5

(f) Transect 6

**Figure 5.7:** Comparison of observed (circles) [Vincent & Briggs, 1989] and predicted (solid line) normalized zeroth-moment significant wave heights for case B1 (see Table 5.2).

Given these moderate levels of nonlinearity and dissipation, the present comparison does not represent a decisive test with respect to the accuracy of the combined representation of nonlinearity, dissipation and topographical focusing, for which further verification is needed. Nevertheless, the good agreement with these observations in terms of the wave height evolution does indicate that, given the restrictions on lateral depth variations implied by the underlying deterministic model, the SAM formalism is capable of accurately predicting the propagation of random directionally-spread wave evolution over two-dimensional topography, including localized wave breaking.
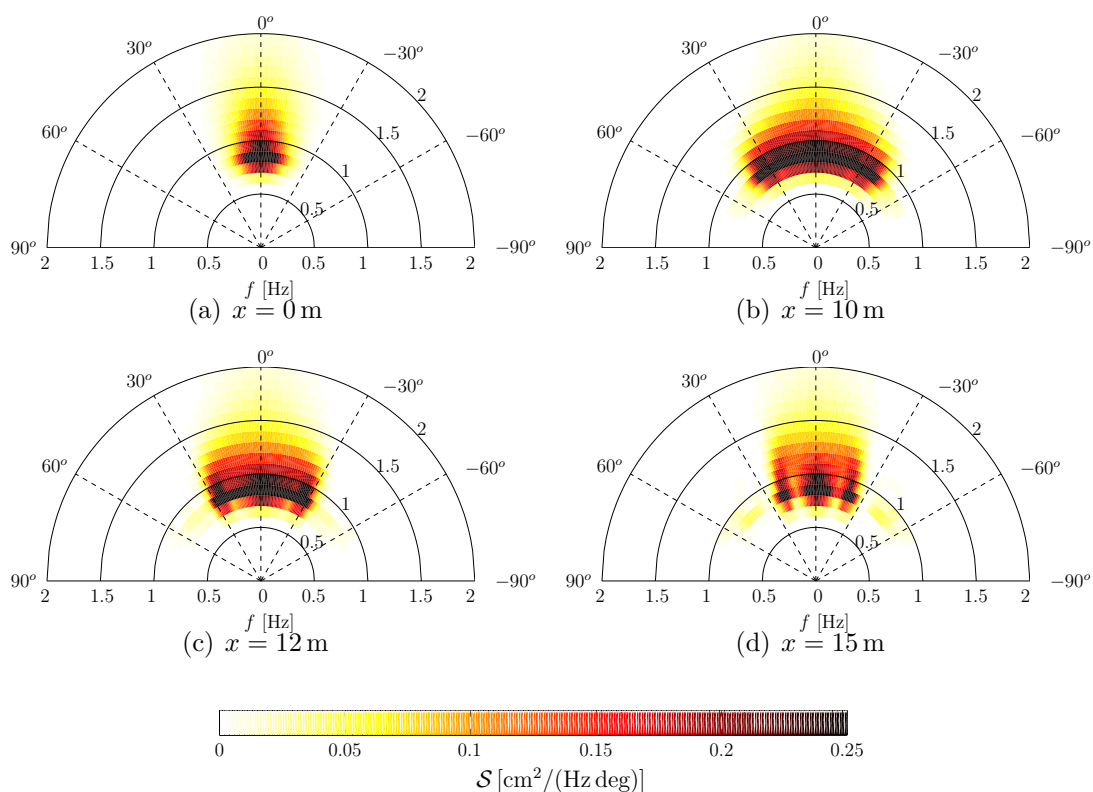
**Figure 5.8:** Computed spectra condition N1 (see Table 5.2) along $y = 13.8\,\text{m}$ (near center shoal) at positions in front and behind the shoal (see captions).

## 5.4 Directional waves on a near-cylindrical beach: field observations

During field campaigns in the fall of 1994 (Duck94) and 1997 (Sandyduck), extensive measurements of shoaling waves across a natural beach were collected at the U.S. Army Corps of Engineers' Field Research Facility (FRF), located near Duck, North Carolina [see e.g. Elgar *et al.*, 1997; Feddersen *et al.*, 1998; Ruessink *et al.*, 2001; Herbers *et al.*, 2003]. Figure 5.9 shows the instrument locations and depth contours in the local beach coordinate system. The $y$ coordinate is aligned with the alongshore, oriented $20^o$ West of true North and positive in Northerly direction; the $x$ is the cross-shore coordinate, oriented $70^o$ East of true North and increasing in offshore direction (Figure 5.9).

During the Duck94 campaign, 14 co-located pressure gauges, current meters and downward-looking sonar altimeters were deployed at cross-shore locations ranging from the shoreline to around $5\,\text{m}$ depth (bottom panel Figure 5.9). Seafloor locations were derived from the altimeter radar measurements at the instrument locations [Elgar *et al.*, 1997; Gallagher *et al.*, 1998]; the (one-dimensional) profile along the instrumented transect is estimated through linear interpolation (Figure 5.9). Directional spectra of the incident wave field were estimated from measurements at a linear alongshore array of pressure sensors (9 elements) located in $8\,\text{m}$ water depth (approximately $800\,\text{m}$ offshore),

indicated as FRF in the figure. For further details with respect to the instrumentation and wave conditions we refer to e.g. Elgar *et al.* [1997] and Herbers *et al.* [2003].

During Sandyduck (1997), four linear alongshore arrays (indicated by B, C, E and F in Figure 5.9) of co-located pressure gauges and current meters were deployed [Elgar *et al.*, 2001], from which directional spectra are derived at the discrete cross-shore locations [Herbers *et al.*, 2003]. In addition to the arrays, three additional pressure sensors were placed (two between array E and C and one just shoreward of array B) to improve the cross-shore resolution of the observational array for frequency spectra and bulk statistics. The bathymetry, extending from the beach up to $x = 950\,\mathrm{m}$ (approximately 8 m water depth), is obtained from regular surveys conducted by the FRF staff (Figure 5.9). Seaward of $x = 950\,\mathrm{m}$, bathymetry data is obtained from ship-based depth soundings in that area (Herbers 2005, personal communication). A one-dimensional profile is estimated by laterally averaging the depth over $700\,\mathrm{m} < y < 1000\,\mathrm{m}$. Directional spectra of the incident wave conditions are available at the FRF array (located approximately 800 m, indicated in Figure 5.9) and at an array installed at approximately 5 km offshore (20 m depth, not shown in figure).

The nearshore bottom topography at Duck is nearly laterally homogeneous [see also Ruessink *et al.*, 2001; Elgar *et al.*, 2001] and thus we compare observations to predictions with the alongshore-uniform SAM1D model (§5.1). Unless stated otherwise, the model is initialized at the FRF array with the observed spectrum, discretized into 60 frequencies ($\Delta\omega = 0.0137\pi\,\mathrm{rad/s}$) and 128 alongshore wavenumbers ($\Delta\lambda = 0.0018\pi\,\mathrm{rad/m}$). Note that, although the model has no inherent angle limitation, the inclusion of propagating modes only, and the discretization, implies an aperture limitation for locations shallower than the offshore boundary, given as

$$\theta_{\max}(\omega, x) = \arcsin\left(\frac{\min\{k(\omega, 0), \lambda_{\max}\}}{k(\omega, x)}\right). \tag{5.13}$$

For instance, when considering the offshore boundary at the FRF array at 8 m depth, the aperture at 2 m depth (the shallow end of the beach) is restricted to $\pm 30^o$ and $\pm 29^o$ for the lowest and highest frequencies respectively. The aperture is wider for intermediate frequencies with a maximum around 0.3 Hz ($\theta = \pm 49^o$).

A relatively fine, cross-shore step size, $\Delta x = 0.5\,\mathrm{m}$, is required to resolve the anticipated rapid bi-spectral modulations. These contributions indicate the presence of a mixed free-bound wave field, and although cumulatively of little consequence to the wave field evolution, such oscillations restrict grid size spacing in relatively deeper water (see also discussion on outlook and applicability in §5.5).

The cases considered here are the same as considered by [Herbers *et al.*, 2003], who compare observations to predictions with a stochastic Boussinesq model. We initialize the present model at greater depth (FRF- and 20m-array, whereas Herbers *et al.* initialize at the F- and FRF-array respectively) to exploit and verify the deep-water capability of the present model with respect to shoaling, refraction and (linear) dispersion.
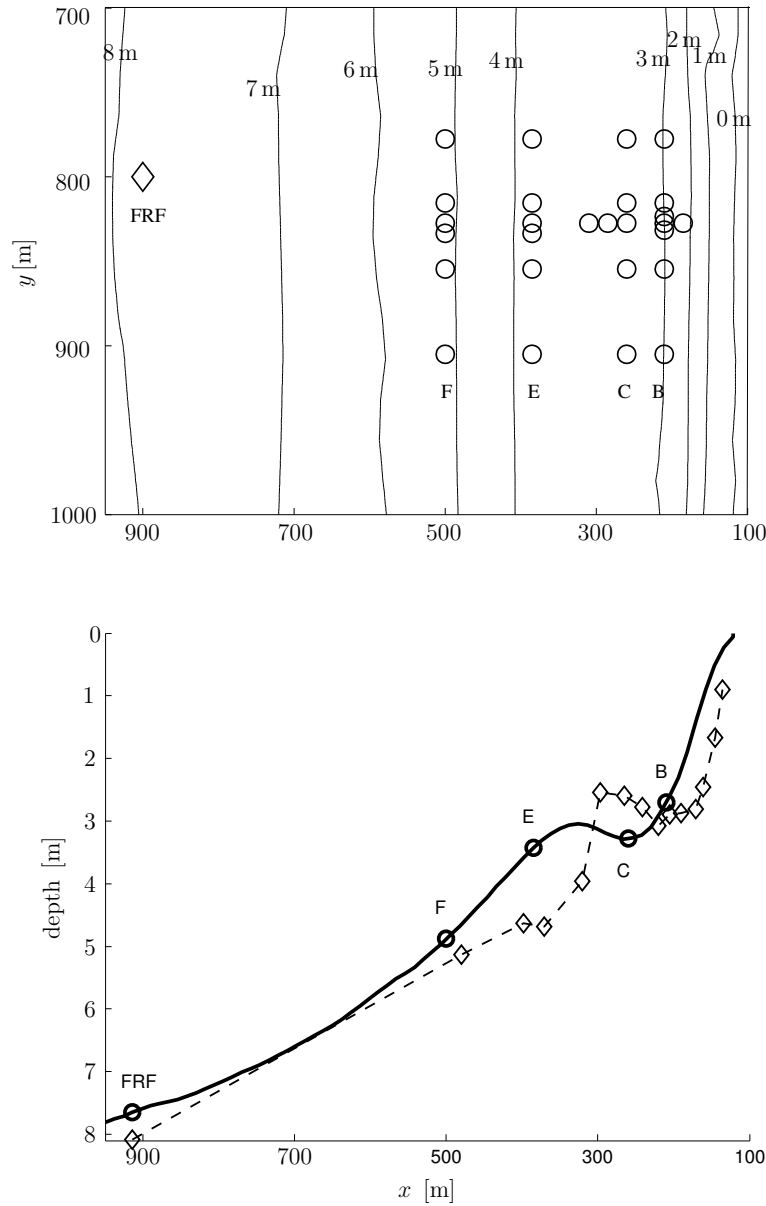
**Figure 5.9:** Bottom profiles and sensor locations in local beach coordinate system of Field Research Facility. Top panel: plan view of FRF array and four alongshore arrays (F,E,C,B) of co-located pressure sensors and current meters deployed during Sandyduck; solid lines indicate depth contours. Bottom panel: representative depth profiles for Sandyduck (solid line, array locations indicated) and DUCK94 (dashed line; each marker shoreward of the FRF array indicates a co-located pressure and velocity sensor).

### 5.4.1 Moderate conditions: conservative nonlinear shoaling

During Sandyduck, the nearshore sandbar was further offshore, in deeper water with a lower crest elevation, than during Duck94 (see Figure 5.9). For moderate incident wave conditions, generally no breaking occurs over the bar so that the observational

arrays are outside the surf zone. Although intermittent breaking occurs between arrays C and B for the larger sets of waves, wave breaking is primarily confined to the steep foreshore shoreward of the B-array [Herbers *et al.*, 2003]. Therefore, the comparison of predictions to observations for moderate energetic incident swell mainly verifies the model representation of the conservative processes such as refraction, shoaling and quadratic nonlinear interactions; dissipation on account of depth-induced wave breaking is very weak for these cases.

For the cases considered here, the model is initialized with discretized directional wave spectra observed at the FRF array (8 m depth) and with the bi-spectrum in accordance with Stokes' second-order theory (see §5.1).

*August 10, 1997*

On August 10, a narrow-band wave field is incident at the FRF array, with $f_p = 0.09$ Hz and $H_{m0} = 0.85$ m (Figure 5.10). Here and throughout this section, the directional convention is as follows. The directions, $\theta$, indicate the *arrival* directions of the wave energy with $\theta = 0$ indicating shore-normal wave incidence, corresponding to $70^o$ clockwise from true North. The direction $\theta$ is positive(negative) for waves approaching from Northerly(Southerly) directions with respect to the shore-normal. The mean wave direction is indicated by $\theta_m$. In this convention, the swell on August 10 is arriving from a slightly southerly direction ($\theta_m \approx -5^o$, Figure 5.10).
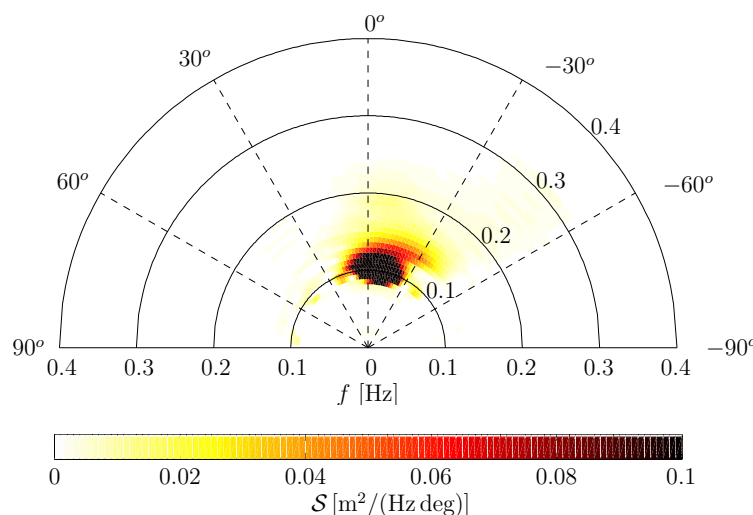


**Figure 5.10:** Observed two-dimensional spectrum at the FRF array on August 10, 1997. Unimodal wave field incident from the Southerly direction ($\theta_m = -5^o$) , $f_p = 0.09$ Hz and wave height $H_{m0} = 0.85$ m.

The propagation from the offshore array (FRF) to the F and E array (Figure 5.11) is typified by enhancement of energy at super-harmonic frequencies and a considerable amplification of low-frequency motion (difference interactions), qualitatively consistent with the interaction rules for quadratic nonlinear interactions. Over the bar and upon

reaching array C, energy levels at harmonic frequencies are further amplified (Figure 5.12), at the expense of the main peak. At array B, located right behind the trough, the distinct harmonic peak around $2f_p$ is somewhat reduced, which is attributed to a reversal of the energy flow toward the peak when traversing the trough (right panels Figure 5.12).

Model predictions are in overall good agreement with the observations, both for harmonic frequencies and at the low-frequency end of the spectrum; in particular for the F and E array, where the agreement is excellent. We note that generally the agreement at low frequencies, say below 0.03 Hz, is less good; in part this can be attributed to the fact that these long-wave components are likely to include reflected components [e.g. Elgar *et al.*, 1997; Battjes *et al.*, 2004], for which the model does not account. Moreover, for very low frequencies, the assumed slow variation of the topography, relative to the wavelength, may be violated.

For the C- and B-array, model-predicted spectra are somewhat narrower in directional space than the observed ones, and the model predicts waves at a slightly smaller angle with the shore-normal, than those observed (Figure 5.12).

Also notable is the fact that reversal of the cross-spectral transport of energy toward the peak is not accurately represented in the model, resulting in what appears a 'smearing out' of energy over frequency space at harmonic ranges, and an underestimation of energy levels at the peak (Figure 5.12). In part we attribute this to an artifact of the relaxation term; turning it off produces a slightly more featured spectral shape at B (not shown) but the overall agreement is similar.

The third-order bulk statistics of skewness and asymmetry are obtained from [see e.g. Elgar & Guza, 1985]

$$\text{Skewness} = \frac{6 \iint_0^\infty d\omega_1 d\omega_2 \iint_{-\infty}^\infty d\lambda_1 d\lambda_2 \, \Re\{\mathcal{B}(\omega_1, \omega_2, \lambda_1, \lambda_2)\}}{\left(\iint_{-\infty}^\infty d\omega d\lambda \, \mathcal{S}(\omega, \lambda)\right)^{3/2}} \tag{5.14}$$

and

$$\text{Asymmetry} = \frac{6 \iint_0^\infty d\omega_1 d\omega_2 \iint_{-\infty}^\infty d\lambda_1 d\lambda_2 \, \Im\{\mathcal{B}(\omega_1, \omega_2, \lambda_1, \lambda_2)\}}{\left(\iint_{-\infty}^\infty d\omega d\lambda \, \mathcal{S}(\omega, \lambda)\right)^{3/2}}, \tag{5.15}$$

where $\mathcal{B}(\omega_1, \omega_2, \lambda_1, \lambda_2) = \mathcal{C}(\omega_1, \omega_2, \lambda_1, \lambda_2)/\sqrt{V_1^1 V_2^2 V_{(1+2)}^{(1+2)}}$. These quantities measure what is intuitively best described as the 'peakedness' of the wave forms and 'pitching forward/backward' of the waves respectively. The latter is often observed on natural beaches at the onset of breaking, where the waves are generally strongly pitched-forward and saw-tooth shaped.

The computations predict the waves to evolve from symmetrical, slightly peaked waves at the FRF array (Figure 5.13) to skewed, pitched-forward waves over the bar (just offshore of $x = 300\,\text{m}$). In the trough (around $200\,\text{m} < x < 300\,\text{m}$) the waves lean back (negative asymmetry values) somewhat, an effect underestimated by the
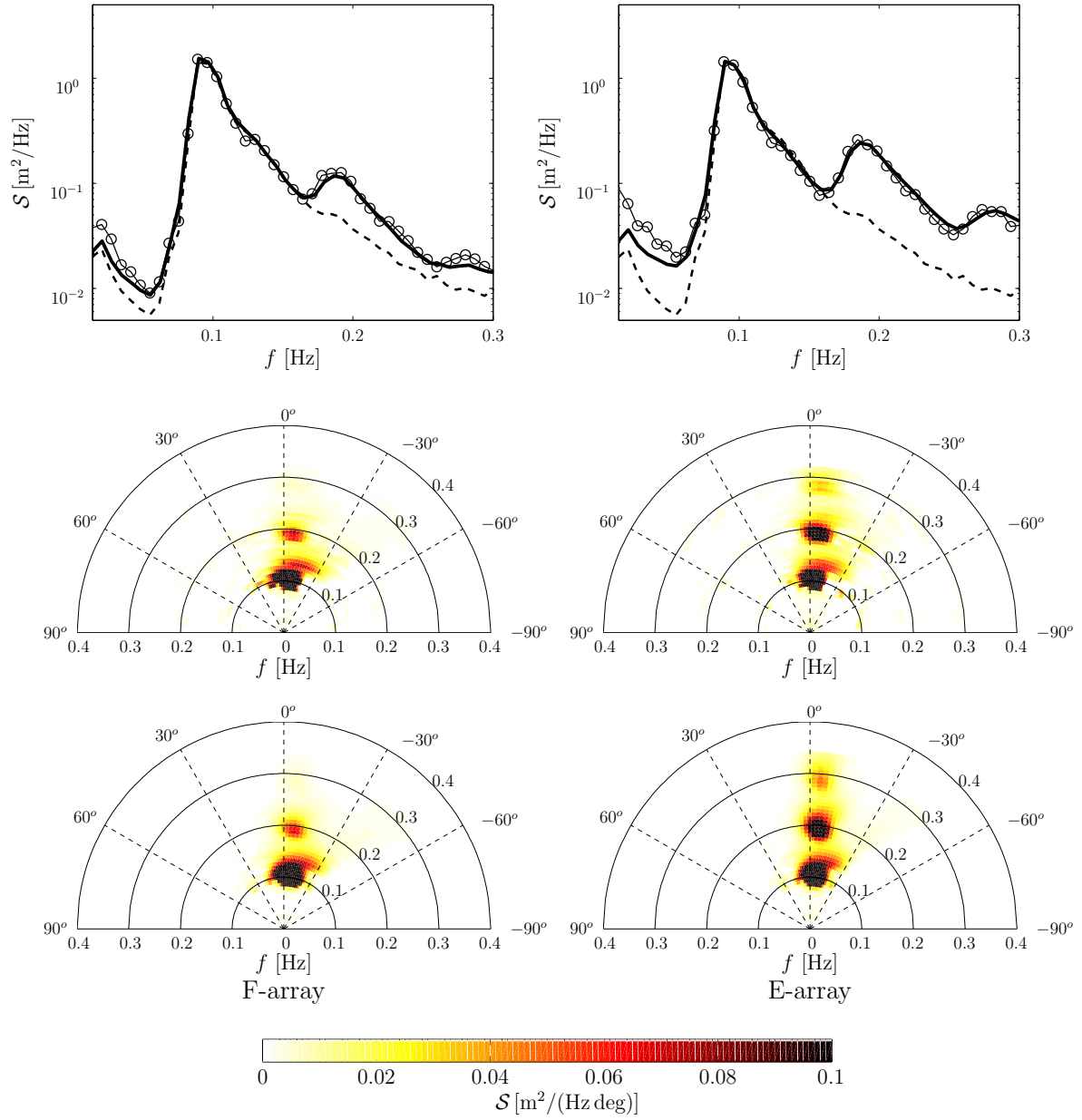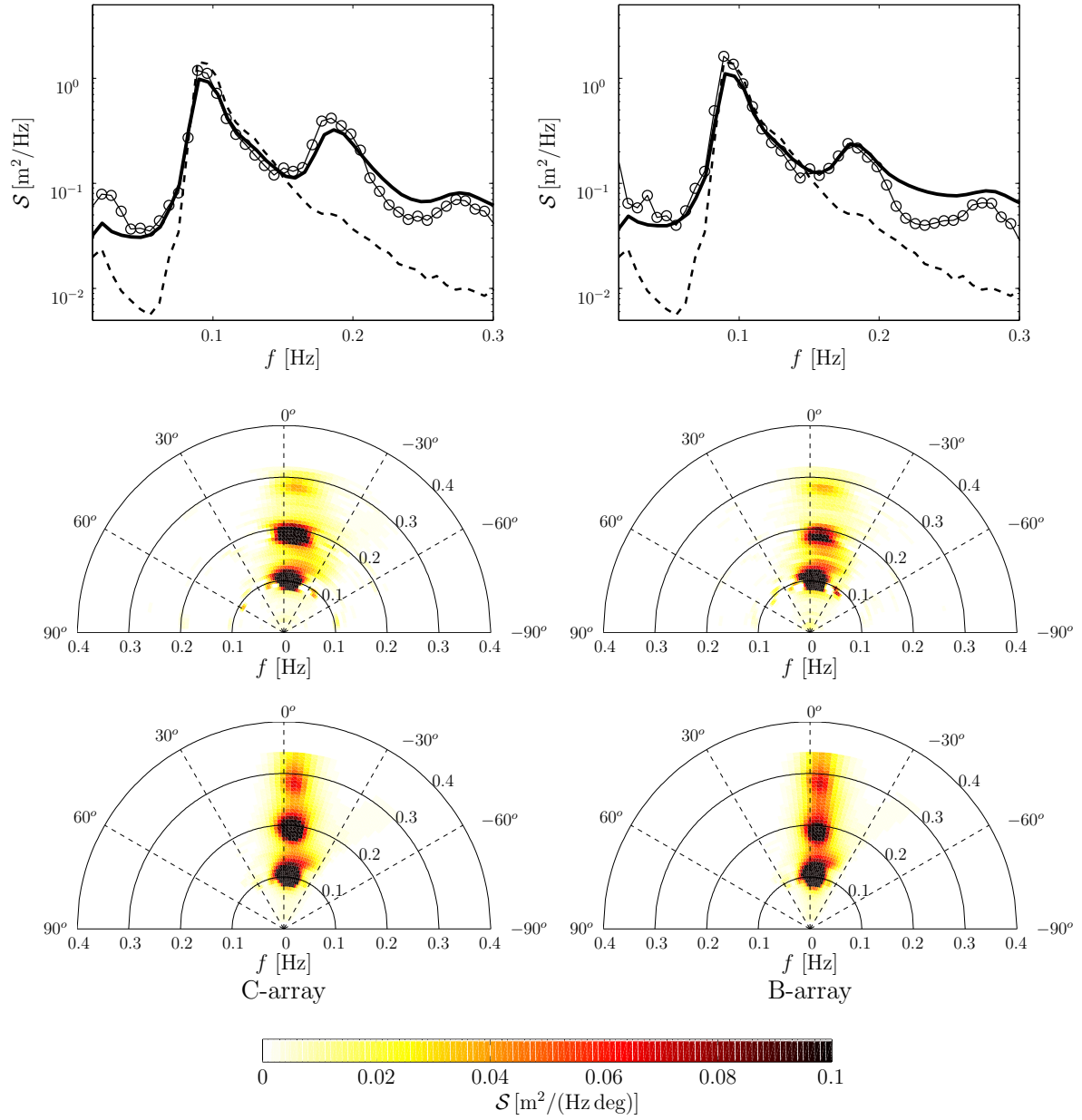
**Figure 5.11:** Comparison of observed and predicted spectra for August 10, 1997, at F- (left panels) and E-array (right panels). Top panels: observed (circles) and predicted (solid line) frequency spectra; dashed line represents offshore spectrum (FRF). Middle and lower panels are observed and predicted directional spectra respectively.

model. With the depth further decreasing shoreward of $x \approx 200\,\mathrm{m}$, skewness drops and asymmetry increases rapidly. The rapidly increasing wave asymmetry in this region indicates the onset of breaking. Apart from the noted discrepancy for the negative asymmetry in the trough, the agreement between predicted and observed third-order bulk statistics in the nearshore is good, particularly if we consider that prediction of such higher-order statistics represents a severe test to the model. We remark that the

**Figure 5.12:** Comparison of observed and predicted spectra for August 10, 1997, at C- (left panels) and B-array (right panels). Top panels: observed (circles) and predicted (solid line) frequency spectra; dashed line represents offshore spectrum (FRF). Middle and lower panels are observed and predicted directional spectra respectively.

dissipation and relaxation term are practically ineffective until shoreward of array B. These comparisons, and in particular those at the F, E and C array, thus verify the first-principle based model-representations of the relevant conservative processes.

PSfrag replacements

PSfrag replacements
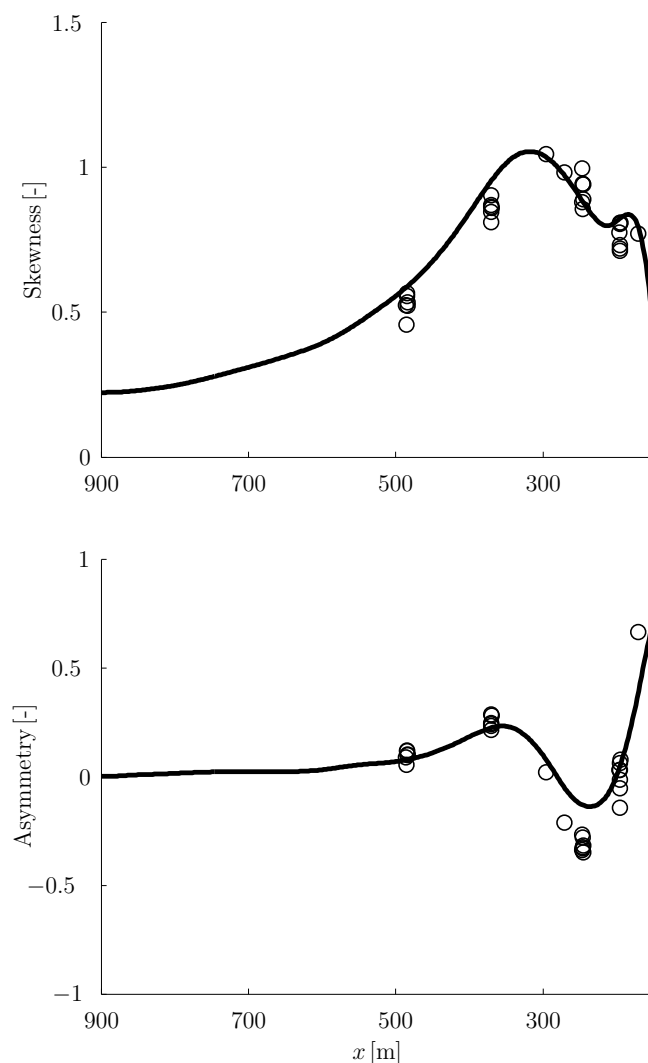


**Figure 5.13:** Comparison of observed (circles) and predicted (solid line) wave skewness (top panel) and asymmetry (lower panel) for August 10, 1997.

*September 9, 1997*
On September 9, 1997 a bi-modal wave field ($H_{m0} = 0.95\,\text{m}$), consisting of a main swell arriving from a Southerly direction ($\theta_m = -28^o$, $f_p = 0.08\,\text{Hz}$) and a Northerly ($34^o$), higher-frequency ($f_p = 0.18\,\text{Hz}$) sea, is incident at the FRF array (Figure 5.14).

The model-predicted spectral transformation is in very good agreement with observations (Figure 5.15 & 5.16), with the notable exception that at C and B the main peak is somewhat underestimated (Figure 5.16), which suggests that the model does not transfer sufficient energy back to the main peak. This is consistent with what was found in the comparison to the August 10 case, and – at least in part – attributable to relaxation being too strong, for such moderate conditions.

Although from the interaction rules for quadratic interactions we anticipate a cross-interaction between the non-collinear seas, such interactions are apparently very weak

for the present case, and do not result in noticeable energy transfers, neither in the observations nor in the model predictions (Figure 5.15 & 5.16). The weakness of these interaction configurations is attributed to the low energy levels of the Northerly sea, and the fact that generally the interaction between such widely separated (in directional space) spectral components is relatively farther from resonance than if they were near-collinear.
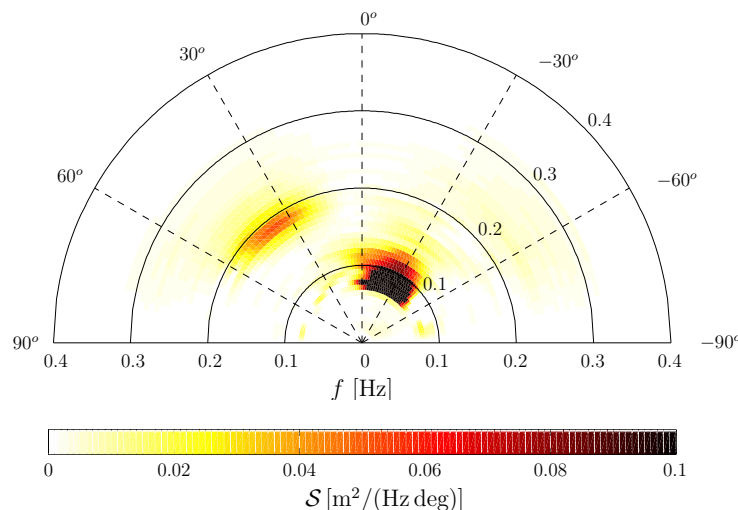


**Figure 5.14:** Observed two-dimensional spectrum at the FRF array on September 9, 1997. Bimodal wave field ($H_{m0} = 0.95\,\mathrm{m}$), consisting of primary swell ($f_p = 0.08$ Hz) from Southerly ($\theta_m = -28^o$) directions, and a shorter-period sea ($f_p = 0.18\,\mathrm{Hz}$) arriving from the North-East ($\theta_m = 34^o$).

The model-predicted spectra are directionally narrower than the observed ones, in particular those at the shallowest observational locations (Figure 5.16). Moreover, we note that the directions appear – on average – somewhat closer to shore-normal, indicating an overestimation of refraction effects. This is substantiated in Figure 5.17 showing directional spectra at $f = f_p = 0.08\,\mathrm{Hz}$, $f = 2f_p = 0.16\,\mathrm{Hz}$ and $f = 3f_p = 0.24\,\mathrm{Hz}$; at $2f_p$ and $3f_p$ the offshore-observed bimodal structure evolves, under the combined effects of nonlinear interactions and refraction, into a near unimodal distribution at the nearshore array B. Apart from a noticeable overly narrowing of the distribution, and prediction of energy at directions that are generally somewhat too close to shore-normal, the redistribution of energy over the directions is well represented by the model.
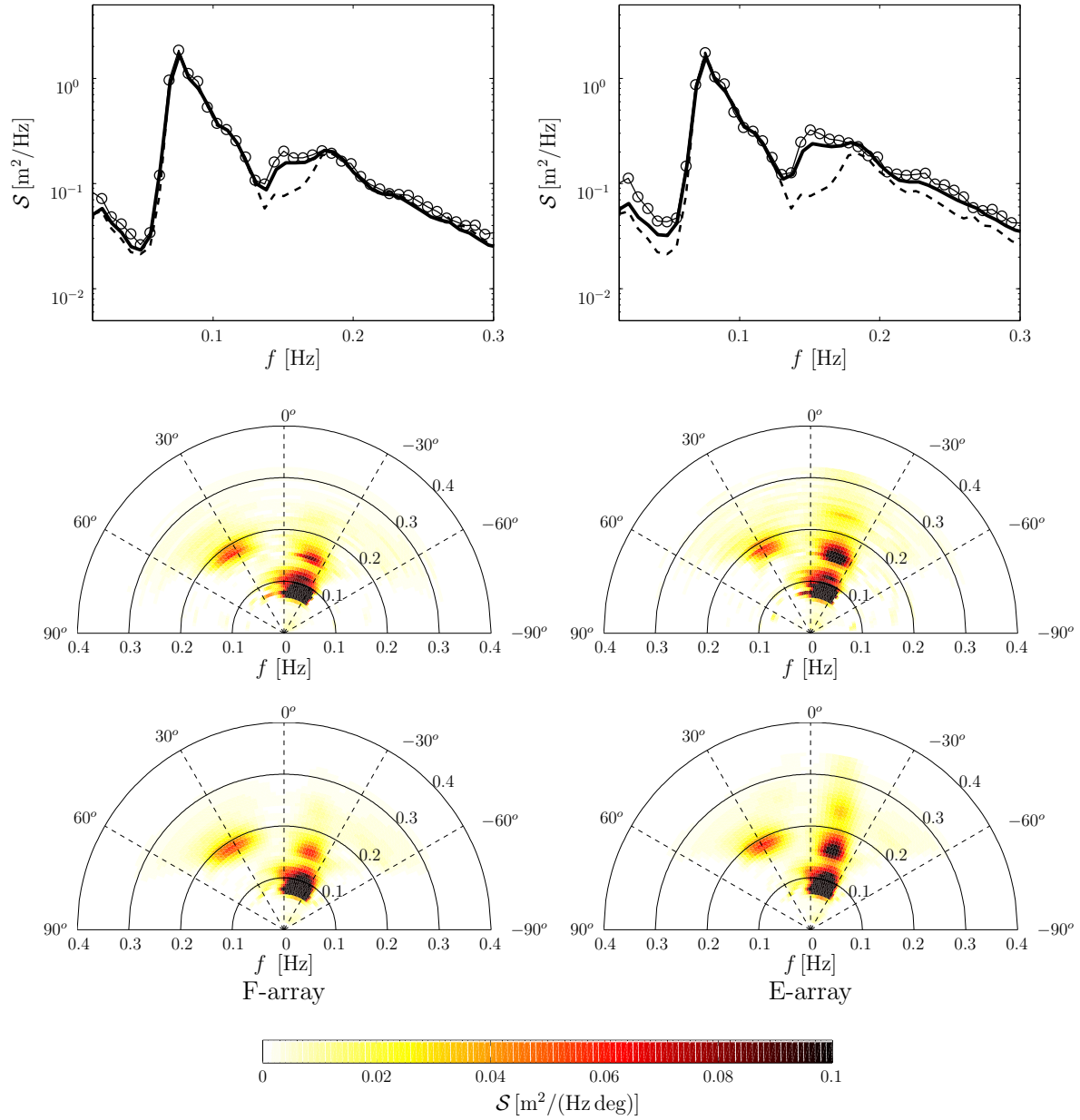
**Figure 5.15:** Comparison of observed and predicted spectra for September 9, 1997, at F- (left panels) and E-array (right panels). Top panels: observed (circles) and predicted (solid line) frequency spectra; dashed line represents offshore spectrum (FRF). Middle and lower panels are observed and predicted directional spectra respectively.
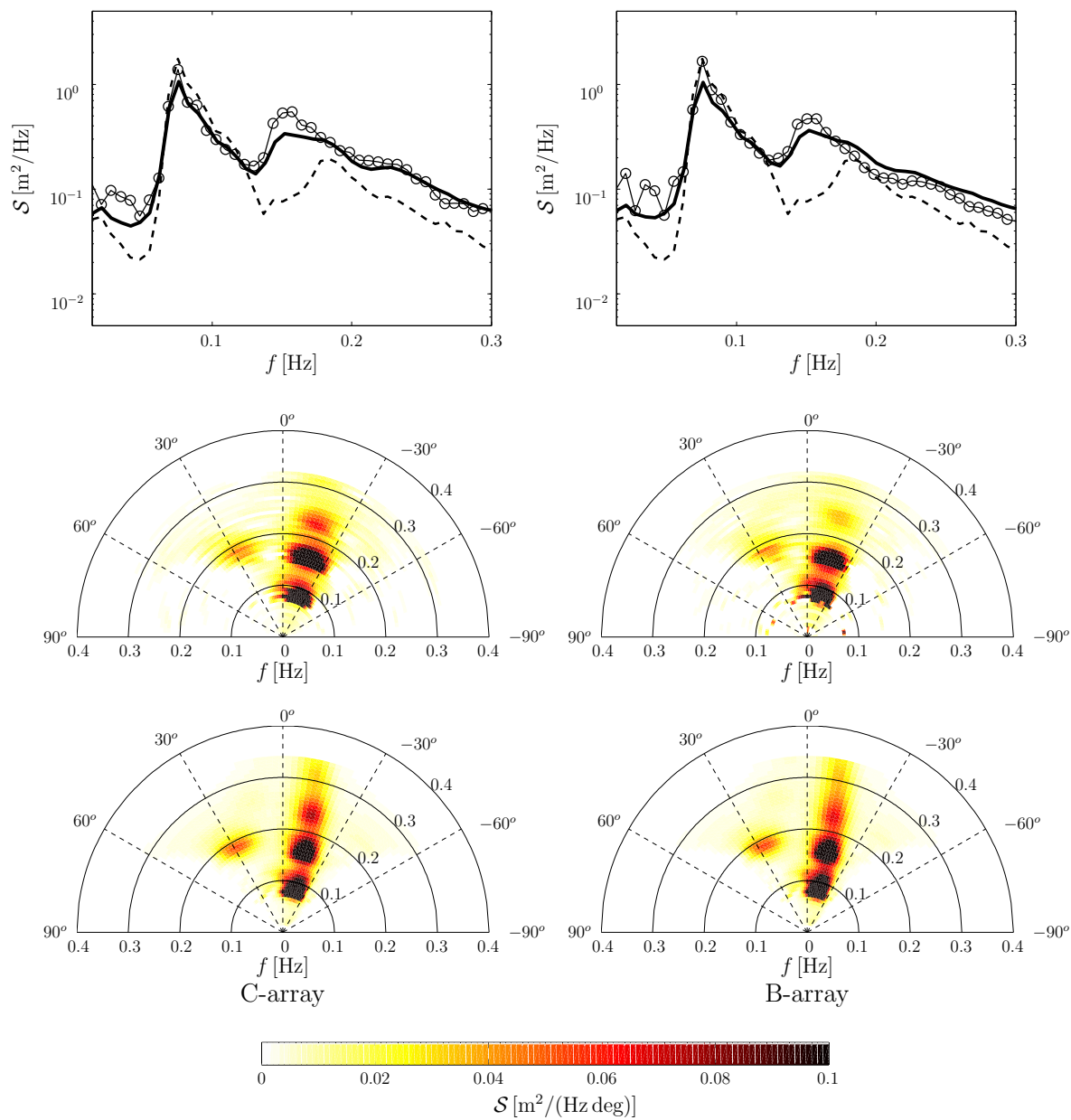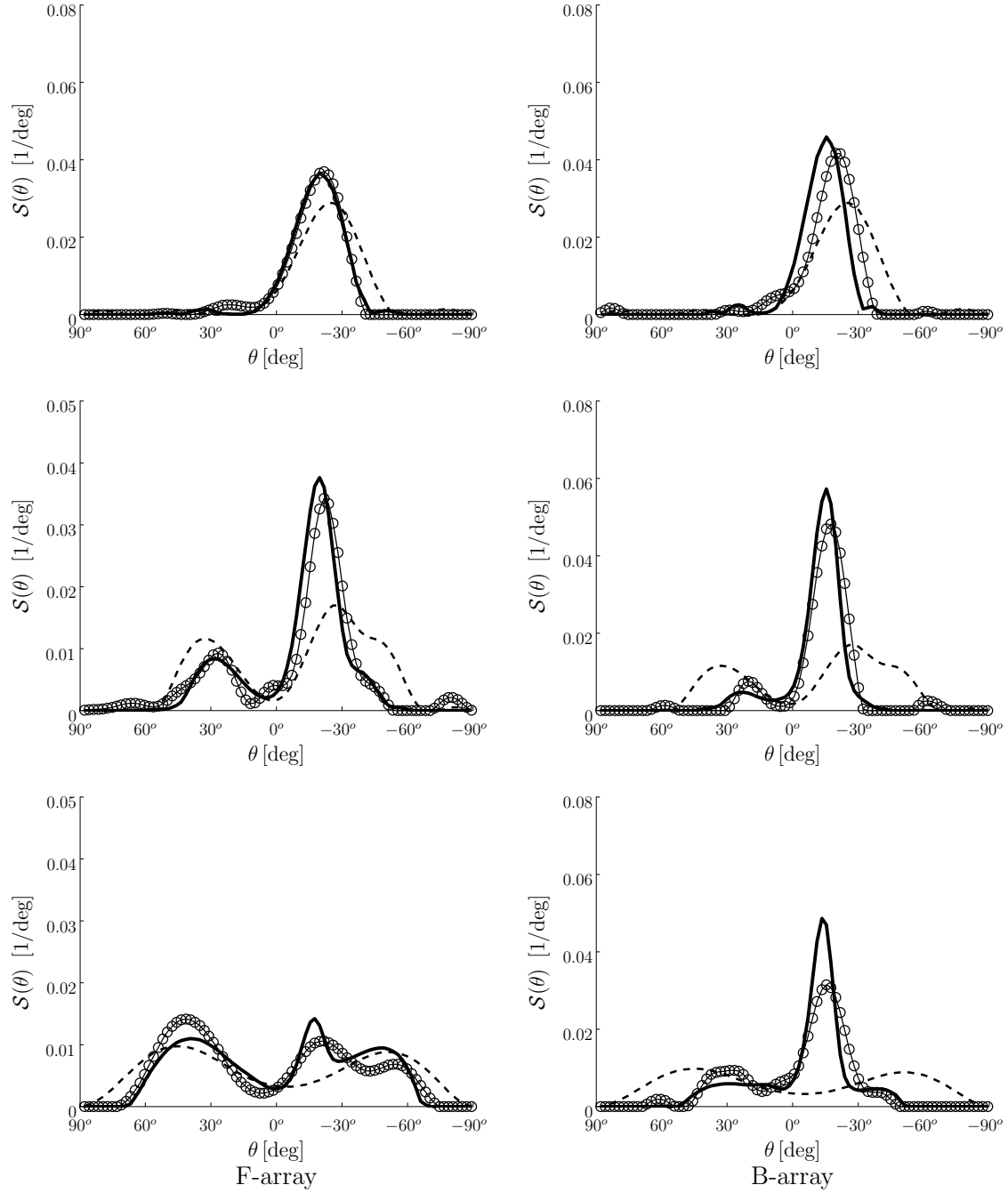
**Figure 5.16:** Comparison of observed and predicted spectra for September 9, 1997, at C- (left panels) and B-array (right panels). Top panels: observed (circles) and predicted (solid line) frequency spectra; dashed line represents offshore spectrum (FRF). Middle and lower panels are observed and predicted directional spectra respectively.

**Figure 5.17:** Evolution of observed (September 9, 1997) and predicted directional spreading $(\mathcal{S}(\theta) = \mathcal{S}(\theta, f)/\mathcal{S}(f))$ function at F-array (left panels) and B-array. Distributions shown for $f_p(= 0.08\,\mathrm{Hz})$ (top panel), $2f_p$ (middle panel), and $3f_p$ (bottom panel). Dashed line indicated offshore (FRF) spreading function, the circles and solid line are observations and predictions respectively.

### 5.4.2 Energetic conditions: dissipative nonlinear shoaling

For moderate conditions, in the absence of wave breaking in the observational area, the quasi-normal closure is accurate (relaxation is negligible) and the model is first-principle based, not involving tuneable, empirical parameters. For more energetic incident wave conditions, such considerations do not apply. With increasing nonlinearity and extended dissipative regions, closure relaxation and dissipation become important and may eventually dominate the nearshore evolution, introducing a dependency on parameterized physics and empirical coefficients. Comparison to observations of waves on the inner shelf under such storm conditions tests the transition from first-principle based modeling of the ensuing conservative processes, to a parametrized modeling of the inner surf zone.

*October 15, 1994*

On October 15 1994, an energetic, unimodal swell ($H_{m0} = 3.4$ m, $f_p = 0.09$ Hz) is incident at the FRF array (Figure 5.18); the waves are nearly shore-normally incident and exhibit moderate directional spreading. The incident wave energy is such that most instrument locations are well inside the surf zone.

Wave heights (Figure 5.18) decay gradually on the outer slope (seaward of the nearshore bar), followed by a fairly abrupt drop in wave height over the nearshore bar – indicating strong energy losses due to intense wave breaking – and a moderate decrease shoreward of the bar. Model-predicted wave height evolution is in good agreement with observations, although the breaker parameterization is unable to capture the abrupt decay across the sandbar.

Under the concomitant action of dissipation and nonlinear interactions, the spectrum evolves from fairly peaked at the offshore location, to a near-featureless spectrum at nearshore positions (Figure 5.19). The model-predicted evolution is generally in good agreement with observations. Notable exception is the fact that, at the most shoreward location ($x = 161$ m), the main peak is reduced to a local minimum, which is at variance with the observed spectra where the (initial) peak remains a local maximum. We hypothesize that this is due to an insufficient return of energy to the main peak when the waves traverse the trough ($200$ m $< x < 300$ m), indicating that the nonlinear coupling may be overly damped. In Figure 5.19 also predictions for $\beta = 0$ (QN, no relaxation) and $\beta = 2.5$ (RQN, stronger relaxation) are shown. Relaxation has a particularly large effect on model predictions in the very nearshore; omitting relaxation altogether ($\beta = 0$) renders the nearshore spectra quite irregular and at considerable variance with observations (e.g. $x = 161$ m in Figure 5.19). Stronger relaxation ($\beta = 2.5$) tends to produce smoother spectra.

Predicted skewness and asymmetry evolution is in good agreement with observations, although notably, on the outer slope, seaward of the bar, skewness values appear overestimated (Figure 5.20). Variations in $\beta$ affect the higher-order statistics. Without relaxation ($\beta = 0$) skewness is grossly over-estimated, while asymmetry ranges are considerably larger than observed. Increasing relaxation strength from $\beta = 1.5$ to $\beta = 2.5$ further
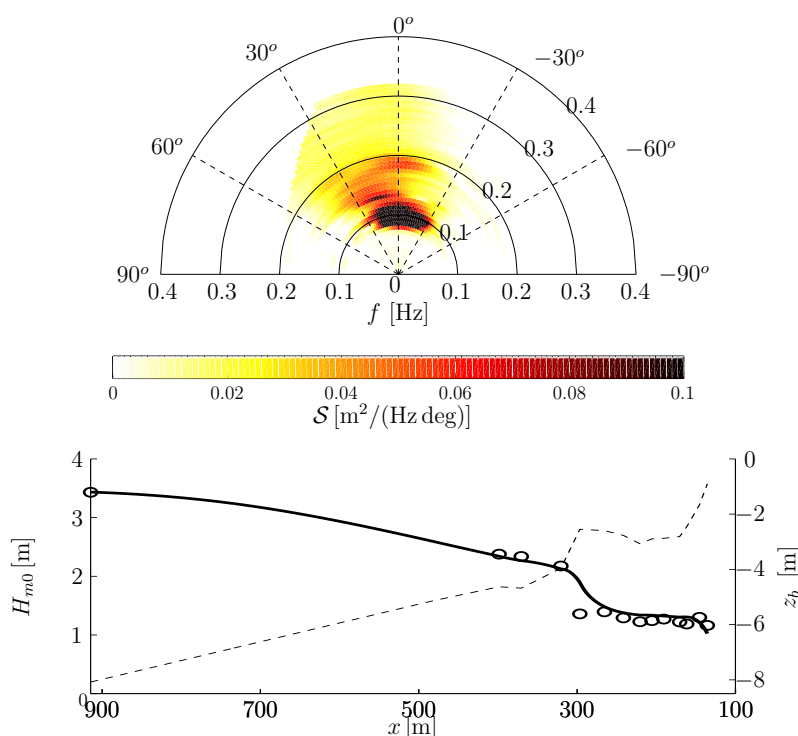
**Figure 5.18:** Observed two-dimensional spectrum at the FRF array on October 15, 1994 (top panel). Unimodal wave field, shore-normally incident ($\theta_m \approx 0$), with $f_p \approx 0.09$ Hz and $H_{m0} = 3.4$ m. Lower panel shows comparison of observed (circles) and model-predicted zeroth-moment wave heights (solid line, left axis); dashed line indicates the depth profile (right axis).

suppresses nonlinear coupling, resulting in lower skewness values and somewhat smaller asymmetry ranges.

Generally the agreement is fair and the improvements on account of the coupling relaxation are considerable when compared to model predictions utilizing the QN closure without relaxation. However, there remain some discrepancies in spectral shape, in particular the fact that spectra are overly smoothed, and skewness on the outer slope is over-predicted. The latter findings indicate that further refinement, either of the tuning parameter or – more fundamentally – the scaling of the relaxation term as a whole, is needed. The present work merely explores the potential of the approach, without performing a sensitivity analysis to determine optimal values of the empirical tuning coefficients [Herbers *et al.*, 2003]. Instead, we have used reasonable, and widely accepted, values for $B$ and $\gamma$ (tuning parameters for the dissipation terms), and an ad hoc choice for $\beta$. The fact that with a single $O(1)$ choice for $\beta$ ($\beta = 1.5$), kept constant for a wide range of conditions (computations with different values of $\beta$ are given solely for the purpose of illustration), good agreement to observations is generally found, evidently illustrates the robustness of the approach.
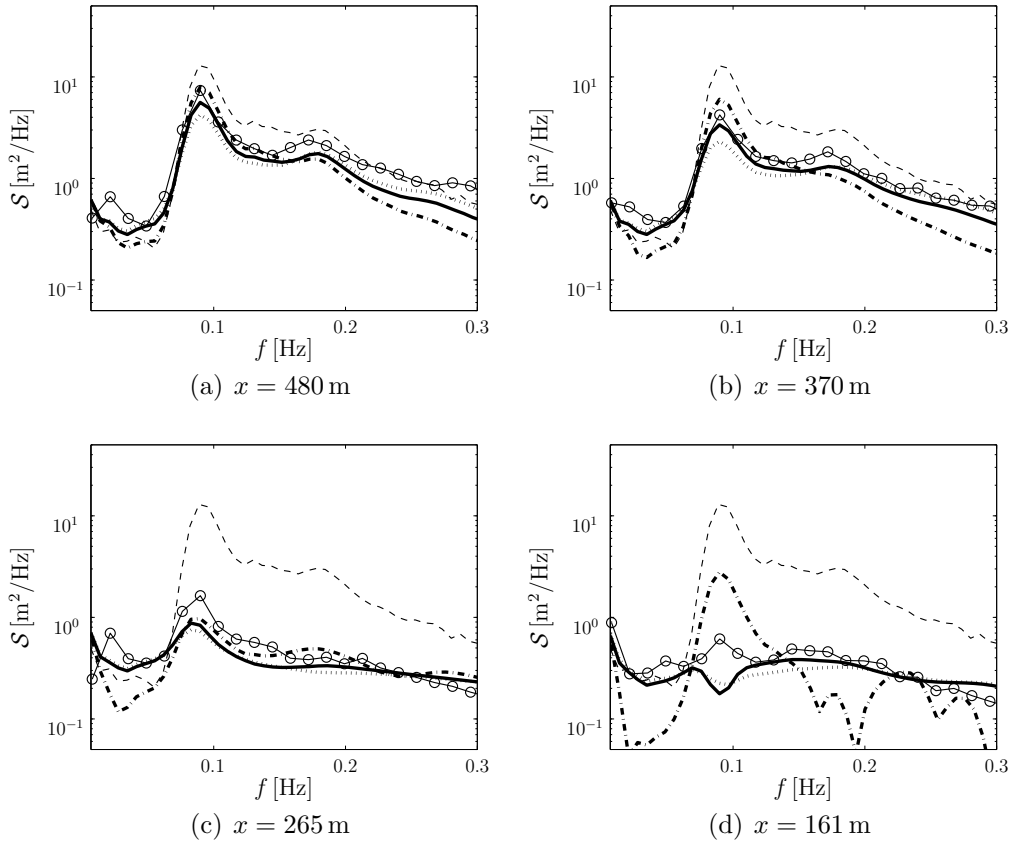
**Figure 5.19:** Comparison of observed (circles) and predicted spectra for October 15, 1994 at discrete cross-shore locations (see panel captions). Model predictions for $\beta = 0$ (dash-dot), $\beta = 1.5$ (solid line), and $\beta = 2.5$ (dotted line) are shown. The thin dashed line represents the offshore spectrum (FRF).
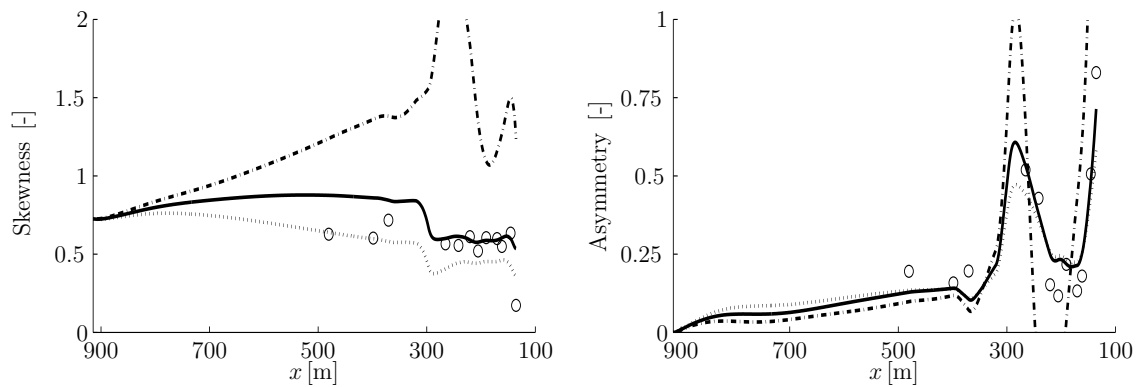


**Figure 5.20:** Comparison of observed (circles) and predicted skewness (top panel) and asymmetry (lower panel) for conditions October 15, 1994. Model predictions for $\beta = 0$ (dash-dot), $\beta = 1.5$ (solid line), and $\beta = 2.5$ (dotted line) are shown.

*October 19, 1997*

Observations on October 19 1997, recorded during Sandyduck, include measurements obtained at 20 m water depth (5 km offshore), which – when used as an offshore boundary – provides a means to assess the model's applicability on the scale of the extended coastal zone or inner shelf. The incident wave field consists of an energetic ($H_{m0} = 3.4$ m) unimodal (in frequency space) swell arriving from Northerly directions, including waves coming at very large angles (Figure 5.21). For these conditions the nearshore instruments – apart from the FRF array at 8 m depth – are well inside the surf zone.
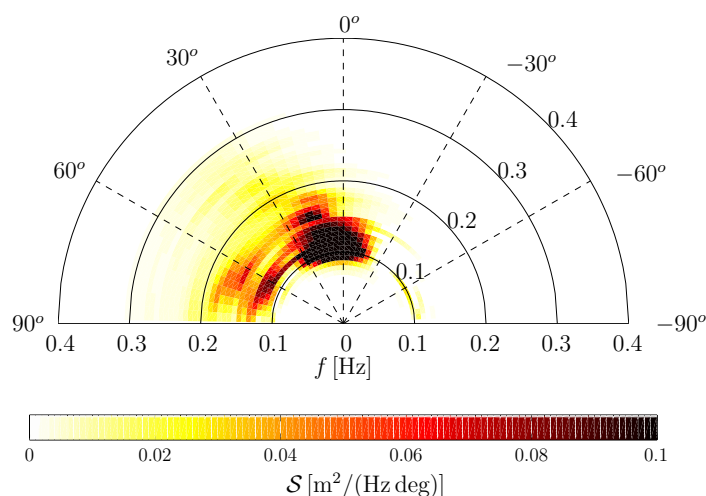


**Figure 5.21:** Observed two-dimensional spectrum at 20m-array on October 19, 1997. Wide-aperture incidence at extremely large angles (coming from Northerly directions) with $H_{m0} = 3.4$ m and $f_p \approx 0.13$ Hz.

The computations for this case are performed with a coarser spectral discretization than the previous cases; as before, 60 frequencies ($\Delta\omega = 0.0137\pi$ rad/s) are considered but the alongshore wavenumber array is reduced to 64 components with $\Delta\lambda = 0.0021\pi$ rad/m. Cross-shore step size is the same as before ($\Delta x = 0.5$ m).

To illustrate the effect of inclusion of the nonlinear terms, two additional linear model runs are performed, with distinct frequency-weighting of the dissipation: one with $r_0 = 0.1$ (see eq. (5.4) for definition) as in the nonlinear model, and another with $r_0 = 1$, implying distribution of the bulk dissipation in proportion to the local spectral density. The latter ($r_0 = 1$) is expected more realistic for a linear model since, in absence of nonlinearity, there is no cascade mechanism to sustain energy levels at higher frequencies.

Although observations along the cross-shore transect are sparse in most of the domain (only two observations over nearly 4 km in the offshore region), the comparison of computations to observations are useful to qualitatively assess shelf-scale application potential of the present modeling approach.
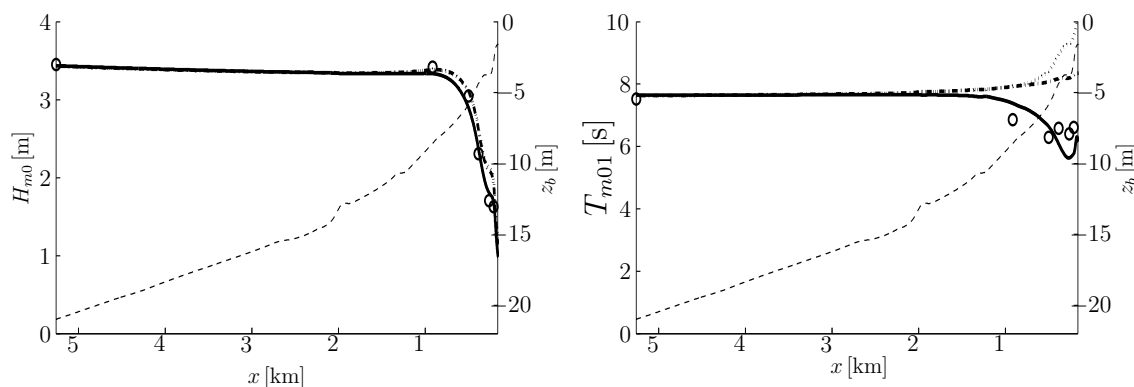
**Figure 5.22:** Observations October 19, 1997. Comparison of observed (circles) and predicted zeroth-moment wave heights (top panel) and mean periods ($T_{m01} = 2\pi m_0/m_1$, bottom panel). Solid line is nonlinear model prediction; dotted and dash-dot line represent linear model predictions with $r_0 = 0.1$ and $r_0 = 1$ respectively. The bottom profile is indicated with a dashed line.

Model-predicted wave heights are in good agreement with observations at the discrete locations where observations are available (Figure 5.22). In particular, wave heights are nearly constant seaward of the FRF array ($x = 900\,\mathrm{m}$) and decay rapidly shoreward of this location, indicative of intense dissipation due to depth-induced wave breaking (surf zone). The linear model predicts quite similar, but overall slightly larger, wave heights in the surf zone, for both values for $r_0$.

The nearshore evolution of the mean period $T_{m01} = 2\pi m_0/m_1$ is markedly different for the various model settings (lower panel Figure 5.22). In the linear model, without spectral redistribution due to nonlinearity, the mean periods increase with decreasing depth on account of the shoaling effects being strongest for the lower frequency components; for lower $r_0$ values this increase of the mean period is further amplified (more energy being dissipated at higher frequencies). This linear behavior contradicts the observed *decrease* of the mean period values in the nearshore. The decrease in mean period predicted by the nonlinear model, on account of the re-distribution of energy from the main peak to harmonic ranges, is in fair agreement with observations (Figure 5.22) .

The directionally integrated frequency spectra (Figure 5.23 & 5.24) predicted by the nonlinear model are in fair agreement with the observations, but do not fully resolve all the spectral features present in the observed spectra. In particular, the spectral trough in the observations around $0.04\,\mathrm{Hz}$ is lacking in the model predictions at the F-, E- and B-array. In contrast, the spectral shapes predicted by the linear model – although in reasonable agreement at the FRF array – are at considerable variance with the observations in shallow water. This comes as no suprise. After all, in the linear approximation, the spectral components evolve in isolation from their environment and the associated lack of spectral coupling deprives the model of a means to redistribute energy, causing the resulting frequency spectra to be overly peaked compared with the

near-featureless shapes (invariably) observed in shallow water [e.g. McKee Smith & Vincent, 2003].

The directional spectra (Figure 5.23 & 5.24) predicted by the nonlinear model are in fair agreement at the FRF, F- and E-array. However, for the nearshore C- (not shown) and B-arrays, the agreement is at best qualitative. The observed spectra have a wider support in directional space, while in frequency space they exhibit more variability than their model-predicted counterparts. The observed variance between predicted and observed spectral distributions can originate from various sources. Firstly, we have assumed a laterally uniform topography, which – given the present topography – is reasonable over short distances but may not be tenable when considering such long propagation distances. On a similar note, even when lateral depth variations were included, the model does not include resonant scattering on smaller-scale topography (Bragg scattering on topography with length scales of roughly half the surface wave length), the forward scattering component of which is known to attribute to an increase in directional width of the spectrum [Ardhuin & Herbers, 2002]. Secondly, including only the propagating modes at the offshore boundary implies an aperture limitation that is expected to contribute to the overly narrow (in the directional sense) predicted spectral shapes. Thirdly, the assumption of spatial homogeneity of the wave field at the 20 m location may not be warranted. Seaward of the 20 m array large scale topographical features are present, which may invalidate the assumed homogeneity of the wave field, both in the analysis of the data and the initiation of the model. Lastly, the omission of relevant physical mechanisms that may contribute to an increase in directional spreading. For such long propagation distances cubic resonances (quadruplet interactions), wind generation and e.g. steepness breaking ('whitecapping') may have to be accounted for. However, although the differences in directional spreading between predicted and observed spectra are most evident from the present case, similar differences were found in the comparison with observations from August 10 and September 9, which involved only moderate propagation distance and relatively shallow water. Therefore, we attribute the model-data variance primarily to a lack of model-representation of certain nearshore processes such as directional effects in breaking waves [Herbers *et al.*, 1999] or anomalous refraction due to the presence of shear instabilities in the nearshore current field [Henderson *et al.*, 2006].

Although the model-predicted directional spreading in the nearshore appears overly narrow in directional space and too spread out in frequency space, the overall agreement between observations and predictions is encouraging considering the large propagation distances and highly dissipative surf zone, which represents a severe test for the parameterizations of the stochastic closure and depth-induced breaking.
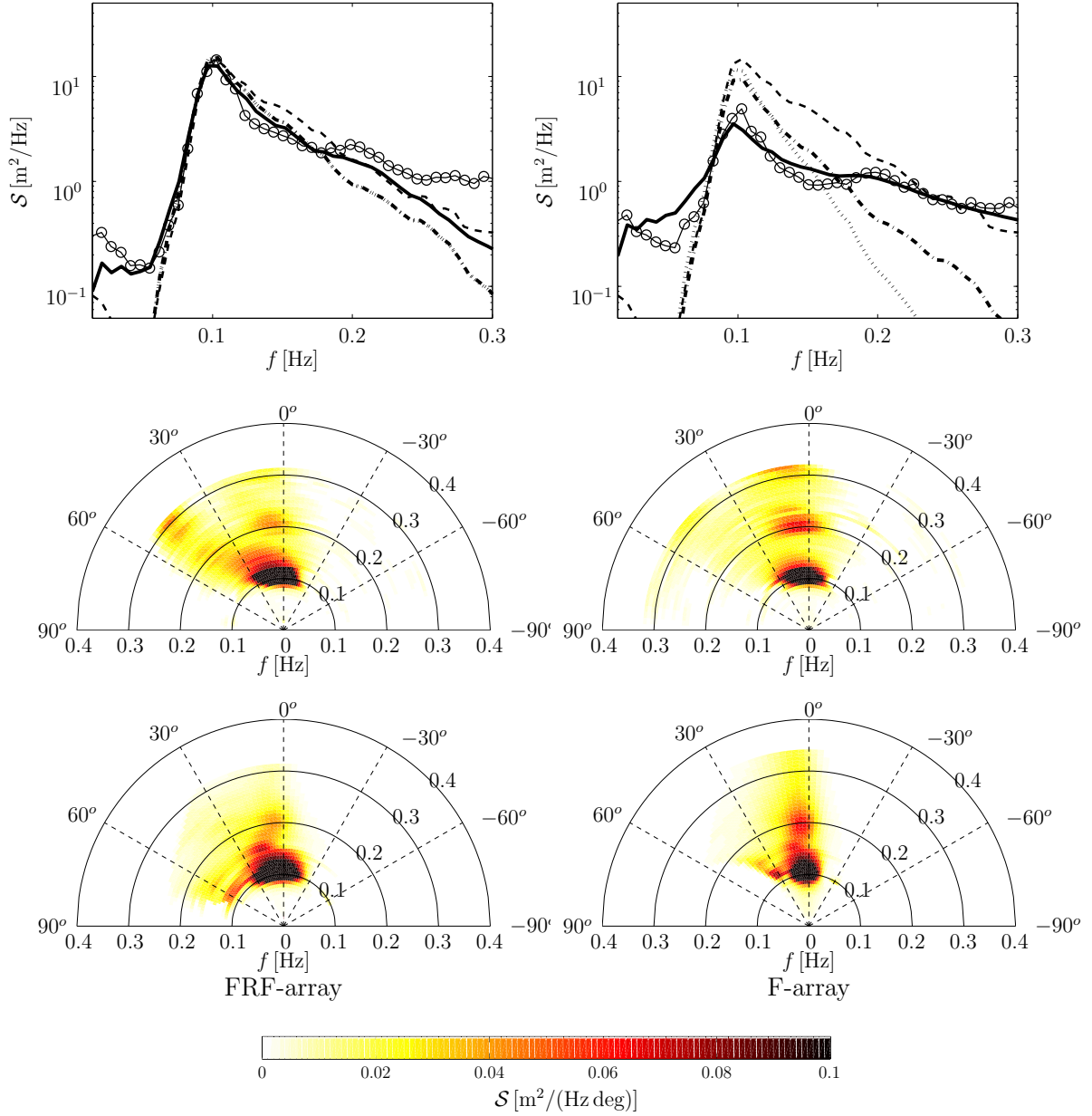
FRF-array

F-array

FRF-array

FRF-array

F-array

$\mathcal{S}\,[\mathrm{m^2/(Hz\,deg)}]$

**Figure 5.23:** Comparison of observed and predicted spectra for October 19, 1997 at FRF-
(left panels) and F-array (right panels). Top panels: observed (circles) and predicted (solid line)
frequency spectra; dotted and dash-dot line represent linear model predictions with $r_0 = 0.1$
and $r_0 = 1$ respectively; dashed line represents offshore spectrum (20m-array, 5 km offshore).
Middle and lower panels are observed and predicted directional spectra respectively.

**Figure 5.24:** Comparison of observed and predicted spectra for October 19, 1997 at E- (left panels) and B-array (right panels). Top panels: observed (circles) and predicted (solid line) frequency spectra; dotted and dash-dot line represent linear model predictions with $r_0 = 0.1$ and $r_0 = 1$ respectively; dashed line represents offshore spectrum (20m-array, 5 km offshore). Middle and lower panels are observed and predicted directional spectra respectively. Note difference in color scaling between left and right panels.
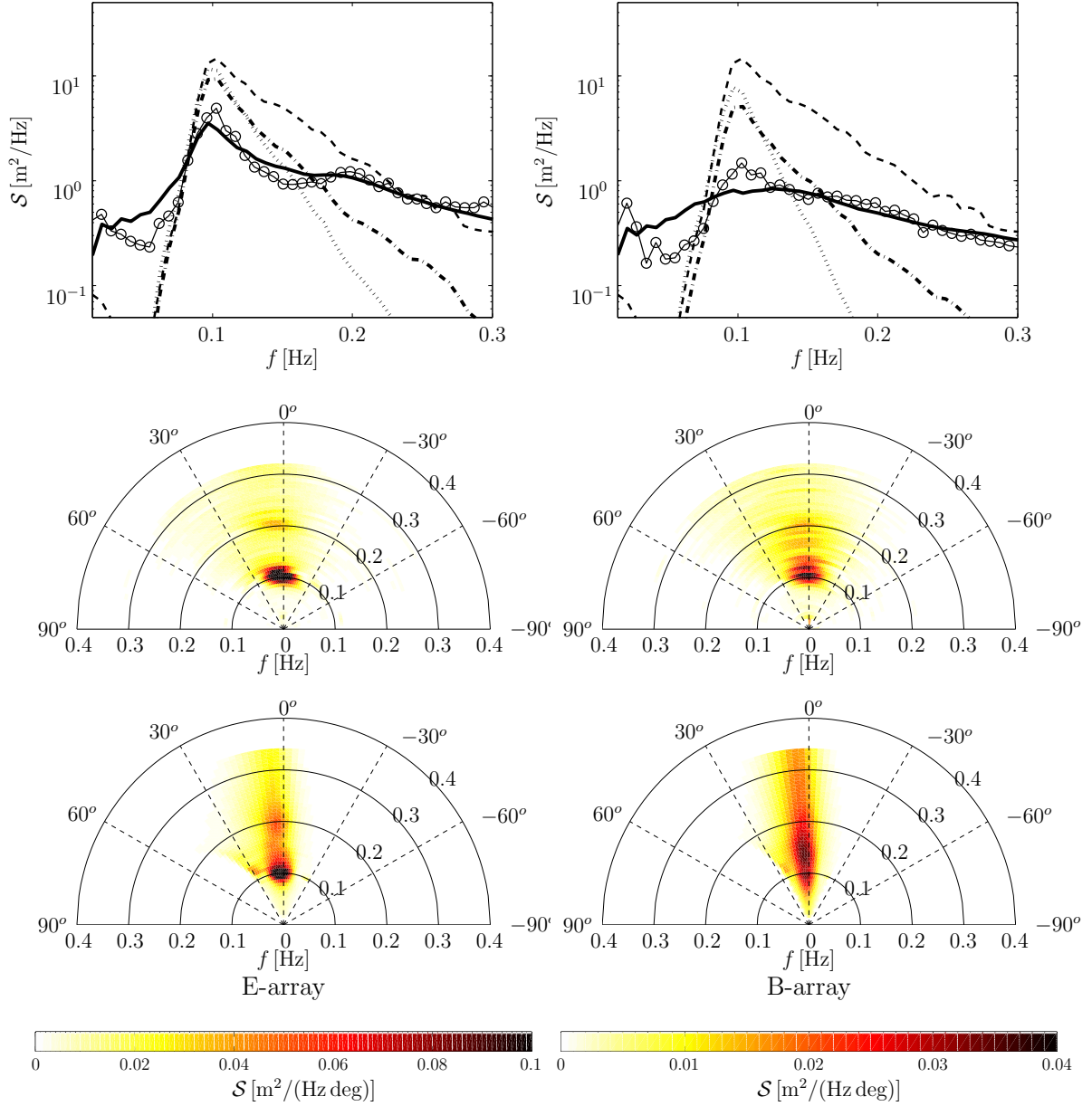
## 5.5  Discussion stochastic modeling approaches

### 5.5.1 Outlook on applicability

The stochastic angular spectrum formalism describes the propagation of random, directionally spread waves over laterally heterogeneous topography through a set of ODE's in one-dimensional, physical space $(x)$ for the three-dimensional (in spectral space) spectrum and five-dimensional bi-spectrum. The lateral heterogeneity thus comes at the expense of a dimensional extension by one in the lateral wavenumber space, consistent with the notion of a correlation function of a heterogeneous (or 'non-stationary' if the heterogeneity is in time) process, of which the spectrum is the (multi-dimensional) Fourier transform.

With the embedded parameterization of surf zone dynamics, the present modeling approach is applicable to typical operational scales in coastal engineering practice, including the very nearshore. However, through the omission of third-order interactions, it is implicitly restricted to relatively shallow water or relatively short length scales, over which higher-order contributions (e.g. cubic/quadruplet interactions) are ineffective. Moreover, for extended domains, physical processes other than those accounted for in the present model can contribute significantly to the wave field evolution. Likely candidates are the action of the wind on the fluid surface [Phillips, 1957; Miles, 1957] and the scattering of waves on meso-scale topography, or Bragg scatter [Mei, 1985; Ardhuin & Herbers, 2002]. However, stochastic formulations to account for e.g. wind, higher-order nonlinearity and bottom scatter are well established [e.g. Hasselmann, 1962; Cavaleri & Malanotte-Rizzoli, 1981; Ardhuin & Herbers, 2002] and if needed they can be added to the present stochastic evolution model in the form of additional forcing (source) terms.

In the nearshore, and in particular for highly energetic conditions, predicted spectra are narrower in directional space than observed spectra (§5.4). The fact that these mismatches occur consistently in the very nearshore, suggests that it is related to a nearshore scattering process for which the model does not account, such as directional scattering of breaking waves [Herbers *et al.*, 1999, 2003] and the interaction with nearshore currents [Henderson *et al.*, 2006].

Comparisons to observations indicate that the parameterization of depth-induced breaking and the stochastic closure approximation, to support wave propagation at high Stokes numbers, are robust. However, it is noted that spectra tend to be over-smoothed, and the decay of energy levels at the high-frequency spectral tail is too gradual. A possible remedy for the latter can be conceived through relaxation of the spectral tail to an equilibrium shape, the existence of which is indicated by recent empirical evidence [McKee Smith & Vincent, 2003].

Although the model is a stochastic one and does not resolve the individual waves, it must resolve the resonance mismatch, which – in relatively deeper water – implies variations on the intra-wave length scale. These rapid modulations are of no dynamical consequence, but constrain the grid spacing, a restriction that becomes particularly prohibitive when applied to larger domains, e.g. a typical coastal scale. This situation can

effectively be alleviated through a twofold extension. Firstly, the addition of a relaxation term to the transport equation for the bi-spectrum which is effective only in the off-resonant region (in contrast to the relaxation discussed in §4.4.3 which only acts close to resonance), and which enforces a return to the real bi-spectrum (quadrature), corresponding to the steady, Stokes solution ('Stokes relaxation'); secondly, the implementation of an adaptive step size algorithm in the numerical integration. Although adaptive step size algorithms are abundant and implementation is straightforward [Press *et al.*, 1986, and many others], they are wholly ineffective if the wave field evolution is characterized by incessant oscillations (of roughly the same length scale) throughout most of the domain. By means of the aforementioned damping these oscillations are made transient so that the use of a variable step size then provides a means to more efficiently advance the solution in space.

The abovementioned 'Stokes relaxation' can be formulated as follows. Starting from the one-dimensional bi-spectrum equation of §4.4.3, without dissipation and the relaxation, written as

$$\frac{d\mathcal{C}_{12}}{dx} = i\Lambda_{12}\mathcal{C}_{12} + 2i\mathcal{Q}_{12} = i\Lambda_{12}\left[\mathcal{C}_{12} + \frac{2\mathcal{Q}_{12}}{\Lambda_{12}}\right]. \tag{5.16}$$

For off-resonant conditions and a horizontal bottom, the solution reads

$$\mathcal{C}_{12}(x) = -2\frac{\mathcal{Q}_{12}}{\Lambda_{12}}\left(1 - \exp\left[i\Lambda_{12}x\right]\right) + \mathcal{C}_{12}(0)\exp\left[i\Lambda_{12}x\right]. \tag{5.17}$$

Clearly, when initialized with $\mathcal{C}_{12}(0) = -2\mathcal{Q}_{12}/\Lambda_{12}$, the bi-spectrum will take a real, constant value, placing the interactions in quadrature, rendering the trivial case where energy transfers are absent. However, in anticipation of spectral evolution, which – irrespective of the choice of initialization – will occur when traversing topography, it is more instructive to consider the case $\mathcal{C}_{12}(0) = 0$. This case is typified by (rapid) modulations on account of the exponential function $\exp\left[i\Lambda_{12}x\right]$, which represents the sort of modulations we wish to suppress. The Stokes relaxation is obtained by adding damping to (5.16) in the form

$$\frac{d\mathcal{C}_{12}}{dx} = (i - \operatorname{sgn}(\Lambda_{12})\alpha)\Lambda_{12}\mathcal{C}_{12} + 2(i - \operatorname{sgn}(\Lambda_{12})\alpha)\mathcal{Q}_{12}$$

$$= (i - \operatorname{sgn}(\Lambda_{12})\alpha)\Lambda_{12}\left[\mathcal{C}_{12} + \frac{2\mathcal{Q}_{12}}{\Lambda_{12}}\right], \quad (5.18)$$

with $\alpha$ a real and positive tunable constant, the solution relaxes to

$$\lim_{x\to\infty}\mathcal{C}_{12}(x) = \lim_{x\to\infty} -2\frac{\mathcal{Q}_{12}}{\Lambda_{12}}\left(1 - \exp\left[(i - \operatorname{sgn}(\Lambda_{12})\alpha)\Lambda_{12}x\right]\right) = -2\frac{\mathcal{Q}_{12}}{\Lambda_{12}}. \tag{5.19}$$

This form of damping, through the scaling with $|\Lambda_{12}|$, is effective only in the off-resonant region and enforces a return to the steady, quadrature bi-spectrum, which corresponds to Stokes second-order theory.

Note that when considering the bi-spectral evolution equation in isolation of the energy equation, and considering $\mathcal{Q}_{12}$ a constant, it can be argued that similar damping characteristics can be obtained by simply adding a linear damping term of the form $-\alpha|\Lambda_{12}|\mathcal{C}_{12}$. Although internally consistent, this would imply a phase-shifted (thus complex) steady state, consequently resulting in a continuous energy transfer across the triad constituents, which must be rejected on physical grounds.

### 5.5.2 Diffraction of random wave fields around thin barriers

The stochastic angular spectrum approach has been shown successful at modeling the physics of a refractive focus (§5.3.1), including the effects of diffraction and coherence in crossing wave trains behind a topographical lens. In fact, the present stochastic modeling approach inherits its wide-aperture diffraction capability from the underlying, deterministic framework [Stamnes, 1986; Dalrymple & Kirby, 1988]. Consequently it is expected to be particularly well-suited for wide-angle diffraction in random, directionally spread waves as typically encountered around thin barriers such as e.g. breakwater tips or harbor entrances.

Conventional stochastic models [e.g. Komen *et al.*, 1994; Booij *et al.*, 1999] are generally of limited use in such regions. Firstly, this class of models assumes homogeneity of the wave field, a premise, which – for the conditions mentioned – is invalid [see e.g. O'Reilly & Guza, 1991]. Secondly, they are based on the refraction or geometrical optics approximation that does not account for the effects of diffraction. Although phase-decoupled (homogeneous) diffraction approximations can improve the predictive capability around harbor mouths and breakwaters [e.g. Holthuijsen *et al.*, 2003], the heterogeneity of the waves remains unaccounted for.

To illustrate how the present formalism – in the linear approximation – can be applied around thin barriers we consider an idealized breakwater gap problem, with the depth momentarily assumed uniform and the breakwater represented as a thin, impermeable barrier along the line $x = 0$. A gap through which the waves can penetrate extends over $-G_1 < y < G_2$. Waves originate from sources in the half plane $x < 0$, in which region the spectrum is known. The objective is to determine the spectrum in the half plane $x > 0$ from the matching condition at $x = 0$; the latter is obtained from geometrical optics, an approximation which is commonly referred to as the physical optics or Kirchhoff approximation, and reads

$$\left.\frac{d\Phi}{dx}\right|_{0^+} = \begin{cases} \left.\frac{d\Phi}{dx}\right|_{0^-}, & -G_1 < y < G_2 \\ 0, & -G_1 > y > G_2 \end{cases} \tag{5.20}$$

where $x = 0^{+/-}$ denotes locations just inside/outside the domain $x > 0$. Say that the potential function at $x = 0^-$ is written as

$$\Phi(0^-, y, z, t) = \sum_{\boldsymbol{v}_1} \widetilde{\varphi}_{1,i}^1(x) \frac{\mathrm{Ch}\, Q_1}{\mathrm{Ch}\, q_1} \exp\left[i(\lambda_1 y - \omega_1 t)\right]; \qquad \frac{d\widetilde{\varphi}_{1,i}^1}{dx} = i\varkappa_1^1 \widetilde{\varphi}_{1,i}^1, \tag{5.21}$$

where the subscript i on $\widetilde{\varphi}_{1,i}^1$ designates the incident wave field. Through the matching at the gap (viz. (5.20)), we find

$$\mathcal{S}(\omega_1, \lambda_1, \lambda_2, x^+) = \frac{1}{\pi^2} \int d\lambda_3 \frac{(\varkappa_1^3)^2}{\varkappa_1^1 \varkappa_1^2} \mathcal{S}(\omega_1, \lambda_3, 0^-) \frac{\sin\left((\lambda_3 - \lambda_1)G_m\right)}{(\lambda_3 - \lambda_1)} \frac{\sin\left((\lambda_3 - \lambda_2)G_m\right)}{(\lambda_3 - \lambda_2)}$$
$$\cdot \exp\left[i\left((\varkappa_1^1 - \varkappa_1^2)x + (\lambda_1 - \lambda_2)G_\Delta\right)\right], \quad (5.22)$$

where $G_m = (G_1 + G_2)/2$ and $G_\Delta = (G_1 - G_2)/2$. The $\mathcal{S}$ are surface elevation spectra defined as

$$\mathcal{S}(\omega_1, \lambda_1, \lambda_2, x^+) = \lim_{\Delta\omega, \Delta\lambda \to 0} \frac{\langle \widetilde{\zeta}_1^1 (\widetilde{\zeta}_1^2)^* \rangle}{\Delta\omega \Delta\lambda^2}, \qquad \mathcal{S}(\omega_1, \lambda_3, 0^-) = \lim_{\Delta\omega, \Delta\lambda \to 0} \frac{\langle |\widetilde{\zeta}_{1,i}^3|^2 \rangle}{\Delta\omega \Delta\lambda}. \quad (5.23)$$

The $\widetilde{\zeta}_1^1$ denotes the surface elevation amplitude which, in the present linear approximation, is related to the potential amplitude through $\widetilde{\zeta}_1^1 = -i\omega_1/g\widetilde{\varphi}_1^1$. Local spectra (in the lateral sense) in the half plane $x^+$ are readily obtained through (viz. §4.2)

$$\mathcal{S}(\omega_1, \lambda, y, x^+) = \int \mathcal{S}(\omega_1, \lambda + \lambda'/2, \lambda - \lambda'/2, x^+) \exp\left[i\lambda'y\right] d\lambda'. \quad (5.24)$$

For the present, uniform depth case, the algebraic relations (5.22) and (5.24) determine the wave spectrum at any location in the half plane $x^+$ from the known spectrum at $x = 0^-$.

This solution is not exact. Its approximate nature, even apart from the simplifications implied by the use of an inviscid theory, originates from the use of geometrical optics for the matching condition (5.20), and the neglect of evanescent modes [Stamnes, 1986]. Nevertheless, it is a first-principle based description of the evolution of directional spectra, including the effects of diffraction in laterally heterogeneous wave fields, which – as such – may be suitable for engineering purposes e.g. for determining wave-induced forces on mooring systems in sheltered areas.

To verify the present stochastic representation of diffraction around thin barriers, we compare our stochastic model to analytical expressions for wave diffraction around obstacles [Penney & Price, 1952]. We consider two cases: a semi-inifinite screen ($G_1 = L_y/2$, $G_2 = 0$, $L_y$ is the lateral extent of the domain) and a breakwater gap ($G_1 = G_2 = 2.65$ wavelengths $\ll L_y$). The expressions in Penney & Price [1952] for the semi-infinite screen represent the exact solution by Sommerfeld [1896]. The expressions for the breakwater gap (their eq.'s (39-40) and (43)) are not exact as the secondary diffraction waves are omitted; however, the approximation is very good for gaps wider than a wavelength. To be consistent with the angular spectrum model, which considers solely wave components that propagate into the positive half plane, we omit the contribution from the reflected waves in the Penney & Price expressions.

For both cases we consider a monochromatic wave field incident in the outer domain ($x^-$) with angular frequency $\omega = \pi$ rad/s; the relative water depth $kh = 1.2$. Since we

(a) Semi-infinite breakwater
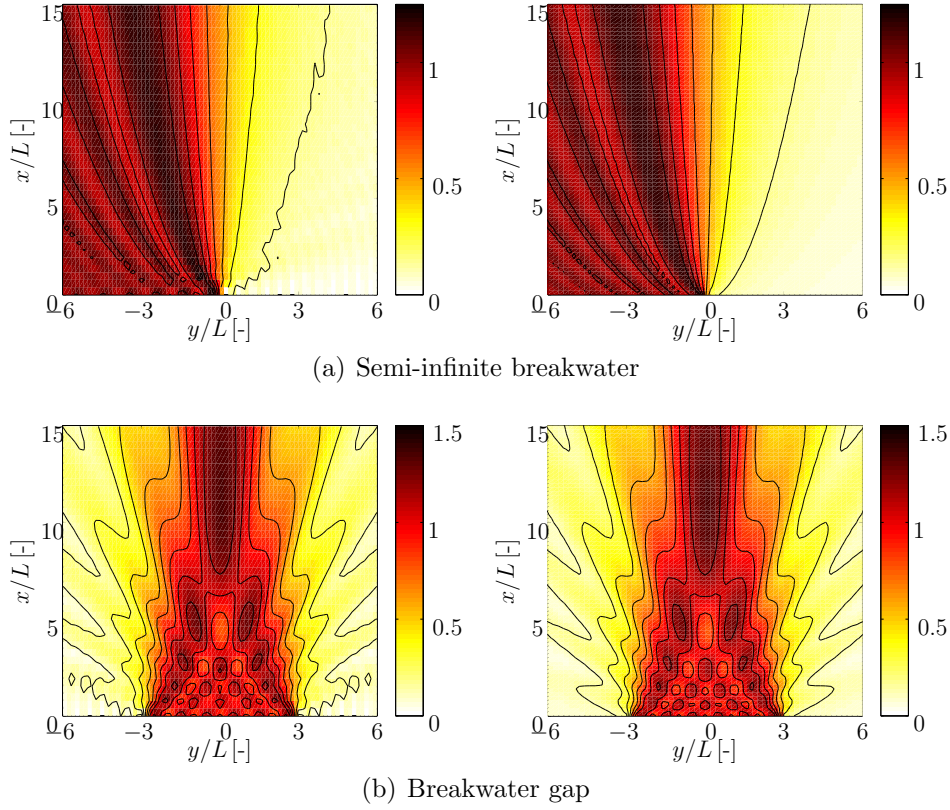


(b) Breakwater gap

**Figure 5.25:** Contours of (normalized) wave height behind semi-infinite breakwater (top panels) and breakwater gap (lower panels). Comparison between stochastic angular spectrum model (left panels) and analytical expression [Penney & Price, 1952] (right panels).

presently consider the stochastic model in the linear approximation the wave height is arbitrary. The discrete spectrum predicted by the stochastic angular spectrum model (SAM) can be written as

$$\mathcal{S}(\omega, \lambda_1, \lambda_2, x) = \frac{\Delta\lambda}{\pi^2} \frac{(\varkappa_1^{\lambda=0})^2}{\varkappa_1^1 \varkappa_1^2} \mathcal{S}(\omega, 0, 0^-) \frac{\sin(\lambda_2 G_m)\sin(\lambda_1 G_m)}{\lambda_1 \lambda_2}$$
$$\cdot \exp\left[i\left((\varkappa_1^1 - \varkappa_1^2)x + (\lambda_1 - \lambda_2)G_\Delta\right)\right], \tag{5.25}$$

with $\sin(\lambda_j G_m)/\lambda_j$ replaced by $G_m$ if $\lambda_j = 0$. Since the discrete SAM formalism implies laterally periodic boundary conditions we consider a domain sufficiently wide such that the boundary periodicity does not affect the region of interest. Accordingly we set $\Delta\lambda = k/80$ and the discrete lateral wavenumber arrays for $\lambda_1$ and $\lambda_2$ range $[-79\ldots79]\Delta\lambda$. The spatial domain is discretized as $\Delta x = \Delta y = 1\,\mathrm{m}$.

In Figure 5.25 we show normalized, two-dimensional wave height variations predicted by the SAM model and the analytical model in the diffraction area for the semi-infinite breakwater and the breakwater gap case. Apart from minor differences in the near field of the line $x = 0$, attributed primarily to the neglect of evanescent modes in the SAM formalism, the wave height variations are in good agreement. The quantitative

(a) Semi-infinite breakwater



(b) Breakwater gap
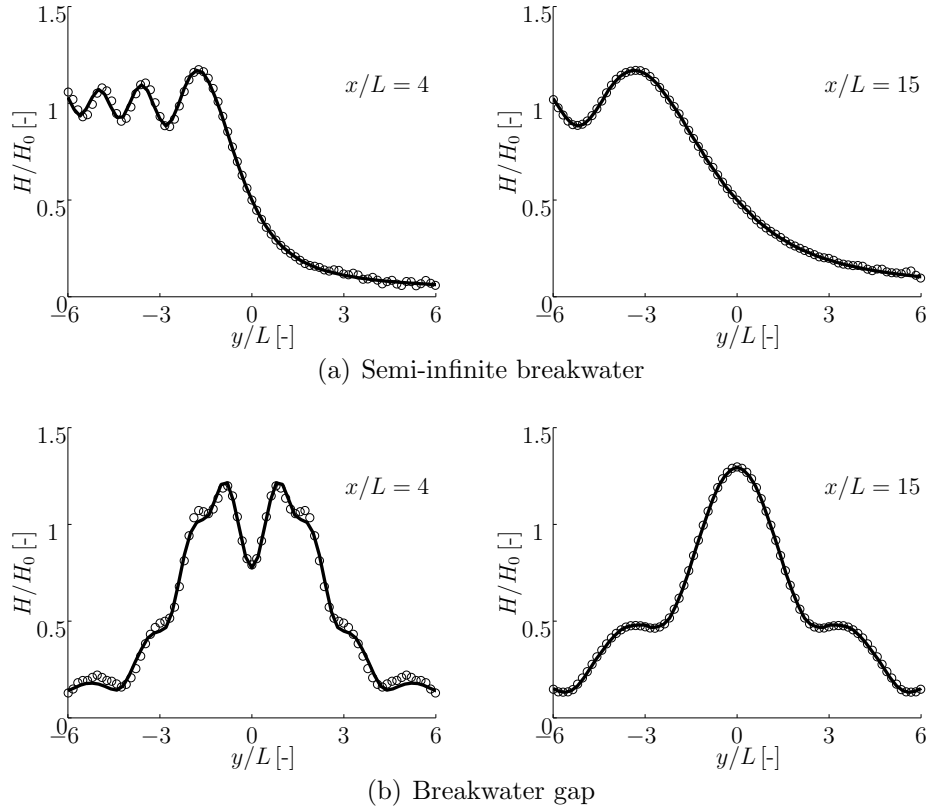
**Figure 5.26:** Comparison of normalized wave height along transects (transects indicated in figures); solid line represent analytical model predictions [Penney & Price, 1952], circles are predictions stochastic angular spectrum model.

agreement along transects is excellent (Figure 5.26), in particular along the transect farthest away from $x = 0$. This confirms that the SAM model accurately accounts for wide-angle diffraction and coherence in heterogeneous wave fields.

For illustrational purposes we have considered the simplest non-trivial cases and verified the stochastic model's diffraction capability through comparison to well-known analytical expressions for pure diffraction of a monochromatic wave field. Naturally, the stochastic model is not restricted to such narrow-band wave fields but is suited for arbitrary spectral shapes in frequency and directional space from which, through similar operations, the diffracted, nonhomogeneous wave spectrum can be computed. Moreover, this reasoning can be extended to less trivial cases involving shoaling, lateral depth variations, nonlinearity and potentially even breaking waves. For such cases, the matching condition (5.20) provides a boundary condition for the domain $x^+$, on the basis of which the spectral evolution inside the domain of interest can be computed utilizing the more general SAM2D implementation (§5.1).

# Wave-group induced long waves over varying depth **6**

In shallow coastal waters, near-resonant quadratic interactions enhance harmonics, and amplify wave motion at beat-frequency ranges (typically $0.004 - 0.04\,\mathrm{Hz}$). The latter are an important factor in the driving of nearshore morphological evolution [e.g. Symonds *et al.*, 1982; Roelvink & Stive, 1989]. The depth modulations associated with these long waves affect design wave height on coastal structures and the excitation of resonant modes can be important for the design of harbors and large-vessel mooring systems.

Munk [1949] was the first to report observations of this class of low-frequency (lf) motion which – based on his inference that these waves are induced by the variability of wave-induced mass transport into the surf zone – he coined *surf beat*[†]. Observations by Tucker [1950] confirmed the linear relation between the amplitude of the incident swell and the amplitude of the attendant beat motion reported by Munk. Also, Tucker cross-correlated the short-wave envelope and the local low-frequency motion, one thousand yards offshore, and found a distinct peak of negative correlation at a lag approximately equal to the sum of the travel times of a wave group travelling to the shoreline and of a free wave, reflected from the shoreline, returning to the position of observation. Although the conceptual notion of variable mass-transport into the surf zone is consistent with the observed time lag, it is at variance with the observed linear dependence on incident wave height and the correlation being *negative* at the appropriate time lag.

By solving the governing equations to second-order in nonlinearity, Biésel [1952] and later Longuet-Higgins & Stewart [1962] showed that the modulations in the primary wave field induce water level variations, usually referred to as *bound* or *forced* long waves, such that the water level is depressed under groups of high waves. The conceptual model of radiation-stress variations forcing beat-frequency waves [Longuet-Higgins & Stewart, 1962] is consistent with the negative correlation reported by Tucker, however,

---

[†]In the literature these lf wave motions, occurring at beat frequencies of the primary waves, are often referred to by the synonyms 'infragravity waves' [e.g. Reniers *et al.*, 2002; Van Dongeren *et al.*, 2003; Janssen *et al.*, 2003], 'surfbeat' [Munk, 1949] and 'subharmonics' [Janssen *et al.*, 2003; Battjes *et al.*, 2004]. We will refrain from their use here. This is a matter of preference, substantiated somewhat by the following considerations. The term 'infragravity' suggests that gravity is not the restoring force, which is at variance with our conceptual understanding of their physics. Although historically justified, 'surfbeat' reflects the (incomplete) inference that these beat motions solely originate from surf zone processes. The wording 'subharmonics' is ambiguous as it is extensively used in various fields of physics to indicate motion at integer fractional frequencies of the primary harmonic frequencies [Guza 2005, personal communication].

the antinomy with the observed linear dependence on incident swell amplitude remains. With respect to the latter, Longuet-Higgins and Stewart argued (similar to an argument used by Tucker) that, since waves of smaller amplitude are allowed to propagate into shallower water, and thus are amplified more strongly, the relation between swell and low frequency is at least weaker than quadratic (and thus closer to the observed linear one).

The shallow-water asymptote of the equilibrium response derived by Longuet-Higgins & Stewart [1962], upon substituting Green's law for the primary wave amplitude variation, predicts an amplitude variation of the bound wave proportional to $h^{-5/2}$; the latter is often interpreted as a shoaling law (although Longuet-Higgins and Stewart do make reservations about this). This interpretation is generally incorrect. After all, the uniform-depth solution does not account for the depth variability. Moreover, the premise of the primary waves being in shallow water (Green's law shoaling), is inconsistent with the notion of an (off-resonant) bound wave and instead the wave evolution should be described by near-resonant interaction theory [e.g. Mei & Ünlüata, 1972; Bryant, 1973, see also Chapter 2].

In a saturated surf zone, a modulated incident wave train gives rise to excursions of the initial point of wave breaking at the time and length scale of the wave modulation. Symonds et al. [1982] show that for a weakly-modulated incident wave train this results in radiation of free long waves away from the region of initial breaking. Symonds & Bowen [1984] extend this model to include a barred depth profile shoreward of the breaking region, allowing a half-wave resonance in that region; in particular they investigate the coincidence of this resonance condition with that of the quarter-wave resonance of the moving breakpoint mechanism. Both models neglect incident forced lf wave motion, but since the description of the low frequency motion is linear, solutions may be superposed.

Schäffer [1993] presents a semi-analytical model that combines long wave generation due to variations in the initial breakpoint position, with local forcing due to modulations of the primary waves both inshore (partial transmission of modulation) and offshore of the breakpoint for a plane sloping beach. Various numerical models, capable of modeling the forcing of lf wave motion by considering spatial gradients in the radiation stress function, were developed [e.g. Van Leeuwen & Battjes, 1990; Van Leeuwen, 1992; List, 1992; Roelvink, 1993; Reniers et al., 2002; Van Dongeren et al., 2003].

Several experimental laboratory studies of the generation and propagation of lf motion on beaches, have been conducted [e.g. Mansard & Barthel, 1984; Kostense, 1984; Van Leeuwen, 1992; Janssen et al., 2000; Baldock et al., 2000]. Kostense [1984] performed experiments on a relatively steep beach $(1:20)$ and found qualitative but poor quantitative agreement with predictions of the Symonds et al. model. Observations by Mansard & Barthel [1984] on a $1:40$ beach and those reported by Janssen et al. [2000] on a $1:50$ beach, indicate a dominance of the group-bound long waves accompanying (but lagging) the short-wave groups over the varying depth. In contrast, Baldock et al.

[2000], performing experiments on a 1 : 10 slope, attribute the attendant lf wave motion mainly to the time variation of the initial breakpoint. The prevalence of either breakpoint radiation of long waves or shoaling enhancement of group-forced waves is related to the relative bed slope by Battjes *et al.* [2004]; this supports earlier suggestions by e.g. List [1992] and is consistent with empirical evidence.

In the field, the generation and propagation of lf motion in the nearshore region is complicated due to the two-dimensional nature of the wave field and bed topography. Refractive trapping of long waves may occur, resulting in edge waves [e.g. Gallagher, 1971; Bowen & Guza, 1978]. Field observations [e.g. Elgar *et al.*, 1992; Okihiro *et al.*, 1992; Herbers *et al.*, 1994; Ruessink, 1998] show that the attendant lf motion seaward of the surf zone is a combination of forced components and locally or remotely generated free waves. Also, these observations support an increasing dominance of forced waves (relative to the total lf wave field) with more energetic seas and swell.

The effects of a varying bathymetry on the low-frequency response, in particular the radiation of free waves away from a local region of varying depth, is studied by Molin [1982] for normal wave incidence and deep water conditions for the primary (forcing) waves. This is extended by Mei & Benmoussa [1984] for obliquely incident waves and intermediate water depth for the forcing waves, based on a WKB expansion described by Chu & Mei [1970]; part of this is re-examined by Liu [1989]. The forcing and radiation of long waves by a wave group over variable depth is investigated by Dingemans *et al.* [1991] based on a numerical implementation of the third-order evolution equations presented in Liu & Dingemans [1989].

The effect of a variable depth on the forcing of beat-waves is considered by Bowers [1992], Van Leeuwen [1992] and Janssen *et al.* [2003]. These authors analytically express the effect of the depth gradient on the local, forced response as a perturbation of the flat bottom situation and show that the depth variability results in a phase shift between the local response and the forcing short-wave groups away from the $\pi$ radians phase difference implied by uniform depth theory; it provides a theoretical explanation for the changing phase relation observed in the laboratory [e.g. Mansard & Barthel, 1984; Van Leeuwen, 1992; Janssen *et al.*, 2000], in the field [e.g. Elgar & Guza, 1985; List, 1992; Masselink, 1995] and in numerical studies [e.g. List, 1992; Herbers & Burton, 1997].

The phase shift between the primary wave envelope and forced lf waves on a slope (away from the $\pi$ radians phase difference) affects the shoaling of these components; it results in an off-quadrature interaction and is therefore a necessary condition for net energy exchanges to occur. In the present chapter we address in particular the phase relation between the short-wave envelope and ensuing forced low-frequency wave motion. To that end, we analyze the experimental data reported by Boers [1996, 2005]. The high spatial resolution of the observational array allows for a detailed investigation of the wave field evolution. Utilizing the cross-correlation function between high-frequency envelope and forced low-frequency modes [e.g. List, 1992; Roelvink, 1993], it allows visualization of the phase relations between the wave groups and accompanying bound wave motion.

Model simulations are performed based on the stochastic model derived in Chapter 4, and predictions are compared to observations.

This chapter is organized as follows. In §6.1 we describe the experimental set-up by Boers [1996] and outline our cross-correlation analysis. The data analysis and interpretation is given in §6.2. We compare model predictions to observations in §6.3, and in §6.4 present an analysis of the shoaling behavior of group-induced long waves embedded in the stochastic model, with particular consideration of the depth-induced phase shift. Main findings are discussed in §6.5.

The analysis of experimental data (§6.1) and interpretation thereof (§6.2) is a selection of the more elaborate analysis results presented in Janssen *et al.* [2003] with minor textual and notational modifications.

0

## 6.1 Experimental arrangement and method of analysis

### 6.1.1 Experimental set-up

Boers [1996] conducted experiments in a 40 m long, 0.8 m wide wave flume of the Fluid Mechanics Laboratory at Delft University of Technology. The flume was equipped with a hydraulically driven, piston-type wave generator. The bottom profile was adopted from an actual barred sandy beach (Figure 6.1). The origin of the x-axis is at the beginning of the slope, where also the wave gauge nearest to the wave board was positioned (Figure 6.1). The mean position of the wave generator is at $x = -4.5$ m. The observational transect consists of 70 wave gauge positions, with the highest spatial resolution (0.2 m) in the nearshore region ($19\,\text{m} \leq x \leq 28.5\,\text{m}$).
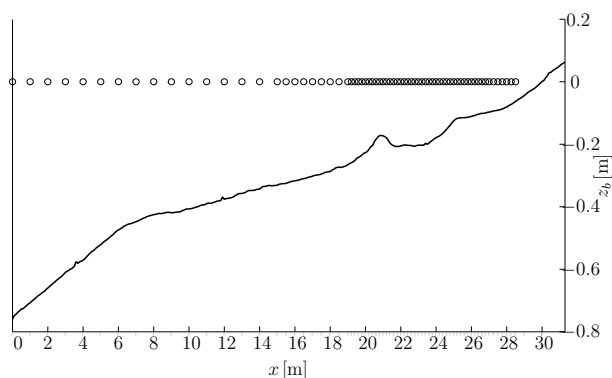


**Figure 6.1:** Beach profile Boers [1996], positive x-direction from left to right. Circles at SWL and x-axis ticks indicate wave gauge positions.

The control signal for the wave board consists of a relatively short duration, irregular wave signal repeated several times. Significant wave height, $H_s$, peak period, $T_p$, and signal cycle periods (signal is repeated approximately 75 times) of the cases considered are given in Table 6.1. To avoid confusion we use the labels of the experiments as given

| Name | $H_s$ [m] | $T_p$ [s] | Cycle Period [s] |
|------|-----------|-----------|------------------|
| 1A | 0.16 | 2.05 | 157.079 |
| 1C | 0.10 | 3.33 | 245.441 |

**Table 6.1:** Wave height and peak period as observed at $x = 0$ for experiments considered. Experiment labels as in Boers [1996].

by Boers [1996], but since the phenomena we want to emphasize are most prominent in experiment $1C$ (low wave steepness), we focus on those results in the data analysis and refer to $1A$ mainly where they differ significantly.

Second-order theory is used for the wave generation [Klopman & Van Leeuwen, 1990] to suppress generation of spurious harmonics. Re-reflections off the wave board are reduced through active reflection compensation (ARC) at the wave board. However, in view of restrictions imposed by the limited excursion of the wave board, the signals used in the ARC were high-pass filtered at $f_p/10$ for experiment $1A$ and $1C$. The deterministic wave board control signal was used for multiple repetitions of runs with identical input signals so as to cover a wide cross-shore interval with high spatial resolution (70 positions) using a limited number of wave gauges. Surface elevation records were approximately 30 minutes long and acquired at $20\,\mathrm{Hz}$.

### 6.1.2 Method of analysis

We decompose the surface elevation observed at each measurement location $x_i$, $i = [1 \dots 70]$ in low-frequency (lf) and high-frequency (hf) components

$$\eta(t, x_i) = \eta^{\mathrm{lf}}(t, x_i) + \eta^{\mathrm{hf}}(t, x_i). \tag{6.1}$$

Here $x_1$ corresponds to the offshore boundary at $x = 0$ (the origin) and the index $i$ increases shoreward (see Figure 6.1). The superscripts lf and hf relate to frequency ranges $f < f_p/2$ and $f \geq f_p/2$, where $f_p$ denotes the peak frequency. This somewhat arbitrary distinction between hf and lf motion is motivated by the observation that variance spectra at $x_1$ exhibit a fairly distinct local minimum around $f_p/2$.

We define the hf envelope as

$$A(t, x_i) = \left| \eta^{\mathrm{hf}} + i\widetilde{\eta}^{\mathrm{hf}} \right|^{\mathrm{lf}}, \tag{6.2}$$

where $\widetilde{\eta}^{\mathrm{hf}}$ denotes the Hilbert transform of $\eta^{\mathrm{hf}}$. On the premise that the hf motion, $\eta^{\mathrm{hf}}$, is fairly narrow-banded, $A(t)$ can be interpreted as the envelope function (Figure 6.2). The superscript lf on $\left| \eta^{\mathrm{hf}} + i\widetilde{\eta}^{\mathrm{hf}} \right|$ in (6.2) indicates the operation of low-pass filtering at $f_p/2$.

In our analysis of the experimental data we will make extensive use of correlation functions between various signals. For two (real) realizations $V(t, x_i)$ and $Y(t, x_j)$ of a random, stationary process, observed at location $x_i$ and $x_j$ respectively, the correlation
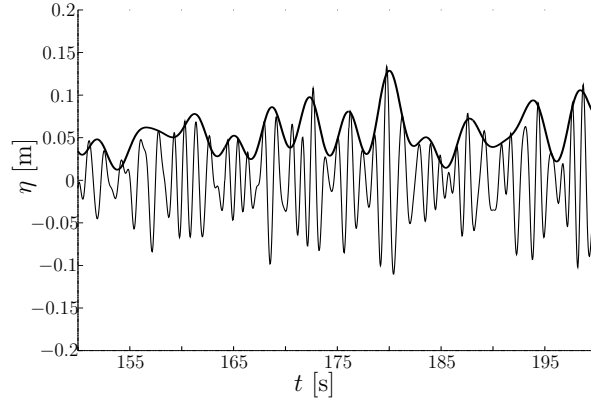
**Figure 6.2:** Example of short-wave envelope, $A(t)$, obtained through Hilbert transform (see eq. (6.2)). Envelope function is plotted as thick solid line; short waves are shown as thin solid line.

coefficient function can be defined as[†] [e.g. Bendat & Piersol, 1986; Oppenheim & Schafer, 1989]

$$\rho_{VY}\left(\tau, x_i, x_j\right) = \frac{\langle(V\left(t + \tau, x_i\right) - \mu_V(x_i))(Y\left(t, x_j\right) - \mu_Y(x_j))\rangle}{\sigma_V(x_i)\sigma_Y(x_j)}, \qquad (6.3)$$

where $\langle\ldots\rangle$ denotes a time averaging operator which, on the premise of weak ergodicity of the signals, replaces the operation of ensemble averaging; $\tau$ is the time separation (lag). The $\mu(x_i)$ and $\sigma(x_i)$ are the mean and standard deviations at position $x_i$ of the signal indicated by the subscript, so that $-1 \leq \rho_{VY} \leq 1$.

We cross-correlate various combinations of signals at different positions and use a corresponding notation to distinguish between them. For example, the sequence of cross-correlations between the lf-signal, $\eta^{\text{lf}}(t, x_i)$, and the squared envelope signal at the same location, $A^2(t, x_i)$, with $i = [1\ldots70]$ is denoted by $\rho_{\eta A}(\tau, x_i)$, in which the subscripts $\eta$ and $A$ correspond to $\eta^{\text{lf}}(t, x_i)$ and $A^2(t, x_i)$ respectively (the square is omitted from the subscript for readability). Alternatively, the set $\rho_{VY}(\tau, x_i; x_r)$ denotes the set of cross-correlation functions obtained by cross-correlating signals $V(t, x_i)$ observed at locations $x_i, i = [1\ldots70]$ and $Y(t, x_r)$ observed simultaneously at a fixed reference position $x_r$.

The values of each of these correlation functions are plotted in the $(x, \tau)$-plane at the discrete values of $x$ and $\tau$ where they are available. By presenting the results in such a manner we exploit the high resolution in space and time in the sense that local correlation maxima/minima that are sustained in cross-shore direction appear as quasi-continuous, two-dimensional ridges/troughs. Since a consistent pattern in the $(x, \tau)$-plane of the cross-correlation function is likely to be caused by a physical phenomenon, rather than by noise, this quasi-continuous presentation supports the identification of

---

[†]The present notation differs from that in Janssen *et al.* [2003] in that the signals are not necessarily zero mean (the envelope function generally is not). Moreover, the sign on $\tau$ in eq. (2) in Janssen *et al.* [2003] is inconsistent with the presentation of their analysis results.

relevant correlation variations and their cross-shore evolution, that may not have been identified from the individual cross-correlation functions.

## 6.2 Correlation analysis experimental data
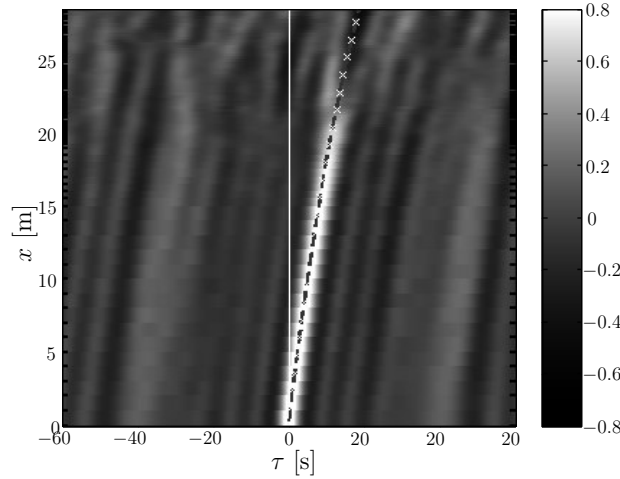
### 6.2.1 Evolution high-frequency envelope



**Figure 6.3:** Cross-correlation functions of the squared short-wave envelope, $\rho_{AA}(\tau, x_i; x_r = 0\,\text{m})$, for experiment $1C$. Dashed line with crosses indicates time lag values for signal propagating at group speed, $C_g$, corresponding to $f_p$.

Figure 6.3 shows the cross-correlation $\rho_{AA}(\tau, x_i; x_r = 0)$, which correlates the squared envelope signal, $A^2(t, x = 0)$, observed at $x = 0$, with those (simultaneously) observed at each of the individual locations $x_i$. The presence of a single dominating ridge of positive correlation indicates that the wave groups propagate shoreward, and are destroyed in the breaking process with negligible reflection from shore. The dashed marker line in the figures indicates time lag values for a signal propagating at the (linear) group velocity, $C_{gp}$, corresponding to the peak frequency, $f_p$ (water depth corrected for measured steady set-up). The computed lags agree very well with the observed lags of maximum correlation, indicating that $C_{gp}$ is indeed a fair approximation of the celerity at which the squared envelope (i.e. the short-wave energy) is propagated.

### 6.2.2 Evolution long waves

In Figure 6.4, the cross-correlation functions of the lf surface elevation, $\rho_{\eta\eta}(\tau, x_i; x_r)$, for experiment $1C$ are shown for $x_r = 0$. Comparison is made to time lag values corresponding to an incident signal propagating with $C_{gp}$, reflected at the still-water line at $x = 30\,\text{m}$ and propagating in the offshore direction at the free shallow-water wave celerity ($\sqrt{gh}$). The asymmetry of the curves in Figure 6.4 is due to the fact that $C_{gp}$ (for $f_p$) is less than the long-wave velocity, except for the limit of shallow water. The difference in gradient ($dx/d\tau$) between the ridge of positive correlation associated with

the incident lf-signal and the curve corresponding to $C_{gp}$, indicates that the lf-signal propagates at a celerity that is somewhat *smaller* than $C_{gp}$. The celerity of the outgoing lf-waves is well approximated by $\sqrt{gh}$ (Figure 6.4).
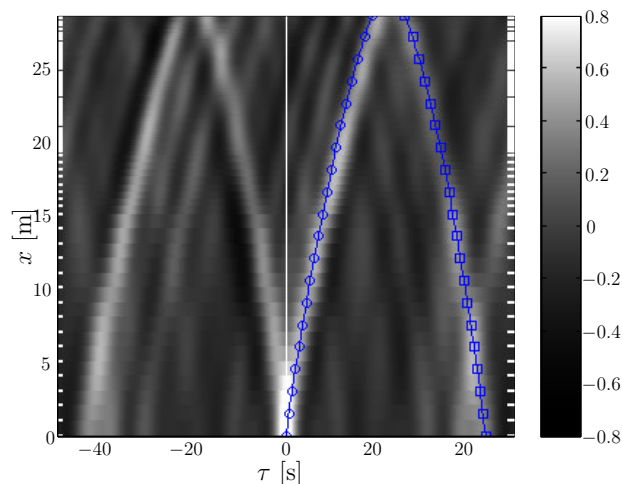


**Figure 6.4:** Correlation functions of the low frequency surface elevation, $\rho_{\eta\eta}(\tau, x_i; x_r = 0)$ experiment $1C$. Line with circles indicates time lag values for signal propagating in shoreward direction at group speed, $C_g$ (for $f_p$). Line with squares indicates time lag values corresponding to signal reflected at $x = 30\,\mathrm{m}$ propagating in offshore direction at $\sqrt{gh}$.

### 6.2.3 Concomitant wave-group and long-wave evolution

Figure 6.5 shows the cross-correlations $\rho_{\eta A}(\tau, x_i)$ between the observed lf surface elevation and squared envelope at the same position (no fixed reference location). This analysis visualizes the evolution of the *local* relation between the envelope and lf waves.

In the shoaling regime ($0 \leq x \leq 21\,\mathrm{m}$), i.e. in absence of significant wave breaking, the correlation functions form a ridge of negative correlation near zero time lag (Figure 6.5), consistent with the notion of bound wave motion being locally forced by short-wave groupiness [Longuet-Higgins & Stewart, 1962]. However, this ridge of negative correlation shifts toward positive time lag as the depth decreases (Figure 6.5), which is at variance with uniform-depth theory [Longuet-Higgins & Stewart, 1962]. The observed lag is consistent with inferences regarding the envelope and lf wave celerities in the shoaling region (see Figures 6.3 & 6.4). Moreover, such a phase shift away from $\pi$ radians (implied by the time lag shift of the bar of negative correlation) agrees with earlier field and laboratory observations [Elgar & Guza, 1985; List, 1992; Masselink, 1995; Mansard & Barthel, 1984; Van Leeuwen, 1992; Janssen *et al.*, 2000], where such a phase lag was invariably observed.
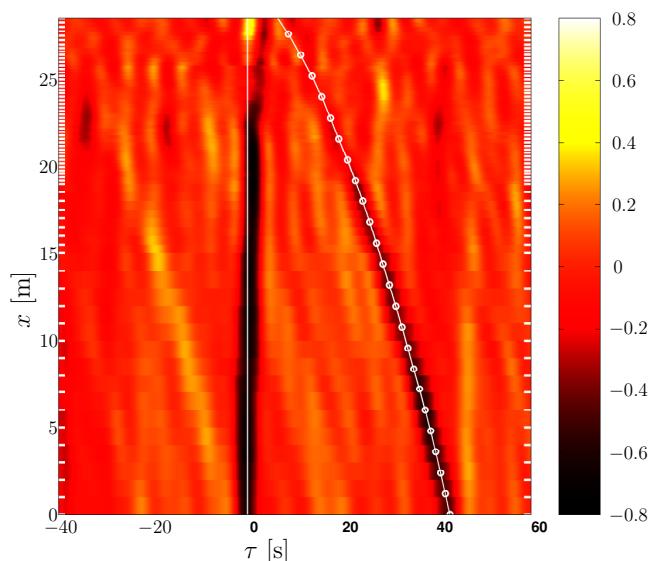
**Figure 6.5:** Cross-correlation function $\rho_{\eta A}(\tau, x_i)$ between squared short-wave envelope, $A^2$, and lf surface elevation, $\eta^{\mathrm{lf}}(t)$ (at the same location) observed in experiment $1C$. Line with circles indicates $(x, \tau)$ trajectory for summed travel times $(\tau)$ for wave signal propagating shoreward from $x$ at the group celerity $C_g$ (corresponding to $f_p$), reflected at the shoreline $(x = 30\,\mathrm{m})$, and returning to $x$ propagating seaward at celerity $\sqrt{gh}$.

## 6.3 Stochastic modeling of group-induced low-frequency motion

The cross-correlation analysis of observations of random waves over variable depth reveals a spatially varying phase shift between the squared hf envelope and the ensuing lf wave motion, away from the $\pi$ radians phase difference predicted by uniform-depth, second-order theory [e.g. Biésel, 1952; Longuet-Higgins & Stewart, 1962, 1964; Hasselmann, 1962]. This finding is consistent with earlier observations in the field [e.g. Elgar & Guza, 1985; List, 1992; Masselink, 1995] and in the laboratory [e.g. Mansard & Barthel, 1984; Van Leeuwen, 1992; Janssen *et al.*, 2000]. Bowers [1992], Van Leeuwen [1992] and more recently Janssen *et al.* [2003], have shown analytically that the varying depth, when considered as a perturbation of a horizontal bottom, induces a phase shift between the primary wave envelope and lf response that is qualitatively consistent with observations. However, these approaches invariably consider the nonlinear coupling as a one-way forcing of long waves, assuming that the long wave presence may be ignored for the evolution of the primary waves; this is reasonable in the shoaling regime if the water is sufficiently deep, and we will apply similar reasoning in the analysis presented in §6.4, but in shallow regions (such that also the forcing waves are in fairly shallow water), where the interaction approaches resonance and the long waves are potentially of the same order as the forcing waves, this perturbation breaks down [Janssen *et al.*, 2003]. In such regions wave evolution must instead be described through near-resonant

interaction theory [see e.g. Mei & Ünlüata, 1972; Bryant, 1973; Freilich & Guza, 1984; Madsen & Sørensen, 1993], which takes full account of the mutual interactions between the spectral components.

In the present work we model the wave evolution with the stochastic model of Chapter 4. The emphasis in the modeling effort is – in line with the analysis of the experimental data – on the spatially varying phase lag between hf envelope and lf surface elevation in the shoaling region. The reduced set of stochastic equations, suitable for unidirectional wave propagation, consists of coupled equations for the one-dimensional (in frequency space) spectrum ($\mathcal{E}$) and two-dimensional bi-spectrum ($\mathcal{C}$). For convenience we repeat the governing equations here (see also §5.1)

$$\frac{d\mathcal{E}_1}{dx} = -D_1\mathcal{E}_1 - 2\int \mathcal{W}_{(1-2)2}\Im\{\mathcal{C}_{(1-2)2}\}\, d\omega_2, \tag{6.4a}$$

$$\frac{d\mathcal{C}_{12}}{dx} = \left[i\Lambda_{12} - \mu_{12} - \frac{1}{2}\left(D_1 + D_2 + D_{(1+2)}\right)\right]\mathcal{C}_{12} + 2i\mathcal{Q}_{12}. \tag{6.4b}$$

Definitions of $\Lambda_{12}, \mu_{12}, D_1, \mathcal{Q}_{12}$ and the nonlinear coupling coefficient $\mathcal{W}_{12}$ are detailed in Chapter 4 and references therein; for brevity they will not be repeated here.

The stochastic model (6.4) assumes unidirectional wave propagation, whereas the observed evolution of the lf waves shows significant reflections at the shoreline (see §6.2.2). In order to properly initialize the model at the seaward boundary and allow for a meaningful comparison to local spectra and bulk statistics, a decomposition of the lf wave motion into incoming and outoing (reflected) components is pursued. To that end we write the observed lf wave motion at location $x_i$ as

$$\eta^{\text{lf}}(t, x_i) = \sum_{n=1}^{U_L} \widetilde{\zeta}_{n,i} \exp\left[-i\omega_n t\right] + * = \sum_{n=1}^{U_L} \sum_s \widetilde{\zeta}_{n,i}^s \exp\left[-i\omega_n t\right] + \epsilon_{n,i} + *, \tag{6.5}$$

with $U_L$ corresponding to the upper frequency limit of the lf motion $f_p/2$; the $\epsilon_{n,i}$ is the signal residue (noise), and $s = \pm$ is a sign index to distinguish incoming/outgoing wave components propagating in the positive/negative $x$ direction.

The directional decomposition, applied to the surface elevation records, is based on a standard array method [e.g. Jolas, 1960; Mansard & Funke, 1980; Zelt & Skjelbreia, 1992; Janssen *et al.*, 2001; Battjes *et al.*, 2004], each array consisting of $M$ gauges so that the decomposition of the signal at location $x_i$ for each frequency $\omega_n$ can be written in matrix form as

$$\begin{bmatrix} Q_{n,1,i}^+ & Q_{n,1,i}^- \\ \vdots & \vdots \\ Q_{n,M,i}^+ & Q_{n,M,i}^- \end{bmatrix} \begin{bmatrix} \widetilde{\zeta}_{n,i}^+ \\ \widetilde{\zeta}_{n,i}^- \end{bmatrix} = \begin{bmatrix} \widetilde{\zeta}_{n,1} \\ \vdots \\ \widetilde{\zeta}_{n,M} \end{bmatrix} + \underbrace{\begin{bmatrix} \epsilon_{n,1} \\ \vdots \\ \epsilon_{n,M} \end{bmatrix}}_{\boldsymbol{\epsilon}}. \tag{6.6}$$

A least-squares solution for $\widetilde{\zeta}_{n,i}^+$ and $\widetilde{\zeta}_{n,i}^-$ (minimizing $|\boldsymbol{\epsilon}|^2$) is obtained by means of a singular value decomposition [Press *et al.*, 1986; Janssen *et al.*, 2001; Battjes *et al.*, 2004].

The (complex) amplitudes $\widetilde{\zeta}_{n,j}^{s}$ across the array are related to those at $x_i$ through the $Q_{n,j,i}^{s}$ which account for the shoaling and propagation across the array, given as

$$Q_{n,j,i}^{s} = \sqrt{\frac{C_{g,n,j}^{s}}{C_{g,n,i}^{s}}} \exp\left[is \int_{x_i}^{x_j} k_n^s(x')\,dx'\right]. \tag{6.7}$$

We tentatively set $C_{g,n}^{+}$ (group speed for the incident waves) equal to the group speed (in the linear approximation) corresponding to the peak frequency $f_p$. For the offshore directed components we assume $C_{g,n}^{-} = C_{g,n}$, thus the linear group speed corresponding to frequency $\omega_n$. The wavenumber $k_n^{+} = \omega_n/C_{g,n}^{+}$ and $k_n^{-}$ is the linear wavenumber corresponding to $\omega_n$. This description of the lf wave evolution is particularly approximate for the *incident* long waves that are assumed bound waves, locked to the incident waves groups that propagate at the group speed corresponding to the peak of the spectrum, while in fact we are unsure of the celerity and shoaling rate of these components (that is why we consider numerical simulation with the evolution-type stochastic model in the first place). Although more accurate approximations, such as further decomposing the incident wave signal into free and bound components [Bakkenes, 2002] or multi-step predictor-corrector type methods [Van Dongeren *et al.*, 2004; Steenbergen, 2005; Van Dongeren *et al.*, 2005] are possible, we do not pursue such refinements here. The accuracy of the present approach is acceptable for eliminating seaward propagating waves from the observations in the shoaling region [Battjes *et al.*, 2004; Steenbergen, 2005], which suffices for our present purpose.

From the time series for the incident wave field the incident spectrum $\mathcal{E}^{+}$ is estimated, which is used to initialize the model (viz. (6.4a)) at $x_1$. The bi-spectral evolution equation (6.4b) is initialized at that location with the steady form as in §5.1, corresponding to a skewed, symmetrical wave field. The spectral discretization consists of 256 equidistant frequencies with $\Delta\omega = 0.02\pi\,\text{rad/s}$. Further, with respect to the model settings, the relaxation constant $\beta = 1.5$ and the dissipation frequency weighting is determined by $r_0 = 1/10$ and $r_2 = 9/10$ (these settings are the same as in Chapter 5). The breaker index $\gamma$ is set at a fixed value $\gamma = 0.85$, instead of using the relation (4.32) as proposed by Battjes & Stive [1985] (as done in Chapter 5). Although the values prescribed by (4.32) [which are lower, see Boers, 2005] render good agreement to observed wave heights for linear wave model simulations (not shown), they result in under-prediction of surf zone wave heights for nonlinear simulations. The value $\gamma = 0.85$ is chosen ad hoc on the basis of comparison of model-predicted and observed (bulk) wave height ($H_{m_0}$) evolution.

Model-predicted hf and lf wave heights ($H_{m_0}$) for cases 1A and 1C (Figure 6.6) are in good agreement with observed wave heights (of shore-directed components) in the shoaling region (up to $x \approx 20\,\text{m}$). For case 1A both lf and hf wave heights are somewhat overestimated for $x > 10\,\text{m}$, in particular for lf waves shoreward of the breaker bar. Although the directional decomposition is expected less accurate in the nearshore region (shoreward of the breaker bar) on account of inhomogeneity of the wave field over the array (due to e.g. dissipation and potentially even local reflections),

the mismatch between observations and predictions is at least in part ascribed to inaccuracies in the modeling. Firstly, we apply a (nearly) frequency-squared dissipation weighting, which provides only very weak dissipation to the lower-frequency spectral regions and may not be physically realistic in shallow water where dissipation due to breaking may be significant, even for such long waves [Van Dongeren *et al.*, 2004, 2005]; secondly, alternative dissipative processes such as bottom friction [Henderson & Bowen, 2002; Van Dongeren *et al.*, 2004], which are not represented in the present model, may be important. However, since the directional decomposition we applied is of limited accuracy in the very nearshore, we refrain from further discussion of the relative importance of competing dissipation mechanisms. More accurate approaches to the directional decomposition are needed [Steenbergen, 2005; Van Dongeren *et al.*, 2005] which is outside the scope of the present work.

The model-predicted third-order bulk statistics (Figure 6.6) are overall in fair agreement with observations in most of the shoaling region and even shoreward of the breaker bar. For case 1A (steeper waves) the observed skewness and asymmetry exhibit rapid spatial variations in the deeper part of the flume, suggesting spurious free wave motion owing to inaccuracies in the wave generation or re-reflections originating from the wave board; these are not accounted for in the boundary condition of the model and therefore not found in the simulations.

The spatial evolution of the wave spectra (Figure 6.7 & Figure 6.8) is characterized by an initial amplification of spectral levels at harmonic- and beat-frequency ranges, consistent with three-wave interaction rules, followed by a transformation toward a broad, almost featureless shape in the very nearshore, attributed to the concomitant action of sustained nonlinear couplings and dissipation. Although model-predicted spectra are generally somewhat smoother, the model captures the dominant features of the attendant spectral evolution, both in the shoaling regime and the surf zone. However, consistent with the observation that the model over-predicts lf variances in the nearshore, the lf spectral levels are generally overestimated in this region, in particular for experiment 1A (Figure 6.7). Also for 1A, the model-predicted spectral shape around the (initial) peak is at variance with observations at locations well inside the surf zone (for instance $x = 24.8\,\mathrm{m}$ Figure 6.7), which is ascribed mainly to the approximate nature of the stochastic closure (see also Chapter 5).

The comparison of model-predicted spectra and bulk statistics to observations validates the stochastic modeling approach of the experimental data. However, our main objective is to asses the ability of the present stochastic approach to model the phase relation between squared hf envelope and the lf surface elevation. Thereto, we first derive an expression for the correlation between the lf surface elevation and the squared hf envelope in terms of the spectral and bi-spectral densities. This is achieved by writing the incoming[†] hf and lf wave field as

---

[†]Although we do not use explicit notation here to distinguish incoming from outgoing modes, only incoming modes are included in (6.8) and (6.9).
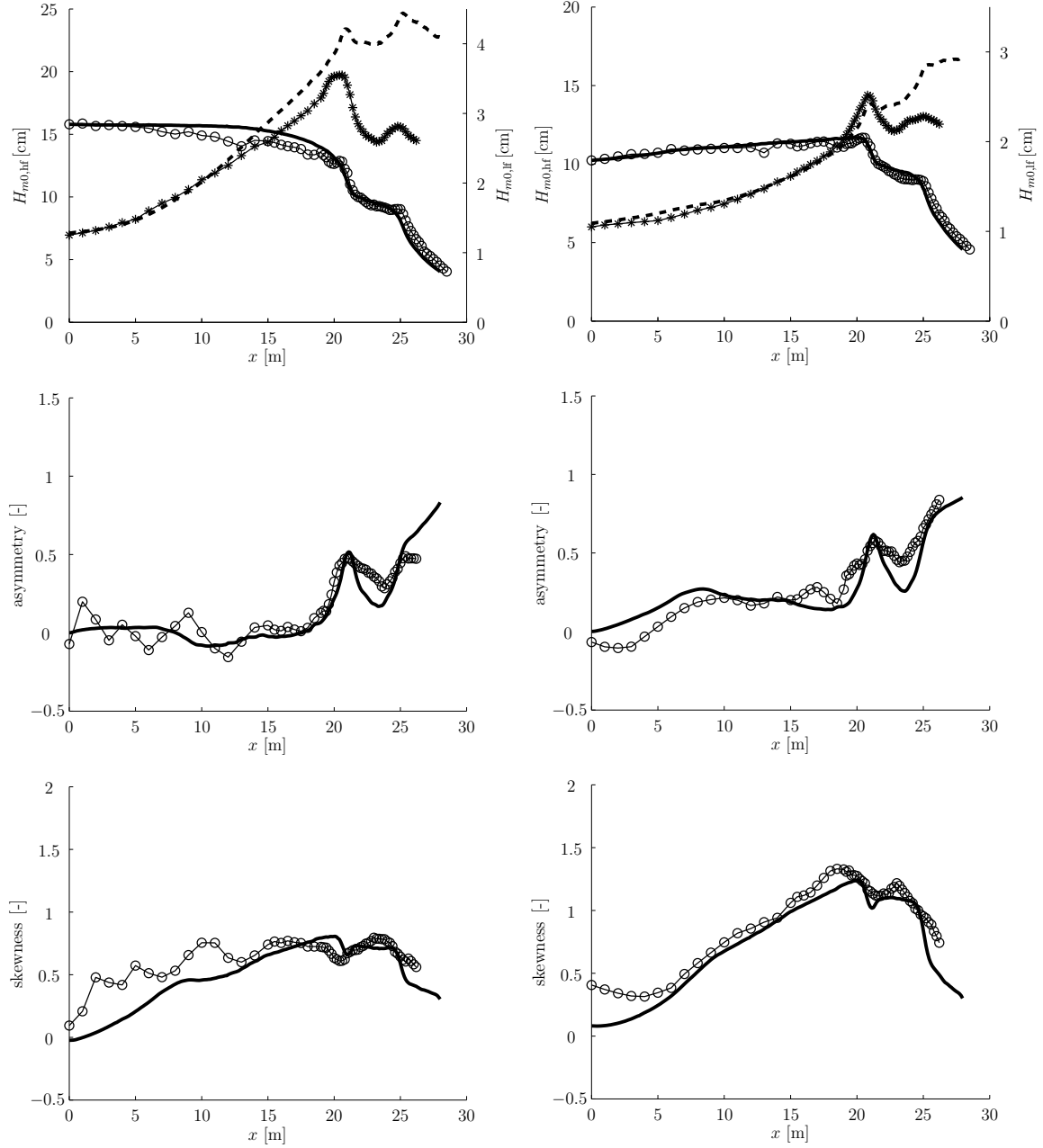
**Figure 6.6:** Observed and predicted evolution of shoreward propagating waves for case 1A (left panels) and 1C (right panels) of Boers [1996] . Top panels: observed $H_{m0,\mathrm{hf}}$ (left axis) and $H_{m0,\mathrm{lf}}$ (right axis) indicated by circles and asterices respectively; corresponding model predictions shown as solid and dashed line respectively. Middle & bottom panels: observed (circles) and predicted (solid line) asymmetry & skewness.
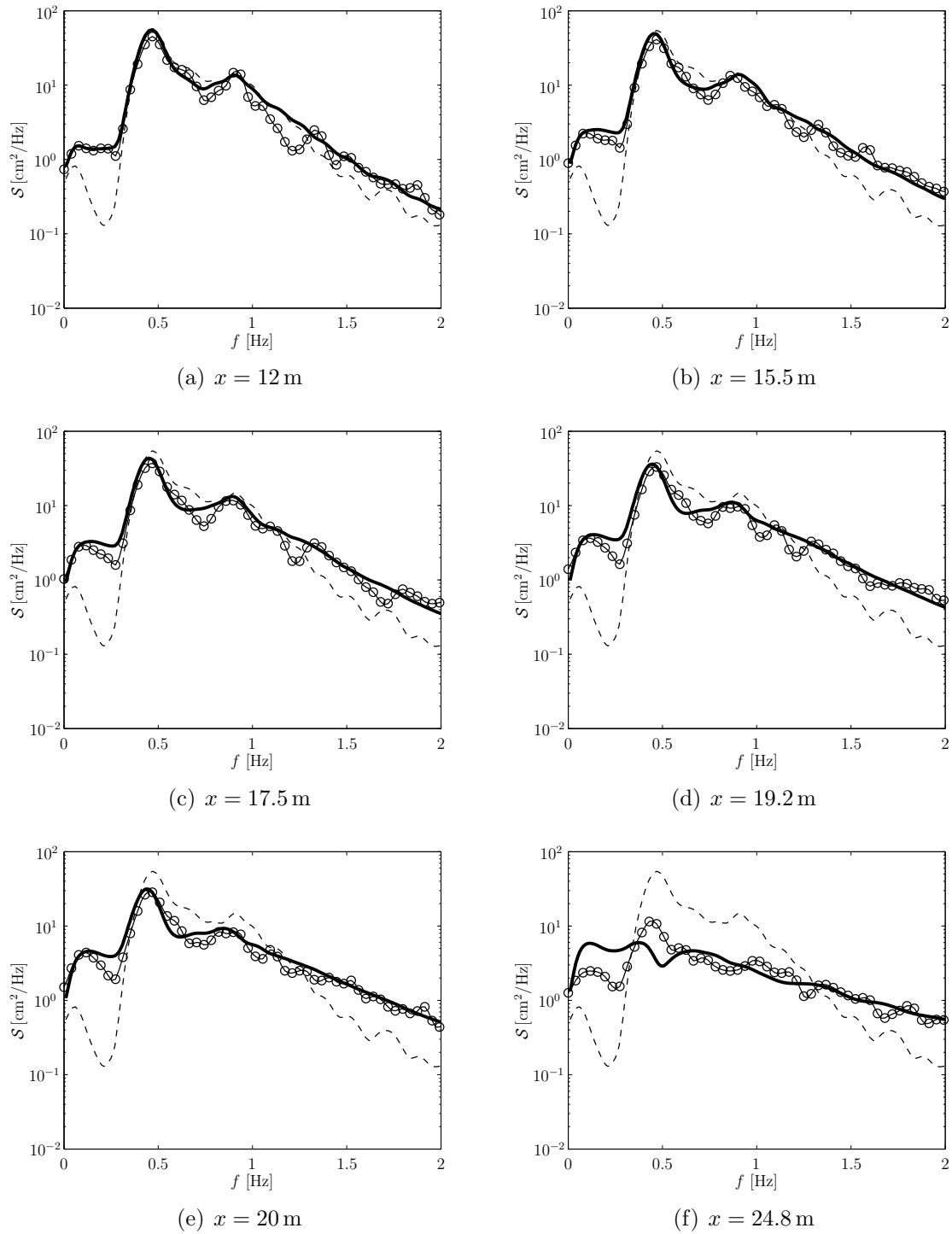
**Figure 6.7:** Observed (circles) and predicted (solid line) spectra of shoreward propagating waves at discrete locations (sub-labels) for case 1A [Boers, 1996]. Dashed line is spectrum at $x = 0\,\text{m}$.
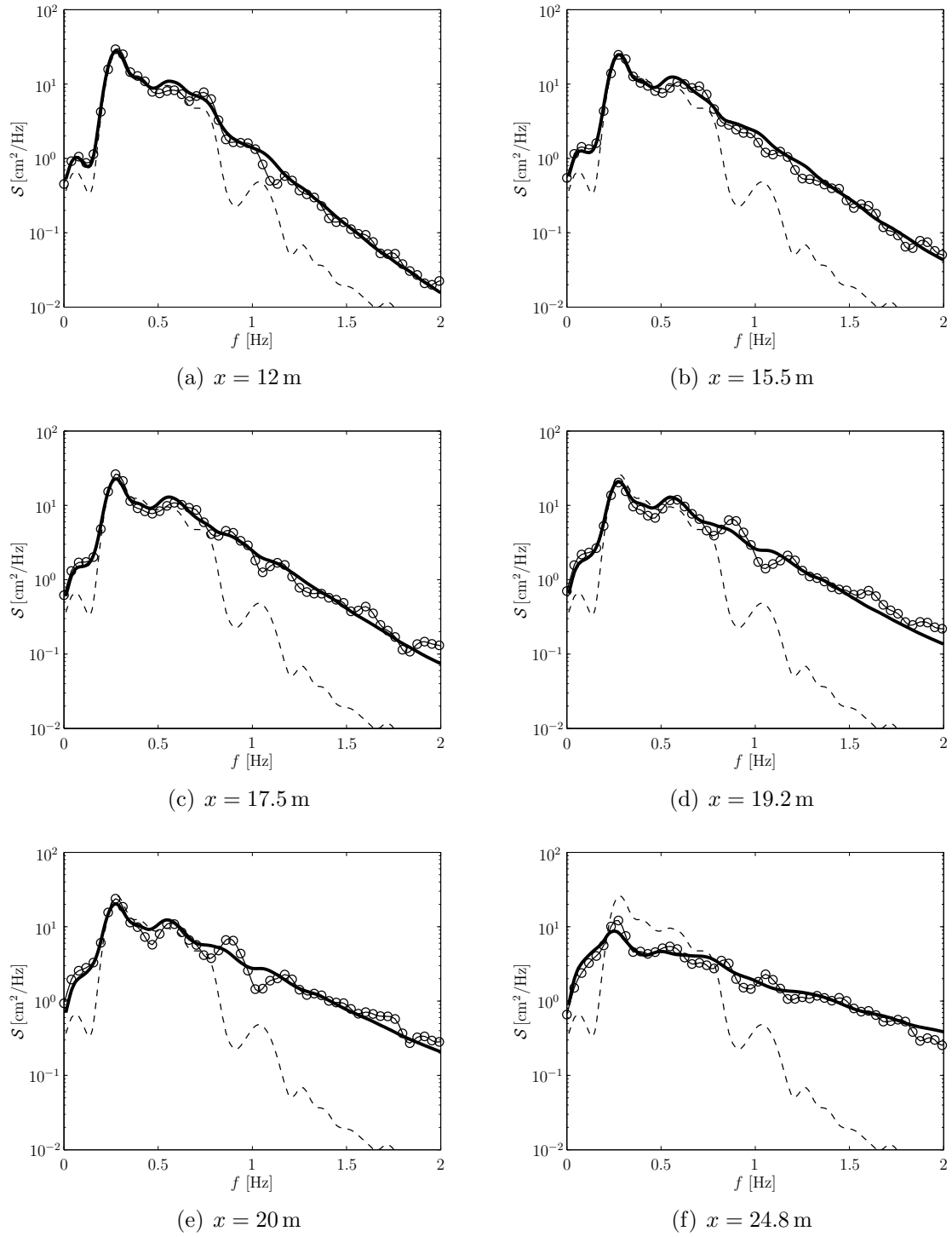
**Figure 6.8:** Observed (circles) and predicted (solid line) spectra of shoreward propagating waves at discrete locations (sub-labels) for case 1C [Boers, 1996]. Dashed line is spectrum at $x = 0\,\mathrm{m}$.

$$\eta^{\text{hf}}(t) = \sum_{p_1=L_H}^{U_H} \widetilde{\zeta}_1 \exp\left[-i\omega_1 t\right] + * \tag{6.8}$$

and

$$\eta^{\text{lf}}(t) = \sum_{p_1=1}^{U_L} \widetilde{\zeta}_1 \exp\left[-i\omega_1 t\right] + * \tag{6.9}$$

respectively. The $L_H$ and $U_H$ denote the high- and low-pass band limits for the hf band respectively, whereas $U_L$ represents the upper frequency limit of the lf wave motion[†].

By expressing the squared envelope in terms of the hf wave field decomposition, the covariance function between the latter and the lf motion can be expressed as

$$\text{Cov}_{\eta A}(\tau) = \left\langle \left(\eta^{\text{lf}}(t+\tau) - \mu_\eta\right)\left(A^2(t) - \mu_A\right) \right\rangle \tag{6.10}$$

$$= 4 \sum_{p_1=1}^{U_L} \left( \sum_{p_2=L_H}^{U_H-p_1} \left\langle \widetilde{\zeta}_1 \widetilde{\zeta}_2 \widetilde{\zeta}_{(1+2)}^* \right\rangle \right) \exp\left[-i\omega_1\tau\right] + *,$$

where $\tau$ denotes the time separation (lag); $\mu_\eta$ and $\mu_A$ denote the mean of $\eta^{\text{lf}}(t)$ and $A^2(t)$ respectively. Applying the appropriate normalization, and taking the limit to continuous variables, the correlation coefficient function can be written as

$$\rho_{\eta A}(\tau) = \frac{\int_0^{\omega_{ul}} d\omega_1 \left( \int_{\omega_{lh}}^{\omega_{uh}-\omega_1} d\omega_2 \mathcal{B}_{12} \right) \exp\left[-i\omega_1\tau\right] + *}{2\left[ \iint_0^{\omega_{ul}} d\omega_1 d\omega_2 \left( \int_{\omega_{lh}}^{\omega_{uh}-\omega_2} d\omega_3 \mathcal{S}_1 \mathcal{S}_2 \mathcal{S}_{(2+3)} \right) \right]^{1/2}}, \tag{6.11}$$

with $\mathcal{B}_{12} = \mathcal{C}_{12}/\sqrt{C_{g,1}C_{g,2}C_{g,(1+2)}}$ and $\mathcal{S}_1 = \mathcal{E}_1/C_{g,1}$. The integration limits coincide with the discrete summation ranges in (6.8) and (6.9), such that $\omega_{ul} = U_L\Delta\omega$, $\omega_{lh} = L_H\Delta\omega$ and $\omega_{uh} = U_H\Delta\omega$. To support meaningful comparison to the analysis of the experimental data we let $\omega_{ul} = \omega_{lh} = f_p/2$, and the upper band limit of the hf waves $\omega_{uh}$ is set at $2f_p$.

Substitution of model-predicted values for the spectral and bi-spectral densities in the *RHS* of (6.11) yields what we refer to as the 'predicted' correlation function which is to be compared to the correlation function estimated directly from the time series of $\eta$ and $A^2$ (the 'observed' correlation function). Since in the shoaling region ($0 \leq x \leq 20\,\text{m}$) the incoming and outgoing lf waves are well separated in time, the observed correlation function is obtained from the original bi-directional data, without preprocessing through the directional decomposition. Although small differences may occur on account of the normalization (after all the model considers only the incident lf wave motion), this is preferred over the potential errors implied when applying the (approximate)

---

[†]Note that, as before, the summations are over $p_1$ and the numeral subscripts on frequency and surface elevation components should be interpreted as a shorthand for $p_1$. We again utilize this convention here since it allows for a compact representation of mixed subscripts in multi-dimensional summations and/or integrations as present in the following (see also §2.1 where a similar convention is introduced which has been used throughout this thesis).

directional decomposition on the experimental data prior to cross-correlating the signals [e.g. Steenbergen, 2005].

In Figure 6.9 and Figure 6.10 the observed and predicted cross-correlation between squared envelope and lf surface elevation are compared at discrete locations. Of particular interest are the values of the correlation function close to $\tau = 0$ as these are associated with the local forcing relation between the lf waves and the squared envelope. From Figure 6.9 and Figure 6.10 we see overall, in the vicinity of $\tau = 0$, good agreement between model-predicted and data-derived correlation functions (Figure 6.9 and Figure 6.10). The observed and model-predicted correlation both exhibit a shift of the main peak of negative correlation toward positive time lag as the waves propagate toward the shoreline (particularly for experiment $1C$), indicating a lagging of the lf wave motion with respect to the envelope, consistent with the findings in §6.2. This time lag is substantiated in Figure 6.11, where the time lags corresponding to the local minimum of the correlation function closest to $\tau = 0$ are plotted as a function of $x$ over the interval $0 \leq x \leq 20\,\mathrm{m}$ (the shoaling region); model-predicted positive time lag values, associated with the local minimum of the correlation function, agree quite well with the observed lags.

$-2$
$-1.5$

$1.5$
$2$

$-2$
$-1.5$

$1.5$
$2$

(a) $x = 12\,\mathrm{m}$

(b) $x = 15.5\,\mathrm{m}$

$-2$
$-1.5$

$1.5$
$2$

$-2$
$-1.5$

$1.5$
$2$

(c) $x = 17.5\,\mathrm{m}$

(d) $x = 19.2\,\mathrm{m}$

$-2$
$-1.5$

$1.5$
$2$

$-2$
$-1.5$

$1.5$
$2$

(e) $x = 20\,\mathrm{m}$

(f) $x = 22.4\,\mathrm{m}$
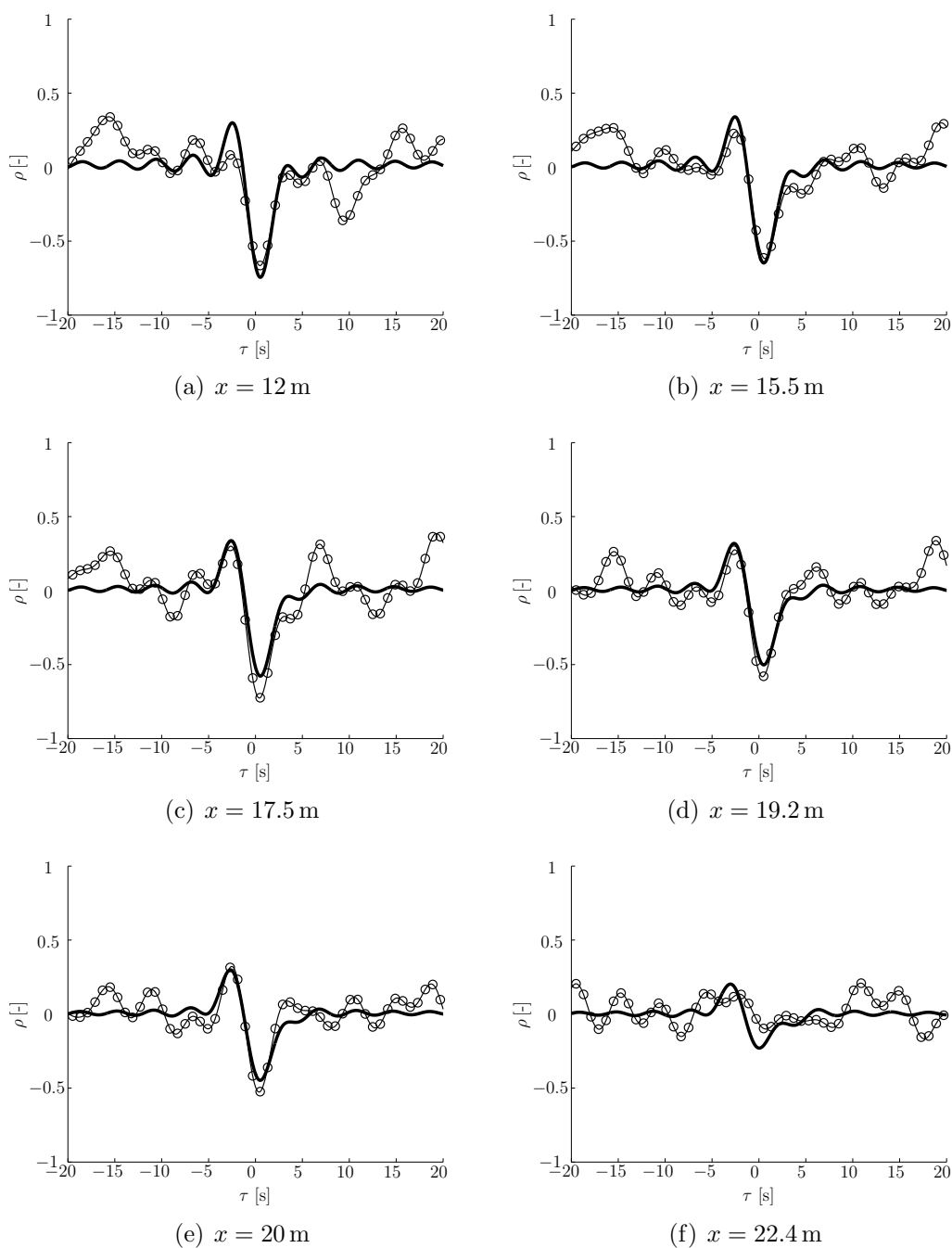
**Figure 6.9:** Observed (circles) and predicted (solid line) correlation function $\rho_{\eta A}$ at discrete locations (sub-captions) for case 1A [Boers, 1996].

PSfrag replacements

PSfrag replacements

PSfrag replacements

PSfrag replacements

PSfrag replacements

PSfrag replacements

(a) $x = 12\,\mathrm{m}$

(b) $x = 15.5\,\mathrm{m}$

(c) $x = 17.5\,\mathrm{m}$

(d) $x = 19.2\,\mathrm{m}$

(e) $x = 20\,\mathrm{m}$

(f) $x = 22.4\,\mathrm{m}$
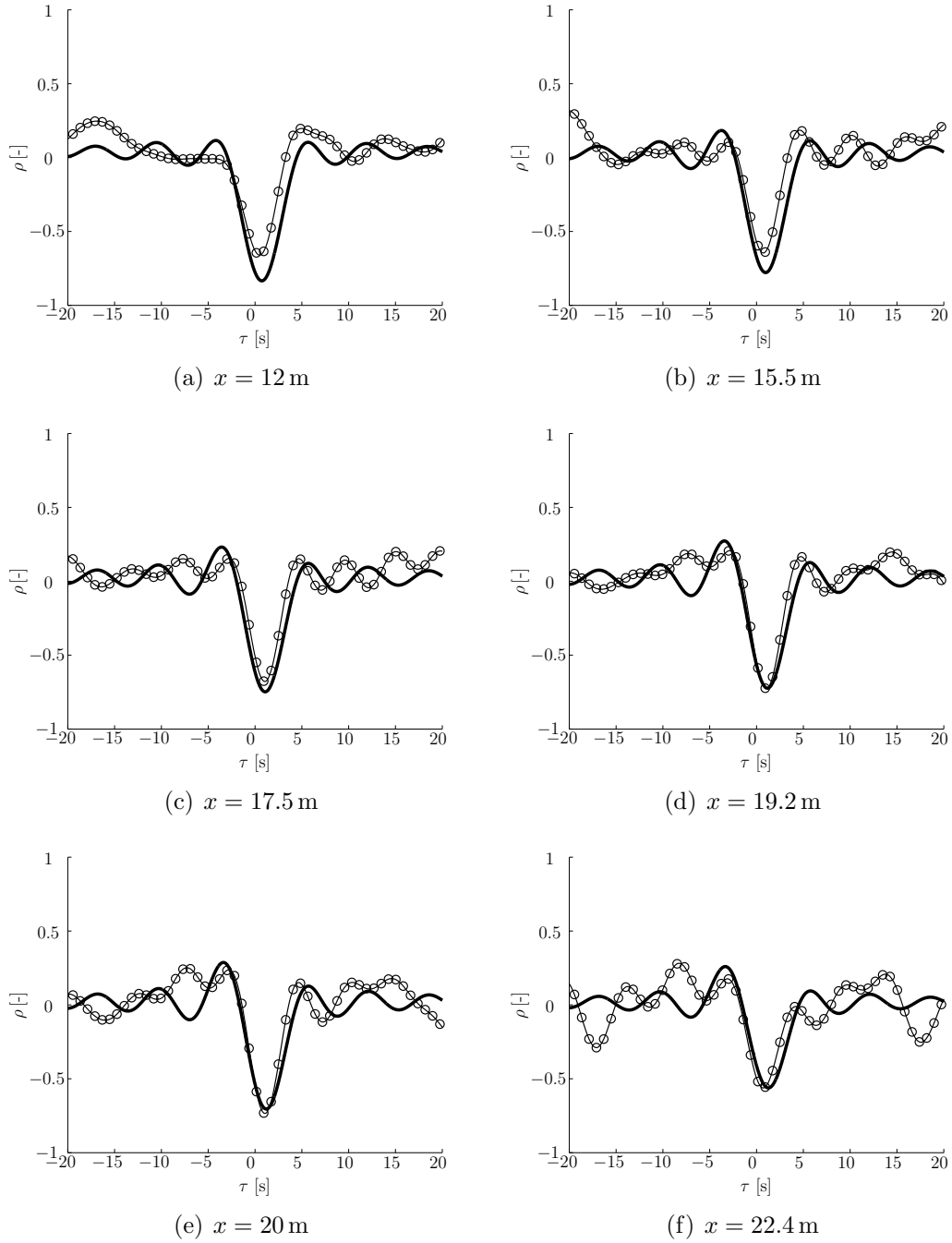
**Figure 6.10:** Observed (circles) and predicted (solid line) correlation function $\rho_{\eta A}$ at discrete locations (sub-captions) for case 1C [Boers, 1996].
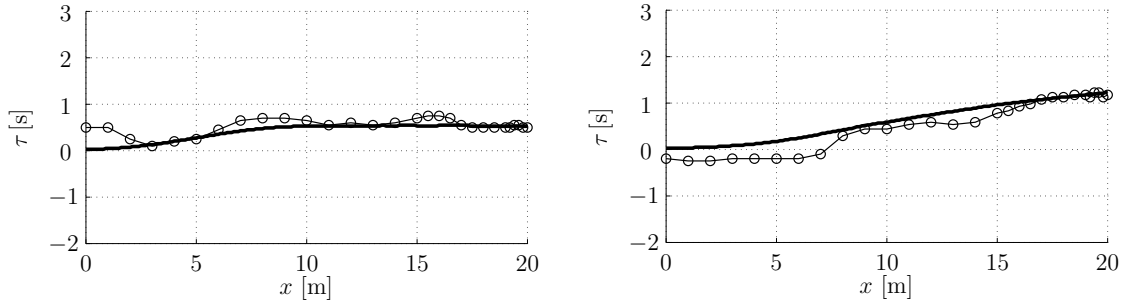
**Figure 6.11:** Observed (circles) and predicted (solid line) time lag corresponding to maximum negative correlation for case 1A (top panel) and 1C (bottom panel) of Boers [1996].

## 6.4 Dynamics of shoaling forced waves

Comparison to observational data (see §6.3) indicates that the stochastic formalism is well suited to predict the shoaling of long waves driven by nonlinear quadratic difference interactions. Here we present an analysis of the governing equations in what we refer to as the shoaling regime, typified by a slowly varying depth, off-resonant forcing and relatively low energy levels in the lf forced modes. The objective of this analysis is to investigate the shoaling behavior of forced lf modes while traversing a (very) mild slope; to that end we derive explicit expressions for energy and phase-coupling evolution of the lf spectral range. From the outset, we consider the primary waves narrow-banded, and momentarily reduce the mutual interaction description to a one-way forcing relation, thus ignoring the presence of the (presumed small) forced components on the evolution of the primary waves. In particular, we consider (dis-)similarities to uniform-depth theory [Longuet-Higgins & Stewart, 1962, 1964] and discuss the occurrence of the bottom-induced phase shift between forcing and response on a slope.

In accordance with these assumptions the primary waves shoal conservatively, i.e. such that in the primary wave band $\omega_{lh} \leq \omega_1 \leq \omega_{uh}$, the evolution is governed by the homogeneous set

$$\frac{d\mathcal{E}_1}{dx} = 0. \tag{6.12}$$

In the lf band the wave motion is forced and the spectral evolution is given by the (de-coupled) set

$$\frac{d\mathcal{E}_1}{dx} = -4 \int_{\omega_{lh}}^{\omega_{uh}-\omega_1} \mathcal{W}_{(1+2)(-2)} \Im\{\mathcal{C}_{21}^*\} \, d\omega_2, \qquad 0 < \omega_1 \leq \omega_{ul} \tag{6.13a}$$

$$\frac{d\mathcal{C}_{21}^*}{dx} = -i\Lambda_{21}\mathcal{C}_{21}^* - 2i\mathcal{W}_{(1+2)(-2)}\mathcal{E}_{(1+2)}\mathcal{E}_2, \qquad \omega_{lh} \leq \omega_2 \leq \omega_{uh}-\omega_1 \tag{6.13b}$$

with $\omega_{ul}$ the upper limit of the lf band. The decoupling of the equations (6.13a) and (6.13b) is on account of the fact that the products $\mathcal{E}_{(1+2)}\mathcal{E}_2$ in the *RHS* of (6.13b) involve only spectral components in the primary spectral range which, on account of the presumed conservative shoaling, are constant. Products involving lf spectral components are neglected in (6.13b).

Assuming narrow-band primary wave motion with a center-frequency $\omega_0$ and using the long-wave approximations for the forced lf waves yields the expressions

$$\Lambda_{21} \approx \Lambda_{10} = \frac{\omega_1}{C_{g0}} \left( \frac{C_{g0}}{\sqrt{gh}} - 1 \right), \tag{6.14a}$$

$$\mathcal{W}_{(1+2)(-2)} \approx \mathcal{W}_{10} = \frac{g^{5/4} h^{1/4} \Lambda_{10}}{C_{g0} \left( gh - C_{g0}^2 \right)} \left[ 2 \frac{C_{g0}}{C_0} - \frac{1}{2} \right]. \tag{6.14b}$$

Back-substituting these expressions into the governing equations for the lf range (viz. the set (6.13)) yields the (de-coupled) set

$$\frac{d\mathcal{E}_1}{dx} = 8\mathcal{W}_{10} \mathcal{F}_1 \Re\{\mathcal{P}_1\}, \tag{6.15a}$$

$$\frac{d\mathcal{P}_1}{dx} = -i\Lambda_{10}\mathcal{P}_1 + \mathcal{W}_{10}, \tag{6.15b}$$

with $0 < \omega_1 \leq \omega_{ul}$ and the variables $\mathcal{P}_1$ and $\mathcal{F}_1$ defined as

$$\mathcal{P}_1 = \frac{i}{2\mathcal{F}_1} \int_{\omega_{lh}}^{\omega_{uh}-\omega_1} \mathcal{C}_{21}^* \, d\omega_2, \qquad \mathcal{F}_1 = \int_{\omega_{lh}}^{\omega_{uh}-\omega_1} \mathcal{E}_{1+2} \mathcal{E}_2 \, d\omega_2, \tag{6.16}$$

where $\mathcal{F}_1$ is a constant on account of the presumed conservative shoaling in the hf range. The set (6.15) can be integrated numerically. Here we consider further simplifications to obtain analytical expressions that provide insight in the long wave behavior over variable depth.

The set (6.15) is implicitly restricted to off-resonant conditions, requiring $\Lambda_{10} \sim O(1)$. After all, the one-way forcing model assumes the energy in the forced lf modes is small relative to the driving modes. This is valid only for off-resonant interactions, or very short propagation distances such that the loss of energy to the hf modes can be neglected.

Upon integrating eq. (6.15b) by parts once we can write $\mathcal{P}_1$ as

$$\mathcal{P}_1(x) = \left[ \left( \frac{\mathcal{W}_{10}(x)}{i\Lambda_{10}(x)} + \frac{1}{\Lambda_{10}(x)} \frac{d}{dx} \left( \frac{\mathcal{W}_{10}(x)}{\Lambda_{10}(x)} \right) \right) \exp \left[ i \int_x^{x'} \Lambda_{10} \, dx'' \right] \right]_0^x$$
$$- \int_0^x \frac{d}{dx} \left( \frac{1}{\Lambda_{10}(x)} \frac{d}{dx} \left( \frac{\mathcal{W}_{10}(x)}{\Lambda_{10}(x)} \right) \right) \exp \left[ i \int_x^{x'} \Lambda_{10} \, dx'' \right] dx'$$
$$+ \mathcal{P}_1(0) \exp \left[ -i \int_0^x \Lambda_{10} \, dx' \right]. \tag{6.17}$$

Assuming that the depth is (very) slowly varying, we omit the integral on the *RHS* of (6.17), thus neglecting terms that are of the order of the bottom slope squared and smaller. This approximation is reasonable if the depth variation over a lf wave length is small relative to the depth. Further, if we omit the oscillatory part of the solution on account of the initial conditions, which, cumulatively, do not contribute to the net spectral evolution in (6.15a), we can approximate the $\mathcal{P}_1$ by

$$\mathcal{P}_1 \approx \frac{\mathcal{W}_{10}}{i\Lambda_{10}} + \frac{1}{\Lambda_{10}}\frac{d}{dx}\left(\frac{\mathcal{W}_{10}}{\Lambda_{10}}\right). \qquad (6.18)$$

The variable depth thus results in a real contribution to $\mathcal{P}_1$. In terms of the spectral evolution, governed by (6.15a), this phase shift implies that the forcing is pushed away from exact quadrature (imaginary $\mathcal{P}_1$) such that the lf range is permitted to shoal non-conservatively.

Through back-substitution of the approximate expression for $\mathcal{P}_1$ (viz. (6.18)) into (6.15a) and, omitting constants on account of the integration, the forced long-wave energy flux in a mildly sloping region is given by

$$\mathcal{E}_1(x) = 4\mathcal{F}_1\left(\frac{\mathcal{W}_{10}(x)}{\Lambda_{10}(x)}\right)^2. \qquad (6.19)$$

To illustrate the significance of the expression (6.19) for the lf fluxes, we momentarily consider the equilibrium solution by Longuet-Higgins & Stewart [1962, 1964] written for the $\omega_1$ component of the low-frequency spectral range as

$$\widetilde{\zeta}_1 = -\frac{RS_1}{\rho\left(gh - C_{g,0}^2\right)}, \qquad\qquad p_1 \in [1, 2, \ldots, U_L] \qquad (6.20)$$

where $RS_1$ is the $\omega_1$ Fourier component of the radiation stress function, and the $\widetilde{\zeta}_1$ are the lf surface elevation components as in (6.9). The radiation stress component can be written in terms of the narrow-band hf surface elevation (see (6.8)) as

$$RS_1 = 2\rho g\left[\frac{2C_{g,0}}{C_0} - \frac{1}{2}\right]\sum_{p_2=L_H}^{U_H-p_1}\widetilde{\zeta}_{(1+2)}\widetilde{\zeta}_2^* = 2\frac{\rho g}{C_{g,0}}\left[\frac{2C_{g,0}}{C_0} - \frac{1}{2}\right]\sum_{p_2=L_H}^{U_H-p_1}\widetilde{A}_{(1+2)}\widetilde{A}_2^*, \quad (6.21)$$

where $\widetilde{A}_1 = \sqrt{C_{g,0}}\widetilde{\zeta}_1$. Multiply both sides of (6.20) by their complex conjugates, ensemble average the result, multiply by $\sqrt{gh}/\Delta\omega$, and upon letting $\Delta\omega \to 0$ we obtain the expression

$$\mathcal{E}_1 = \frac{\sqrt{gh}}{\rho^2\left(gh - C_{g,0}^2\right)^2}\lim_{\Delta\omega\to0}\frac{<|RS_1|^2>}{\Delta\omega}$$

$$= 4\mathcal{F}_1\frac{g^{(5/2)}h^{(1/2)}}{C_{g,0}^2\left(gh - C_{g,0}^2\right)^2}\left[\frac{2C_{g,0}}{C_0} - \frac{1}{2}\right]^2 = 4\mathcal{F}_1\left(\frac{\mathcal{W}_{10}(x)}{\Lambda_{10}(x)}\right)^2, \qquad (6.22)$$

were we have used (6.21) and (6.14). Note that (6.22) is identical to the prediction of the stochastic model (6.19).

Thus, for off-resonant forcing on a very mild slope, the evolution of the forced lf spectrum is faithfully represented by the local uniform-depth solution. To sustain such a solution over variable depth, energy must be passed to (or from, depending on whether the depth is in- or decreasing) the long-wave spectral range, which requires a phase shift (i.e. the real contribution to $\mathcal{P}_1$ (see (6.15a)) between forcing and response away from

the quadrature relation associated with the equilibrium solution in uniform depth. Such a phase shift is not predicted if the problem were treated with uniform-depth theory from the outset but is implicit in the evolutionary-type description used here.

To relate the model-predicted phase shift to a time lag between the lf surface elevation and the squared hf envelope, we express the covariance function as (see (6.10))

$$\mathrm{Cov}_{\eta A}(\tau, x) = -\frac{16}{C_{g0}\,(gh)^{1/4}} \int_0^{\omega_{ul}} \mathcal{F}_1 |\mathcal{P}_1| \cos\left(\omega_1 \tau + \theta_1\right) d\omega_1, \qquad (6.23)$$

with

$$\theta_1 = \arg\{i\mathcal{P}_1\}. \qquad (6.24)$$

From (6.23) and (6.24) we see that the equilibrium solution in uniform depth yields $\theta_1 = 0$ and the covariance function has a negative peak at $\tau = 0$, corresponding to the bound wave motion being $\pi$ radians out of phase with the forcing envelope (see §6.2.3). For the off-resonant mild-slope conditions (viz. (6.18)) the bottom-induced phase shift is (for small $\theta$) given as

$$\theta_1 \approx \frac{h_x}{\mathcal{W}_{10}} \frac{d}{dh} \left(\frac{\mathcal{W}_{10}}{\Lambda_{10}}\right). \qquad (6.25)$$

Since $\left(\mathcal{W}_{10}/\Lambda_{10}\right)_h / \mathcal{W}_{10} > 0$ we note from (6.25) that $\theta_1 < 0$ on an up-slope ($h_x < 0$). Consequently, on an up-slope, the minimum of the correlation function, associated with the bound motion, is pushed toward positive time lag, which indicates a lagging of the forced waves with respect to the envelope. This is qualitatively consistent with the analysis results presented in §6.2 where indeed we found a positive time lag on the up-slope in the experimental set-up. From similar reasoning we see that on a down-slope ($h_x > 0$) the minimum of the covariance function is shifted to negative time, physically interpretable as the lf response leading the short-wave envelope. The latter prediction cannot be verified on the basis of the present data set but requires observations of wave-groups on a mildly declining bottom.

## 6.5  Discussion

A detailed analysis has been made of a data set for one-dimensional shoaling and breaking random surface waves on a slope, and the attendant forced and free low-frequency motions. The high cross-shore resolution allowed a quasi-continuous space-time visualization of the propagation of the incident short-wave envelope as well as the incoming (bound) and outgoing lf-waves, with a spatial detail that has not been available before. The analysis of the experimental data largely confirms existing notions concerning the propagation characteristics of the system of primary wave groups and forced lf waves, in particular the lagging of the lf waves behind the group envelope on a sloping beach.

Stochastic simulations are performed and model predictions of spectral evolution and third-order bulk statistics compare favorably to the observations. To relate the

model predictions to the cross-correlation analysis of the experimental data, we have derived an expression that relates the spectral and bi-spectral densities (which constitute the typical output of a nonlinear stochastic model) to the cross-correlation function between the squared short-wave envelope and lf motion. The model-predicted correlation functions thus obtained compare favorably to correlation functions derived directly from the observed time series. In particular, the model-predicted phase lag between the lf wave motion and the forcing groups in the shoaling regime is in very good agreement with observations, which indicates that the stochastic model representation faithfully captures the characteristics of the nonlinear phase coupling over variable depth.

In the nearshore, the model over-predicts incoming lf wave heights consistently. Although uncertainty remains with regards to the accuracy of the array decomposition technique in this region, the overestimation does seem to indicate insufficient dissipation in the low-frequency spectral regime. We attribute the latter primarily to the frequency weighting of the dissipation due to depth-induced breaking. Although arguably other effects such as e.g. bottom friction [Henderson & Bowen, 2002; Van Dongeren *et al.*, 2004] also affect the long wave evolution, their contributions are usually secondary in magnitude [Van Dongeren *et al.*, 2004, 2005]. The frequency-squared weighting of the breaking dissipation is applied to improve predictions of the third-order bulk statistics [Chen *et al.*, 1997], but this weighting deprives the long-wave spectral regime of its primary dissipation mechanism. In fact, applying a near-uniform weighting of the breaker dissipation greatly improves the predicted wave height evolution (not shown) but at the expense of a deterioration of the model-predicted third-order statistics.

In the shoaling regime, where the forced long waves are secondary in magnitude relative to the primary waves, the stochastic model equations can be simplified. Upon assuming the forced waves long relative to the water depth and the primary waves as narrow-band, we have shown that the varying depth induces a phase shift between forcing and response and that – on a very mild slope and off-resonant conditions– the stochastic evolution model predicts a spectral evolution in the long wave range that maintains the local equilibrium solution by Longuet-Higgins & Stewart [1962, 1964]. However, in contrast to uniform-depth theory, the present evolution-type model also predicts a phase shift between the low-frequency response and the short-wave envelope, a necessary condition for the growth of shoaling lf waves associated with the local equilibrium solution, even on very mild beaches. Without it there can be no energy exchange between the hf and lf frequency ranges and the waves would shoal conservatively (Green's law).

# Conclusions and outlook $\mathbf{7}$

With the present work we have aimed at developing and validating a stochastic model suitable for the prediction of the nonlinear evolution of random surface gravity waves over two-dimensional topography in shallow coastal waters.

Thereto, we have derived a deterministic, discrete spectral model based on an angular spectrum decomposition of the sea surface elevation (Chapter 2); in turn, based on the deterministic transport equations, we derived evolution equations for the statistical moments, i.e. a stochastic model (Chapter 4).

The deterministic model and its stochastic counterpart have been verified, both analytically, through comparison of asymptotic limits to established expressions in the literature, and empirically, by means of comparison to observations (Chapters 3 & 5).

Our main findings with respect to the development and verification of the respective models are summarized below.

*A generalized deterministic evolution model*

On the premise of weak lateral depth variability, we derived a discrete spectral evolution model, based on an angular-spectrum decomposition of the wave field, while accounting for two-dimensional topography through a scattering mechanism. The resulting model consists of a set of coupled-mode transport equations that account for the linear effects of refraction, shoaling, diffraction and non-stationarity as well as quadratic and cubic nonlinear effects. It is a generalization and extension of previous work in the sense that: (i) arbitrary resonance mismatch for quadratic interactions in a multi-frequency, multi-directional wave field propagating over weakly two-dimensional topography is included, with exact correspondence to well-known deep-intermediate (Stokes) and shallow water (Boussinesq) limits; (ii) it accounts for cubic near-resonances in deep-intermediate water without suffering the breakdown in shallow water typically associated with Stokes-type expansions.

The equivalence with well-known expressions for nonlinear wave propagation in deep-intermediate and shallow water is shown (§3.1); by taking appropriate limits, the model is shown to include both narrow-band cubic Schrödinger-type equations (§3.1.1) and models for quadratic resonant interactions as special cases, while reducing to a classical Boussinesq formulation in shallow water (§3.1.2).

The representation of the quadratic nonlinear interactions in the present formulation is in exact agreement with second-order theory, both for sum- and difference-interactions [e.g. Stokes, 1847; Hasselmann, 1962; Longuet-Higgins & Stewart, 1964]; in that sense

it is a generalization of more approximate, so-called resonant and quasi-resonant formulations [e.g. Kaihatu & Kirby, 1995; Eldeberky & Madsen, 1999]. However, differences between the respective formulations for quadratic interactions are mostly for off-resonant configurations that force non-secular components, necessarily of small amplitude, without affecting the dynamical evolution of the wave field.

Comparisons of numerical simulations to laboratory observations of one-dimensional wave propagation demonstrate that the model accurately predicts both cubic nonlinear effects on the evolution of wave groups in relatively deep water, and harmonic generation in waves propagating in relatively shallow water over a submerged obstacle. The successful modeling of such disparate nonlinear cases with a single model illustrates the general validity of the present formulation (§3.2).

Comparisons to laboratory observations of two-dimensional wave propagation over a convex beach confirm the robustness of the weakly two-dimensional approximation of topographical features to describe the combined effects of refraction, diffraction and harmonic generation in a realistic focusing region on a beach (§3.4).

*A stochastic model for heterogeneous, nonlinear shallow-water waves*

Based on the deterministic angular spectrum model we have derived transport equations for the statistical moments, while accounting for the effects of quadratic nonlinearity and lateral heterogeneity over topography.

In the linear approximation the stochastic model is closed, so that it accounts for shoaling, refraction and diffraction with the same accuracy as the underlying deterministic model. Two-dimensional topography is accounted for through a scattering mechanism, whereas the topography-induced phase coupling in the wave field is resolved through the explicit evolution of correlations between non-collinear wave components. Combined with the wide-angle capability inherited from the angular spectrum formalism, this renders the model particularly well suited for the modeling of wave propagation across e.g. focal regions behind topographical lenses or around thin barriers such as breakwater tips, where the effects of diffraction and lateral heterogeneity are important.

Dissipation associated with depth-induced wave breaking is parameterized through a bore-analogy and, after Baldock *et al.* [1998], assumes surf-zone wave heights Rayleigh-distributed, regardless whether they are broken or not; an inconsistency in the derivation by Baldock *et al.* is corrected. This parameterization results in an explicit expression for the bulk rate of dissipation and is shown robust, even on steep slopes (§4.3).

Nonlinear closure of the stochastic hierarchy is obtained by means of replacing the fourth cumulant contribution by a linear damping term in the bi-spectral evolution equation, to enable relaxation toward Gaussian statistics in the presence of strong nonlinearity. The length scale over which the triple correlations are relaxed is governed by both the intensity of cross-spectral energy transfers associated with nonlinearity, and the intensity of energy losses through depth-induced wave breaking (§4.4).

Comparison to laboratory observations of one-dimensional random wave propagation, confirms that the stochastic model accurately predicts the evolution of bulk second- and third-order statistics over variable depth. Model-predicted spectra compare favorable to observations, although the high-frequency tail of model-predicted spectra generally exhibit a somewhat slower drop-off toward higher frequencies than the observed spectra (§5.2). The predicted energy levels in the low-frequency spectral ranges, associated with group-forced long wave motion, are predicted quite accurately (§5.2 and §6.3). The predicted phase relation between forcing primary waves and low-frequency response over variable depth is in good agreement with what was found from the cross-correlation analysis of observations (§6.3).

The two-dimensional capability of the stochastic model is verified through comparison of simulation results to laboratory observations of random, directionally spread waves over two-dimensional topography. The agreement between predicted and observed wave heights along instrumented transects is generally good, both for relatively narrow- and wide-aperture incident wave fields. Since the wave fields considered were of low steepness, this two-dimensional verification confirms the model's 2D-capability in the linear sense (including dissipation) but further verification is needed to verify the model-representation of the combined topography-nonlinear effects (§5.3).

Empirical verification of the stochastic model through comparisons to field observations on a near-cylindrical beach indicates that: (i) the conservative processes of shoaling, refraction and quadratic nonlinear coupling are accurately presented by the model, (ii) surf zone parameterizations are robust; the model faithfully captures the dominant features of the spectral evolution in the presence of strong nonlinearity and dissipation; notable however is the fact that – in such regions – the predicted spectra generally tend to be overly smooth in frequency space; (iii) over long propagation distances, model-predicted bulk statistics are predicted accurately but the details of the spectral evolution – in particular in the very nearshore and inside the surf zone – are not fully resolved, rendering the agreement with observations more qualitative; in particular, the predicted spectra tend to be too narrow in directional space and overly smeared out in frequency space.

Overall, the level of agreement between stochastic model predictions and observations in the empirical verification of the stochastic model is quite favorable, particularly in view of the fact that a wide range of wave conditions and topographies were modeled, including strongly nonlinear waves across surf zone regions, utilizing a single set of empirical constants for the surf-zone parameterizations (which were chosen in an ad hoc manner). The present modeling approach, although based on the assumption that both nonlinearity and lateral depth variations are weak, is robust and well suited to wave prediction on the continental shelf and beaches, including the surf zone.

## Outlook on applicability and future developments

The stochastic angular-spectrum model derived in the present work inherits full frequency dispersion and wide-angle diffraction capability from the underlying deterministic framework; moreover, it accounts for arbitrary resonance mismatch in the quadratic nonlinear coupling coefficient. Notwithstanding the deep-water capability in the linear and quadratic nonlinear sense, the model is limited to relatively shallow water on account of the omission of cubic resonances; after all, the nonlinear dynamics in deeper water is governed by cubic, not quadratic interactions. Therefore, in its present form, the anticipated domain of operation is the nearshore region, either in stand-alone form, with boundary conditions derived from observations, or nested at the shallow-end of a larger domain, with boundary conditions provided by a model that *does* account for the relevant deep-water physics.

Alternatively, instead of nesting the model, extension to deeper water and longer propagation distances can be pursued through addition of the relevant deep-water physics to the present stochastic formalism. With respect to the nonlinear evolution, this requires accounting for the effects of quartet resonances through extension of the stochastic model, essentially following the lines of Hasselmann [1962]. On larger scales of operation, apart from the higher-order nonlinearity, additional physics such as e.g. wind forcing and steepness-breaking [e.g. Cavaleri & Malanotte-Rizzoli, 1981; Hasselmann, 1974] should generally also be taken into account; such effects can – in principle – be accounted for through a posteriori inclusion of existing source terms, where these are available.

For operational use at larger scales, numerical efficiency needs to be addressed. Particular consideration should be given to the rapid modulations that occur on account of the resonance mismatches for the quadratic interactions, and the numerically intensive convolution-type forcing terms in the governing equations, which are typical for nonlinear spectral models. The former require phase-resolving grid sizes, a restriction that can be relaxed through adding damping toward a quadrature bi-spectrum in off-resonant regions combined with an adaptive step size algorithm for the numerical integration (see §5.5). Efficiency gain with respect to the convolution operators can be achieved through application of common pseudo-spectral techniques [Canuto *et al.*, 1987].

We remark that in the present work emphasis has been on the development of the stochastic model formulation, and consequently the deterministic model was considered primarily an intermediate result. However, Monte-Carlo simulations with the underlying deterministic model (Chapter 2) may in some cases be preferred over – more approximate – stochastic simulations. After all, for sufficiently large ensemble size, the Monte-Carlo approach is generally the more accurate, since (i) the deterministic model includes both quadratic and cubic interactions, which extends the applicability to deeper water; (ii) the stochastic model relies on a parameterized stochastic closure, which may be inaccurate in the presence of strong (shallow-water) nonlinearity. With efficiency of the deterministic model improved through pseudo-spectral evaluation of the multi-dimensional nonlinear

convolutions, the additional cost in computational effort associated with Monte-Carlo simulations, may be an acceptable investment for the gain in predictive value.

Numerous models exist for nonlinear wave propagation, from detailed, time-domain Navier-Stokes models and high-order Boussinesq implementations, to operational phase-averaged models, suitable for ocean-scale operation, such as e.g. SWAN and WAVE-WATCH [Tolman, 1991; Booij *et al.*, 1999]; the evolutionary-type deterministic and stochastic model developed in the present work hold the middle ground somewhere between these two classes of models. The sheer variety of numerical model implementations, suitable for surface wave modeling, will – as a consequence of advances in our theoretical understanding of the ensuing physics and development of more accurate and efficient numerical techniques – only increase, not decrease. Furthermore, with the staggering rate at which capacity of present-day computers increases, more and more of such models will become operational at ever larger scales, while others – on the same account – may at some point become obsolete or considered overly parameterized. Nonetheless, the various approaches are often complementary, each carrying its own merits and limitations, and it would be illusory to pursue the 'best' model in a general sense. Instead, for particular engineering or science problems we should choose models that are 'optimal' with respect to the specifics of the 'reality' that is being modeled, and to a myriad of practical considerations among which there is usually time and – of course – money.

# Appendix A
# Wave-wave interaction coefficients

## A.1 Quadratic coefficients

The quadratic wave–wave interaction coefficients are

$$\mathcal{D}_{1,2} = -\frac{1}{2}\left[\omega_1 k_2^2\left(1 - \frac{\omega_2^2}{gk_2}T_2\right) + \omega_2 k_1^2\left(1 - \frac{\omega_1^2}{gk_1}T_1\right) - 2\left(\omega_1 + \omega_2\right)\left(k_1 k_2 T_1 T_2 - \boldsymbol{k}_1 \cdot \boldsymbol{k}_2\right)\right],$$

and

$$\mathcal{R}_{1,2} = \frac{1}{2g}\left[\omega_1\omega_2\left(k_1 T_1 + k_2 T_2\right) + g\left(k_1 k_2 T_1 T_2 - \boldsymbol{k}_1 \cdot \boldsymbol{k}_2\right)\right].$$

## A.2 Cubic coefficients

For the cubic wave–wave interaction coefficient we have

$$\mathcal{D}_{1,2,3} = \tfrac{1}{3}\left[\widehat{\mathcal{D}}_{1,2,3} + \widehat{\mathcal{D}}_{2,1,3} + \widehat{\mathcal{D}}_{3,1,2}\right],$$

where

$$\widehat{\mathcal{D}}_{1,2,3} = \frac{\omega_1}{g}\left(\omega_2 + \omega_3\right)\left(\boldsymbol{k}_2 \cdot \boldsymbol{k}_3\left(k_2 T_2 + k_3 T_3\right) - k_3 k_2\left(k_3 T_2 + k_2 T_3\right)\right)$$
$$+ \boldsymbol{k}_1 \cdot \left(\boldsymbol{k}_2 + \boldsymbol{k}_3\right)\left(k_2 k_3 T_2 T_3 - \tfrac{1}{2}\boldsymbol{k}_2 \cdot \boldsymbol{k}_3\right) - k_1^2 k_2 k_3 T_2 T_3 + k_1^2\left(1 - T_1^2\right)\mathcal{R}_{2,3}.$$

Note that the $\widehat{\mathcal{D}}_{1,2,3}$ are symmetrical in the last two indices so that $\mathcal{D}_{1,2,3}$ is symmetrical in all three indices.

# Appendix B
# Forcing terms amplitude evolution equations

The forcing terms on the transport equation (2.42) in physical variables and coordinates are

$$\xi_1^{(\text{wb})}\{a_2\} = i\frac{g}{2\omega_1}\left(1 - T_1^2\right)\left[k_1^2 \mathcal{G}_1\{\widetilde{h}, a_2\} + i\lambda_1\left(q_1 T_1 - 1\right)\mathcal{G}_1\{\widetilde{h}_y, a_2\}\right.$$
$$\left. + i\varkappa_1\left(\frac{C_{g,1}}{2C_1} + q_1 T_1 - 1\right)\left[\mathcal{G}_1\{\widetilde{h}_x, a_2\} + 2\mathcal{G}_1\{\widetilde{h}, a_{2,x}\}\right]\right], \tag{B.1}$$

$$\xi_1^{(\text{wbb})}\{a_2\} = i\frac{g}{2\omega_1}\left(1 - T_1^2\right)\frac{k_1^3\left(1 + 3T_1^2\right)}{4T_1}\mathcal{G}_1\{\widetilde{h}^2, a_2\}, \tag{B.2}$$

$$\xi_1^{(\text{www})}\{a_2 a_3 a_4\} = \frac{i}{2\omega_1}\sum_{\boldsymbol{v}_2,\boldsymbol{v}_3,\boldsymbol{v}_4}\mathcal{H}_{2,3,4}a_2 a_3 a_4 \delta_{234;1}^{\lambda,\omega}E_{234;1}, \tag{B.3}$$

$$\xi_1^{(\text{wc})}\{a_2\} = i\frac{k_1^2}{2\omega_1}(1 - T_1^2)\mathcal{G}_1\{\overline{\overline{\phi}}_t, a_2\} - \mathcal{G}_1\{\overline{\overline{\phi}}_x, i\varkappa_2 a_2\} - \mathcal{G}_1\{\overline{\overline{\phi}}_y, i\lambda_2 a_2\}. \tag{B.4}$$

where the $a_{\text{j}}$ are dummy variables used for convenience and should be replaced with the appropriate operand. Further we have

$$\mathcal{H}_{1,2,3} = \tfrac{1}{3}\left[\widehat{\mathcal{H}}_{1,2,3} + \widehat{\mathcal{H}}_{2,1,3} + \widehat{\mathcal{H}}_{3,1,2}\right], \qquad \widehat{\mathcal{H}}_{1,2,3} = \widehat{\mathcal{D}}_{1,2,3} - 2\frac{\mathcal{D}_{2,3}}{gk_{23}T_{23}\Delta_{23}}\mathcal{D}_{1,23}. \tag{B.5}$$

The quadratic and modified cubic nonlinear term in (2.44) are

$$\xi_1^{(\text{ww})}\{a_2 a_3\} = -V_1\sum_{\boldsymbol{v}_2,\boldsymbol{v}_3}\frac{\mathcal{D}_{2,3}}{gJ_{2,3}}a_2 a_3 \delta_{23;1}^{\lambda,\omega}E_{23;1}, \tag{B.6}$$

$$\xi_1^{(\text{M,www})}\{a_2 a_3 a_4\} = \frac{i}{2\omega_1}\sum_{\boldsymbol{v}_2,\boldsymbol{v}_3,\boldsymbol{v}_4}\mathcal{W}_{2,3,4}a_2 a_3 a_4 \delta_{234;1}^{\lambda,\omega}E_{234;1}, \tag{B.7}$$

where in (B.7)

$$\mathcal{W}_{1,2,3} = \tfrac{1}{3}\left[\widehat{\mathcal{W}}_{1,2,3} + \widehat{\mathcal{W}}_{2,1,3} + \widehat{\mathcal{W}}_{3,1,2}\right] \tag{B.8}$$

and

$$\widehat{\mathcal{W}}_{1,2,3} = \widehat{\mathcal{D}}_{1,2,3} - 2\frac{\mathcal{D}_{2,3}}{gk_{23}T_{23}\Delta_{23}}\left(\mathcal{D}_{1,23} - 2\omega_{1+2+3}V_{1+2+3}\frac{\mathcal{D}_{1,2+3}}{gJ_{1,2+3}}\right). \tag{B.9}$$

The forcing operators on the transport equation for a stationary wave field, (3.29), are

$$\widehat{\Xi}_1^{(\text{wb})}\{a_2\} = i\frac{g}{2\omega_1 V_1}\left(1 - T_1^2\right)\left[k_1^2 \mathcal{G}_1\{\widetilde{h}, a_2\} + i\varkappa_1 P_1 \mathcal{G}_1\{\widetilde{h}_x, a_2\}\right. \tag{B.10}$$

$$\left. + i\lambda_1\left(q_1 T_1 - 1\right)\mathcal{G}_1\{\widetilde{h}_y, a_2\}\right],$$

$$\widehat{\Xi}_1^{(\text{wbb})}\{a_2\} = i\frac{g}{2\omega_1 V_1}k_1^3\frac{C_1}{2C_{g,1}}\frac{(1 - T_1^2)^2}{T_1}\left[\frac{1}{(1 - T^2)} - P_1\right]\mathcal{G}_1\{\widetilde{h}^2, a_2\}, \tag{B.11}$$

$$\widehat{\Xi}_1^{(\text{wc})}\{a_2\} = -\frac{1}{V_1}\left(\mathcal{G}_1\{\overline{\overline{\phi}}_x, i\varkappa_2 a_2\} + \mathcal{G}_1\{\overline{\overline{\phi}}_y, i\lambda_2 a_2\}\right), \tag{B.12}$$

where

$$P_1 = \frac{1}{2}\left[\left(\frac{k_1}{\varkappa_1}\right)^2 - 1\right] - \frac{C_1}{2C_{g,1}}\left(1 - q_1 T_1\right).$$

# Appendix C
# Wave-driven mean flow and set-down

Governing equations for the wave-driven mean flow are given to facilitate comparison to experimental (flume) data. Results are presented directly in physical variables and coordinates and we use the actual, two-dimensional depth $h$ instead of the decomposition applied to derive the wave field evolution. The current-related quantities are assumed to depend on the slow scales in $x$, $y$ and $t$:

$$
\left[ \begin{array}{c} \Phi^{(n,0)} \\ \eta^{(n,0)} \end{array} \right] = \left[ \begin{array}{c} \Phi^{(n,0)}(z, x_1, y_1, t_1, x_2, y_2, t_2) \\ \eta^{(n,0)}(x_1, y_1, t_1, x_2, y_2, t_2) \end{array} \right].
\tag{C.1}
$$

To the order of approximation required we obtain from the kinematic and dynamic free surface boundary condition:

$$
\bar{\bar{\eta}}_t + \boldsymbol{\nabla} \cdot \left( h \boldsymbol{\nabla} \bar{\bar{\Phi}} + \boldsymbol{L} \right) = 0, \qquad\qquad \bar{\bar{\eta}} = -\frac{1}{g} \bar{\bar{\Phi}}_t + B,
\tag{C.2}
$$

where $\bar{\bar{\Phi}} = \epsilon \Phi^{(1,0)}$ and $\bar{\bar{\eta}} = \epsilon \eta^{(1,0)} + (\epsilon^2/\mu)\,\eta^{(2,0)}$. The wave-induced, depth-averaged mass flux $\boldsymbol{L}$ and the wave-induced water level correction $B$ are given by

$$
\boldsymbol{L} = \sum_{p_1} \frac{\omega_1}{g} \mathcal{F}^{-1}\{\varphi_1 e^{i\psi_1}\} \left\langle \mathcal{F}^{-1}\{\varkappa_1 \varphi_1 e^{i\psi_1}\}^*, \mathcal{F}^{-1}\{\lambda_1 \varphi_1 e^{i\psi_1}\}^* \right\rangle,
\tag{C.3}
$$

$$
B = \sum_{p_1} \frac{1}{2g} \left[ (k_1 T_1)^2 \|\mathcal{F}^{-1}\{\varphi_1 e^{i\psi_1}\}\|^2 - \|\mathcal{F}^{-1}\{i\varkappa_1 \varphi_1 e^{i\psi_1}\}\|^2 - \|\mathcal{F}^{-1}\{i\lambda_1 \varphi_1 e^{i\psi_1}\}\|^2 \right],
\tag{C.4}
$$

where $\varphi_1 = \epsilon \varphi_1^{(1,1)} + (\epsilon/\mu)^2 \varphi_1^{(2,2)}$. For a stationary wave field the depth-averaged, wave-driven mean flow and water level corrections are given by

$$
\boldsymbol{\nabla} \cdot \left( h \boldsymbol{\nabla} \bar{\bar{\Phi}} + \boldsymbol{L} \right) = 0, \qquad\qquad \bar{\bar{\eta}} = B.
\tag{C.5}
$$

# Appendix D
# Verification of third order interaction coefficient

We have

$$\widehat{\mathcal{H}}_{1,2,3} = \widehat{\mathcal{D}}_{1,2,3} - 2\mathcal{D}_{1,23}\left(\frac{\mathcal{D}_{2,3}}{g\Delta_{2,3}}\right)$$

$$= -\frac{\mathcal{D}_{2,3}}{g\Delta_{2,3}}\left[2\left(\omega_1 + \omega_2 + \omega_3\right)\left(k_1 T_1 k_{2,3} T_{2,3} - \boldsymbol{k}_1 \cdot \left(\boldsymbol{k}_2 + \boldsymbol{k}_3\right)\right)\right.$$

$$\left. -\omega_1 k_{2,3}^2 \left(1 - T_{2,3}^2\right) - \omega_{2,3} k_1^2 \left(1 - T_1^2\right)\right] + \mathcal{D}_{2,3}\frac{\omega_1}{g} k_{2,3} T_{2,3}$$

$$+ \mathcal{R}_{2,3}\left(k_1^2\left(1 - T_1^2\right) + \boldsymbol{k}_1 \cdot \left(\boldsymbol{k}_2 + \boldsymbol{k}_3\right)\right)$$

$$+ \frac{\omega_1}{g}\left(\frac{\omega_1}{2} + \omega_2 + \omega_3\right)\left(\boldsymbol{k}_2 \cdot \boldsymbol{k}_3 \left(k_3 T_3 + k_2 T_2\right) - k_2 k_3 \left(T_2 k_3 + T_3 k_2\right)\right)$$

$$- \boldsymbol{k}_2 \cdot \boldsymbol{k}_3 \left[\frac{\omega_1^3}{2g^2}\left(\omega_2 + \omega_3\right) + \frac{\omega_1}{2g^2}\left(\omega_2^3 + \omega_3^3\right)\right].$$

Note that

$$\boldsymbol{k}_2 \cdot \boldsymbol{k}_3 \frac{\omega_1^3}{2g^2}\left(\omega_2 + \omega_3\right) = \mathcal{R}_{2,3}\frac{\omega_1^3}{g^2}\left(\omega_2 + \omega_3\right) - \mathcal{D}_{2,3}\frac{\omega_1^3}{g^2} - \frac{\omega_1^3}{2g^2}\left(\omega_2 k_3^2 + \omega_3 k_2^2\right).$$

After some manipulation the interaction coefficient can be written as

$$\widehat{\mathcal{H}}_{1,2,3} = -\frac{\mathcal{D}_{2,3}}{g\Delta_{2,3}}\left[2\left(\omega_1 + \omega_2 + \omega_3\right)\left(k_1 T_1 k_{2,3} T_{2,3} - \boldsymbol{k}_1 \cdot \left(\boldsymbol{k}_2 + \boldsymbol{k}_3\right)\right)\right. \tag{D.1}$$

$$\left. -\omega_1 k_{2,3}^2 \left(1 - T_{2,3}^2\right) - \omega_{2,3} k_1^2 \left(1 - T_1^2\right)\right] + \mathcal{D}_{2,3}\frac{\omega_1}{g}\left(\frac{\omega_1^2}{g} + k_{2,3} T_{2,3}\right)$$

$$+ \mathcal{R}_{2,3}\left(k_1^2\left(1 - T_1^2\right) + \boldsymbol{k}_1 \cdot \left(\boldsymbol{k}_2 + \boldsymbol{k}_3\right) - \frac{\omega_1^3}{g^2}\left(\omega_2 + \omega_3\right)\right)$$

$$+ \frac{\omega_1}{2g}\boldsymbol{k}_2 \cdot \boldsymbol{k}_3\left(\left(\omega_1 + \omega_2 + \omega_3\right)\left(\omega_3^2 + \omega_2^2\right) + \omega_2 \omega_3 \left(\omega_2 + \omega_3\right)\right)$$

$$- \frac{\omega_1 k_3^2 \omega_2^2}{2g^2}\left(\omega_1 + \omega_2 + 2\omega_3\right) - \frac{\omega_1 k_2^2 \omega_3^2}{2g^2}\left(\omega_1 + 2\omega_2 + \omega_3\right),$$

which is equivalent to Herterich & Hasselmann [1980] eq. (B 2) applied to the present wave field decomposition (the original derivation due to Hasselmann [1962] lacks two finite depth terms as noted by Herterich & Hasselmann [1980]).

If – after Longuet-Higgins & Phillips [1962] – we consider the directional interaction of a couple of waves in deep water then the evolution of $\varphi_2$ say, as a consequence of pair-wise, third-order interaction with $\varphi_1$ reads:

$$\frac{d\varphi_2}{dt} = -iK_{1,2}|\varphi_1|^2\varphi_2 - 2i\frac{k_2^4}{\omega_2}|\varphi_2|^2\varphi_2, \tag{D.2}$$

where

$$K = \frac{2\omega_1 k_1 k_2}{g\omega_2}\left[\omega_1\left(k_1 - k_2 + \underbrace{2k_2\left(\sin\frac{\theta_{1,2}}{2}\cos\frac{\theta_{1,2}}{2}\right)^2}\right) + \omega_2(k_1 + k_2)\cos\theta_{1,2}\right.$$

$$+ (\omega_1 - \omega_2)|\boldsymbol{k}_1 - \boldsymbol{k}_2|\cos^2\frac{\theta_{1,2}}{2}\left[1 - \frac{4\omega_1\omega_2\sin^2\frac{\theta_{2-1,1}}{2}}{g\Delta_{2,-1}}\right]$$

$$\left.+ (\omega_2 + \omega_1)|\boldsymbol{k}_1 + \boldsymbol{k}_2|\sin^2\frac{\theta_{1,2}}{2}\left[1 + \frac{4\omega_1\omega_2\cos^2\frac{\theta_{2+1,1}}{2}}{g\Delta_{2,1}}\right]\right] \tag{D.3}$$

and

$$\cos\theta_{1,2} = \frac{\boldsymbol{k}_1 \cdot \boldsymbol{k}_2}{k_1 k_2}, \quad \cos\theta_{2+1,1} = \frac{(\boldsymbol{k}_2 + \boldsymbol{k}_1) \cdot \boldsymbol{k}_1}{|\boldsymbol{k}_2 + \boldsymbol{k}_1|k_1}, \quad \cos\theta_{2-1,1} = \frac{(\boldsymbol{k}_2 - \boldsymbol{k}_1) \cdot \boldsymbol{k}_1}{|\boldsymbol{k}_2 - \boldsymbol{k}_1|k_1}. \tag{D.4}$$

Note that (D.3) is entirely consistent with equation (2.8) of Longuet-Higgins & Phillips [1962] in their work except the underbraced term which differs by a factor 2; this discrepancy in expressions does not affect the interaction of mutually perpendicular, opposing and parallel propagating wave trains but indeed that of any other mutual angle. Internal consistency of the present derivation was confirmed from many re-derivations, all leading to the same result. Corroboration of the present expressions was found in Willebrand [1973, 1975], and Hogan *et al.* [1988]. The latter authors also find this factor 2 missing in Longuet-Higgins & Phillips [1962].

# References

ABLOWITZ, M. J., KAUP, D. J., NEWELL, A. C. & SEGUR, H. 1973a Method for solving the sine-Gordon equation. *Phys. Rev. Lett.* **30**, 1262–1264.

ABLOWITZ, M. J., KAUP, D. J., NEWELL, A. C. & SEGUR, H. 1973b Nonlinear evolution equations of physical significance. *Phys. Rev. Lett.* **31**, 125–127.

ABLOWITZ, M. J., KAUP, D. J., NEWELL, A. C. & SEGUR, H. 1974 The inverse scattering transform – a fourier analysis for nonlinear problems. *Stud. Appl. Math.* **53**, 249–315.

ABLOWITZ, M. J. & SEGUR, H. 1981 *Solitons and the inverse scattering transform.* Philadelphia, USA: Siam.

ABREU, M., LARAZZA, A. & THORNTON, E. 1992 Nonlinear transformation of directional wave spectra in shallow water. *J. Geophys. Res.* **97** (C10), 15,579–15,589.

AGNON, Y., MADSEN, P. A. & SCHÄFFER, H. A. 1999 A new approach to high-order Boussinesq models. *J. Fluid Mech.* **399**, 319–333.

AGNON, Y. & SHEREMET, A. 1997 Stochastic nonlinear shoaling of directional spectra. *J. Fluid Mech.* **345**, 79–99.

AGNON, Y. & SHEREMET, A. 2000 Stochastic evolution models for nonlinear gravity waves over uneven topography. In *Adv. Coast. Ocean Eng.* (ed. P. L.-F. Liu), pp. 103–131. New Jersey: World Scientific.

AGNON, Y., SHEREMET, A., GONSALVES, J. & STIASSNIE, M. 1993 Nonlinear evolution of a unidirectional shoaling wave field. *Coastal Eng.* **20**, 29–58.

ALBER, I. E. 1978 The effects of randomness on the stability of two-dimensional surface wave trains. *Proc. Roy. Soc. Lond. A* **363**, 525–546.

ARDHUIN, F. & HERBERS, T. H. C. 2002 Bragg scattering of random surface gravity waves by irregular sea bed topography. *J. Fluid Mech.* **451**, 1–33.

ARMSTRONG, J. A., BLOEMBERGEN, N., DUCUING, J. & PERSHAN, P. S. 1962 Interactions between Light Waves in a Nonlinear Dielectric. *Phys. Rev.* **127** (6), 1918–1939.

BAKKENES, H. J. 2002 Observation and separation of bound and free low-frequency waves in the nearshore zone. MSc-thesis. Delft University of Technology.

BALDOCK, T. E., HOLMES, P., BUNKER, S. & VAN WEERT, P. 1998 Cross-shore hydrodynamics within an unsaturated surf zone. *Coastal Eng.* **34**, 173–196.

BALDOCK, T. E., HUNTLEY, P. A. D., BIRD, T. & BULLOCK, G. N. 2000 Breakpoint generated surfbeat induced by bichromatic wave groups. *Coastal Eng.* **39**, 213–242.

BASTIAANS, M. J. 1979 Transport equations for the Wigner distribution function. *Optica Acta* **26** (10), 1265–1272.

BATTJES, J. A. 1968 Refraction of water waves. *J. waterw. and harbors div.* **94** (4), 113–121.

BATTJES, J. A. 1972 Set-up due to irregular waves. In *Proc. 13$^{th}$ Int. Conf. Coastal Eng.*, pp. 1993–2004. ASCE.

BATTJES, J. A., BAKKENES, H. J., JANSSEN, T. T. & VAN DONGEREN, A. R. 2004 Shoaling of subharmonic gravity waves. *J. Geophys. Res.* **109** (C02009), doi:10.1029/2003JC001863.

BATTJES, J. A. & BEJI, S. 1992 Breaking waves propagating over a shoal. In *Proc. 23$^{rd}$ Int. Conf. Coastal Eng.*, pp. 42–50. ASCE.

BATTJES, J. A. & JANSSEN, J. P. F. M. 1978 Energy loss and set-up due to breaking of random waves. In *Proc. 16$^{th}$ Int. Conf. Coastal Eng.*, pp. 569–588. ASCE.

BATTJES, J. A. & STIVE, M. J. F. 1985 Calibration and verification of a dissipation model for random breaking waves. *J. Geophys. Res.* **90** (C5), 9159–9167.

BECQ, F. 1998 Extension de la modélisation spectrale des états de mer vers le domaine côtier. PhD dissertation, l'Université de Toulon et du Var, Toulon, La France.

BECQ, F., BENOIT, M. & FORGET, P. 1998 Numerical simulations of directionally spread shoaling surface gravity waves. In *Proc. 26$^{th}$ Int. Conf. Coastal Eng.*, pp. 523–536.

BEJI, S. 1995 Note on a nonlinearity parameter of surface waves. *Coastal Eng.* **25**, 81–85.

BEJI, S. & BATTJES, J. A. 1993 Experimental investigation of wave propagation over a bar. *Coastal Eng.* **19**, 151–162.

BEJI, S. & BATTJES, J. A. 1994 Numerical simulation of nonlinear wave propagation over a bar. *Coastal Eng.* **23**, 1–16.

BENDAT, J. S. & PIERSOL, A. G. 1986 *Random data, analysis and measurement*. NY, USA: John Wiley & Sons, inc.

BENNEY, D. J. 1971 Nonlinear waves. In *Mathematical problems in the geophyisical sciences* (ed. W. H. Reid), pp. 103–120.

BENNEY, D. J. & NEWELL, A. C. 1969 Random wave closures. *Stud. Appl. Math.* **48**, 29–53.

BENNEY, D. J. & SAFFMAN, P. G. 1966 Nonlinear interactions of random waves in a dispersive medium. *Proc. Roy. Soc. Lond. A* **289**, 301–320.

BERKHOFF, J. C. W. 1976 Mathematical models for simple harmonic linear water waves; wave diffraction and refraction. Publ. No. 163. Delft Hydr. Lab.

BERKHOFF, J. C. W., BOOIJ, N. & RADDER, A. C. 1982 Verification of numerical wave propagation models for simple harmonic linear water waves. *Coastal Eng.* **20**, 255–279.

BIÉSEL, F. 1952 Équations générales au second ordre de la houle irréguliere. *La Houille Blanche* pp. 372–376.

BOERS, M. 1996 Simulation of a surf zone with a barred beach, part 1: Wave heights and wave breaking. Comm. on Hydr. and Geotechn. Eng. 96-5. Delft Univ. of Techn., 116 p.

BOERS, M. 2005 Surf zone turbulence. PhD dissertation, Delft, The Netherlands.

BOOIJ, N., RIS, R. C. & HOLTHUIJSEN, L. H. 1999 A third-generation wave model for coastal regions. Part 1, model description and validation. *J. Geophys. Res.* **104** (c4), 7649–7666.

BOUSSINESQ, J. 1871 Théorie générale des mouvements qui sont propagés dans un canale rectangulaire horizontal. *C. r. hebd. Séanc, Acad. Sci., Paris* **73**, 256–260, (in French).

BOUSSINESQ, J. 1872 Théorie des ondes et des remous qui se propagent le long d'un canal rectanguliere horizontal, en communiquant au liquide contenu dans ce canal des vitesses sensiblement pareilles de la surface au fond. *J. Math. Pures et Appl., Ser. 2* **17**, 55–108, (in French).

BOUWS, E., GUNTHER, H., ROSENTHAL, W. & VINCENT, C. 1985 Similarity of the wind wave spectrum in finite depth water. *J. Geophys. Res.* **90** (c1), 975–986.

BOWEN, A. J. & GUZA, R. T. 1978 Edge waves and surf beat. *J. Geophys. Res.* **83** (c4), 1913–1920.

BOWERS, E. C. 1992 Low frequency waves in intermediate water depths. In *Proc. 23$^{rd}$ Int. Conf. Coastal Eng.*, pp. 832–845. ASCE, Venice.

BREDMOSE, H. 2002 Deterministic modelling of water waves in the frequency domain. PhD dissertation, University of Denmark, Lyngby, Denmark.

BREDMOSE, H., AGNON, Y., MADSEN, P. A. & SCHÄFFER, H. A. 2005 Wave transformation models with exact second-order transfer. *Eur. J. Mech. B/Fluids* **24** (6), 659–798.

BREDMOSE, H., MADSEN, P. A., SCHÄFFER, H. A. & AGNON, Y. 2002 Fully dispersive evolution equations: wave breaking and efficiency. In *Proc. 28$^{th}$ Int. Conf. Coastal Eng.*, pp. 281–292. ASCE, Cardiff.

BREDMOSE, H., SCHÄFFER, H. A., MADSEN, P. A. & AGNON, Y. 2004 Boussinesq evolution equations: Numerical efficiency, breaking and amplitude dispersion. *Coastal Eng.* **51** (11-12), 1117–1142.

BRETHERTON, F. P. 1964 Resonant interactions between waves. The case of discrete oscillations. *J. Fluid Mech.* **20**, 457–479.

BRYANT, P. J. 1973 Periodic waves in shallow water. *J. Fluid Mech.* **59**, 625–644.

BRYANT, P. J. 1974 Stability of periodic waves in shallow water. *J. Fluid Mech.* **66**, 81–96.

BYRNE, R. J. 1969 Field occurences of induced multiple gravity waves. *J. Geophys. Res.* **74** (10), 2590–2596.

CANUTO, C., HUSSAINI, M. Y., QUARTERONI, A. & ZANG, T. A. 1987 *Spectral methods in Fluid Dynamics*. NY, USA: Springer.

CAVALERI, L. & MALANOTTE-RIZZOLI, P. 1981 Wind wave prediction in shallow water: Theory and applications. *J. Geophys. Res.* **86** (C11), 10,961–10,973.

CHAWLA, A. 1995 Wave transformation over a submerged shoal.

CHAWLA, A., ÖZKAN HALLER, H. T. & KIRBY, J. T. 1996 Experimental study of breaking waves over a shoal. In *Proc. 25$^{th}$ Int. Conf. Coastal Eng.*, pp. 2–15. ASCE.

CHAWLA, A., ÖZKAN HALLER, H. T. & KIRBY, J. T. 1998 Spectral model for wave transformation and breaking over irregular bathymetry. *J. Wat., Port, Coast. Ocean Eng.* **124** (4), 189–198.

CHEN, Y. & LIU, P. L.-F. 1995 Modified Boussinesq equations and associated parabolic models for water wave propagation. *J. Fluid Mech.* **288**, 351–381.

CHEN, Y. R., GUZA, R. T. & ELGAR, S. 1997 Modeling spectra of breaking surface waves in shallow water. *J. Geophys. Res.* **102**, 25,035–25,046.

CHU, V. H. & MEI, C. C. 1970 On slowly varying Stokes waves. *J. Fluid Mech.* **41**, 873–887.

CRAIK, A. D. D. 2004 The origins of water wave theory. *Ann. Rev. Fluid Mech.* **36**, 1–28.

DALRYMPLE, R. A. & KIRBY, J. T. 1988 Models for very wide-angle water waves and wave diffraction. *J. Fluid Mech.* **192**, 33–50.

DALRYMPLE, R. A., SUH, K. D., KIRBY, J. T. & CHAE, J. W. 1989 Models for very wide-angle water waves and wave diffraction. part 2. irregular bathymetry. *J. Fluid Mech.* **201**, 299–322.

DAVEY, A. & STEWARTSON, K. 1974 On three-dimensional packets of surface waves. *Proc. Roy. Soc. Lond. A* **338**, 101–110.

DINGEMANS, M. W. 1997 *Water wave propagation over uneven bottoms*. NY, USA: World Scientific.

DINGEMANS, M. W., PETIT, H. A. H., MEIJER, T. J. G. P. & KOSTENSE, J. K. 1991 Numerical evaluation of the third-order evolution equations for weakly nonlinear water waves propagating over uneven bottoms. In *Computer modelling in Ocean Engeering* (ed. M. Arcilla, M. Pastor, O. C. Zienkiewicz & B. A. Schrefler), pp. 361–370. Rotterdam, The Netherlands: Balkema.

DJORDJEVIĆ, V. D. & REDEKOPP, L. G. 1978 On the development of packets of surface gravity waves moving over an uneven bottom. *Z. angew. Math. Phys.* **29**, 950–962.

DYSTHE, K. B. 1979 Note on a modification to the nonlinear Schrödinger equation for application to deep water waves. *Proc. Roy. Soc. Lond. A* **369**, 105–114.

ELDEBERKY, Y. 1996 Nonlinear transformation of wave spectra in the nearshore zone. PhD dissertation, Delft, The Netherlands.

ELDEBERKY, Y. & BATTJES, J. A. 1996 Spectral modeling of wave breaking: Application to Boussinesq equations. *J. Geophys. Res.* **101**, 1253–1264.

ELDEBERKY, Y. & MADSEN, P. A. 1999 Deterministic and stochastic evolution equations for fully dispersive and weakly non-linear waves. *Coastal Eng.* **38**, 1–24.

ELDEBERKY, Y., POLNIKOV, V. & BATTJES, J. A. 1996 A statistical approach for modelling triad interactions in dispersive waves. In *Proc. 25th Int. Conf. Coastal Eng.*, pp. 1088–1101.

ELGAR, S., FREILICH, M. H. & GUZA, R. T. 1990 Recurrence in truncated Boussinesq models for nonlinear waves in shallow water. *J. Geophys. Res.* **95** (C7), 11,547–11,556.

ELGAR, S. & GUZA, R. T. 1985 Observations of bispectra of shoaling waves. *J. Fluid Mech.* **161**, 425–448.

ELGAR, S., GUZA, R. T. & FREILICH, M. H. 1993 Observations of nonlinear interaction in directionally spread shoaling surface gravity waves. *J. Geophys. Res.* **98**, 20,299–20,305.

ELGAR, S., GUZA, R. T., RAUBENHEIMER, B. & HERBERS, T. H. C. 2001 Wave energy and direction observed near a pier. *J. Wat., Port, Coast. Ocean Eng.* **127**, 2–6.

ELGAR, S., GUZA, R. T., RAUBENHEIMER, B., HERBERS, T. H. C. & GALLAGHER, E. L. 1997 Spectral evolution of shoaling and breaking waves on a barred beach. *J. Geophys. Res.* **102** (C7), 15,797–15,805.

ELGAR, S., HERBERS, T. H. C., OKIHIRO, M., OLTMAN-SHAY, J. & GUZA, R. T. 1992 Observations of infragravity waves. *J. Geophys. Res.* **97** (C10), 15,573–15,577.

ELGAR, S., RAUBENHEIMER, B. & HERBERS, T. H. C. 2003 Bragg reflection of ocean waves from sandbars. *Geoph. Res. Lett.* **30** (1), doi:10.1029/2002GL016351.

FEDDERSEN, F., GUZA, R. T., ELGAR, S. & HERBERS, T. H. C. 1998 Alongshore momentum balance in the nearshore. *J. Geophys. Res.* **103**, 15,667–15,676.

FEIR, J. E. 1967 Discussion: some results from wave pulse experiments. *Proc. Roy. Soc. Lond. A* **299**, 54–58.

FENTON, J. D. 1985 A fifth-order Stokes theory for steady waves. *J. Wat., Port, Coast. Ocean Eng.* **111** (2), 216–234.

FERMI, E., PASTA, J. & ULAM, S. 1955 Studies of nonlinear problems, I. Los Alamos Rep. LA1940. Los Alamos, reprod. in *Nonlinear wave motion* (A.C. Newell, ed.), Lectures in Applied Mathematics, **15**, 1974, Am. Math. Soc., 143 – 156.

FREILICH, M. H. & GUZA, R. T. 1984 Nonlinear effects on shoaling surface gravity waves. *Phil. Trans. Roy. Soc. London* **A311**, 1–41.

FUHRMAN, D. R., MADSEN, P. A. & BINGHAM, H. B. 2004 A numerical study of crescent waves. *J. Fluid Mech.* **513**, 309–342.

GALLAGHER, B. 1971 Generation of surf beat by non-linear wave interactions. *J. Fluid Mech.* **49**, 1–20.

GALLAGHER, E. L., ELGAR, S. & GUZA 1998 Observations of sandbar evolution on a natural beach. *J. Geophys. Res.* **103**, 3203–3215.

GARDNER, C. S., GREENE, J. M., KRUSKAL, M. D. & MIURA, R. M. 1967 Method for solving the Korteweg-deVries equation. *Phys. Rev. Lett.* **19**, 1095–1097.

GARDNER, C. S., GREENE, J. M., KRUSKAL, M. D. & MIURA, R. M. 1974 The Korteweg-deVries equation and generalizations. VI. Methods for exact solution. *Comm. Pure Appl. Math.* **27**, 97–133.

GODA, Y. 1975 Irregular wave deformation in the surf zone. *Coastal Eng. Jap.* **18**, 13–26.

GODA, Y. & SUZUKI, Y. 1976 Estimation of incident and reflected waves in random wave experiments. In *Proc. 15$^{th}$ Int. Conf. Coastal Eng.*, pp. 828–845. ASCE, Hawaii.

GRIFFITHS, D. J. 1994 *Introduction to quantum mechanics*. NJ, USA: Prentice Hall.

HAMMACK, J., MCCALLISTER, D., SCHEFFNER, N. & SEGUR, H. 1995 Two-dimensional periodic waves in shallow water. Part 2, asymmetric waves. *J. Fluid Mech.* **285**, 95–122.

HAMMACK, J., SCHEFFNER, N. & SEGUR, H. 1989 Two-dimensional periodic waves in shallow water. *J. Fluid Mech.* **209**, 567–589.

HASIMOTO, H. & ONO, H. 1972 Nonlinear Modulation of Gravity Waves. *J. Phys. Soc. Japan* **33** (3), 805–811.

HASSELMANN, K. 1962 On the non-linear energy transfer in a gravity-wave spectrum, I. *J. Fluid Mech.* **12**, 481–500.

HASSELMANN, K. 1963 On the non-linear energy transfer in a gravity-wave spectrum, II. *J. Fluid Mech.* **15**, 273–281.

HASSELMANN, K. 1974 On the spectral dissipation of ocean waves due to whitecapping. *Bound.-layer Meteor.* **6**, 107–127.

HASSELMANN, K., MUNK, W. & MACDONALD, G. 1963 Bispectra of ocean waves. In *Time series analysis* (ed. M. Rosenblatt), , vol. 7, pp. 125–139. New York: John Wiley.

HENDERSON, S. M. & BOWEN, A. J. 2002 Observations of surf beat forcing and dissipation. *J. Geophys. Res.* **107** (C11), doi:10.1029/2000JC000498.

HENDERSON, S. M., GUZA, R. T., ELGAR, S. & HERBERS, T. H. C. 2006 Refraction of surface gravity waves by shear waves. *Submitted to J. Phys. Oceanogr.* .

HERBERS, T. H. C. & BURTON, M. C. 1997 Nonlinear shoaling of directionally spread waves on a beach. *J. Geophys. Res.* **102**, 21,101–21,114.

HERBERS, T. H. C., ELGAR, S. & GUZA, R. T. 1994 Infragravity-frequency (0.005 − 0.05 Hz) motions on the shelf. Part I: Forced waves. *J. Phys. Oceanogr.* **24**, 917–927.

HERBERS, T. H. C., ELGAR, S. & GUZA, R. T. 1999 Directional spreading of waves in the nearshore. *J. Geophys. Res.* **104**, 7683–7693.

HERBERS, T. H. C., ORZECH, M., ELGAR, S. & GUZA, R. T. 2003 Shoaling transformation of wave frequency-directional spectra. *J. Geophys. Res.* **108**, doi:10.1029/2001JC001304.

HERBERS, T. H. C., RUSSNOGLE, N. R. & ELGAR, S. 2000 Spectral energy balance of breaking waves within the surf zone. *J. Phys. Oceanogr.* **30**, 2723–2737.

HERTERICH, K. & HASSELMANN, K. 1980 A similarity relation for the non-linear energy transfer in a finite-depth gravity-wave spectrum. *J. Fluid Mech.* **97**, 215–224.

HOEFEL, F. & ELGAR, S. 2003 Wave-induced sediment transport and sandbar migration. *Science* **299**, 1885–1887.

Hogan, S. J., Gruman, I. & Stiassnie, M. 1988 On the changes in phase speed of one train of water waves in the presence of another. *J. Fluid Mech.* **192**, 97–114.

Holloway, G. 1979 On the spectral evolution of strongly interacting waves. *Geophys. Astrophys. Fluid Dynamics* **11**, 271–287.

Holloway, G. & Hendershott, M. C. 1977 Stochastic closure for nonlinear rossby waves. *J. Fluid Mech.* **82**, 747–765.

Holthuijsen, L. H., Herman, A. & Booij, N. 2003 Phase-coupled refraction-diffraction for spectral wave models. *Coastal Eng.* **49**, 291–305.

Isobe, M. & Kraus, N. C. 1983 Derivation of a third-order Stokes wave theory. Tech. rep. no.83-1. Dep. Civil Eng., Yokohama Nat. Universit.

Ito, Y. & Tanimoto, K. 1972 A method of numerical analysis of wave propagation: Application to wave diffraction and refraction. In *Proc. 13$^{th}$ Int. Conf. Coastal Eng.*, pp. 503–522. ASCE.

Janssen, T. T., Battjes, J. A. & Van Dongeren, A. R. 2003 Long waves induced by short-wave groups over a sloping bottom. *J. Geophys. Res.* **108** (C8), doi:10.1029/2002JC001515.

Janssen, T. T., Herbers, T. H. C. & Battjes, J. A. 2004 A discrete spectral evolution model for nonlinear waves over 2D topography. In *Proc. 29$^{th}$ Int. Conf. Coastal Eng.*, pp. 119–131. ASCE.

Janssen, T. T., Herbers, T. H. C. & Battjes, J. A. 2006 Generalized evolution equations for nonlinear surface gravity waves over two-dimensional topography. *J. Fluid Mech.* **552**, 393–418.

Janssen, T. T., Kamphuis, J. W., Van Dongeren, A. R. & Battjes, J. A. 2000 Observations of long waves on a uniform slope. In *Proc. 27$^{th}$ Int. Conf. Coastal Eng.*, pp. 2192–2205. ASCE.

Janssen, T. T., Van Dongeren, A. R. & Kuiper, C. 2001 Phase resolving analysis of multidirectional wave trains. In *4$^{th}$ International Symposium on Ocean Wave Measurement and Analysis*. ASCE.

Johnson, J. W., Fuchs, R. A. & Morison, J. R. 1951 The damping action of submerged breakwaters. *Eos Trans. AGU* **32** (5), 704–718.

Jolas, P. 1960 Passage de la houle sur un seuil. *La Houille Blanche* **15** (2), 148–151, (in French).

Kadomtsev, B. B. & Petviashvili, V. I. 1970 On the stability of solitary waves in weakly dispersing media. *Sov. Phys. Doklady* **15**, 539–541.

Kaihatu, J. M. 2001 Improvement of parabolic nonlinear dispersive wave model. *J. Wat., Port, Coast. Ocean Eng.* **127** (2), 113–121.

Kaihatu, J. M. & Kirby, J. T. 1995 Nonlinear transformation of waves in finite water depth. *Phys. Fluids* **7**, 1903–1914.

Kelland, P. 1840 On the theory of waves: Part 1. *Trans. R. Soc. Edinburgh* **14**, 497–545.

Keller, J. B. 1988 Resonantly interacting water waves. *J. Fluid Mech.* **191**, 529–534.

Kennedy, A. B. & Kirby, J. T. 2003 An unsteady wave driver for narrowbanded waves: modeling nearshore circulation driven by wave groups. *Coastal Eng.* **48**, 257–275.

Kim, Y. C. & Powers, E. J. 1979 Digital bispectral analysis and its applications to nonlinear wave interactions. *Trans. plasma science* **7** (2), 120–131.

Kinsman, B. 1965 *Wind waves, their generation and propagation on the ocean surface*. NJ,USA: Prentice-Hall.

Kirby, J. T. 1986 Higher-order approximations in the parabolic equation method for water waves. *J. Geophys. Res.* **91**, 933–952.

Kirby, J. T. 1995 Nonlinear, dispersive long waves in water of variable depth. In *Gravity waves in water of finite depth* (ed. J. N. Hunt), , vol. 10, pp. 55–125. Comp. Mech. Publ., Adv. in Fluid Mech.

Kirby, J. T. 1998 Discussion of 'note on a nonlinearity parameter of surface waves' by S. Beji. *Discusion in Coast. Eng.* **34**, 163–168.

Kirby, J. T. & Dalrymple, R. A. 1983 A parabolic equation for the combined refraction-diffraction of Stokes waves by mildly-varying topography. *J. Fluid Mech.* **136**, 453–466.

Klopman, G. & Van Leeuwen, P. J. 1990 An efficient method for the reproduction of non-linear waves. In *Proc. 22$^{nd}$ Int. Conf. Coastal Eng.*, pp. 478–488. ASCE.

Kofoed-Hanssen, H. & Rasmussen, J. H. 1998 Modelling of nonlinear shoaling based on stochastic evolution equations. *Coastal Eng.* **33**, 203–232.

Komen, G. J., Cavaleri, M., Donelan, M., Hasselmann, K., Hasselmann, S. & Janssen, P. A. E. M. 1994 *Dynamics and modelling of ocean waves*. London: Cambridge University Press.

Korteweg, D. J. & De Vries, G. 1895 On the change of form of long waves advancing in a rectangular channel, and on a new type of long stationary waves. *Phil. Mag.* **39**, 422–443.

Kostense, J. K. 1984 Measurements of surf beat and setdown beneath wave groups. In *Proc. 19$^{th}$ Int. Conf. Coastal Eng.*, pp. 724–740. ASCE.

Lamb, H. 1932 *Hydrodynamics*, 6th edn. NY, USA: Dover.

Lau, J. & Barcilon, A. 1972 Harmonic generation of shallow water waves over topography. *J. Phys. Oceanogr.* **2**, 405–410.

Lesieur, M. 1997 *Turbulence in fluids*, 3rd edn. Dordrecht, The Netherlands: Kluwer Academic Publishers.

Leslie, D. 1973 *Developments in the theory of turbulence*. Oxford: Oxford: Clarendon Press.

Lighthill, J. 1978 *Waves in fluids*. Cambridge University Press.

List, J. H. 1992 A model for the generation of 2-dimensional surfbeat. *J. Geophys. Res.* **97** (C4), 5623–5635.

Liu, P. L. F. 1989 A note on long waves induced by short wave groups over a shelf. *J. Fluid Mech.* **205**, 163–170.

Liu, P. L. F. & Dingemans, M. W. 1989 Derivation of the third-order evolution equations for weakly nonlinear water waves propagating over uneven bottoms. *Wave Motion* **11**, 41–64.

Liu, P. L. F., Yoon, S. B. & Kirby, J. T. 1985 Nonlinear refraction-diffraction of waves in shallow water. *J. Fluid Mech.* **153**, 185–.

Lo, E. & Mei, C. C. 1985 A numerical study of water-wave modulation based on a higher-order nonlinear Schrödinger equation. *J. Fluid Mech.* **150**, 395–416.

Longuet-Higgins, M. S. & Phillips, O. M. 1962 Phase velocity effects in tertiary wave interaction. *J. Fluid Mech.* **12**, 333–336.

Longuet-Higgins, M. S. & Stewart, R. W. 1962 Radiation stress and mass transport in gravity waves, with application to 'surf beats'. *J. Fluid Mech.* **13**, 481–504.

Longuet-Higgins, M. S. & Stewart, R. W. 1964 Radiation stresses in water waves: a physical discussion, with applications. *Deep Sea Res.* **11**, 529–562.

Luth, H. R., Klopman, G. & Kitou, N. 1994 Kinematics of waves breaking partially on an offshore bar; ldv measurements for waves with and without a net onshore current. Delft-hydraulics report h1573. Delft Hydraulics.

Mach, E. 1926 *The principles of physical optics*. Dover.

Madsen, O. S. & Mei, C. C. 1969 The transformation of a solitary wave over an uneven bottom. *J. Fluid Mech.* **39** (4), 781–791.

Madsen, O. S., Mei, C. C. & Savage, R. P. 1970 The evolution of time-periodic long waves of finite amplitude. *J. Fluid Mech.* **44** (1), 195–208.

Madsen, P. A., Bingham, H. B. & Schäffer, H. A. 2003 Boussinesq-type formulations for fully nonlinear and extremely dispersive water waves: derivation and analysis. *Proc. Roy. Soc. Lond. A* **459**, 1075–1104.

Madsen, P. A. & Schäffer, H. A. 1998 Higher-order Boussinesq-type equations for surface gravity waves: derivation and analysis. *Proc. Roy. Soc. Lond. A* **356**, 3123–3184.

Madsen, P. A. & Schäffer, H. A. 1999 A review of Boussinesq-type equations for gravity waves. In *Adv. Coast. Eng.* (ed. P.-F. Liu), , vol. 5, pp. 1–94. Singapore: World Scientific.

Madsen, P. A. & Sørensen, O. R. 1992 A new form of the Boussinesq equations with improved linear dispersion characteristics. Part 2: A slowly varying bathymetry. *Coastal Eng.* **18** (4), 183–204.

Madsen, P. A. & Sørensen, O. R. 1993 Bound waves and triad interactions in shallow water. *Ocean Eng.* **15**, 371–388.

Mallat, S. 1998 *A wavelet tour of signal processing*. Academic Press.

Mansard, E. P. D. & Barthel, V. 1984 Shoaling properties of bounded long waves. In *Proc. 19$^{th}$ Int. Conf. Coastal Eng.*, pp. 798–814. ASCE.

MANSARD, E. P. D. & FUNKE, E. R. 1980 The measurement of incident and reflected spectra using a least squares method. In *Proc. 17<sup>th</sup> Int. Conf. Coastal Eng.*, pp. 154–172. ASCE.

MARDIA, K. V. & JUPP, P. E. 2000 *Directional statistics*. NY,USA: John Wiley & Sons, inc.

MASE, H. & KIRBY, J. T. 1992 Hybrid frequency-domain kdv equation for random wave transformation. In *Proc. 23<sup>rd</sup> Int. Conf. Coastal Eng.*, pp. 474–487. ASCE.

MASSELINK, G. 1995 Group bound long waves as a source of infragravity energy in the surf zone. *Cont. Shelf Res.* **15**, 1525–1547.

McKEE SMITH, J. & VINCENT, C. L. 2003 Equilibrium ranges in surf zone wave spectra. *J. Geophys. Res.* **108** (C11), doi:10.1029/2003JC001930.

MEI, C. C. 1983 *The Applied Dynamics of Ocean Surface Waves*. NY, USA: John Wiley & Sons, inc.

MEI, C. C. 1985 Resonant reflection of surface water waves by periodic sandbars. *J. Fluid Mech.* **152**, 315–335.

MEI, C. C. & BENMOUSSA, C. 1984 Long waves induced by short-wave groups over an uneven bottom. *J. Fluid Mech.* **130**, 219–235.

MEI, C. C. & LEMÉHAUTÉ 1966 Note on the long waves over an uneven bottom. *J. Geophys. Res.* **71**, 393–400.

MEI, C. C. & ÜNLÜATA, U. 1972 Harmonic generation in shallow water waves. In *Waves on beaches* (ed. R. E. Meyer), pp. 181–202. Academic Press.

MILES, J. W. 1957 On the generation of surface waves by shear flows. *J. Fluid Mech.* **3**, 185–204.

MOLIN, B. 1982 On the generation of long period second order free waves due to changes in the bottom profile. Rapp. ifp:30167 [also in: Ship. res. inst. rep. 68, tokyo, japan]. Inst. Francais du Petrol.

MUNK, W. H. 1949 Surf beats. *Eos Trans. AGU* **30** (6), 849–854.

MUNK, W. H. & TRAYLOR, M. A. 1947 Refraction of ocean waves: A process linking underwater topography to beach erosion. *J. of Geology* **LV**, 1–26.

NEWELL, A. & AUCOIN, P. J. 1971 Semidispersive wave systems. *J. Fluid Mech.* **49**, 593–609.

NORHEIM, C. A., HERBERS, T. H. C. & ELGAR, S. 1998 Nonlinear evolution of surface wave spectra on a beach. *J. Phys. Oceanogr.* **28**, 1534–1551.

NWOGU, O. 1993 Alternative form of Boussinesq equations for nearshore wave propagation. *J. Wat., Port, Coast. Ocean Eng.* **119**, 618–638.

OGURA, Y. 1962 Energy transfer in a normally distributed and isotropic turbulent velocity field in two dimensions. *Phys. Fluids* **5**, 395.

OKIHIRO, M., GUZA, R. T. & SEYMOUR, R. J. 1992 Bound infragravity waves. *J. Geophys. Res.* **97** (C7), 11,453–11,469.

OPPENHEIM, A. V. & SCHAFER, R. W. 1989 *Discrete-time signal processing*. New Jersey, USA: Prentice-Hall.

O'Reilly, W. C. & Guza, R. T. 1991 Comparison of spectral refraction and refraction-diffraction wave models. *J. Wat., Port, Coast. Ocean Eng.* **117** (3), 119–215.

Orszag, S. A. 1970 Analytical theories of turbulence. *J. Fluid Mech.* **41**, 363–386.

Orszag, S. A. 1972 Comparison of pseudospectral and spectral approximations. *Stud. Appl. Math.* **51**, 253–259.

Papoulis, A. 1968 *Systems and transforms with application in optics*. NY,USA: McGraw-Hill.

Penney, W. G. & Price, A. T. 1952 Part I. The diffraction theory of sea waves and the shelter afforded by breakwaters. *Phil. Trans. Roy. Soc. London* **244**, 236–253.

Peregrine, D. H. 1967 Long waves on a beach. *J. Fluid Mech.* **27**, 815–827.

Peregrine, D. H. 1983a Breaking waves on beaches. *Ann. Rev. Fluid Mech.* **15**, 149–178.

Peregrine, D. H. 1983b Water waves, nonlinear Schrödinger equations and their solutions. *J. Austral. Math. Soc. B* **25**, 16–43.

Phillips, O. M. 1957 On the generation of waves by turbulent wind. *J. Fluid Mech.* **2**, 417–445.

Phillips, O. M. 1960 On the dynamics of unsteady gravity waves of finite amplitude, 1, the elementary interactions. *J. Fluid Mech.* **9**, 193–217.

Phillips, O. M. 1977 *The Dynamics of the Upper Ocean*, 2nd edn. Cambridge University Press.

Phillips, O. M. 1981 Wave interaction – the evolution of an idea. *J. Fluid Mech.* **106**, 215–227.

Press, W. H., Flannery, B. P., Teukolsky, S. A. & Vetterling, W. T. 1986 *Numerical recipes*. NY, USA: Cambridge University Press.

Priestley, M. B. 1981 *Spectral analysis and time series*. Academic Press.

Proudman, I. & Reid, W. H. 1954 On the decay of a normally distributed and homogeneous turbulent field. *Phil. Trans. Roy. Soc. London* **A247**, 163.

Rasmussen, J. H. 1998 Deterministic and stochastic modelling of surface gravity waves in finite depth. PhD dissertation, University of Denmark, Lyngby, Denmark.

Rayleigh, A. M. 1876 On waves. *Phil. Mag.* **1** (4), 257–279.

Reniers, A. J. H. M., Van Dongeren, A. R., Battjes, J. A. & Thornton, E. B. 2002 Linear modelling of infragravity waves during Delilah. *J. Geophys. Res.* **107** (C10), 10.1029/2001JC001083.

Roelvink, J. A. 1993 Surf beat and its effect on cross-shore profiles. Phd dissertation, Delft University of Technology, Delft, The Netherlands.

Roelvink, J. A. & Stive, M. J. F. 1989 Bar-generating cross-shore flow mechanisms on a beach. *J. Geophys. Res.* **94** (C4), 4785–4800.

Ruessink, B. G. 1998 The temporal and spatial variability of infragravity energy in a barred nearshore zone. *Cont. Shelf Res.* **18**, 585–605.

RUESSINK, B. G., MILES, J. R., FEDDERSEN, F., GUZA, R. T. & ELGAR, S. 2001 Modeling the alongshore current on barred beaches. *J. Geophys. Res.* **106**, 22,451–22,463.

RUSSELL, J. S. 1838 Report of the committee on waves. Report of the 7$^{th}$ meeting of the British assocation for the advancements of science.

RUSSELL, J. S. 1844 Report on waves. Report of the 14$^{th}$ meeting of the British assocation for the advancements of science.

SABRA, A. I. 1981 *Theories of light, from Descartes to Newton.* NY,USA: Cambridge University Press.

SAFFMAN, P. G. 1967 Discussion on: Nonlinear interactions treated by the methods of theoretical physics. *Proc. Roy. Soc. Lond. A* **299**, 101–103.

SALMON, R. 1998 *Lectures on Geophysical Fluid Dynamics*, 1st edn. New York: Oxford University Press, 378 p.

SCHÄFFER, H. 1993 Infragravity waves induced by short wave groups. *J. Fluid Mech.* **247**, 551–588.

SEGUR, H. & FINKEL, A. 1985 An analytical model of periodic waves in shallow water. *Stud. Appl. Math.* **73**, 183–220.

SHEMER, L., JIAO, H., KIT, E. & AGNON, Y. 2001 Evolution of a nonlinear wave field along a tank: experiments and numerical simulations based on the spatial Zakharov equation. *J. Fluid Mech.* **427**, 107–129.

SHEMER, L., KIT, E., JIAO, H. & EITAN, O. 1998 Experiments on nonlinear wave groups in intermediate water depth. *J. Wat., Port, Coast. Ocean Eng.* **124**, 320–327.

SHEREMET, A. 1996 Wave interactions in shallow water. Ph.d. thesis, Technion, Haifa, Israel.

SHI, F., DALRYMPLE, R. A., KIRBY, J. T., CHEN, Q. & KENNEDY, A. B. 2001 A fully nonlinear Boussinesq model in generalized curvilinear coordinates. *Coastal Eng.* **42** (4), 337–358.

SOMMERFELD, A. 1896 Mathematische theorie der diffraktion. *Math. Ann.* **47**, 317–374, (in German).

STAMNES, J. J. 1986 *Waves in focal regions.* Adam Hilger.

STEENBERGEN, G. J. A. M. 2005 Bi-directional decomposition of subharmonic gravity waves. MSc-thesis. Delft University of Technology.

STELLING, G. & ZIJLEMA, M. 2003 An accurate and efficient finite-difference algorithm for non-hydrostatic free-surface flow with application to wave propagation. *Int. J. Num. Meth. Fluids* **43**, 1–23.

STIASSNIE, M. & SHEMER, L. 1984 On modifications of the Zakharov equation for surface gravity waves. *J. Fluid Mech.* **143**, 47–67.

STOKES, G. G. 1847 On the Theory of Oscillatory Waves. *Trans. Cambr. Philos. Soc.* **8**, 441–455.

STOKES, G. G. 1880 Supplement to a paper on the theory of oscillatory waves. In *Math. Phys. Papers*, pp. 314–326. Cambridge University Press.

SUH, K. D., DALRYMPLE, R. A. & KIRBY, J. T. 1990 An angular spectrum model for propagation of Stokes waves. *J. Fluid Mech.* **221**, 205–232.

SYMONDS, G. & BOWEN, A. J. 1984 Interactions of nearshore bars with incoming wave groups. *J. Geophys. Res.* **89** (C2), 1953–1959.

SYMONDS, G., HUNTLEY, D. A. & BOWEN, A. J. 1982 Two dimensional surfbeat: long wave generation by a time varying breakpoint. *J. Geophys. Res.* **87** (C1), 492–498.

TANG, Y. & OUELLET, Y. 1997 A new kind of nonlinear mild-slope equation for combined refraction-diffraction of multifrequency waves. *Coastal Eng.* **31**, 3–36.

THORNTON, E. B. & GUZA, R. T. 1983 Transformation of wave height distribution. *J. Geophys. Res.* **88**, 5925–5938.

TOLMAN, H. L. 1991 A third-generation model for wind waves on slowly varying, unsteady and inhomogeneous depths and currents. *J. Phys. Oceanogr.* **21**, 782–797.

TUCKER, M. J. 1950 Surf beats: sea waves of 1 to 5 min. period. *Proc. Roy. Soc. Lond. A* **202**, 565–573.

TUCKER, M. J., CHALLENOR, P. G. & CARTER, D. J. T. 1984 Numerical simulation of random seas: a common error and its effect upon wave group statistics. *Appl. Ocean Res.* **6**, 118–122.

VAN DONGEREN, A. R., BATTJES, J. A., JANSSEN, T. T., NOORLOOS, J., STEENHAUER, K., STEENBERGEN, G. J. A. M. & RENIERS, A. J. H. M. 2005 Shoaling and shoreline dissipation of subharmonic gravity waves. *under preparation* .

VAN DONGEREN, A. R., NOORLOOS, J., STEENHAUER, K., BATTJES, J. A., JANSSEN, T. T. & RENIERS, A. J. H. M. 2004 Shoaling and shoreline dissipation of subharmonic gravity waves. In *Proc. 29$^{th}$ Int. Conf. Coastal Eng.*, pp. 1225–1237. ASCE.

VAN DONGEREN, A. R., RENIERS, A. J. H. M., BATTJES, J. A. & SVENDSEN, I. A. 2003 Numerical modeling of infragravity wave response during Delilah. *J. Geophys. Res.* **108** (C9), 10.1029/2002JC001332.

VAN LEEUWEN, P. J. 1992 Low frequency wave generation due to breaking waves. Phd dissertation, Delft Univ. of Techn., Delft, The Netherlands.

VAN LEEUWEN, P. J. & BATTJES, J. A. 1990 A model for surfbeat. In *Proc. 22$^{nd}$ Int. Conf. Coastal Eng.*, pp. 151–164. ASCE, Delft.

VINCENT, C. L. & BRIGGS, M. J. 1989 Refraction-diffraction of irregular waves over a mound. *J. Wat., Port, Coast. Ocean Eng.* **115** (2), 269–284.

WEI, G., KIRBY, J. T., GRILLI, S. T. & SUBRAMANYA, R. 1995 A fully nonlinear Boussinesq model for surface waves. I. Highly nonlinear, unsteady waves. *J. Fluid Mech.* **294**, 71–92.

WESTHUIS, J. 2001 The numerical simulations of nonlinear waves in a hydrodynamic model test basin. PhD dissertation, Twente University of Technology, Enschede, The Netherlands.

WHALIN, R. W. 1971 The limit of application of linear wave refraction theory in a convergence zone. Res. Rep. No. H-71-3. U.S. Army Engineer WES, Vicksburg(MS).

WHALIN, R. W. 1972 Wave refraction theory in a convergence zone. In *Proc. 13$^{th}$ Int. Conf. Coastal Eng.*, pp. 451–470. ASCE.

WHITHAM, G. B. 1974 *Linear and nonlinear waves*. NY, USA: World Scientific, 636p.

WIGNER, E. 1932 On the quantum correction for thermodynamic equilibrium. *Phys. Rev.* **40**, 749–759.

WILLEBRAND, J. 1973 Energy transport in a nonlinear and inhomogeneous random gravity wave field. PhD dissertation, Der Christian-Albrechts-Universität, Kiel, Germany.

WILLEBRAND, J. 1975 Energy transport in a nonlinear and inhomogeneous random gravity wave field. *J. Fluid Mech.* **70**, 113–126.

WILLMOTT, C. J. 1981 On the validation of models. *Phys. Geogr.* **2** (2), 219–232.

YOUNG, I. R. 1989 Wave transformation over coral reefs. *J. Geophys. Res.* **94** (C7), 9779–9789.

ZABUSKY, N. J. 1981 Computational synergetics and mathematical innovation. *J. Comp. Phys.* **43**, 195–249.

ZABUSKY, N. J. & KRUSKAL, M. D. 1965 Interaction of 'solitons' in a collisionless plasma and the recurrence of initial states. *Phys. Rev. Lett.* **15**, 240–243.

ZAKHAROV, V. E. 1968 Stability of periodic waves of finite amplitude on the surface of a deep fluid. *J. Appl. Mech.* **4**, 86–94.

ZAKHAROV, V. E. & SHABAT, P. B. 1972 Exact theory of two-dimensional self-focusing and one-dimensional self-modulation of waves in nonlinear media. *Sov. Phys. JETP* **34**, 62–69.

ZELT, J. A. & SKJELBREIA, J. E. 1992 Estimating incident and reflected wave fields using an arbitrary number of wave gauges. In *Proc. 23$^{rd}$ Int. Conf. Coastal Eng.*, pp. 777–789. ASCE, Venice.

# List of Figures

# List of main symbols

## Roman symbols

| Symbol | Description |
| --- | --- |
| $a$ | wave surface elevation amplitude [m] |
| $A_i, A_i^i$ | flux amplitude [$\mathrm{m}^{3/2}/\mathrm{s}^{1/2}$] |
| $B$ | breaking intensity |
| $\mathcal{B}_{ij}^{ij}$ | bispectral density [$\mathrm{m}^5\mathrm{s}^2/\mathrm{rad}^4$] |
| $C$ | phase speed [m/s] |
| $C_g$ | group speed [m/s] |
| $C_{ij}^{ijk}$ | flux bispectrum [$\mathrm{m}^{9/2}/\mathrm{s}^{3/2}$] |
| $\mathcal{C}_{ij}^{ijk}$ | flux bispectral density [$\mathrm{m}^{15/2}\mathrm{s}^{1/2}/\mathrm{rad}^5$] |
| $C_{ij}^{(4)}$ | flux fourth cumulant [$\mathrm{m}^{9/2}/\mathrm{s}^{3/2}$] |
| $\mathcal{C}_{ij}^{(4)}$ | flux fourth cumulant [$\mathrm{m}^{9/2}\mathrm{s}^{1/2}/\mathrm{rad}^2$] |
| $d$ | Willmott index |
| $D$ | bulk breaking dissipation rate [$\mathrm{m}^2/\mathrm{s}$] |
| $D_i$ | frequency weighted breaking dissipation rate [1/m] |
| $\mathcal{D}_{i,j}$ | quadratic interaction coefficient potential evolution [$1/(\mathrm{m}^2\mathrm{s})$] |
| $E_i^{ij}$ | flux spectrum [$\mathrm{m}^3/\mathrm{s}$] |
| $\mathcal{E}_i^{ij}$ | flux density spectrum [$\mathrm{m}^5/\mathrm{rad}^3$] |
| $f$ | frequency [1/s] |
| $f_p$ | peak frequency [1/s] |
| $F_{a_m}^{(n,m)}$ | $n$-th order bottom boundary forcing term (free waves, $m=1$; bound waves $m=2$) [m/s] |
| $\mathcal{F}_i$ | integrated short-wave forcing [$\mathrm{m}^6/(\mathrm{s\ rad})$] |
| $g$ | gravitational acceleration [$\mathrm{m}/\mathrm{s}^2$] |
| $h$ | (still) water depth [m] |
| $h^*$ | dynamically delimited (still) water depth [m] |
| $\overline{h}$ | laterally averaged depth [m] |
| $\widetilde{h}$ | residual depth [m] |
| $h_m$ | half the lateral range of depth $h$ [m] |
| $h_m^*$ | half the lateral range of delimited depth $h^*$ [m] |
| $H_b$ | breaking wave height [m] |
| $H_{m0}$ | zeroth moment wave height [m] |
| $H_{rms}$ | root-mean-square wave height [m] |

*Continued on next page*

| Symbol | Description |
|---|---|
| $H_{a_m}^{(n,m)}$ | $n$-th order free surface boundary forcing term (free waves, $m=1$; bound waves, $m=2$) $[\text{m}^2/\text{s}^2]$ |
| $k$ | scalar wavenumber $[\text{rad/m}]$ |
| $\overline{k}$ | laterally averaged wavenumber $[\text{rad/m}]$ |
| $\widetilde{k}$ | wavenumber correction $[\text{rad/m}]$ |
| $\boldsymbol{k}$ | wavenumber vector $[\text{rad/m}]$ |
| $\mathcal{R}_{i,j}$ | quadratic interaction coefficient nonlinear relation potential free surface elevation $[1/\text{m}^2]$ |
| $m_n$ | $n$-th moment variance spectrum $[\text{m}^2(\text{rad/s})^n]$ |
| $\widetilde{m}_n$ | $n$-th moment flux spectrum $[\text{m}^3/\text{s} \ (\text{rad/s})^n]$ |
| $\mathcal{P}_i$ | integrated long/short-wave coupling $[\text{s}^{1/2}/\text{m}^{3/2}]$ |
| $Q$ | fraction of broken waves |
| $R_{a_m}^{(n,m)}$ | $n$-th order fluid body forcing term (free waves, $m=1$; bound waves, $m=2$) $[1/\text{s}]$ |
| $RS$ | radiation stress function $[\text{kg/s}^2]$ |
| $S_0$ | offshore steepness |
| $S_i^i$ | wave-bottom interaction forcing contribution $[1/(\text{sm})^{1/2}]$ |
| $S_{a_m}^{(n,m)}$ | $n$-th order free surface boundary condition forcing term (free waves, $m=1$; bound waves, $m=2$) $[\text{m}^2/\text{s}^3]$ |
| $\mathcal{S}_i^i$ | variance density spectrum $[\text{m}^3\text{s}/\text{rad}^2]$ |
| $V_i, V_i^i$ | principal component group speed vector $[\text{m/s}]$ |
| $\mathcal{W}_{i,j}, \mathcal{W}_{ij}^{ij}$ | composite quadratic interaction coefficient flux amplitude $[\text{s}^{1/2}/\text{m}^{5/2}]$ |
| $x$ | principal horizontal coordinate $[\text{m}]$ |
| $y$ | lateral horizontal coordinate $[\text{m}]$ |
| $z$ | vertical coordinate $[\text{m}]$ |
| $\mathcal{Z}_{i,j}, \mathcal{Z}_{ij}$ | composite quadratic interaction coefficient surface elevation amplitude evolution $[1/\text{m}^2]$ |

## Greek symbols

| Symbol | Description |
|---|---|
| $\beta$ | bispectral relaxation strength parameter |
| $\gamma$ | wave height/depth ratio |
| $\delta^{\lambda,\omega}$ | discrete delta function |
| $\delta^{(r)}$ | normalized resonance mismatch |
| $\Delta_{a_m}$ | resonance mismatch (free waves, $m=1$; bound waves, $m=2$) |
| $\epsilon$ | wave steepness |

| Symbol | Description |
|---|---|
| $\zeta_{a_m}^{(n,m)}$ | $n$-th order slowly varying angular component amplitude surface elevation (free waves, $m = 1$; bound waves, $m = 2$) [m] |
| $\widetilde{\zeta}_{a_m}^{(n,m)}$ | $n$-th order angular component amplitude surface elevation (free waves, $m = 1$; bound waves, $m = 2$) [m] |
| $\eta$ | surface elevation function [m] |
| $\eta^{(n,m)}$ | $n$-th order surface elevation (free waves, $m = 1$; bound waves, $m = 2$) [m] |
| $\overline{\overline{\eta}}$ | mean-flow surface elevation [m] |
| $\theta$ | wave angle |
| $\kappa$ | principal component wave number vector [rad/m] |
| $\lambda$ | lateral component wave number vector [rad/m] |
| $\Lambda_{i,j}, \Lambda_{ij}^{ij;k}$ | principal wavenumber mismatch [rad/m] |
| $\mu$ | relative water depth |
| $\mu_V$ | mean of signal V |
| $\mu_{ij}, \mu_{ij}^{ijk}$ | bispectral damping/relaxation [1/m] |
| $\xi_i\{\}$ | forcing operator for wave-bottom, wave-current and wave-wave-wave interactions on non-stationary evolution equation for velocity potential amplitude |
| $\Xi\{\}$ | forcing operator for wave-bottom, wave-current and wave-wave-wave interactions on stationary evolution equation for flux amplitude |
| $\widetilde{\Xi}\{\}$ | forcing operator for wave-bottom, wave-current, wave-wave, and wave-wave-wave interactions on stationary evolution equation for velocity potential amplitude |
| $\rho_{VY}$ | cross-correlation coefficient function between subscripted signals Y and V |
| $\sigma$ | frequency spectrum spreading parameter [rad/s] |
| $\sigma_D$ | directional spectrum spreading parameter [rad] |
| $\tau$ | time lag [s] |
| $\phi_{a_m}^{(n,m)}$ | slowly varying, $n$-th order velocity potential angular component (free waves, $m = 1$; bound waves, $m = 2$) [m$^2$/s] |
| $\widetilde{\phi}_{a_m}^{(n,m)}$ | $n$-th order velocity potential angular component (free waves, $m = 1$; bound waves, $m = 2$) [m$^2$/s] |
| $\Phi$ | velocity potential function [m$^2$/s] |
| $\Phi^{(n,m)}$ | $n$-th order velocity potential function (free waves $m = 1$, bound waves $m = 2$) [m$^2$/s] |
| $\varphi_{a_m}^{(n,m)}$ | slowly varying $n$-th order velocity potential angular component at $z = 0$ (free waves, $m = 1$; bound waves, $m = 2$) [m$^2$/s] |

| Symbol | Description |
|--------|-------------|
| $\widetilde{\varphi}_{a_m}^{(n,m)}$ | $n$-th order velocity potential angular component at $z = 0$ (free waves, $m = 1$; bound waves, $m = 2$) [m$^2$/s] |
| $\omega$ | angular frequency [rad/s] |
| $\overline{\omega}$ | mean angular frequency [rad/s] |

# Abbreviations/Acronyms

| Symbol | Description |
|--------|-------------|
| CRAD | Consistent RAyleigh Dissipation model |
| lf | low frequency |
| hf | high frequency |
| SAM | Stochastic Angular-spectrum Model |
| SAM2D | fully two-dimensional implementation of the Stochastic Angular-spectrum Model |
| SAM1D | one-dimensional (in the topography) implementation of Stochastic Angular-spectrum Model |
| SAMuD | unidirectional implementation of Stochastic Angular-spectrum Model |
| QN | Quasi-Normal |
| RQN | Relaxed Quasi-Normal |

# Curriculum Vitae

Geboren op 8 December 1973 te Heumen (gld), ben ik opgegroeid in het landelijke Hengevelde (ov). Mijn middelbaar onderwijs (Atheneum) genoot ik te Haaksbergen van 1986 tot 1992. Ik studeerde van 1992 tot 1993 Milieuhygiëne aan de Landbouwuniversiteit te Wageningen. Van 1993 tot 1999 studeerde ik Civiele Techniek aan de Technische Universiteit te Delft en na afronding van mijn studie in 1999 begon ik mijn ingenieurscarrière als zelfstandig technisch/strategisch adviseur (XS Engineerig Consult). In 2000 werd ik adviseur bij Delft Hydraulics, gecombineerd met een gedeeltelijke aanstelling als toegevoegd onderzoeker aan de TU Delft. Ik begon in 2001 als voltijds promovendus bij de TU Delft en in die hoedanigheid was ik gastonderzoeker bij het Woods Hole Institute of Oceanography te Woods Hole, Massachusetts (2001/2002) en de Naval Postgraduate School te Monterey, California (2002/2003). Het werk in het kader van mijn promotieonderzoek is vastgelegd in deze dissertatie, welke ik verdedig in mei 2006. Aansluitend begin ik in juni 2006 een aanstelling als post-doctoraal onderzoeker aan de Naval Postgraduate School te Monterey.